Investigations of Electron Transport Properties in Metal-Organic Frameworks for Catalytic Applications

Spencer R. Ahrenholtz

Dissertation submitted to the faculty of the Virginia Polytechnic Institute and State University in partial fulfillment of the requirements for the degree of

Doctor of Philosophy

In

Chemistry

Amanda J. Morris, Chair

John R. Morris

Brian M. Tissue

Louis A. Madsen

Karen J. Brewer

August 2, 2016

Blacksburg, Virginia

Keywords: metal-organic frameworks, MOFs, thin film, electron transport, gas storage, electrochemistry, catalysis, electrocatalysis, alternative energy, water oxidation

Investigations of Electron Transport Properties in Metal-Organic Frameworks for Catalytic Applications

Spencer R. Ahrenholtz

Abstract

Metal-organic frameworks (MOFs) have attracted much attention in the past few decades due to their ordered, crystalline nature, synthetic tunability, and porosity. MOFs represent a class of hybrid inorganic-organic materials that have been investigated for their applications in areas such as gas sorption and separation, catalysis, drug delivery, and electron or proton conduction. It has been the goal of my graduate research to investigate MOFs for their ability to transport electrons and store and separate gases for ultimate catalytic applications in alternative energy generation. I aim to provide new insight into the design and development of stable MOFs for such applications.

We first investigated a cobalt(III) porphyrin based MOF comprised of Co^{II}-carboxylate nodes, designated as CoPIZA, for its electron transport capabilities. Thin films of CoPIZA were formed solvothermally on conductive fluorine-doped tin oxide (FTO) substrates and used for electrochemical characterization. Electrochemistry coupled with spectroscopic analysis of the CoPIZA film revealed reversible reduction of the cobalt centers of the porphyrin linkers with maintenance of the overall framework structure. The mechanism of charge transport throughout the film was facilitated by redox hopping of electrons between the metal centers of the nodes and linkers.

The ability to incorporate desired properties, such as pore functionalities or open metal centers, into frameworks makes them attractive for applications in separation of gaseous mixtures, such as CO_2/N_2 from combustion power plants. To investigate the selective adsorption

properties, we performed gas sorption measurements on bulk MOF materials to determine their affinity toward CO_2. Two Zn-based MOFs containing 2,5-pyridine dicarboxylate linkers were prepared in our laboratory and contained unsaturated Zn(II) metal centers, which possess a binding site on the metal without an activation procedure to remove bound solvent molecules. These MOFs were compared to the well-known Zn-based MOF-69C containing 1,4-benzene dicarboxylate linkers. Thermodynamic analysis of the gas sorption data revealed that the mechanism of CO_2 binding involved the coordinatively unsaturated Zn(II) center. The microporous MOF also demonstrated selectivity for CO_2 over N_2 under the same conditions. As these materials were able to uptake CO_2, their ability to transport electrons was also investigated for ultimate applications in catalysis. Electrochemical impedance spectroscopy was performed on the bulk MOF powders and was coupled with solid-state nuclear magnetic resonance spectroscopy. These results determined that the conduction mechanism proceeded via solvent molecules within the pores of the framework.

The catalytic ability toward water oxidation of two MOFs was investigated electrochemically. Initial studies focused on a cobalt-based MOF comprised of 2-pyrimidinolate (pymo) linkers, designated as $Co(pymo)_2$, which was prepared on FTO via drop-casting and used for electrochemical experiments. At applied anodic potentials, the Co^{II} centers of $Co(pymo)_2$ became oxidized to form a Co-oxide species on the electrode surface, which was found to be the active catalysis for water oxidation. Further investigations utilized a notably more stable Zr-based MOF with nickel(II) porphyrin linkers, designated as PCN-224-Ni. PCN-224-Ni was prepared solvothermally on FTO and used directly for electrochemical water oxidation. The mechanism of water oxidation at PCN-224-Ni proceeds via oxidation of the porphyrin macrocycle followed by binding of water to the Ni(II) center. Cooperative proton transfer to the

Zr-oxo node facilitated water oxidation with the eventual release of O_2. Thorough characterization revealed that PCN-224-Ni retained its structural integrity over the course of electrochemical catalysis.

These results have allowed us a deeper understanding of the mechanisms of electron transport and conduction throughout frameworks. Specifically, the incorporation of metalloporphyrin molecules with redox active metal centers coupled with the presence of redox active metal nodes resulted in redox hopping charge transport throughout the MOF. In addition, the presence of solvent molecules in the pores of the framework provided an extended network for charge transport. We have gained insight into the structure-function relationship of MOFs for applications in selective gas sorption, where an unsaturated metal center serves as the binding site for gas molecules. Finally, through selection of the components that comprise the framework, a stable metalloporphyrin MOF was found to be capable of electrochemically facilitating the water oxidation reaction. As a result, we have gained valuable insight into the properties of frameworks necessary for charge transport and stability, which will allow for further improvements in the smart design of MOFs for catalytic applications.

Acknowledgements

First, I would like to thank my graduate advisor, Professor Amanda Morris. I began as a young, naive graduate student in your lab who could barely set up a reflux condenser, which eventually resulted in a trip to the emergency room. Under your guidance and mentorship, I was able to mature into the confident scientist I am today. I am incredibly thankful for the faith you put in me, as well as for the opportunities you have provided to me. You have taught me so many things, not only about science, but also about life in general, that will always be with me. I would also like to thank Professor Felicia Etzkorn for mentoring me during my first year of graduate school and allowing me to follow my passion.

I owe much appreciation to my other committee members, Professors John Morris, Brian Tissue, and Louis Madsen. I began as a first year graduate student in classes with both Professor Morris and Professor Tissue, and at times had absolutely no idea what I was doing or how I was going to answer a question on the midterm. You have both been there throughout my graduate career to teach and mentor me, and your guidance has been invaluable to me. I am also deeply appreciative to Professor Madsen for stepping in on my committee during my final graduate school years. While you might now be mentoring me in an official capacity, I have always thought of you as a mentor and appreciate the advice you have given me. I owe a great deal of thanks to the late Professor Karen Brewer, who served on my committee for my first three years of graduate school. Her comments to me after committee meetings often included things such as "you need to relax", which has been great advice and something that I have kept with me throughout my graduate career.

I am also incredibly thankful to the Virginia Tech Department of Chemistry and all of the support they have provided to me throughout my graduate studies. I am very proud to have

Virginia Tech on my degree and to be a Hokie for the rest of my life. I owe a great deal of thanks to Dr. Carla Slebodnick for her mentorship and assistance with single crystal data collection and analysis. To everyone who provided analytical and technical support, including Ms. Joli Huynh, Mr. Larry Jackson, Mr. John Burleson, Mr. Tom Wertalik, Ms. Sharelle Carbaugh, and the many others who work to ensure our research carries on smoothly, I am deeply appreciative. Thank you to the Institute for Critical Technology and Applied Science at Virginia Tech, as well as the U.S. Department of Energy Office of Basic Energy Sciences and the National Science Foundation for providing generous financial support of my research, including several years of Research Assistantship support.

To the past and present members of the Morris research group, I am so thankful to have been able to learn and grow as scientists together. I owe much appreciation to Dr. William Maza, who mentored me as a post-doc in our lab for several years, as well as to Charity C. Epley, whose support and friendship helped me tremendously throughout my graduate career. To the wonderful friends I have made along this journey, I am so grateful to have met you and shared this experience with you.

To my wonderful husband, Bryce Kidd, I do not think I would have made it this far without you to push and support me along the way. You have always believed in me and encouraged me to be the best that I can be, and I am so proud to stand by your side. I thank my incredible parents, Ray and Laurie Ahrenholtz, for their never-ending love and support they have provided throughout everything I choose to pursue. I owe a great deal of my success to all of you for your undying encouragement.

Table of Contents

Attributions

Chapters 2 and 3 of this dissertation were written using published manuscripts to which the author, Spencer R. Ahrenholtz (S.R.A.), majorly contributed. Chapter 6 of this manuscript has been submitted for publication. The contributions of the co-authors to the presented chapters are as follows:

Chapter 2. S.R.A. performed experiments and assisted with manuscript writing and editing. Charity C. Epley performed SEM imaging experiments on the thin films. Dr. Amanda J. Morris, principle investigator, supervised the research project and provided technical insight during experimentation and assisted in writing and editing.

Chapter 3. S.R.A. synthesized and characterized the materials to be used for the gas sorption analysis studies and helped write the manuscript. Carlos Landaverde-Alvarado and S.R.A. performed the gas sorption measurements and fit experimental data to mathematical models. Macauley Whiting, former Amanda J. Morris group member, first synthesized the MOFs, whose structures were determined using single crystal X-ray diffraction by Dr. Carla Slebodnick. Shaoyang Lin performed thermogravimetric analysis on MOF samples. Dr. Eva Marand, Professor in the Department of Chemical Engineering at Virginia Tech and advisor of C.L.A., provided technical insight during experimentation. Dr. Amanda J. Morris was the principle investigator, supervised the research project, and provided technical insight during experimentation and assisted in writing and editing.

Chapter 4. S.R.A. synthesized the MOFs and performed the experiments. Bryce E. Kidd performed solid-state NMR experiments under the advisement of Dr. Louis A. Madsen. Dr. Amanda J. Morris was the principle investigator, supervised the research project, and provided technical insight during experimentation.

Chapter 5. S.R.A. synthesized and characterized the MOF and performed the experiments. Benjamin Q. Kolb was an undergraduate researcher on the project and assisted in the data collection. Charity C. Epley performed SEM imaging as well as EDX analysis of the thin films. Dr. Amanda J. Morris was the principle investigator, supervised the research project, and provided technical insight during experimentation.

Chapter 6. S.R.A. and Dr. Pavel M. Usov performed catalytic experiments and co-wrote the paper. Dr. William A. Maza initiated catalytic investigations and contributed intellectually and to the writing of the paper. Bethany Stratakes was an undergraduate researcher on the project and performed electrochemical experiments. Charity C. Epley took the SEM images of the films. Matthew C. Kessinger performed XPS measurements. Jie Zhu prepared samples for ICP-MS analysis. Dr. Amanda J. Morris oversaw the development and execution of the research.

1. Introduction

1.1 Research Motivation

The motivation behind this research has been the increasing global energy demand and the imminent need for alternative, renewable energy sources.[1] The combustion of carbon-based fossil fuels accounts for approximately 80% of our global energy consumption.[2] While there are currently enough fossil fuels to continue to supply the increasing energy demand, their quantity is limited, non-renewable, and their utilization results in the release of significant quantities of greenhouse gases, irreparably altering the global environment.[1] In fact, the burning of fossil fuels accounts for ~ 80% of the total anthropogenic CO_2 emissions, which are projected to increase further.[3,4] Therefore, one of the greatest challenges facing our civilization is the development of a clean, sustainable energy source capable of satisfying the world's increasing energy demands, as well as the development of materials for capture and utilization of greenhouse gases and reduce their atmospheric concentrations.[4,5]

1.1.1 Solar energy

Solar energy is an abundant, inexpensive, clean, and renewable carbon-neutral energy source. In fact, in just 1.5 hours, enough energy from the sun reaches the Earth's surface to fulfill the world's energy demands for an entire year.[6] The implementation of solar energy resources would decrease dependence on fossil fuels, ensuring national energy security and providing a safer, more stable global political environment.[7] However, the primary challenge of utilizing solar energy is the variable amount of available sunlight based on daily and seasonal cycles, as

well as geographical location. Therefore, an efficient means of capturing the energy when it is available and storing it until needed is an essential requirement for solar energy to be readily deployed on a large-scale basis.[8,9]

1.1.2 Artificial photosynthetic approaches

Biology has evolved the ability to store energy from sunlight in the form of chemical bonds in organic molecules through photosynthesis, providing much of the energy needed to sustain life on Earth. The great success of this energy generation process is a result of the abundance of the needed raw materials (i.e., sunlight, carbon dioxide, and water).[10] In plants, this process occurs at Photosystem II, where a manganese-oxide cluster catalyzes the thermodynamically unfavorable water oxidation reaction to produce oxygen gas, protons and electrons (Equation 1.1).[8,9,11]

$$2H_2O \rightarrow O_2 + 4H^+ + 4e^- \qquad (1.1)$$

Artificial photosynthesis research focuses on the development of chemical systems that can mimic the biological process, transforming solar energy into chemical energy. These systems must be robust, efficiently capture sunlight, separate charge, and perform electron transfer events that result in the oxidation of water near the thermodynamic limit (at pH 0 and 25 °C, $E° = 1.23$ V vs. NHE).[9,12] Bioinspired catalysts, mainly transition metal oxides emulating the photosynthetic system have been explored.[13-16] Often, however, these catalysts are not synthetically tunable and, as a result, are limited in their applicability. It has been the focus of my research to investigate materials that can be designed and modified for their desired applications.

1.1.3 Carbon capture and storage

The increasing concentrations of CO_2 in the atmosphere, which are the direct result of the combustion of carbon-based fossil fuels, have a detrimental affect on the global environment. While research into alternative, carbon neutral energy sources is vital to fulfilling global energy requirements in a sustainable manner, materials developed for these purposes would not be immediately implemented due to necessary modifications of the existing energy infrastructure.[4] Until these alternative energy sources can be utilized on a large-scale basis, current energy demands will likely continue to be met by the combustion of fossil fuels.[17,18] Therefore, the ability to capture greenhouse gases, such as CO_2, from current energy-generating facilities is critical for mitigation of their accumulation in the atmosphere. Materials used for this purpose could be incorporated into the existing infrastructure of power plants in order to separate CO_2 from other flue gas components. Solid, porous adsorbents exhibiting high affinity for CO_2 have shown promise for these applications.[4] An area of focus for my research involved the design and study of porous inorganic-organic materials for their CO_2 adsorption, which were found to selectively adsorb CO_2 over N_2 via the incorporation of an unsaturated metal center for binding of the CO_2 molecule.

1.2 Metal-organic frameworks

Since their first introduction in the literature, metal-organic frameworks (MOFs) have emerged as a novel class of materials featuring a wide variety of structures and potential applications, ranging from gas storage and separation,[4,19,20] catalysis,[21-24] drug delivery,[25,26] and

sensing and electronic applications.[27-29] The structures of MOFs are based on coordination bonds between metal cations and electron donating functionalities, such as carboxylate groups, of organic molecules, which are self-assembled in solution to generate one-, two-, or three-dimensional frameworks that can exhibit high porosity and surface areas.[30] MOFs are comprised of both inorganic and organic components, which can be selected to generate desired framework morphology or incorporate functionalities. This synthetic tunability sets MOFs apart from inorganic porous materials, such as zeolites, and results in a variety of chemical and functional diversity for further study in a range of applications.

1.2.1 Designing MOFs

MOFs are porous, crystalline materials composed of metal nodes connected by multidentate organic linker molecules.[31,32] The frameworks are comprised of secondary building units (SBUs) constructed from metal ions and coordinating oxygen atoms of the ligand functionalities (e.g., carboxylate, phosphonate, sulfonate groups), which are bridged by the organic linker to form extended networks.[33-37] For example, a common SBU found in MOFs has an octahedral geometry (Figure 1.1A), as observed in MOF-5 ($Zn_4O(bdc)_3$, where bdc = 1,4-benzenedicarboxylate) comprised of Zn_4O tetrahedra bound by bdc linkers to form a cubic framework (Figure 1.1B).[34,38]

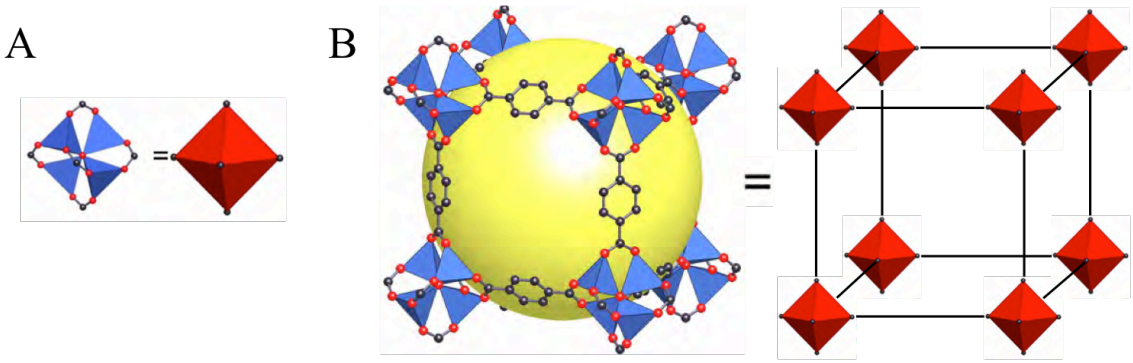

Figure 1.1. (A) Zn_4O tetrahedra (blue polyhedra) comprise the octahedral SBU (red polyhedra) of MOF-5, where the carboxylate carbon atoms are the prism vertices; (B) Extended cubic framework of MOF-5 (Black: C; Red: O; Yellow sphere represents the internal void space). Hydrogen atoms have been omitted for clarity. Reproduced from ref. 34 with permission. Copyright 2005, American Chemical Society.

The SBUs are formed *in situ* and their geometry depends on the coordination geometry of the metal ion employed and the nature of its binding to the linker. They serve as building blocks for the framework architecture to generate varying topologies. Therefore, careful selection of metal ions and possible SBU geometries allows for the rational design of MOF structures, examples of which are shown in Figure 1.2.[33,35,38-42] The Zn_4O unit of the MOF-5 octahedral SBU (*vide supra*) is coordinated by 6 carboxylates of bdc (Figure 1.2A).[38] In changing the metal from Zn^{2+} in MOF-5 to Cr^{3+} in MIL-101 ($Cr_3F(H_2O)_2O(bdc)_3$, where MIL = Matérial Institut Lavoisier), the resulting trigonal prism SBU consists of octahedrally coordinated Cr^{3+} centers and generates an entirely different framework morphology (Figure 1.2B).[39,43] Another common SBU consists of a paddlewheel geometry where 4 carboxylate groups equatorially bind two metal centers with the axial positions typically occupied by solvent.[44,45] This geometry is observed in the HKUST-1 framework (where HKUST = Hong Kong University of Science and Technology; $Cu_3(btc)_2(H_2O)_3$, btc = 1,3,5-benzenetricarboxylate) (Figure 1.2C).[41] Furthermore,

the incorporation of high valent metal ions, such as in the Zr-based MOF UiO-66 (where UiO = University of Oslo; $Zr_6O_4(OH)_4(bdc)_6$), allows for more complex geometries about the metal centers. The SBU of UiO-66 consists of eight-coordinating Zr^{4+} centers to give $Zr_6O_4(OH)_4$ clusters bound by 6 carboxylate groups of the 1,4-benzenedicarboxylate linker (Figure 1.2D).[40]

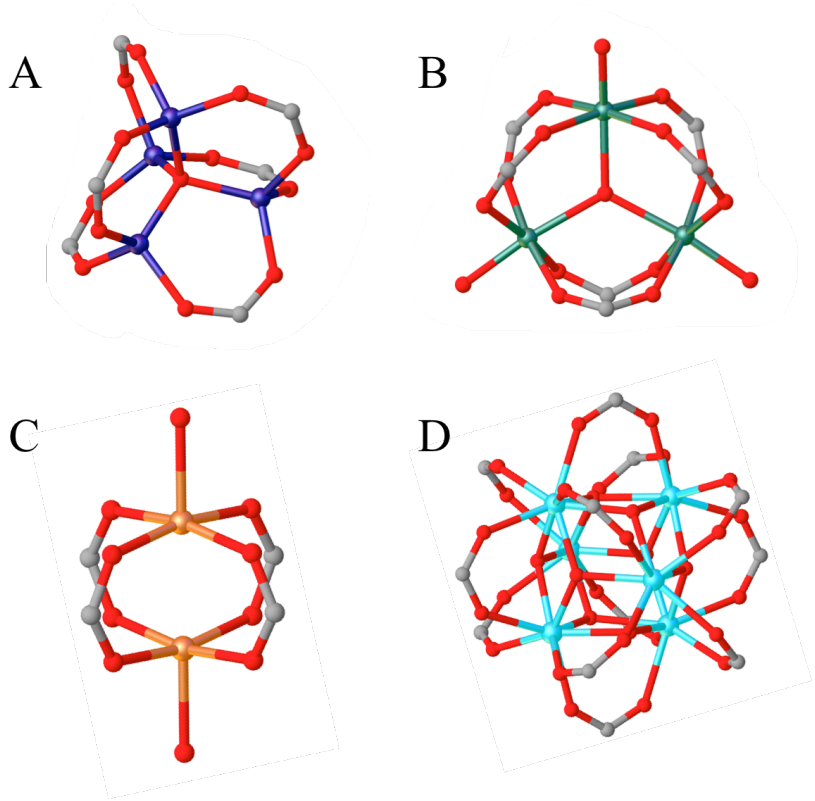

Figure 1.2. Commonly observed SBU geometries within (A) MOF-5;[38] (B) MIL-101;[39] (C) HKUST-1;[41] and (D) UiO-66.[33] Gray: C; Red: O; Blue: Zn; Green: Cr; Orange: Cu; Light Blue: Zr. Hydrogen atoms have been omitted for clarity.

The identity of the organic strut also plays an important role in directing the framework structure. Typical organic linkers employed in MOFs contain aromatic components with multiple ligating functionalities, which bind to the metal centers, and the geometry of the linker governs the overall framework topology. For example, varying the identity of the linker while keeping

the metal nodes unchanged results in different MOF structures (Figure 1.3). As discussed above, MOF-5 consists of a bidentate bdc linker to give a cubic framework (Figure 1.3A).[38] However, when using a tetradentate linker, such as 2,5-dihydroxyterephthalate (dhtp) in MOF-74 ($Zn_2(dhtp)(DMF)_2$), the resulting framework has a honeycomb-like structure with pore diameters of ~ 1.5 nm (Figure 1.3B).[34,46,47] Additionally, altering the linker geometry changes the angle between SBUs, such as with the triangular 1,3,5-benzenetribenzoate (btb) in MOF-177 ($Zn_4O(btb)_2$), which has a trigonal framework topology (Figure 1.3C).[48]

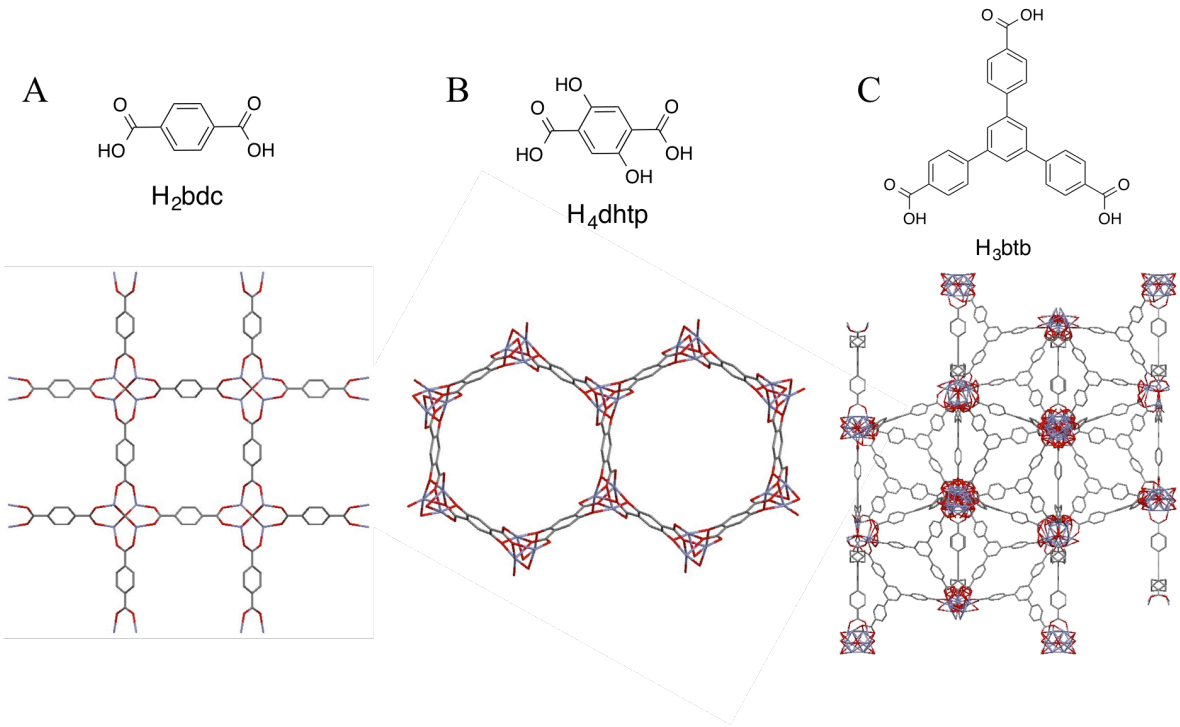

Figure 1.3. (A) 1,4-benzenedicarboxylic acid linker, H_2bdc, (top) and MOF-5 structure (bottom);[38] (B) 2,5-dihydroxyterephthalic acid linker, H_4dhtp, (top) and MOF-74 viewed down the [001] axis (bottom);[46] (C) 1,3,5-benzenetribenzoic acid linker, H_3btb, (top) and MOF-174 viewed down the [010] axis (bottom).[48] Gray: C; Red: O; Blue: Zn. Hydrogen atoms have been omitted for clarity.

1.2.2 Synthetic approaches

The molecular building blocks of MOFs (SBUs and multidentate linkers) assemble to form rigid, ordered frameworks, whose structures can be tailored via modification of the generated SBUs and selection of organic linkers. The synthesis of MOFs can proceed under a variety of reaction conditions using several techniques, which will be discussed in the following sections.

1.2.2.1 Solvothermal.

Most commonly, MOFs are synthesized under solvothermal conditions, which utilize conventional heating of the starting materials (e.g., solvent, metal salt, linker) in a sealed vessel. As discussed above, the SBUs are formed *in situ* and are connected by the organic linker to form the framework structures. Common solvents employed for MOF synthesis include dimethylformamide, diethylformamide, ethanol, or methanol, as well as various mixtures.[49,50] The reaction vessels are heated to a temperature near the boiling point of the solvent system or higher to ensure solubility of the starting materials with typical reaction times of ~12-72 h.[30,33,51] Under these conditions, crystalline materials can be formed in high yields. As many conventional solvents contain coordinating groups, many synthetic procedures result in solvent bound to the coordinatively unsaturated sites on the metal centers. Also, it is common for the pores of the frameworks to contain solvent molecules, which are known as solvents of crystallization. Because of these characteristics, varying the synthetic conditions (e.g., solvent system) can result in isostructural MOFs with differing solvent content (see Table 1.1, entries 4 and 5).[34,46] Table 1.1 highlights well-known MOFs that have been synthesized solvothermally.

Table 1.1. Representative MOFs synthesized via solvothermal method.

Entry	MOF	Metal salt	Ligand[a]	Conditions	Formula
1	MOF-5[38]	$Zn(NO_3)_2{\cdot}4H_2O$	H_2bdc	DMF/C_6H_5Cl; 120 °C, 24 h	$Zn_4O(bdc)_3{\cdot}(DMF)_8(C_6H_5Cl)$
2	UiO-66[40,52]	$ZrCl_4$	H_2bdc	DMF/acetic acid; 120 °C, 24 h	$Zr_6O_4(OH)_4(bdc)_6$
3	MIL-101[39]	$Cr(NO_3)_2{\cdot}9H_2O$	H_2bdc	H_2O/HF 220 °C, 8 h	$Cr_3F(H_2O)_2O(bdc)_3{\cdot}25H_2O$
4	CPO-27-Zn[46]	$Zn(NO_3)_2{\cdot}4H_2O$	H_4dhtp	THF/NaOH (aq); 110 °C, 72 h	$Zn_2(dhtp)(H_2O){\cdot}8H_2O$
5	MOF-74[34]	$Zn(NO_3)_2{\cdot}4H_2O$	H_4dhtp	DMF/2-propanol/H_2O; 105 °C; 20 h	$Zn_2(dhtp)(DMF)_2{\cdot}2H_2O$
6	HKUST-1[41]	$Cu(NO_3)_2{\cdot}3H_2O$	H_3btc	H_2O/EtOH; 180 °C, 12 h	$Cu_3(btc)_2(H_2O)_3$

[a]H_2bdc = 1,4-benzenedicarboxylic acid; H_4dhtp = 2,5-dihydroxyterephthalic acid; H_3btc = 1,3,5-benzenetricarboxylic acid

1.2.2.2 Microwave-assisted solvothermal.

Microwave-assisted synthetic techniques have been applied to a broad range of chemical reactions, including organic synthetic procedures[53,54] and metal oxide and nanoparticle preparation.[55,56] This procedure utilizes the oscillating electric field of the microwave radiation, which interacts with dipole moments of the molecules. This effect increases the molecular rotational energy in solution, resulting in increased kinetic energy and frequency of collisions between molecules, which increases the rate of nucleation.[30,33,50] Recently, it has been employed as an attractive approach for MOF synthesis due to the significantly decreased reaction times (minutes/hours vs. days) and the high degree of control over crystal phase, size, and morphology.[33,57,58] One of the first reports of a MOF synthesized via microwave irradiation was the preparation of MOF-5, which took just 25 seconds to crystallize, compared to the 24 h required by the conventional solvothermal method (Table 1.2).[38,59]

Since this report, many MOFs have been prepared via the microwave-assisted solvothermal method, some of which are summarized in Table 1.2.[60-66] There are several reaction conditions to take into consideration when using this method, such as radiation power, temperature, and reaction time. For example, the microwave-assisted solvothermal synthesis of both MOF-5 and HKUST-1 has been reported under several reaction conditions with varying reaction time and radiation power.[59,61-63] Upon irradiation times > 30 min, the MOF-5 structure was unstable and degraded.[63] On the other hand, increasing the reaction time of HKUST-1 synthesis resulted in more crystalline material with greater surface area than the same MOF prepared via conventional solvothermal heating.[61]

Table 1.2. Comparison of solvothermal and microwave-assisted solvothermal synthetic conditions for representative MOFs.

Entry	MOF	Metal	Ligand[a]	Synthesis Method[b]	Conditions
1	MOF-5	$Zn(NO_3)_2 \cdot 4H_2O$	H_2bdc	S[38]	DMF/C_6H_5Cl; 120 °C, 24 h
2				MW[59]	DEF; 150 W, 25 s
3				MW[63]	N-methyl-2-pyrrolidone; 800 W, 105 °C, 30 min
4	MIL-101	$Cr(NO_3)_2 \cdot 9H_2O$	H_2bdc	S[39]	H_2O/HF 220 °C, 8 h
5				MW[60]	H_2O/EtOH; 600 W, 210 °C, 40 min
6	HKUST-1	$Cu(NO_3)_2 \cdot 3H_2O$	H_3btc	S[41]	H_2O/EtOH; 180 °C, 12 h
7				MW[62]	EtOH 300 W, 140 °C, 1 h
8				MW[61]	H_2O/EtOH; 1200 W, 110 °C, 4 h

[a] H_2bdc = 1,4-benzenedicarboxylic acid; H_3btc = 1,3,5-benzenetricarboxylic acid

[b] S = solvothermal; MW = microwave-assisted solvothermal

1.2.2.3 Electrochemical.

The electrochemical synthesis of MOFs utilizes an electrochemical cell comprised of an anodic metal plate and dissolved linker molecules. The metal ions are supplied via anodic dissolution of the metal plate, which then react with the organic linker in solution to form the framework.[33,49,50] This technique offers several advantages over solvothermal methods, such as high purity products, decreased reaction times, and control over the metal oxidation state.[33,49,67] One of the first reports of the electrochemical synthesis of a MOF is the industrial preparation of HKUST-1 ($Cu_3(btc)_2(H_2O)_3$) at BASF (Figure 1.4A). This procedure utilized copper plates immersed into a methanol solution containing 1,3,5-benzenetricarboxylic acid. The crystalline HKUST-1 framework was formed when a potential of 12-19 V was applied for 150 min (Figure 1.4B and C).[68,69] In order to avoid reduction of the metal ions in solution, electrons at the counter electrode are used to reduce protons and evolve H_2.[67] Since this initial report, the electrochemical synthetic technique has been applied to the preparation of other MOFs, such as a Zn-based zeolitic imidazolate framework (ZIF-8: $Zn(mim)_2$, where mim = 2-methylimidazole) and Al-based MOFs (MIL-53(Al), NH_2-MIL-53(Al): $Al(OH)(NH_2\text{-bdc})$ and MIL-100(Al): $Al_3O(OH)(H_2O)_2(btc)_2$).[70,71]

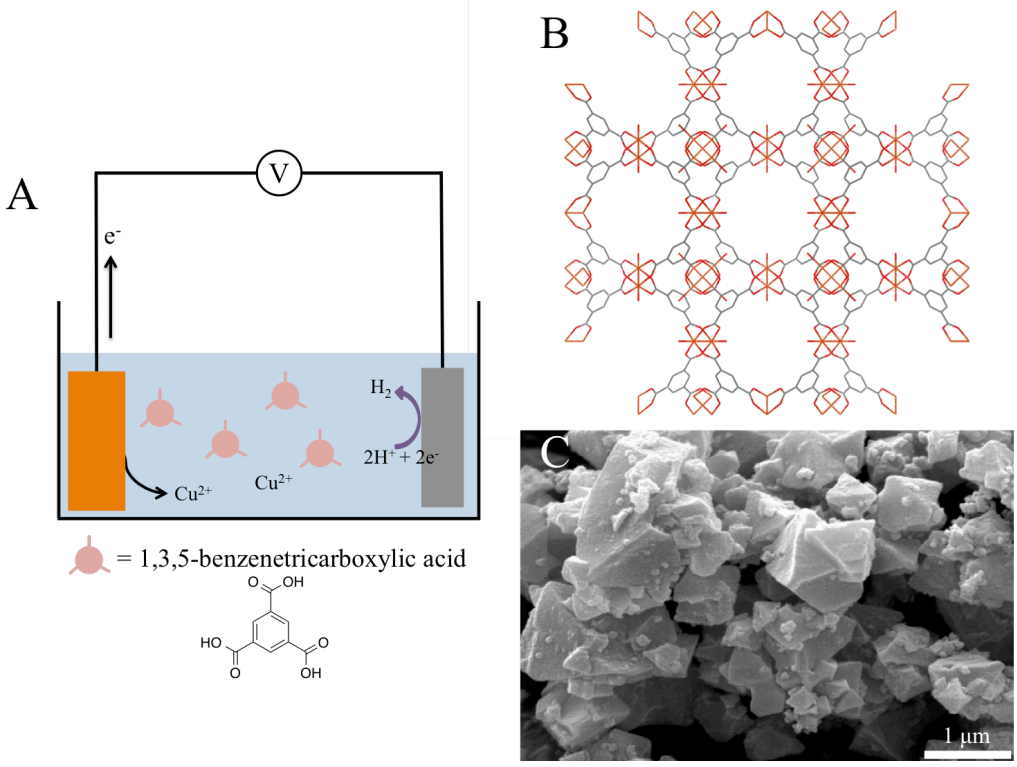

Figure 1.4. (A) Scheme of the electrochemical synthesis of HKUST-1 formed from anodic dissolution of Cu^{2+} ions from a copper plate (orange electrode) into a methanolic solution of 1,3,5-benzenetricarboxylic acid; (B) Framework of HKUST-1 viewed down the [100] axis; Gray: C: Red: O; Orange: Cu. Hydrogen atoms have been omitted for clarity;[41] (C) SEM image of crystalline MOF produced from this method (reprinted with permission from ref. 69 with permission of the Royal Society of Chemistry).

1.2.3 Characterization techniques

Once synthesized, the absolute structure of the resulting crystalline material is typically determined via single crystal X-ray diffraction. As this technique requires single crystals of adequate size, purity, and diffraction quality, it is not applicable to all frameworks. Therefore, MOFs are also characterized via several other methods, such as powder X-ray diffraction (PXRD) to determine phase purity, thermogravimetric analysis (TGA) to investigate thermal stability, as well as scanning electron microscopy (SEM) to confirm crystal morphology.

Examples of these characterization techniques applied to a well-known MOF are shown in Figure 1.5.

The Zr-based MOF UiO-66 ($Zr_6O_4(OH)_4(bdc)_6$) is comprised of $Zr_6O_4(OH)_4$ octahedral SBUs bound by 1,4-benzenedicarboxylate linker molecules to form a framework whose structure was solved using single crystal X-ray diffraction. UiO-66 crystallizes in a cubic unit cell and contains both tetrahedral and octahedral cages (Figure 1.5A).[40,52,72,73] From single crystal diffraction data, a powder pattern can be simulated and powder X-ray diffraction (PXRD) is used to determine phase purity of bulk MOF powder. Unlike single crystal measurements, diffraction of powder samples results from the randomized orientation of individual crystallites, where the peaks represent diffraction from a plane within the unit cell. Therefore, analysis of the peak positions from the experimental powder X-ray diffraction pattern with those obtained from single crystal data allows for comparison of the unit cells. As demonstrated with UiO-66, the peak positions in the PXRD pattern of the synthesized material correlate well with that simulated from single crystal data, suggesting the bulk material maintains long-range order and matches the unit cell and structure of UiO-66 (Figure 1.5B).[74] The temperature at which frameworks lose solvent and ligand molecules can be determined by TGA. For example, the TG curve of UiO-66 shows losses corresponding to physisorbed water (9% loss) and DMF (19.5% loss) molecules centered at ~ 80 and 250 °C, respectively (Figure 1.5C).[73] The desolvation steps are followed by thermal degradation of the framework and loss of the organic linker molecules (36% loss) at temperatures greater than 375 °C.[73] The SEM image of UiO-66 crystals (Figure 1.5D) shows the octahedral morphology of the crystal, which arises from the structure of cages comprising the framework.[75]

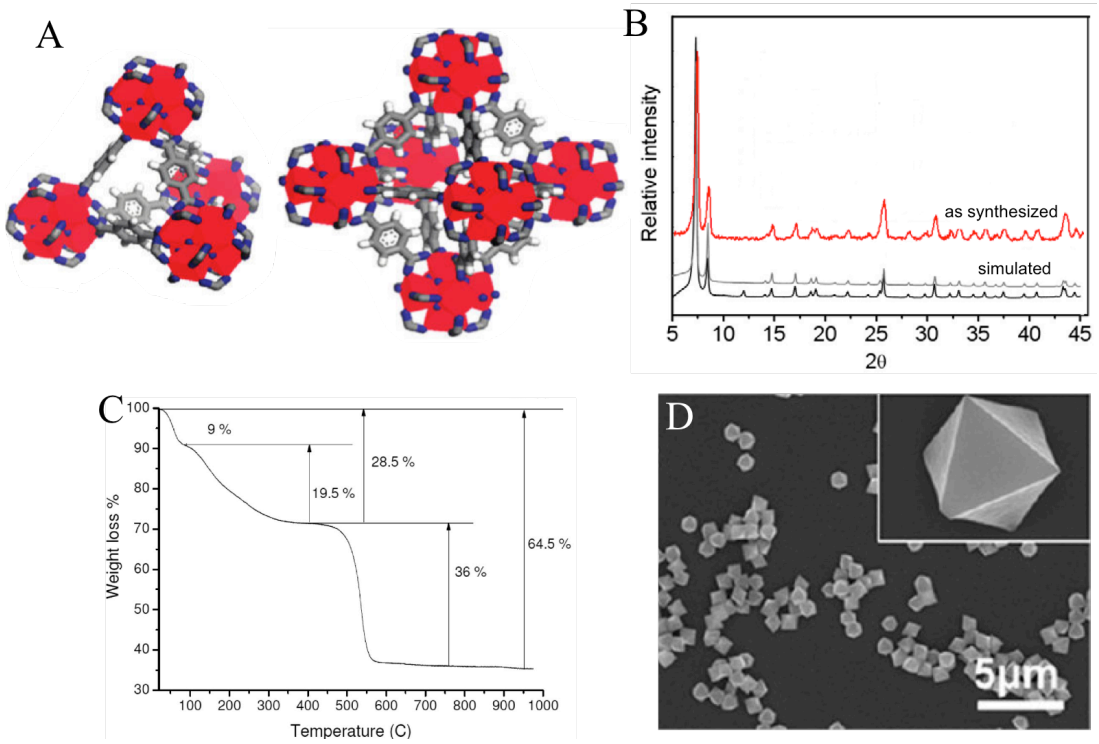

Figure 1.5. (A) Tetrahedral (left) and octahedral (right) cages of UiO-66: Zr: red; O: blue; C: gray; H: white. (Reproduced with permission from ref. 73. Copyright 2008 American Chemical Society.); (B) PXRD of UiO-66 as synthesized (red) and simulated (black and gray) (Reproduced from ref. 74 with permission of the PCCP owner societies.); (C) TG curve of UiO-66 (Reprinted with permission from ref. 73. Copyright 2011 American Chemical Society); (D) SEM of UiO-66 (Reprinted with permission from ref. 75. Copyright 2014 American Chemical Society).

1.2.4 Structural stability

In order for MOFs to be useful in practical applications, such as gas sorption and separation and catalysis, they must remain stable upon exposure to a wide variety of conditions (e.g., heat, pressure, solvents, pH).[44] Due to the nature of the strong coordination bonds that hold the structure together (typically metal-carboxylate), MOFs have been shown to retain their structural integrity up to ~ 250-500 °C.[31,39,40,76-79] However, the stability of MOFs toward different chemical environments has been an area of increasing interest. The earlier MOFs

comprised of tetrahedral Zn^{2+} centers have generally displayed poor stability, as the metal-carboxylate bonds in these frameworks are particularly vulnerable to ligand exchange and displacement with water or other polar solvents.[44,80] This behavior has been observed in the Zn-based MOF-5 with Zn_4O SBUs (Figure 1.2A),[38] where the bdc linker was displaced by water molecules upon exposure to humid air (< 4% H_2O), resulting in framework collapse and loss of porosity.[81-83]

Despite this initial limitation, the improved stability of MOFs has been realized by employing metals in higher oxidation states, such as Zr^{4+}, Cr^{3+}, and Al^{3+}, which will form stronger bonds with the carboxylate groups in the linker molecules.[39,40,76,84,85] As a result, the frameworks containing these metal ions are less likely to undergo ligand substitution. In addition, these metal centers are capable of accommodating a higher number of coordinating groups, leading to larger SBU clusters, which can undergo a ligand displacement without the collapse of the framework structure.[44] A particularly good example of improved stability is the Zr-based UiO-66 and -67 frameworks, which are composed of octahedral SBUs comprised of $Zr_6O_4(OH)_4$ clusters (Figure 1.2D)[40] and have demonstrated stability in air and a wide range of chemical environments.[73,78,86] Improving the stability and understanding the metal-ligand interactions inside frameworks allows for the design and development of more robust MOFs to realize their applications in gas separation and catalysis.

1.2.5 Postsynthetic modification

Postsynthetic modification (PSM) of MOFs is a technique that allows for the incorporation of additional chemical functionalities (e.g., polarity, reactivity) into frameworks after they have been synthesized. This synthetic tool has become increasingly popular, spurred by the design of MOFs for more advanced applications.[21,30,87] PSM is a more practical approach over *in situ* installation of these higher complexities on the frameworks since it avoids synthetic complications, as well as the control it offers over the incorporation of functional groups.[87,88] In the PSM strategy, both the metal and organic linker can be modified to generate a large library of functionalized MOFs while maintaining framework topology and stability.[88]

The simplest type of PSM employed in MOFs is the exchange or removal of labile ligands or solvents of crystallization from the pores of the frameworks to generate an open metal site, which are useful in a variety of applications, such as catalysis or gas storage.[21] The removal of a bound solvent molecule can result in a change in geometry of the metal center and/or collapse of the framework altogether. Therefore, the MOF must be robust enough to accommodate the removal of these guests to generate the open metal sites.[89,90] This procedure is commonly referred to as "activation", since the framework is being activated for its intended application, and typically involves soaking the MOF in a volatile solvent (e.g., methanol, ethanol, acetone, or chloroform), resulting in exchange of the crystallization solvent, followed by heating under vacuum to remove the volatile solvent.[21]

A MOF activation procedure generating open metal sites has been demonstrated in the CPO-27-M series (M_2(dhtp), where dhtp = 2,5-dihydroxyterephthalic acid and M = Mn, Co, Ni, Zn).[46,47,91,92] In this series, the solvated MOFs contain octahedrally coordinated metal centers,

with five coordination sites occupied by the organic linker and the sixth occupied by H_2O, which protrudes into the solvent-occupied hexagonal channels of the framework (Figure 1.6A).[46,91,92] Upon activation, the metal geometry changes from octahedral to square pyramidal accompanied by the loss of bound H_2O to generate an open metal site while maintaining framework topology (Figure 1.6A).[46,91,92] These sites improve gas uptakes of CPO-27-M MOFs due to enhanced interaction between gas molecules and the metal centers.[47,92]

Alternatively, PSM is also applied to impart a specific functionality within the MOF pores, often through modification of the organic ligand (Figure 1.6B),[88] for a specific application. This approach has been demonstrated with the covalent modification of the amine containing MOFs, IRMOF-3 ($Zn_4O(NH_2\text{-bdc})_3$)[93] and UMCM-1-NH_2 (where UMCM = University of Michigan Crystalline Material: $(Zn_4O)_3(NH_2\text{-bdc})_3(btb)_4$).[94] Using this strategy, the amine groups of the organic linker were acylated by reacting with acetic and benzoic anhydrides, respectively, to generate a dangling amide group in the pores of the framework.[93,94] The modified frameworks both showed an increase in H_2 uptake compared to the parent MOF, suggesting a stronger interaction between the H_2 molecules and the amide functionalities in the pores.[80,94]

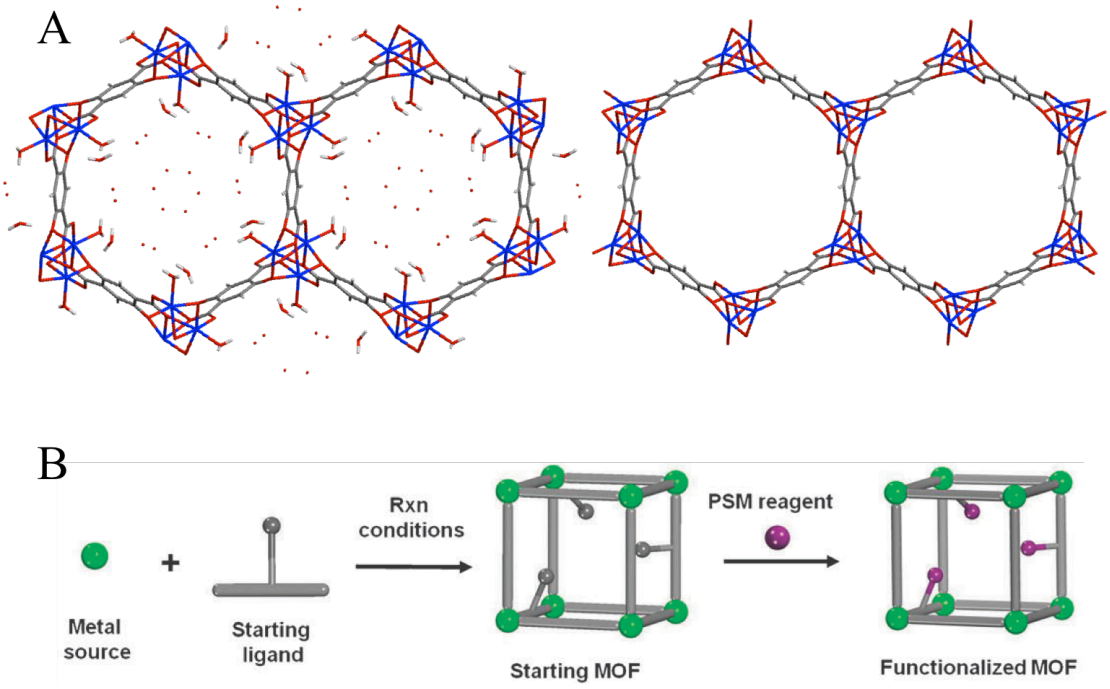

Figure 1.6. (A) Crystal structures viewed down the [001] axis of as synthesized (left) and activated (right) CPO-27-Zn.[46] Gray: C; Red: O; White: H; Blue: Zn; (B) Postsynthetic modification scheme for the functionalization of the organic ligand of a MOF. Reprinted from ref. 88 with permission of The Royal Society of Chemistry.

1.2.6 Applications

Due to the unique properties of MOFs, such as the tunability of their inorganic and organic components, pore sizes and functionalities, and access to metal centers, make MOFs attractive for use in a wide variety of applications.

1.2.6.1 Gas storage and separation.

One of the earliest applications of MOFs has been in the field of gas sorption and separation due to their high surface areas.[4,19,20,95] Specifically, with the increased need for alternative energy sources, much attention is being diverted to materials capable of storing potential gaseous fuels, such as H_2 and CH_4.[80] MOFs are of particular interest for these

applications due to their ability to capture and store gases at high capacities. The first report of hydrogen adsorption using a MOF appeared in 2003, which demonstrated that MOF-5 could uptake 4.5 wt% H_2 at 77 K and 1 bar, which is considerably more than a porous silica material (0.4 wt%) under the same conditions.[96,97] Since then, there have been numerous reports of MOFs exhibiting high H_2 storage capacity.[20,98-102] It has been found both experimentally and computationally, that open metal sites within the framework enhance H_2 and CH_4 uptakes due to stronger interaction between coordinatively unsaturated metal centers and gas molecules.[20,47,49,92,103,104] This phenomenon has been particularly well established in the isostructural CPO-27-M MOF series, which were investigated for their H_2 and CH_4 adsorption properties.[47,103] In this series, the binding site of the gas molecules was confirmed via computational calculations as well as neutron diffraction to be on the unoccupied sixth coordination site of the metal centers (Figure 1.7).[47,103] With these features in mind, the design of MOFs with high gas sorption capacities can be achieved, which is necessary for implementation in fuel cell technologies.

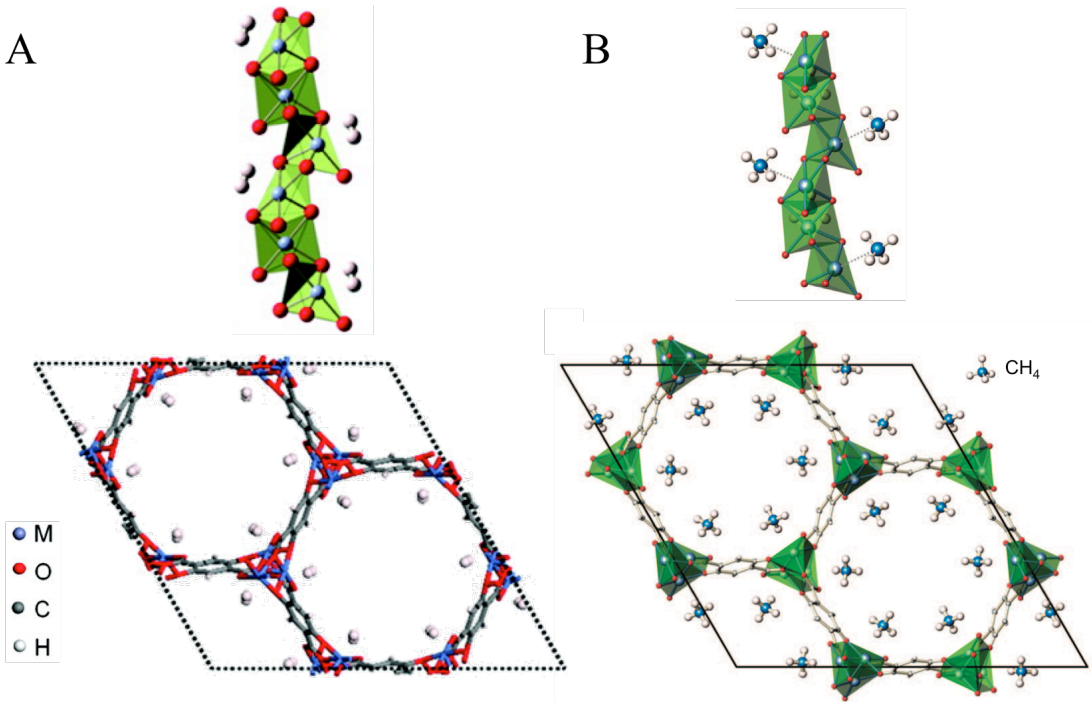

Figure 1.7. View down the [001] axis of CPO-27-M (bottom) and metal oxide polyhedron SBUs (green), which form 1D chains throughout the framework (top) with (A) H_2 adsorption (Reprinted with permission from ref. 47. Copyright 2008 American Chemical Society); (B) CH_4 adsorption (Reprinted with permission from ref. 103. Copyright 2009 American Chemical Society).

Another area of increased interest is the use of MOFs for the capture of environmentally hazardous gases. For example, the burning of fossil fuels from power plants is one of the main causes of increased atmospheric CO_2 concentrations, and the development of materials capable of efficiently separating and storing CO_2 from the combustion products is crucial.[3,4] In order to achieve efficient separation, the materials must have a high selectivity for CO_2 over the other components of the gas mixture, such as N_2 and H_2O. The synthetic tunability of MOFs allows for the selective incorporation of functionalities (e.g., open metal sites, reactive groups), which will result in greater affinity between CO_2 and the framework.[4] In one particular example, MOFs

containing open metal centers have been shown to act as binding sites and interact more strongly with CO_2 over N_2 due to their high charge densities.[105-110]

Additionally, the incorporation of nitrogen-containing functional groups, such as amines, into MOFs has been shown to increase CO_2 adsorption due to the interaction of the quadrupole moment of CO_2 with dipoles generated by the presence of electronegative nitrogen atoms.[4] This can be accomplished through the utilization of organic linker molecules containing $–NH_2$ residues or free N atoms in the heterocycle.[49] For example, enhanced CO_2 uptake was achieved with USO-2-Ni-A (where USO = University of Oslo: $Ni_2(NH_2\text{-bdc})$(dabco), where dabco = 1,4-diazabicyclo[2.2.2] octane) compared to its parent MOF comprised of nonfunctionalized bdc.[111] Similar behavior was observed in bio-MOF-11 ($Co_2(adenine)_2(CH_3CO_2)_2$), which contains Lewis acidic amino and pyrimidine groups lining the pores.[112]

Amine-containing functionalities have also been incorporated into frameworks via PSM in order to increase their sorption capacities and selectivity for CO_2. Postsynthetic incorporation of *N,N*-dimethylethylenediamine (mmen) into of Cu-BTTri ($H_3[(Cu_4Cl)_3(BTTri)_8]$, where BTTri = 1,3,5-tri(1H-1,2,3-triazol-4-yl)benzene)) interacts with the open Cu^{2+} sites to generate mmen-Cu-BTTri.[113] The amine functionalized MOF demonstrated a 15% increase in CO_2 capacity compared to Cu-BTTri.[4,113] As a result of the ability to tailor the selectivity via the approaches discussed above, many MOFs have been designed with a high capacity for CO_2 and therefore, show great promise as potential candidates for CO_2 capture applications.

1.2.6.2 Electronic applications.

As electronic devices continue to become more compact and efficient, there is an increasing demand for the development of nanoscale materials capable of charge transport and mobility.[28,114] Most commonly, preparation of these materials utilizes a "top-down" approach, which relies on implementing current materials into these already designed devices.[115] However, the top-down technique lacks the ability to tailor the electronic properties of the materials, and there is an increasing need for methods to design nanoscale structures capable of long-range charge transport.[116] The recent developments in the MOF field have made them attractive candidates for these applications due to their crystallinity, porosity, and synthetic tunability.[114]

As a result of their structural properties (i.e., hard metal nodes bound via carboxylate oxygen atoms of organic linker molecules), MOFs are typically insulating in nature due to the poor overlap of the metal d orbitals and π orbitals of the linker.[27,117] However, there has been recent progress in the synthetic procedures and design of MOFs that exhibit high degree electronic conductivity and charge mobility.[27,118] One approach to accomplish this task is the incorporation of redox active components capable of donating and accepting electrons to facilitate charge transport throughout the framework. In fact, this technique was utilized in one of the first reports of an electrically conductive MOF ($Cu[Cu(pdt)_2]$, where pdt = 2,3-pyrazinedithiolate), which demonstrated conductivity on the order of 10^{-4} S cm^{-1} (Figure 1.8A).[119] The charge transport within the framework was facilitated by the electron donating/accepting properties of the Cu^{I} nodes and the $[Cu(pdt)_2]^{2-/1-}$ metalloligand.[119] While it displayed semiconductive behavior, the $Cu[Cu(pdt)_2]$ framework collapsed upon removal of solvent. In order to circumvent this limitation, the $Cu(pdt)_2$ linkers were replaced with $Ni(pdt)_2$ to

give the permanently porous framework $Cu[Ni(pdt)_2]$ (Figure 1.8A), which demonstrated conductivity of 10^{-8} S cm^{-1}.[120] The conductivity of $Cu[Ni(pdt)_2]$ increased four orders of magnitude upon doping with I_2 due to oxidation of the $[Ni(pdt)_2]^{2-}$ linkers, which generated additional charge carriers (Figure 1.8B).[120]

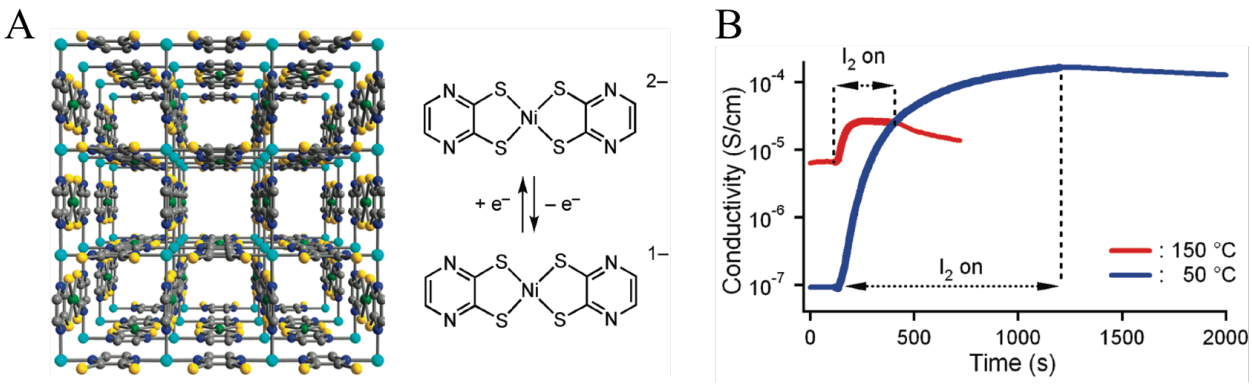

Figure 1.8. (A) 3D framework of $Cu[Ni(pdt)_2]$ and the redox process associated with the $[Ni(pdt)_2]^{2-}$ linker. Light blue: Cu; Green: Ni; Yellow: S; Blue: N; Gray: C; (B) Conductivity of $Cu[Ni(pdt)_2]$ at 50 °C (blue) and 150 °C (red) increases upon treatment with I_2 vapor. Reprinted from ref. 120. Copyright 2010 American Chemical Society.

Conductivity has also been demonstrated in frameworks containing intrinsic pathways for charge transport, either through extended metal-linker chains or with guest molecules acting as bridging units.[27] For an extended metal-linker pathway to be conductive, strong orbital overlap between the metal and organic linker backbone is essential. These properties can be tailored to enhance conduction throughout the frameworks based on redox matching of the framework components.[121,122] For example, the SBU of the CPO-27-M (M_2(DOBDC), where M = Mg, Co, Ni, Zn; and DOBDC = 2,5-dihydroxyterephthalic acid) family of MOFs consists of infinite 1D M-O chains.[46,47,91,92] The orbital overlap between these metals and linkers is improved when oxygen atoms are replaced with sulfur, and thus, it is expected that a framework containing M-S

would have better conduction properties. Therefore, the hydroxyl groups of the linker could be substituted with sulfhydryl groups (DSBDC) to generate the isostructural frameworks containing infinite chains comprised of M-S rather than M-O. The resulting Mn_2(DOBDC) and Mn_2(DSBDC) MOFs displayed conductivity of 10^{-13} S cm^{-1} and 10^{-12} S cm^{-1}, respectively (Figure 1.9A).[27,123] The conductivity of the framework could be increased further by replacement of the Mn^{2+} (d^5) centers with Fe^{2+} (d^6), which provides additional electrons capable of facilitating charge mobility.[124] In fact, the Fe^{2+} analogs Fe_2(DOBDC) and Fe_2(DSBDC) displayed a million-fold enhancement in conductivity (10^{-7} S cm^{-1} and 10^{-6} S cm^{-1}, respectively) compared to the Mn^{2+} (Figure 1.9A).[27,125] The selection of appropriate metal centers and linkers to improve the redox matching led to the design of MOFs with enhanced conductivity.

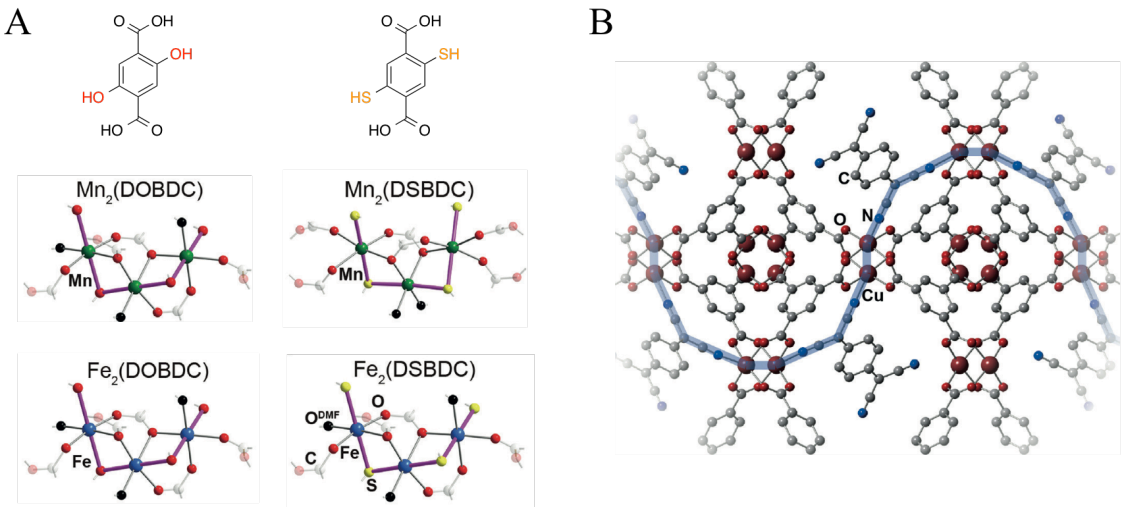

Figure 1.9. (A) M-O chains of M_2(DOBDC) (left) and M-S chains of M_2(DSBDC) (right) for M = Mn^{2+} (middle) and Fe^{2+} (bottom); (B) The predicted structure of TCNQ@Cu_3(btc)$_2$ with the extended pathway for charge transport between TCNQ and Cu centers highlighted in blue. Reprinted with permission from ref. 27. Copyright 2016 John Wiley & Sons.

The extended chains that span the entire framework structures can also be formed via incorporation of guest molecules into the pores, which act as bridges between metal nodes and act as charge transport pathways.[126] For example, HKUST-1 ($Cu_3(btc)_2(H_2O)_3$) contains Cu^{2+} centers occupied by H_2O molecules and demonstrated conductivity on the order of 10^{-8} S cm^{-1}, where conduction is most likely facilitated via a redox hopping mechanism.[127,128] After activation and soaking the MOF in a solution containing 7,7,8,8-tetracyanoquinodimethane (TCNQ), the redox active TCNQ infiltrated the MOF pores and was determined computationally to coordinate to two Cu^{2+} metal centers, generating an extended pathway for charge transport throughout the framework (Figure 1.9B).[27,127] The MOF with TCNQ guest molecules, TCNQ@$Cu_3(btc)_2$, displayed a marked increase in conductivity (10^{-2} S cm^{-1}).[127] These results show promise for the design of conductive MOFs based on selection of metal nodes containing loosely bound electrons, redox matching of the components to generate extended metal-linker chains, or via the incorporation of guest molecules capable of facilitating charge transport.[27,28,126]

1.2.6.3 Catalysis.

As a result of their permanent porosity and structural diversity, MOFs have been promising candidates for catalytic applications.[21,22] MOFs offer several advantages over homogeneous catalysts in their ease of separation and reuse, inherent stability, and control over active site surroundings.[23,24] In addition, the ability to tailor pore sizes and environments and postsynthetically modify the frameworks allows for tunable catalytic activity and selectivity and makes MOFs applicable for a broad range of catalytic reactions.[23] There have been several strategies employed to incorporate the catalytic ability into MOFs, which include the generation

of unsaturated metal catalytic sites,[129-131] incorporating known homogeneous catalysts as the organic struts of frameworks,[132-134] as well as immobilization or encapsulation of molecular catalysts or metal nanoparticles within the MOF pores.[135-139]

Homogeneous catalysts containing transition metals have been extensively investigated for their ability to carry out catalytic transformations at the metal center.[140-143] Therefore, the presence of unsaturated metal centers within MOFs can be very beneficial for catalytic applications since higher density of catalytic sites could lead to improved efficiencies compared to conventional heterogeneous catalysts.[22-24] In addition, the diversity of transition metal ions (e.g., Cr^{3+}, Fe^{3+}, Sc^{3+}, Mn^{2+}, Co^{2+}, etc.) that can be incorporated into MOFs makes these materials useful in a variety of catalytic reactions.[144-149] For example, the hydrazine-mediated reduction of carbon-carbon multiple bonds in organic substrates has been demonstrated with MIL-53-Al ($Al_2(OH)(bdc)$) with high selectivity and yields. This reaction typically requires H_2 gas and a noble metal catalyst to proceed.[150] The proposed catalytic mechanism occurs via hydrazine binding to the Al^{3+} center, followed by a transfer of hydride to reduce a C=C bond.[150] These results demonstrated the utility of MOFs as an inexpensive alternative for the catalytic hydrogenation of carbon-carbon multiple bonds.

Another approach to introduce catalytic activity into MOFs is to incorporate molecular homogeneous catalysts into the backbone of frameworks. While there has been extensive research into discrete systems containing mononuclear or polynuclear metal complexes for catalytic applications, many of these systems suffer from poor solubility and stability under the reaction conditions and, as a result, undergo deactivation during catalytic cycling.[151-153] A common approach to overcome these limitations is to immobilize the catalyst into a rigid, stable

matrix, such as incorporation or encapsulation into a MOF.[132,154-160] This technique was demonstrated with a molecular iron-based proton reduction catalyst, [FeFe](dcbdt)$(CO)_6$, where dcbdt = 1,4-dicarboxylbenzene-2,3-dithiolate, and the UiO-66 MOF ($Zr_6O_4(OH)_4(bdc)_6$).[154] The catalyst was incorporated into the framework postsynthetically via linker exchange with the bdc. Attempts to utilize [FeFe](dcbdt)$(CO)_6$ as a ligand in the solvothermal synthesis of UiO-66 resulted in its decomposition due to the lability of the Fe-S bonds (Figure 1.10A).[154] The doped MOF, UiO-66-[FeFe](dcbdt)$(CO)_6$, was found to be catalytically active toward the reduction of protons in the presence of a $[Ru(bpy)_3]^{2+}$ photosensitizer and ascorbate electron donor (Figure 1.10B).[154] In fact, the framework-immobilized molecular catalyst demonstrated superior activity over the homogeneous system due to structural stabilization of the Fe dimer and elimination of charge recombination processes.

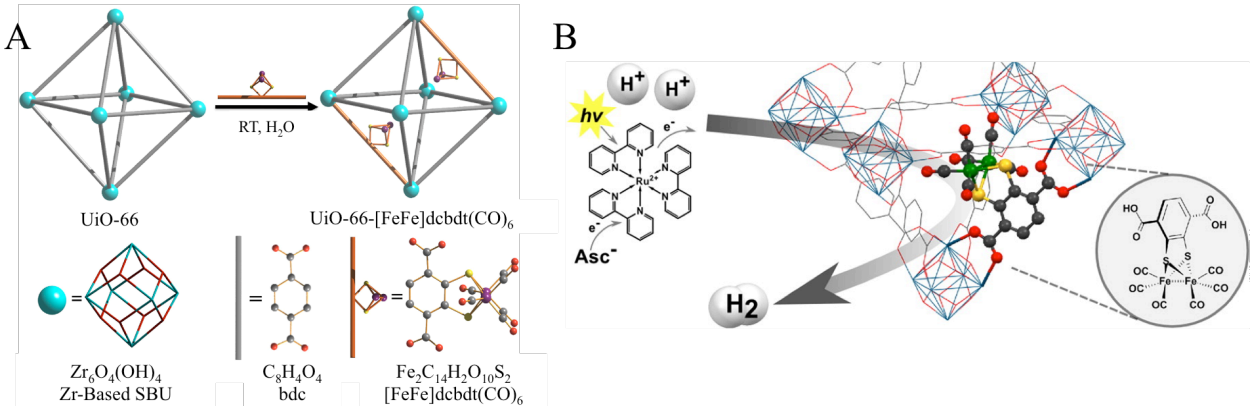

Figure 1.10. (A) Linker exchange process used to postsynthetically incorporate [FeFe](dcbdt)$(CO)_6$ into the UiO-66 framework; (B) Proton reduction activity of UiO-66-[FeFe](dcbdt)$(CO)_6$ in the presence of $[Ru(bpy)_3]^{2+}$ photosensitizer and ascorbate (Asc) electron donor. Reprinted from ref. 154 (http://pubs.acs.org/doi/10.1021/ja407176p). Copyright 2013 American Chemical Society.

1.3 Project description and summary

With the current global energy demand being met with the combustion of non-renewable fossil fuels, as well as the resulting increased atmospheric concentrations of CO_2, there is imminent need for alternative, renewable, carbon-neutral energy sources. Sunlight is the only energy source of sufficient scale to replace our dependence on fossil fuels in a sustainable manner. Taking inspiration from the naturally occurring photosynthetic process, solar energy can be stored in the form of chemical bonds via the water oxidation reaction. As this reaction is thermodynamically unfavorable and requires oxidizing conditions, catalysts capable of facilitating the reaction must be robust, remain structurally sound, and be able to account for the four electron, four proton transfer. It has been the goal of my research to investigate materials capable of facilitating charge transport for ultimate applications in alternative energy catalysis.

Initially, a Co-based metalloporphyrin framework composed of redox active linkers and metal centers (designated as CoPIZA containing Co^{II}-nodes and Co^{III}TCPP struts, where TCPP = 5,10,15,20-(4-carboxyphenyl)porphyrin) was investigated for its electron transport properties. The thin film of CoPIZA on conductive FTO substrate was found to be electrochemically active and facilitates electron transport throughout the framework via a redox hopping mechanism, where electrons are transferred between the individual redox active components. CoPIZA remained structurally stable as a result of applied potentials and electrochemically catalyzed the reduction of CCl_4.

To further investigate the charge transport properties of MOFs, our laboratory synthesized two new frameworks comprising redox-inactive Zn metal centers. These MOFs contained both 5- and 6-coordinate Zn^{II} metal centers bridged by 2,5-pyridinedicarboxylate

linker molecules. The MOFs contained coordinatively unsaturated metal centers, which do not require an activation procedure to remove bound solvent molecules, and were initially investigated for their gas sorption capacity and selectivity. The frameworks demonstrated selectivity for CO_2 over N_2 with the unsaturated Zn^{II} centers serving as the binding sites for CO_2 molecules. Additionally, the MOFs were investigated for their charge transport ability using electrochemical impedance spectroscopy. The charge transport mechanism throughout the framework proceeded by bound solvent molecules, as well as the network of solvents of crystallization extending throughout the MOF structures.

While these frameworks demonstrated charge transport properties, we wanted to focus on MOFs capable of facilitating the water oxidation reaction. Specifically, a Co-based MOF with a pyrimidinolate linker molecule, $Co(pymo)_2$ was investigated for its ability to electrocatalytically oxidize water. Upon the application of electric potential, the $Co(pymo)_2$ framework undergoes a redox transformation to deposit a film of cobalt-oxides onto the electrode surface, which was found to be the active catalytic species for water oxidation. Electrochemical characterization revealed that the catalytic mechanism proceeds via oxidation of the Co^{II} metal centers to Co^{III} followed by binding of a H_2O molecule to facilitate water oxidation and generate O_2.

Additionally, a more stable MOF with Zr-oxo nodes connected by nickel(II) meso-tetrakis(4-carboxyphenyl)porphyrin (Ni(II)TCPP) linkers, designated as PCN-224-Ni, was investigated for its electrochemical water oxidation. Films of PCN-224-Ni were grown solvothermally on FTO and were found to electrochemically facilitate the water oxidation reaction at near neutral pH. The mechanism of water oxidation at PCN-224-Ni proceeds via initial oxidation of the porphyrin linker followed by binding of water to the Ni(II) of Ni(II)TCPP.

The Zr nodes act cooperatively with the linker to abstract protons, which enable the eventual release of O_2. Extensive characterization of films post-electrolysis revealed that the MOF is stable and retains its structure over the course of electrocatalysis.

1.4 References

(1) Lewis, N. S.; Nocera, D. G. *Proc. Natl. Acad. Sci. U. S. A.* **2006**, *103*, 15729.
(2) U.S. Energy Information Administration. International Energy Outlook, 2016.
(3) Earth System Research Laboratory: http://www.esrl.noaa.gov/gmd/ccgg/trends/, 2014.
(4) Sumida, K.; Rogow, D. L.; Mason, J. A.; McDonald, T. M.; Bloch, E. D.; Herm, Z. R.; Bae, T.-H.; Long, J. R. *Chem. Rev.* **2012**, *112*, 724.
(5) Gray, H. B. *Nat. Chem.* **2009**, *1*, 7.
(6) Lewis, N. S. *Science* **2007**, *315*, 798.
(7) Cook, T. R.; Dogutan, D. K.; Reece, S. Y.; Surendranath, Y.; Teets, T. S.; Nocera, D. G. *Chem. Rev.* **2010**, *110*, 6474.
(8) Barber, J. *Chem. Soc. Rev.* **2009**, *38*, 185.
(9) Walter, M. G.; Warren, E. L.; McKone, J. R.; Boettcher, S. W.; Mi, Q.; Santori, E. A.; Lewis, N. S. *Chem. Rev.* **2010**, *110*, 6446.
(10) Barber, J. *Inorg. Chem.* **2008**, *47*, 1700.
(11) Bard, A. J.; Fox, M. A. *Acc. Chem. Res.* **1995**, *28*, 141.
(12) Dismukes, G. C.; Brimblecombe, R.; Felton, G. A. N.; Pryadun, R. S.; Sheats, J. E.; Spiccia, L.; Swiegers, G. F. *Acc. Chem. Res.* **2009**, *42*, 1935.
(13) Jiao, F.; Frei, H. *Angew. Chem.* **2009**, *121*, 1873.
(14) Jiao, F.; Frei, H. *Chem. Commun.* **2010**, *46*, 2920.
(15) Jiao, F.; Frei, H. *Energy Enrivon. Sci.* **2010**, *3*, 1018.
(16) Kanan, M. W.; Surendranath, Y.; Nocera, D. G. *Chem. Soc. Rev.* **2009**, *38*, 109.
(17) McDonald, T. M.; Mason, J. A.; Kong, X.; Bloch, E. D.; Gygi, D.; Dani, A.; Crocella, V.; Giordanino, F.; Odoh, S. O.; Drisdell, W. S.; Vlaisavljevich, B.; Dzubak, A. L.; Poloni, R.; Schnell, S. K.; Planas, N.; Lee, K.; Pascal, T.; Wan, L. F.; Prendergast, D.; Neaton, J. B.; Smit, B.; Kortright, J. B.; Gagliardi, L.; Bordiga, S.; Reimer, J. A.; Long, J. R. *Nature* **2015**, *519*, 303.
(18) U.S. Environmental Protection Agency: http://www3.epa.gov/climatechange/ghgemissions/gases/co2.html, 2016.
(19) Li, J.-R.; Sculley, J.; Zhou, H.-C. *Chem. Rev.* **2012**, *112*, 869.
(20) Suh, M. P.; Park, H. J.; Prasad, T. K.; Lim, D.-W. *Chem. Rev.* **2012**, *112*, 782.
(21) Xamena, F. L. I.; Gascon, J. *Metal organic frameworks as heterogeneous catalysts*; Royal Society of Chemistry, 2013.
(22) Lee, J. Y.; Farha, O. K.; Roberts, J.; Scheidt, K. A.; Nguyen, S. B. T.; Hupp, J. T. *Chem. Soc. Rev.* **2009**, *38*, 1450.
(23) Chughtai, A. H.; Ahmad, N.; Younus, H. A.; Laypkov, A.; Verpoort, F. *Chem. Soc. Rev.* **2015**, *44*, 6804.

(24) Liu, J.; Chen, L.; Cui, H.; Zhang, J.; Zhang, L.; Su, C.-Y. *Chem. Soc. Rev.* **2014**, *43*, 6011.
(25) Huxford, R. C.; Della Rocca, J.; Lin, W. *Curr. Opin. Chem. Biol.* **2010**, *14*, 262.
(26) McKinlay, A. C.; Morris, R. E.; Horcajada, P.; Férey, G.; Gref, R.; Couvreur, P.; Serre, C. *Angew. Chem. Int. Ed.* **2010**, *49*, 6260.
(27) Sun, L.; Campbell, M. G.; Dincă, M. *Angew. Chem. Int. Ed.* **2016**, *55*, 3566.
(28) Allendorf, M. D.; Schwartzberg, A.; Stavila, V.; Talin, A. A. *Chem. Eur. J.* **2011**, *17*, 11372.
(29) Stavila, V.; Talin, A. A.; Allendorf, M. D. *Chem. Soc. Rev.* **2014**, *43*, 5994.
(30) Meek, S. T.; Greathouse, J. A.; Allendorf, M. D. *Adv. Mat.* **2011**, *23*, 249.
(31) Eddaoudi, M.; Kim, J.; Rosi, N.; Vodak, D.; Wachter, J.; O'Keeffe, M.; Yaghi, O. M. *Science* **2002**, *295*, 469.
(32) Yaghi, O. M.; Li, H. *J. Am. Chem. Soc.* **1995**, *117*, 10401.
(33) Gangu, K. K.; Maddila, S.; Mukkamala, S. B.; Jonnalagadda, S. B. *Inorg. Chim. Acta* **2016**, *446*, 61.
(34) Rosi, N. L.; Kim, J.; Eddaoudi, M.; Chen, B.; O'Keeffe, M.; Yaghi, O. M. *J. Am. Chem. Soc.* **2005**, *127*, 1504.
(35) Yaghi, O. M.; O'Keeffe, M.; Ockwig, N. W.; Chae, H. K.; Eddaoudi, M.; Kim, J. *Nature* **2003**, *423*, 705.
(36) Gagnon, K. J.; Perry, H. P.; Clearfield, A. *Chem. Rev.* **2012**, *112*, 1034.
(37) Shimizu, G. K. H.; Vaidhyanathan, R.; Taylor, J. M. *Chem. Soc. Rev.* **2009**, *38*, 1430.
(38) Li, H.; Eddaoudi, M.; O'Keeffe, M.; Yaghi, O. M. *Nature* **1999**, *402*, 276.
(39) Férey, G.; Mellot-Draznieks, C.; Serre, C.; Millange, F.; Dutour, J.; Surblé, S.; Margiolaki, I. *Science* **2005**, *309*, 2040.
(40) Cavka, J. H.; Jakobsen, S.; Olsbye, U.; Guillou, N.; Lamberti, C.; Bordiga, S.; Lillerud, K. P. *J. Am. Chem. Soc.* **2008**, *130*, 13850.
(41) Chui, S. S. Y.; Lo, S. M. F.; Charmant, J. P. H.; Orpen, A. G.; Williams, I. D. *Science* **1999**, *283*, 1148.
(42) Zhao, D.; Timmons, D. J.; Yuan, D.; Zhou, H.-C. *Acc. Chem. Res.* **2011**, *44*, 123.
(43) Bhattacharjee, S.; Chen, C.; Ahn, W.-S. *RSC Advances* **2014**, *4*, 52500.
(44) Bosch, M.; Zhang, M.; Zhou, H.-C. *Advances in Chemistry* **2014**, *2014*, 1.
(45) Bhunia, M. K.; Hughes, J. T.; Fettinger, J. C.; Navrotsky, A. *Langmuir* **2013**, *29*, 8140.
(46) Dietzel, P. D. C.; Johnsen, R. E.; Blom, R.; Fjellvåg, H. *Chem. Eur. J.* **2008**, *14*, 2389.
(47) Zhou, W.; Wu, H.; Yildirim, T. *J. Am. Chem. Soc.* **2008**, *130*, 15268.
(48) Chae, H. K.; Siberio-Perez, D. Y.; Kim, J.; Go, Y.; Eddaoudi, M.; Matzger, A. J.; O'Keeffe, M.; Yaghi, O. M. *Nature* **2004**, *427*, 523.
(49) Dey, C.; Kundu, T.; Biswal, B. P.; Mallick, A.; Banerjee, R. *Acta Crystallogr., Sect. B: Struct. Sci., Cryst. Eng. Mater.* **2014**, *70*, 3.
(50) Stock, N.; Biswas, S. *Chem. Rev.* **2012**, *112*, 933.
(51) Rowsell, J. L. C.; Yaghi, O. M. *Microporous Mesoporous Mater.* **2004**, *73*, 3.
(52) Schaate, A.; Roy, P.; Godt, A.; Lippke, J.; Waltz, F.; Wiebcke, M.; Behrens, P. *Chem. Eur. J.* **2011**, *17*, 6643.
(53) Kappe, C. O. *Angew. Chem. Int. Ed.* **2004**, *43*, 6250.
(54) Kappe, C. O. *Chem. Soc. Rev.* **2008**, *37*, 1127.
(55) Lagashetty, A.; Havanoor, V.; Basavaraja, S.; Balaji, S. D.; Venkataraman, A. *Sci. Technol. Adv. Mater.* **2007**, *8*, 484.
(56) Basith, N. M.; Vijaya, J. J.; Kennedy, L. J.; Bououdina, M.; Jenefar, S.; Kaviyarasan, V. *J. Mater. Sci. Technol.* **2014**, *30*, 1108.

(57) Jhung, S. H.; Chang, J.-S.; Hwang, Y. K.; Park, S.-E. *J. Mater. Chem.* **2004**, *14*, 280.
(58) Hwang, Y. K.; Chang, J.-S.; Park, S.-E.; Kim, D. S.; Kwon, Y.-U.; Jhung, S. H.; Hwang, J.-S.; Park, M. S. *Angew. Chem. Int. Ed.* **2005**, *44*, 556.
(59) Ni, Z.; Masel, R. I. *J. Am. Chem. Soc.* **2006**, *128*, 12394.
(60) Jhung, S. H.; Lee, J.-H.; Yoon, J. W.; Serre, C.; Ferey, G.; Chang, J.-S. *Adv. Mater.* **2007**, *19*, 121.
(61) Khan, N. A.; Haque, E.; Jhung, S. H. *Phys. Chem. Chem. Phys.* **2010**, *12*, 2625.
(62) Seo, Y.-K.; Hundal, G.; Jang, I. T.; Hwang, Y. K.; Jun, C.-H.; Chang, J.-S. *Microporous Mesoporous Mater.* **2009**, *119*, 331.
(63) Choi, J.-S.; Son, W.-J.; Kim, J.; Ahn, W.-S. *Microporous Mesoporous Mater.* **2008**, *116*, 727.
(64) Liang, W.; D'Alessandro, D. M. *Chem. Commun.* **2013**, *49*, 3706.
(65) Hindelang, K.; Vagin, S. I.; Anger, C.; Rieger, B. *Chem. Commun.* **2012**, *48*, 2888.
(66) Klinowski, J.; Almeida Paz, F. A.; Silva, P.; Rocha, J. *Dalton Trans.* **2011**, *40*, 321.
(67) Al-Kutubi, H.; Gascon, J.; Sudhölter, E. J. R.; Rassaei, L. *ChemElectroChem* **2015**, *2*, 462.
(68) Mueller, U.; Puetter, H.; Hesse, M.; Wessel, H.; BASF Aktiengesellschaft, Germany . 2005, p 54 pp.
(69) Mueller, U.; Schubert, M.; Teich, F.; Puetter, H.; Schierle-Arndt, K.; Pastre, J. *J. Mater. Chem.* **2006**, *16*, 626.
(70) Martinez Joaristi, A.; Juan-Alcaniz, J.; Serra-Crespo, P.; Kapteijn, F.; Gascon, J. *Cryst. Growth Des.* **2012**, *12*, 3489.
(71) Schlesinger, M.; Schulze, S.; Hietschold, M.; Mehring, M. *Microporous Mesoporous Mater.* **2010**, *132*, 121.
(72) Katz, M. J.; Brown, Z. J.; Colon, Y. J.; Siu, P. W.; Scheidt, K. A.; Snurr, R. Q.; Hupp, J. T.; Farha, O. K. *Chem. Commun.* **2013**, *49*, 9449.
(73) Valenzano, L.; Civalleri, B.; Chavan, S.; Bordiga, S.; Nilsen, M. H.; Jakobsen, S.; Lillerud, K. P.; Lamberti, C. *Chem. Mater.* **2011**, *23*, 1700.
(74) Zhang, W.; Huang, H.; Zhong, C.; Liu, D. *Phys. Chem. Chem. Phys.* **2012**, *14*, 2317.
(75) Sindoro, M.; Yanai, N.; Jee, A.-Y.; Granick, S. *Acc. Chem. Res.* **2014**, *47*, 459.
(76) Kang, I. J.; Khan, N. A.; Haque, E.; Jhung, S. H. *Chem. Eur. J.* **2011**, *17*, 6437.
(77) Park, K. S.; Ni, Z.; Côté, A. P.; Choi, J. Y.; Huang, R.; Uribe-Romo, F. J.; Chae, H. K.; O'Keeffe, M.; Yaghi, O. M. *Proc. Nat. Acad. Sci.* **2006**, *103*, 10186.
(78) Kandiah, M.; Nilsen, M. H.; Usseglio, S.; Jakobsen, S.; Olsbye, U.; Tilset, M.; Larabi, C.; Quadrelli, E. A.; Bonino, F.; Lillerud, K. P. *Chem. Mater.* **2010**, *22*, 6632.
(79) Colombo, V.; Galli, S.; Choi, H. J.; Han, G. D.; Maspero, A.; Palmisano, G.; Masciocchi, N.; Long, J. R. *Chem. Sci.* **2011**, *2*, 1311.
(80) Furukawa, H.; Cordova, K. E.; O'Keeffe, M.; Yaghi, O. M. *Science* **2013**, *341*, 974.
(81) Li, H.; Shi, W.; Zhao, K.; Li, H.; Bing, Y.; Cheng, P. *Inorg. Chem.* **2012**, *51*, 9200.
(82) Greathouse, J. A.; Allendorf, M. D. *J. Am. Chem. Soc.* **2006**, *128*, 10678.
(83) Huang, L.; Wang, H.; Chen, J.; Wang, Z.; Sun, J.; Zhao, D.; Yan, Y. *Microporous Mesoporous Mater.* **2003**, *58*, 105.
(84) Tan, K.; Nijem, N.; Canepa, P.; Gong, Q.; Li, J.; Thonhauser, T.; Chabal, Y. J. *Chem. Mater.* **2012**, *24*, 3153.
(85) Zhang, M.; Chen, Y.-P.; Bosch, M.; Gentle, T.; Wang, K.; Feng, D.; Wang, Z. U.; Zhou, H.-C. *Angew. Chem. Int. Ed.* **2014**, *53*, 815.
(86) DeCoste, J. B.; Peterson, G. W.; Jasuja, H.; Glover, T. G.; Huang, Y.-g.; Walton, K. S. *J. Mat. Chem. A* **2013**, *1*, 5642.

(87) Wang, Z.; Cohen, S. M. *Chem. Soc. Rev.* **2009**, *38*, 1315.
(88) Tanabe, K. K.; Cohen, S. M. *Chem. Soc. Rev.* **2011**, *40*, 498.
(89) Chen, C.-L.; Goforth, A. M.; Smith, M. D.; Su, C.-Y.; zur Loye, H.-C. *Angew. Chem.* **2005**, *117*, 6831.
(90) Suh, M. P.; Cheon, Y. E.; Lee, E. Y. *Chem. Eur. J.* **2007**, *13*, 4208.
(91) Dietzel, P. D. C.; Morita, Y.; Blom, R.; Fjellvåg, H. *Angew. Chem. Int. Ed.* **2005**, *44*, 6354.
(92) Dietzel, P. D. C.; Panella, B.; Hirscher, M.; Blom, R.; Fjellvag, H. *Chem. Commun.* **2006**, 959.
(93) Wang, Z.; Cohen, S. M. *J. Am. Chem. Soc.* **2007**, *129*, 12368.
(94) Wang, Z.; Tanabe, K. K.; Cohen, S. M. *Chem. Eur. J.* **2010**, *16*, 212.
(95) Getman, R. B.; Bae, Y.-S.; Wilmer, C. E.; Snurr, R. Q. *Chem. Rev.* **2012**, *112*, 703.
(96) Rosi, N. L.; Eckert, J.; Eddaoudi, M.; Vodak, D. T.; Kim, J.; O'Keeffe, M.; Yaghi, O. M. *Science* **2003**, *300*, 1127.
(97) Sheppard, D. A.; Buckley, C. E. *Int. J. Hydrogen Energy* **2008**, *33*, 1688.
(98) Furukawa, H.; Ko, N.; Go, Y. B.; Aratani, N.; Choi, S. B.; Choi, E.; Yazaydin, A. O.; Snurr, R. Q.; O'Keeffe, M.; Kim, J.; Yaghi, O. M. *Science* **2010**, *329*, 424.
(99) Farha, O. K.; Oezguer Yazaydin, A.; Eryazici, I.; Malliakas, C. D.; Hauser, B. G.; Kanatzidis, M. G.; Nguyen, S.-B. T.; Snurr, R. Q.; Hupp, J. T. *Nat. Chem.* **2010**, *2*, 944.
(100) Wong-Foy, A. G.; Matzger, A. J.; Yaghi, O. M. *J. Am. Chem. Soc.* **2006**, *128*, 3494.
(101) Lin, X.; Telepeni, I.; Blake, A. J.; Dailly, A.; Brown, C. M.; Simmons, J. M.; Zoppi, M.; Walker, G. S.; Thomas, K. M.; Mays, T. J.; Hubberstey, P.; Champness, N. R.; Schroder, M. *J. Am. Chem. Soc.* **2009**, *131*, 2159.
(102) Wang, X.-S.; Ma, S.; Forster, P. M.; Yuan, D.; Eckert, J.; Lopez, J. J.; Murphy, B. J.; Parise, J. B.; Zhou, H.-C. *Angew. Chem. Int. Ed.* **2008**, *47*, 7263.
(103) Wu, H.; Zhou, W.; Yildirim, T. *J. Am. Chem. Soc.* **2009**, *131*, 4995.
(104) Lee, Y.-G.; Moon, H. R.; Cheon, Y. E.; Suh, M. P. *Angew. Chem. Int. Ed.* **2008**, *47*, 7741.
(105) Ahrenholtz, S. R.; Landaverde-Alvarado, C.; Whiting, M.; Lin, S.; Slebodnick, C.; Marand, E.; Morris, A. J. *Inorg. Chem.* **2015**, *54*, 4328.
(106) Yazaydin, A. O.; Snurr, R. Q.; Park, T.-H.; Koh, K.; Liu, J.; LeVan, M. D.; Benin, A. I.; Jakubczak, P.; Lanuza, M.; Galloway, D. B.; Low, J. J.; Willis, R. R. *J. Am. Chem. Soc.* **2009**, *131*, 18198.
(107) Millward, A. R.; Yaghi, O. M. *J. Am. Chem. Soc.* **2005**, *127*, 17998.
(108) Caskey, S. R.; Wong-Foy, A. G.; Matzger, A. J. *J. Am. Chem. Soc.* **2008**, *130*, 10870.
(109) Aprea, P.; Caputo, D.; Gargiulo, N.; Iucolano, F.; Pepe, F. *J. Chem. Eng. Data* **2010**, *55*, 3655.
(110) Mason, J. A.; Sumida, K.; Herm, Z. R.; Krishna, R.; Long, J. R. *Energy Environ. Sci.* **2011**, *4*, 3030.
(111) Arstad, B.; Fjellvåg, H.; Kongshaug, K. O.; Swang, O.; Blom, R. *Adsorption* **2008**, *14*, 755.
(112) An, J.; Geib, S. J.; Rosi, N. L. *J. Am. Chem. Soc.* **2010**, *132*, 38.
(113) McDonald, T. M.; D'Alessandro, D. M.; Krishna, R.; Long, J. R. *Chem. Sci.* **2011**, *2*, 2022.
(114) Hendon, C. H.; Tiana, D.; Walsh, A. *Phys. Chem. Chem. Phys.* **2012**, *14*, 13120.
(115) Guldi, D. M.; Nishihara, H.; Venkataraman, L. *Chem. Soc. Rev.* **2015**, *44*, 842.
(116) Patwardhan, S.; Schatz, G. C. *J. Phys. Chem. C* **2015**, *119*, 24238.
(117) Morozan, A.; Jaouen, F. *Energy Environ. Sci.* **2012**, *5*, 9269.

(118) Ramaswamy, P.; Wong, N. E.; Shimizu, G. K. H. *Chem. Soc. Rev.* **2014**, *43*, 5913.
(119) Takaishi, S.; Hosoda, M.; Kajiwara, T.; Miyasaka, H.; Yamashita, M.; Nakanishi, Y.; Kitagawa, Y.; Yamaguchi, K.; Kobayashi, A.; Kitagawa, H. *Inorg. Chem.* **2009**, *48*, 9048.
(120) Kobayashi, Y.; Jacobs, B.; Allendorf, M. D.; Long, J. R. *Chem. Mater.* **2010**, *22*, 4120.
(121) Holliday, B. J.; Swager, T. M. *Chem. Commun.* **2005**, 23.
(122) Komatsu, T.; Taylor, J. M.; Kitagawa, H. *Inorg. Chem.* **2016**, *55*, 546.
(123) Sun, L.; Miyakai, T.; Seki, S.; Dincă, M. *J. Am. Chem. Soc.* **2013**, *135*, 8185.
(124) Zhang, Q.; Li, B.; Chen, L. *Inorg. Chem.* **2013**, *52*, 9356.
(125) Sun, L.; Hendon, C. H.; Minier, M. A.; Walsh, A.; Dincă, M. *J. Am. Chem. Soc.* **2015**, *137*, 6164.
(126) Allendorf, M. D.; Foster, M. E.; Léonard, F.; Stavila, V.; Feng, P. L.; Doty, F. P.; Leong, K.; Ma, E. Y.; Johnston, S. R.; Talin, A. A. *J. Phys. Chem. Lett.* **2015**, *6*, 1182.
(127) Talin, A. A.; Centrone, A.; Ford, A. C.; Foster, M. E.; Stavila, V.; Haney, P.; Kinney, R. A.; Szalai, V.; El Gabaly, F.; Yoon, H. P.; Léonard, F.; Allendorf, M. D. *Science* **2014**, *343*, 66.
(128) Hendon, C. H.; Walsh, A. *Chem. Sci.* **2015**, *6*, 3674.
(129) Hwang, Y. K.; Hong, D.-Y.; Chang, J.-S.; Seo, H.; Yoon, M.; Kim, J.; Jhung, S. H.; Serre, C.; Férey, G. *Appl. Catal., A* **2009**, *358*, 249.
(130) Xie, M.-H.; Yang, X.-L.; Wu, C.-D. *Chem. Eur. J.* **2011**, *17*, 11424.
(131) Cho, H.-Y.; Yang, D.-A.; Kim, J.; Jeong, S.-Y.; Ahn, W.-S. *Catal. Today* **2012**, *185*, 35.
(132) Wang, C.; Xie, Z.; de Krafft, K. E.; Lin, W. *J. Am. Chem. Soc.* **2011**, *133*, 13445.
(133) Hod, I.; Sampson, M. D.; Deria, P.; Kubiak, C. P.; Farha, O. K.; Hupp, J. T. *ACS Catalysis* **2015**, *5*, 6302.
(134) Suslick, K. S.; Bhyrappa, P.; Chou, J. H.; Kosal, M. E.; Nakagaki, S.; Smithenry, D. W.; Wilson, S. R. *Acc. Chem. Res.* **2005**, *38*, 283.
(135) Lykourinou, V.; Chen, Y.; Wang, X.-S.; Meng, L.; Hoang, T.; Ming, L.-J.; Musselman, R. L.; Ma, S. *J. Am. Chem. Soc.* **2011**, *133*, 10382.
(136) Canivet, J.; Aguado, S.; Schuurman, Y.; Farrusseng, D. *J. Am. Chem. Soc.* **2013**, *135*, 4195.
(137) Yang, H.; Li, J.; Wang, L.; Dai, W.; Lv, Y.; Gao, S. *Catal. Commun.* **2013**, *35*, 101.
(138) Alkordi, M. H.; Liu, Y.; Larsen, R. W.; Eubank, J. F.; Eddaoudi, M. *J. Am. Chem. Soc.* **2008**, *130*, 12639.
(139) Sun, Z.; Li, G.; Liu, L.; Liu, H.-o. *Catal. Commun.* **2012**, *27*, 200.
(140) Grinstaff, M. W.; Hill, M. G.; Labinger, J. A.; Gray, H. B. *Science* **1994**, *264*, 1311.
(141) Bhugun, I.; Lexa, D.; Saveant, J.-M. *J. Am. Chem. Soc.* **1996**, *118*, 1769.
(142) Chang, C. J.; Loh, Z.-H.; Shi, C.; Anson, F. C.; Nocera, D. G. *J. Am. Chem. Soc.* **2004**, *126*, 10013.
(143) Moser, W. R.; Slocum, D. W. *Homogeneous Transition Metal Catalyzed Reactions*; American Chemical Society, 1992; Vol. 230.
(144) Zalomaeva, O. V.; Chibiryaev, A. M.; Kovalenko, K. A.; Kholdeeva, O. A.; Balzhinimaev, B. S.; Fedin, V. P. *J. Catal.* **2013**, *298*, 179.
(145) Dhakshinamoorthy, A.; Alvaro, M.; Chevreau, H.; Horcajada, P.; Devic, T.; Serre, C.; Garcia, H. *Catal. Sci. Technol.* **2012**, *2*, 324.
(146) Mitchell, L.; Gonzalez-Santiago, B.; Mowat, J. P. S.; Gunn, M. E.; Williamson, P.; Acerbi, N.; Clarke, M. L.; Wright, P. A. *Catal. Sci. Technol.* **2013**, *3*, 606.
(147) Horike, S.; Dincă, M.; Tamaki, K.; Long, J. R. *J. Am. Chem. Soc.* **2008**, *130*, 5854.
(148) Tonigold, M.; Lu, Y.; Mavrandonakis, A.; Puls, A.; Staudt, R.; Möllmer, J.; Sauer, J.; Volkmer, D. *Chem. Eur. J.* **2011**, *17*, 8671.
(149) Dhakshinamoorthy, A.; Alvaro, M.; Garcia, H. *J. Catal.* **2009**, *267*, 1.

(150) Dhakshinamoorthy, A.; Alvaro, M.; Garcia, H. *Adv. Synth. Catal.* **2009**, *351*, 2271.
(151) Kärkäs, M. D.; Verho, O.; Johnston, E. V.; Åkermark, B. *Chem. Rev.* **2014**, *114*, 11863.
(152) Okada, T.; Kaneko, M. *Molecular Catalysts for Energy Conversion*; Springer, 2009.
(153) Sala, X.; Maji, S.; Bofill, R.; Garcia-Anton, J.; Escriche, L.; Llobet, A. *Acc. Chem. Res.* **2014**, *47*, 504.
(154) Pullen, S.; Fei, H.; Orthaber, A.; Cohen, S. M.; Ott, S. *J. Am. Chem. Soc.* **2013**, *135*, 16997.
(155) Hansen, R. E.; Das, S. *Energy Environ. Sci.* **2014**, *7*, 317.
(156) Wang, C.; Wang, J.-L.; Lin, W. *J. Am. Chem. Soc.* **2012**, *134*, 19895.
(157) Shultz, A. M.; Farha, O. K.; Hupp, J. T.; Nguyen, S. T. *J. Am. Chem. Soc.* **2009**, *131*, 4204.
(158) Xie, M.-H.; Yang, X.-L.; Wu, C.-D. *Chem. Commun.* **2011**, *47*, 5521.
(159) Song, F.; Wang, C.; Falkowski, J. M.; Ma, L.; Lin, W. *J. Am. Chem. Soc.* **2010**, *132*, 15390.
(160) Hou, C.-C.; Li, T.-T.; Cao, S.; Chen, Y.; Fu, W.-F. *J. Mat. Chem. A* **2015**, *3*, 10386.

2. Solvothermal Preparation of an Electrocatalytic Metalloporphyrin MOF Thin Film and its Redox Hopping Charge-Transfer Mechanism

2.1 Motivation and Abstract

The ability of a material to transport charge is a critical requirement in order for ultimate applications in catalysis. There is several charge conduction mechanisms possible depending on the innate properties of the material. In order to gain a deeper understanding of charge transport properties in metal-organic frameworks (MOFs) and what structural features facilitate conduction, our investigations began by selecting a MOF comprised of components capable of undergoing redox reactions and investigating its ability to transport charge throughout the framework. Specifically, a thin film of a metalloporphyrin MOF consisting of [5,10,15,20-(4-carboxyphenyl)porphyrin]Co(III) (CoTCPP) struts bound by linear trinuclear Co^{II}-carboxylate clusters has been prepared solvothermally on conductive fluorine doped tin oxide (FTO) substrates. Characterization of this mesoporous thin film material, designated as CoPIZA/FTO, which is equipped with large cavities and access to metal active sites, reveals an electrochemically active material. Cyclic voltammetry displays a reversible peak with $E_{1/2}$ at −1.04 V vs. ferrocyanide attributed to the ($Co^{III/II}$TCPP)CoPIZA redox couple and a quasi-reversible peak at −1.45 V vs. ferrocyanide, which corresponds to the reduction of ($Co^{II/I}$TCPP)CoPIZA. Analysis of the spectroelectrochemical response for the

($Co^{II/I}$TCPP)CoPIZA redox couple revealed non-Nernstian reduction with a non-ideality factor of 2 and an $E_{1/2}$ of −1.39 V vs. ferrocyanide. The film was shown to retain its structural integrity with applied potential, as was demonstrated spectroelectrochemically with maintenance of isosbestic points at 430, 458 and 544 nm corresponding to the ($Co^{III/II}$TCPP)CoPIZA transition and at 390 and 449 nm corresponding to the ($Co^{II/I}$TCPP)CoPIZA transition. The mechanism of charge transport through the film is proposed to be a redox hopping mechanism, which is supported by both cyclic voltammetry and spectroelectrochemistry. A fit of the time dependent spectroelectrochemical data to a modified Cottrell equation gave an apparent diffusion coefficient of 7.55 (±0.05) x 10^{-14} cm^2 s^{-1} for ambipolar electron and cation transport throughout the film. Upon reduction of the metalloporphyrin struts to (Co^{I}TCPP)CoPIZA, the CoPIZA thin film demonstrated catalytic activity for the reduction of carbon tetrachloride.

2.2 Introduction

Metal-organic frameworks (MOFs) are 3D porous crystalline networks formed through the orientation of metal nodes by multi-dentate organic linkers.[1] The porous nature of these materials has led to various applications in gas storage and separation, as well as drug delivery.[2-6] High surface area, porous materials also have tremendous potential for use in catalysis.[7,8] Theoretically, every catalytic center in the MOF (metal or linker) is accessible for reactivity. Therefore, less material is required in comparison to traditional approaches. Indeed, MOFs have proven to be excellent scaffolds for Lewis acid catalyzed reactions, as well as enantioselective catalysis.[8,9]

Critical environmentally-relevant catalytic processes including CO_2 reduction, H_2O oxidation, and H^+ reduction rely on electron transfer reactivity. Therefore, MOFs capable of driving electron transfer chemistry have the potential to revolutionize the field of envirocatalysis. However, the intrinsic insulating nature of the caboxylate bonds utilized to form MOFs results in low conductivity.[10] Some focus has been placed on the use of band structure to explain electron transport through MOFs.[11-13] However, the predicted band gaps are well above kT and cannot explain conduction in the dark. Also, MOFs are "soft" materials that, upon the addition of charge, are likely to reorganize locally, causing disruption to the band structure. Therefore, the nature of electron transfer through MOFs is most likely an electron hopping mechanism, similar to that demonstrated by Murray in Os and Fe polypyridine redox polymers.[14]

There have been various investigations into photo-initiated electron transfer through MOFs. Indeed, MOFs containing known photoactive H_2O oxidation and CO_2 reduction catalysts have been shown to reduce their substrates with moderate efficiency.[15] In these studies, photo-initiated electron migration to the surface of MOF particles was faster than catalysis. Therefore, while these materials are insulating, conductivity is not limiting. That being said, the conductivity of MOFs has been synthetically tuned by building in linear molecular chains poised for redox hopping throughout the framework.[16,17] In light of this elegant work on photoelectron transfer, few studies on electrochemically driven catalysis exist in the literature.[18-20] Of those that do appear, it is unclear whether the observed reactivity occurs at electrodeposited metals or metal oxides formed at highly reducing or oxidizing potentials or the MOF itself.[21,22]

Metalloporphyrins (Fe and Co) have been shown to promote the reduction of various substrates including H^+, CO_2, and organohalides.[23-26] In addition, their spectral properties (large

extinction coefficients and distinct spectra sensitive to varying oxidation state)[27] make them ideal candidates for spectroelectrochemical studies. Various porous materials comprised of porphyrins have been developed[28], including porphyrinic MOFs with open accessibility to redox active metal centers.[29-35] Efficient exciton migration through a zinc-metallated porphyrin MOF developed by Hupp, et al. has been observed.[36]

For electrocatalysis, it is advantageous to prepare the MOF as a thin film, allowing for direct attachment to the electrode surface, control of film thickness, and unobstructed access to pore cavities and available active sites.[37,38] To date, there exist several methods for the preparation of MOF thin films onto substrates.[37,38] These include the direct adsorption of densely packed individual crystallites formed or preformed in solution onto a modified or unmodified surface and a layer-by-layer (LBL) approach, in which the substrate is alternately exposed to solutions containing metal and linker(s) yielding films of uniform crystallinity whose growth is directional.[39-43] Recently, a LBL approach for oriented porphyrin films has been developed.[44] Porphyrin MOF thin films have previously been prepared by a Langmuir-Blodgett approach yielding layered 2D films.[45-47] Porphyrinic thin films grown directly onto a substrate surface via an alternative third approach, termed solvothermal deposition, have not yet been reported.

Herein, we report the first solvothermal synthesis and spectroelectrochemical investigation of a redox active porphyrinic-MOF thin film for application in envirocatalysis. The metalloporphyrin MOF contains [5,10,15,20-(4-carboxyphenyl) porphyrin]Co(III) (CoTCPP) struts bound by linear trinuclear Co^{II}-carboxylate clusters to form a porous network with large channels (Figure 2.1).[31] The film, grown on a conductive fluorine-doped tin oxide (FTO) substrate, is designated as CoPIZA/FTO and displayed a reversible electrochemical response

while maintaining structural integrity. This provided a scaffold for detailed mechanistic investigation into the action of charge transfer through MOF materials. Analysis of the electrochemical response supports a redox hopping mechanism for charge transport. Lastly, the intact MOF film was demonstrated to be catalytically active, promoting CCl_4 reduction.

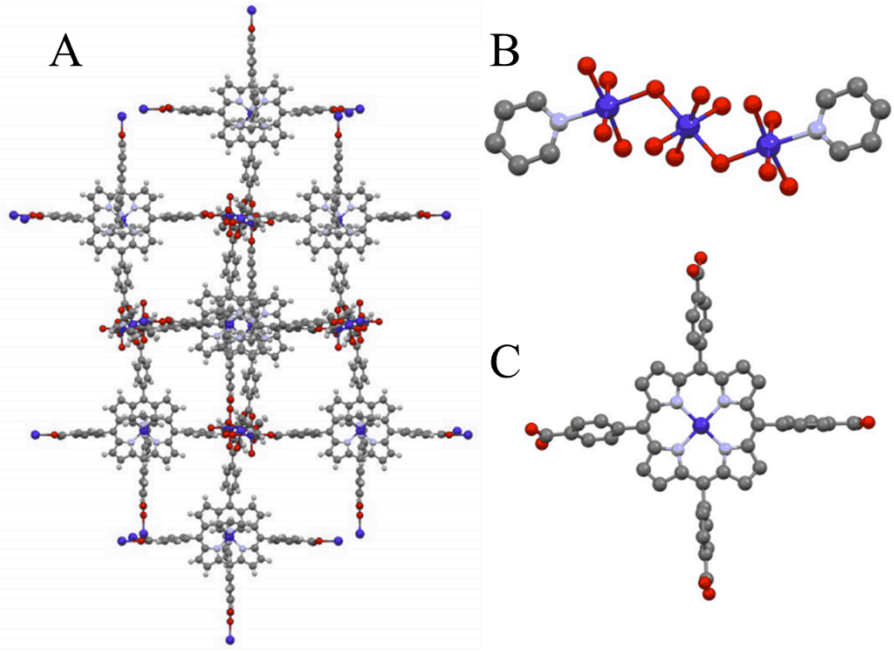

Figure 2.1. (A) CoPIZA as viewed down the (100) direction showing the large channels in the MOF network; (B) The cobalt clusters of CoPIZA; (C) The CoTCPP within the CoPIZA framework.[31] Hydrogen atoms have been omitted for clarity. Dark Gray: C; Red: O; Blue/Gray: N; Blue: Co.

2.3 Experimental

2.3.1 Materials. The following reagents and solvents were purchased from the indicated commercial suppliers: cobalt(II) chloride hexahydrate (Fluka Analytical); meso-tetra-(4-carboxy)tetraphenyl porphine (TCPP; Frontier Scientific); pyridine, ACS, 99.0% min, distilled before use (Alfa Aesar); potassium hydroxide (Sigma Aldrich); *N,N*-dimethylformamide (DMF),

spectrophotometric grade (Spectrum); lithium perchlorate (Sigma Aldrich); fluorine doped tin oxide (FTO; Hartford Glass).

2.3.2 Thin Film Synthesis. The thin film synthesis was developed based on the previously reported CoPIZA MOF synthesis.[31] To prepare a self-assembled monolayer (SAM) of porphyrin, the FTO was first soaked in a pH 10 aqueous solution for 20 minutes. The FTO was then immersed in a TCPP/DMSO (0.1 mM) solution overnight. A mixture of $CoCl_2 \cdot 6H_2O$ (0.15 mmol) and meso-tetra-(4-carboxyphenyl)porphyrin (0.05 mmol) in 3.0 mL of 0.1 M pyridine/KOH was sonicated to mix. The mixture was then combined with the SAM-coated FTO in a sealed tube and heated at 150 °C for two days. The resulting purple powder was filtered, and the powder and thin film was washed with DMF.

2.3.3 Powder X-ray Diffraction (PXRD). PXRD experiments were carried out on a Rigaku Altima IV with Cu(Kα) radiation (Cu-Kα = 0.15418 nm). A grazing incidence angle diffraction was used with a thin film stage. The PXRD measurements were carried out over a 2theta range of 5-50° in continuous scanning mode with 0.05° steps at a rate of 0.5°/minute.

2.3.4 Microscopy Imaging. ***Scanning electron microscopy (SEM)***. A LEO (Zeiss) 1550 field-emission scanning electron microscope at 5.0 kV was used for high-resolution images of the thin films. ***Atomic Force Microscopy (AFM)***. A Veeco MultiMode AFM was operated in tapping mode to obtain the topology of the thin films.

2.3.5 X-ray photoelectron spectroscopy (XPS). XPS was conducted using a PHI 5300 spectrometer with a Perkin-Elmer Dual Anode X-ray source operating with magnesium radiation with monochromatic Mg Kα radiation (hν 1253.6 eV) at 13 kV and 250 W and a pass energy of 17.9 eV. A step size of 0.025 eV was used and 180 sweeps were averaged. Emitted

photoelectrons were detected by a hemispherical analyzer and the operating pressure in the sampling chamber was below 1×10^{-7} Torr. The spectral scanning range for Nitrogen 1s was 410-390 eV and for Cobalt 2p was 765-815 eV. The spectra were calibrated according to the C 1s peak, which is known to occur at 284.6 eV.[48]

2.3.6 Attenuated total reflectance Fourier-transform infrared spectroscopy (ATR-FTIR). ATR-FTIR spectra were obtained on a Varian 670 FT-IR Spectrometer equipped with a diamond Specac Golden Gate attachment. All spectra are an average of 24 scans for powder samples and 6000 scans for thin films and were recorded from 4000 to 400 cm^{-1} with 4 cm^{-1} resolution. A background spectrum collected on air was subtracted from sample spectra. The spectra were not corrected for the depth of wavelength penetration.

2.3.7 Steady-state UV-visible Absorption Spectroscopy. Steady-state UV-visible absorption spectroscopy was performed on a Cary Series UV-vis-NIR spectrophotometer. The wavelength was scanned from 800-200 nm with a data interval of 1.00 nm and scan rate of 600 nm/min.

2.3.8 Electrochemical Impedance Spectroscopy (EIS). EIS was performed with a Solartron SI 1260 Impedance analyzer controlled with a PC interface and Zplot 2.9 software. The sample was positioned between two gold plated stainless steel electrodes to measure through-plane conductivity using a Solartron 12960 sample holder with a built-in micrometer and a frequency range of 3.2 MHz to 100 Hz. The AC amplitude applied was 10 mV with a frequency range of 16 mHz – 0.1 Hz. The film conductivity was obtained using the high frequency intercept of the obtained Nyquist plot.

2.3.9 Electrochemistry. A BASi Epsilon potentiostat was employed for measurements in a three-electrode electrochemical cell with CoPIZA on FTO as the working electrode, platinum

mesh as counter electrode, and Ag/AgCl (saturated KCl, aqueous) as reference in 0.1 M $LiClO_4$/DMF electrolyte. The Ag/AgCl was calibrated against the $Fe(CN)_6^{3-}/Fe(CN)_6^{4-}$ couple, where the expected $E_{1/2}$ is +361 mV vs. NHE and Ag/AgCl is +197 mV vs. NHE.[49] The scan rate was varied over the range 10 – 1000 mV/sec.

2.3.10 Spectroelectrochemistry. Spectroelectrochemistry was performed in a three-electrode arrangement containing the CoPIZA/FTO as working electrode, platinum mesh counter electrode, and Ag/AgCl (saturated KCl, aqueous) as reference. The electrochemical cell was set up in a quartz cuvette with a 24/40 joint capped with a rubber septum. The electrodes were immersed in a 0.1 M $LiClO_4$/DMF electrolyte solution and purged with nitrogen for one hour. The potential was applied with a BASi Epsilon potentiostat while the spectra were observed with a Cary Series UV-vis-NIR spectrophotometer.

2.4 Results and Discussion

2.4.1 Synthesis and Structural Characterization

CoPIZA/FTO was prepared solvothermally via templation by a self-assembled monolayer (SAM) of the porphyrin linker adsorbed onto the FTO substrate. The SAM was formed by immersion of the FTO in a solution of tetrakis(4-carboxyphenyl)porphyrin (TCPP) overnight. Surface analysis using X-ray photoelectron spectroscopy (XPS) detected the presence nitrogen on the sample, which was not present on bare FTO (Figure 2.2A, black) and is suggestive of the SAM formation on the electrode surface. The observed N1s peak at 401 eV is attributed to the pyrrole nitrogens of the TCPP (Figure 2.2A, red).[50] The SAM-coated FTO was then transferred to a glass tube, followed by the addition of $CoCl_2 \cdot 6H_2O$, TCPP, and an aqueous

pyridine/KOH solution.[31] Under solvothermal conditions, the metalloporphyrin MOF grew directly onto the FTO substrate, confirmed by XPS, powder X-ray diffraction (PXRD) and scanning electron microscopy (SEM) (Figure 2.2). XPS confirmed CoPIZA formation after the solvothermal reaction, as indicated by peaks at 782 and 798 eV corresponding to the Co2p binding energy (Figure 2.2B, blue). The N1s peak of CoPIZA (Figure 2.2A, blue) is broadened, consistent with both the pyrrole nitrogen atoms of TCPP and the addition of bound pyridine in the cobalt clusters of the MOF network.[50]

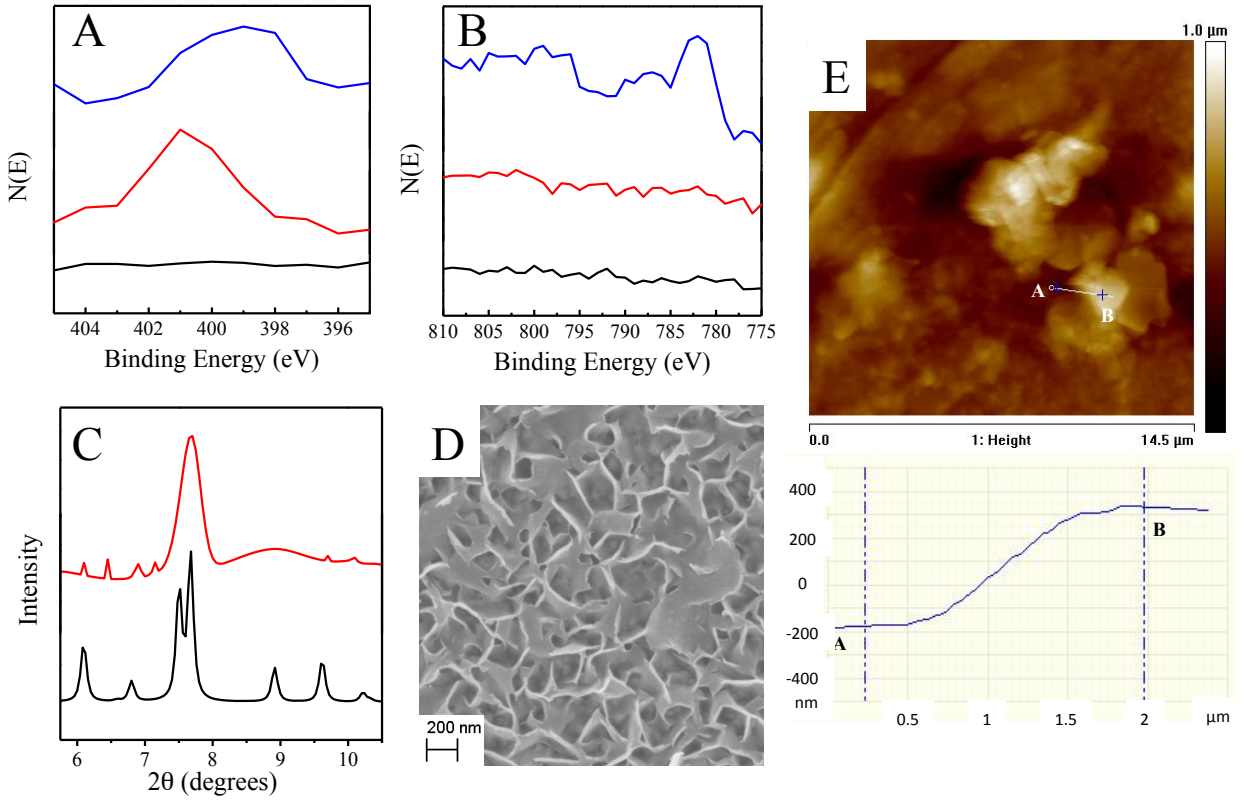

Figure 2.2. XPS of FTO (black), the TCPP SAM/FTO (red) and CoPIZA/FTO (blue) showing the N1s peak (A) and Co2p peak (B); (C) PXRD pattern of CoPIZA/FTO (red) and the simulated CoPIZA single crystal pattern (black); (D) SEM image of CoPIZA/FTO; (E) AFM image of CoPIZA/FTO thin film.

The PXRD of the CoPIZA/FTO displays peaks at 6.1, 6.9, 7.6, 9.7 and 10.1° (Figure 2.2C, red) that coincide with those of the simulated CoPIZA pattern based on the single crystal data previously reported (Figure 2.2C, black).[31] While the peak at 7.6° in the CoPIZA/FTO pattern cannot be fully resolved, it is a characteristic peak of the framework corresponding to reflections associated with the (020) and (002) planes of the unit cell. Therefore, the appearance of this peak and similar matching peak positions suggest that the film maintains the structure of CoPIZA. Additionally, the peaks present at 6.4 and 7.2° in the CoPIZA/FTO pattern that are absent from the CoPIZA single crystal pattern, which, as a result of the orientation and layering of the MOF crystallites in the film, can be due to the multiple diffractions of the X-ray beam from the individual crystallites or unknown impurities.[51] The SEM image of the CoPIZA film (Figure 2.2D) shows a network of intergrown crystals on the surface. The height and topography of the network was investigated using atomic force microscopy imaging. The topography of the film is shown in Figure 2.2E (top) with the MOF particles being the brighter areas on the image. The height (measured from points A and B) of the film was determined to be between 200 and 500 nm (Figure 2.2E, bottom).

Attenuated total reflectance Fourier-transform infrared (ATR-FTIR) spectroscopy was used to characterize CoPIZA powder, CoPIZA/FTO, TCPP, and metallated CoTCPP (Figure 2.3). The TCPP and CoTCPP spectra (black and red, respectively) show features corresponding to the C=O stretch of the carboxylic acids at 1680 cm^{-1} and 1687 cm^{-1}, respectively, and a peak at 1600 cm^{-1}, which corresponds to the C=C stretch of the aromatic carbons of the macrocycle. The CoPIZA powder spectrum (green) shows a shift of the carboxylate stretching band to lower

frequency at 1664 cm^{-1}, due to the transformation of the carboxylic acid groups of the free porphyrin to the carboxylato chelating functionality in the MOF. The appearance of a peak at 1400 cm^{-1} in the CoPIZA spectrum corresponds to the C-N ring stretching of bound pyridine molecules. Similar features are observed in the CoPIZA/FTO spectrum (blue) but cannot be fully resolved due to the nanometer thickness of the film.

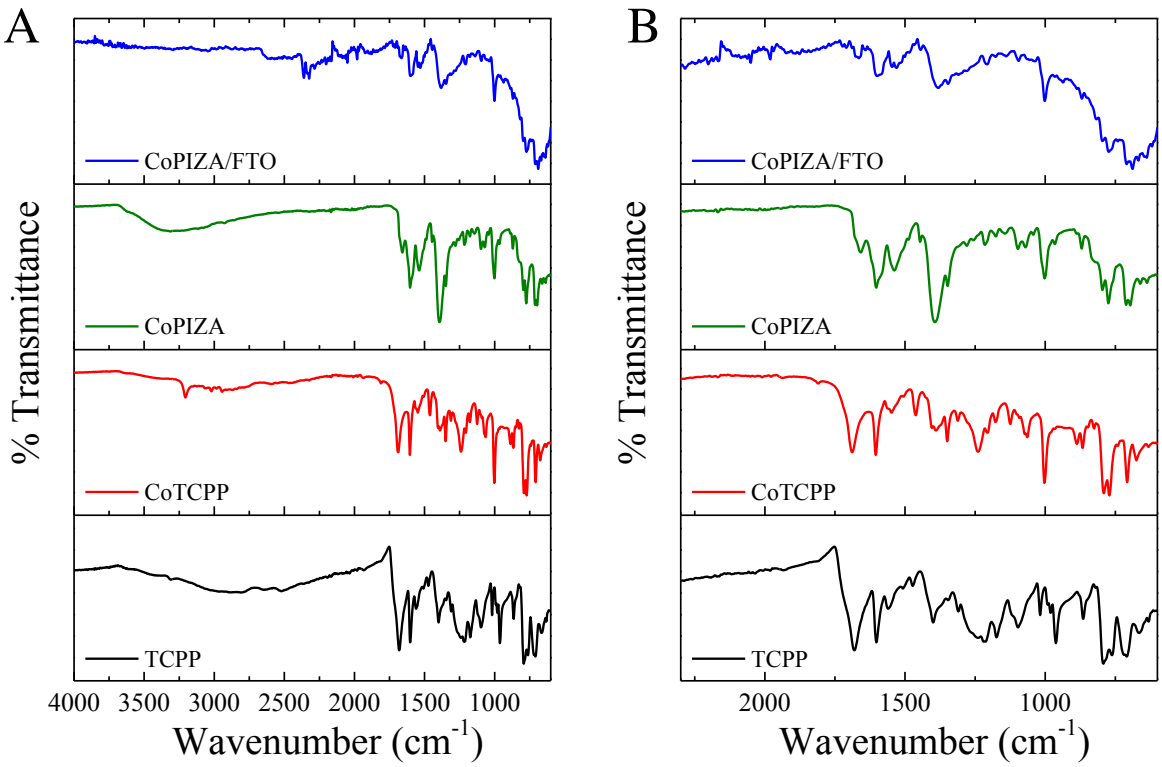

Figure 2.3. ATR-FTIR spectra of TCPP (black), CoTCPP (red), CoPIZA MOF powder (green), and CoPIZA/FTO (blue) with (A) the full range of the spectrum and (B) zooming in at lower wavenumbers.

The steady-state absorption spectrum of TCPP in DMF was characteristic of free-base porphyrins of D_{2h} symmetry in solution, displaying an intense Soret band in the near UV region

centered at 420 nm and four low energy Q bands in the visible region occurring at 515, 549, 590, and 645 nm (Figure 2.4A, black).[52] Upon chelation to the porphyrinic nitrogens to the Co^{III} metal center in CoPIZA/FTO, the symmetry increases to D_{4h} and is accompanied by a red shift of the Soret band to 436 nm and collapse of the four Q-bands into two bands at 548 and 595 nm (Figure 2.4B, red). After purging with nitrogen, CoPIZA/FTO/DMF displayed spectral characteristics of both Co^{III}TCPP and Co^{II}TCPP, as Co^{III}TCPP/CoPIZA undergoes autoreduction by electron donating axial pyridine ligands to form Co^{II}TCPP/CoPIZA (Figure 2.4A, blue).[53] The Co-carboxylate clusters in the CoPIZA framework are also expected to absorb light but are not observed in the steady-state absorption spectra due to the large extinction coefficient of CoTCPP ($\sim 10^5$ M^{-1} cm^{-1}).[27] The effect of varying the pyridine concentration in the solvothermal film synthesis was also investigated using UV-visible spectroscopy. It was observed that with increasing pyridine concentration, the absorbance decreased while the peak wavelength exhibited a red shift (Figure 2.4B). This is attributed to pyridine's effect on the equilibrium between solid CoPIZA crystallites and the molecular components in solution, as well as the CoTCPP ligation environment.

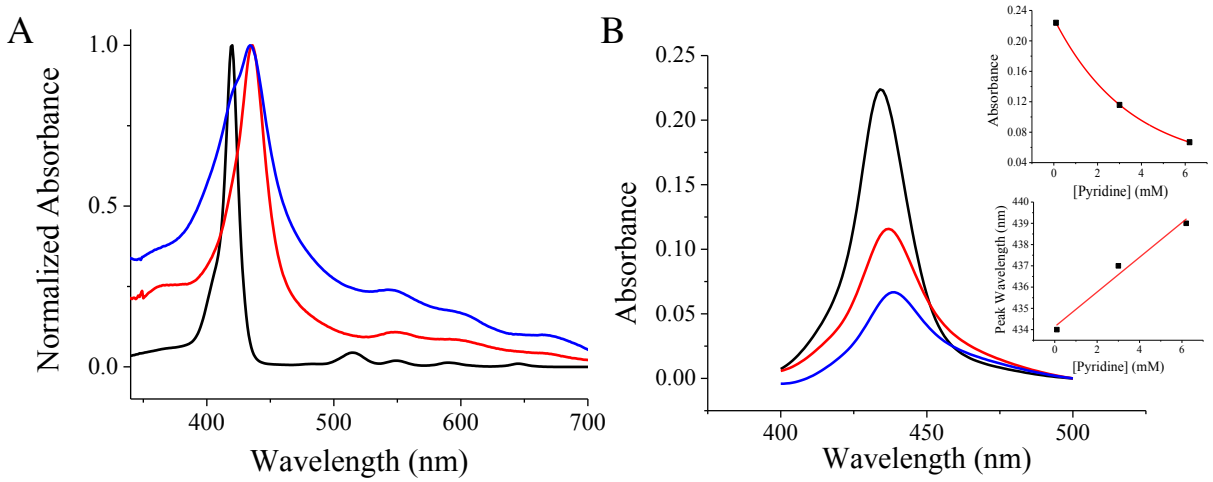

Figure 2.4. (A) Normalized UV-visible spectra of TCPP/DMF (black), CoPIZA/FTO/DMF (red), and CoPIZA/FTO/DMF after purging with nitrogen (blue); (B) Steady-state UV-visible absorption spectra of CoPIZA/FTO synthesized with varying pyridine concentration. With increasing pyridine concentration, the absorbance of the Soret band decreased (inset top) while the Soret band wavelength displayed a red shift (inset bottom).

2.4.2 Investigation of Charge-Transfer Mechanism

With CoPIZA/FTO in hand, efforts shifted to characterizing the charge transport properties of the material. There has been some effort in the literature to computationally determine the energetic position of the filled and unfilled states in MOFs.[8,12,13] In doing so, some have characterized MOFs as "semiconductors", with valence and conduction bands comprised of overlapping molecular HOMO and LUMO orbitals.[54,55] CoPIZA is constructed by CoTCPP struts and trimeric cobalt clusters (Figure 2.1).[31] The bonds forming the cobalt clusters are carboxylate in nature. Carboxylate bonds are known to be insulating and, therefore, it is unlikely that sufficient HOMO-LUMO overlap exists between the two molecular components to justify a band structure. Hence, CoPIZA is proposed to be a 3D network of individual redox centers.

Keeping this in mind, the conductivity of the CoPIZA is expected to be moderate on the edge of insulating. This is indeed the case, as was explored by electrochemical impedance spectroscopy (Figure 2.5). The measured conductivity, determined by the reciprocal of the area and thickness corrected low frequency intercept of the Nyquist plot, was 3.62 x 10^{-8} S cm^{-1} and places the film's dark conductivity on the order of wide band gap semiconductors, σ_{TiO_2} = 1 x 10^{-11} S cm^{-1},[56] and common organic semiconductors, $\sigma_{\text{polybithiophene}}$ = 1 x 10^{-8} S cm^{-1}.[57,58] Therefore, CoPIZA/FTO is semiconducting, but not necessarily a semiconductor. It is important to note that moderate conductivity does not preclude charge transfer chemistry upon applied potential. In fact, there are a number of examples of electrocatalysis at the surface of TiO_2.[59-62]

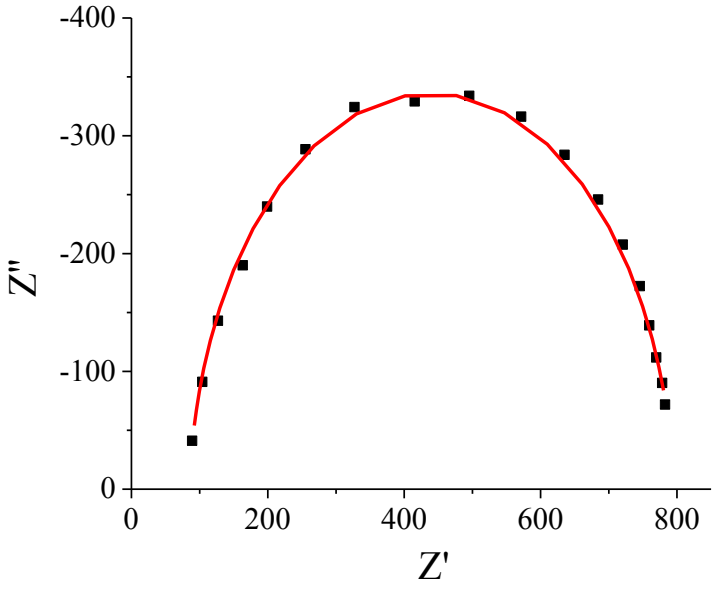

Figure 2.5. Nyquist plot obtained from electrochemical impedance spectroscopy performed on the CoPIZA/FTO. The high frequency intercept corresponds to the conductivity of FTO, while the low frequency intercept displays the conductivity within MOF crystallites and corresponds to a value of 3.62 ×10^{-8} S cm^{-1}.

Given the almost insulating behavior of CoPIZA/FTO, charge transfer is likely to occur via a redox-hopping mechanism.[14] Vital to such a mechanism is the need for the redox centers to have similar or the same reduction potentials and individual immobilized units to be close enough for efficient hopping. Otherwise, an entire molecular component can act as an insulating block to electronic communication across the material. Cyclic voltammetric (CV) analysis of CoPIZA/FTO in 0.1 M $LiClO_4$/DMF displays two cathodic peaks at −1.1 V and −1.45 V and, upon the reverse scan, one anodic peak at −0.975 V vs. ferrocyanide (Figure 2.6A). The relationship between the peak current at −1.1 V and the square root of the scan rate of the CV displays a linear relationship (Figure 2.6A inset, black), while the peak current vs. scan rate (Figure 2.6A inset, red) is non-linear. This behavior is indicative of diffusion limited charge transport throughout the framework (*vide infra*). Voltammograms collected over a smaller potential window (−0.4 to −1.2 V) indicate that the first cathodic wave and the anodic wave correspond to a coupled, reversible redox event (Figure 2.6B). The cathodic and anodic peak currents (i_{pc} and i_{pa}, respectively) were equal at approximately 2.9 μA. The observed peak separation (ΔE_p) was 125 mV. Theoretically, a reversible process should have a peak separation of $\frac{59\,mV}{n}$, where n is the number of electrons transferred. However, peak separation of that magnitude is rarely observed in laboratory experiments, due to uncompensated ohmic drops in the electrochemical set-up (*vide infra*). Therefore, experimental convention defines reversibility at a boundary of approximately $\frac{120\,mV}{n}$. Based on this modified criterion, the first electrochemical wave is reversible.

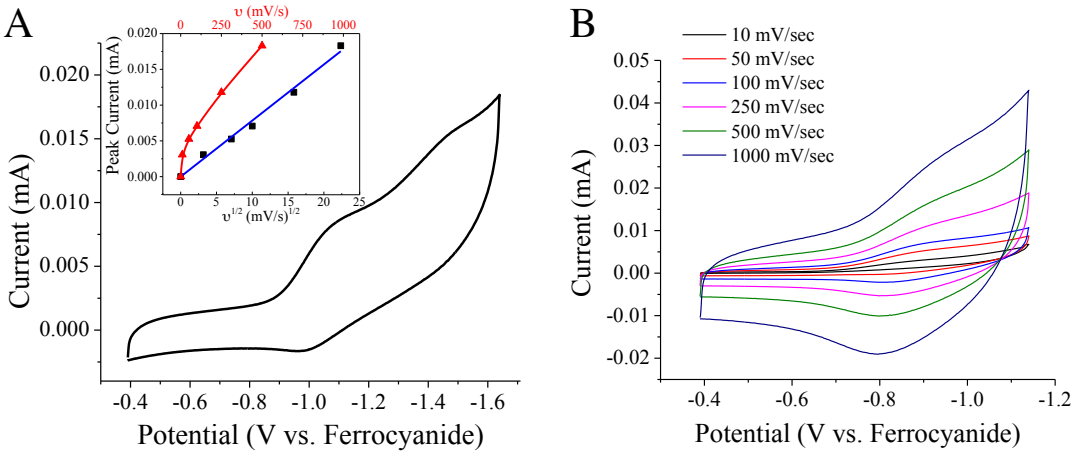

Figure 2.6. (A) Cyclic voltammetry of CoPIZA/FTO in 0.1 M $LiClO_4$/DMF at 100 mV/s. Inset shows the peak current of the reduction at −1.1 V vs. ferrocyanide to be linear with the square root of the scan rate $(\upsilon)^{1/2}$, while the current as a function of scan rate (υ) displays a non-linear relationship; (B) Cyclic voltammogram of CoPIZA/FTO in 0.1 M $LiClO_4$/DMF showing only the first reduction wave with varying the scan rate confirms the reversible nature of the wave. Due to film variations of film properties associated with the synthetic procedure, the error associated with the current is ±10%.

For a redox-hopping mechanism to explain the observed electrochemical events, the response must obey Fick's law of diffusion. This can result in electrochemical signatures unexpected for materials with fixed redox centers, like that in CoPIZA/FTO. The electrochemical response observed in CV is dependent upon the diffusion coefficient (*D*), and, thus, the rate of charge transport (k_{ct}).[63] There are three regimes to observed rate-dependent electrochemical responses: (i) k_{ct} > scan rate (υ), (ii) $k_{ct} \approx \upsilon$, (iii) $k_{ct} < \upsilon$.[63-65]

In the first regime (rapid charge transport), the CV will display electrochemical peaks that have a symmetric shape ($\Delta E_p = 0$) centered about the reduction potential. Additionally, the observed peak current should be proportional to the scan rate. This is exemplified in the work of Chidsey on ferrocene-terminated, thiol-based SAM-modified gold electrodes.[66] In this classic

example, the anodic and cathodic peaks occurred at the same potential with the theoretically predicted ideal 90 mV peak-width at half of the maximum current. In addition to this work, a similar response has been observed with various surface immobilized systems.[64,67-70]

CoPIZA/FTO exhibits nonzero, scan-rate dependent ΔE_p at all scan rates applied (10 mV/sec – 1000 mV/sec). Such behavior is most consistent with regime (iii). In this regime, the CV behavior is quantitatively the same as freely diffusing redox centers in solution. Therefore, the current response should obey the Randles-Sevcik equation, Equation 2.1,

$$i_p = 0.4463nFAC\left(\frac{nF\upsilon D}{RT}\right)^{1/2} \quad (2.1)$$

where i_p is the peak current, n is the number of electrons transferred, F is Faraday's constant, A is the electrode area, C is the concentration of redox active species, υ is scan rate, D is the diffusion coefficient, R is the gas constant, and T is temperature. Thus, the peak current should be linear with a function of $\upsilon^{1/2}$.

The inset in Figure 2.6A shows the relationship between i_{pc} at −1.1 V as a function of υ. As mentioned above, for diffusion-limited processes like those in regime (iii), a linear relationship between i_{pc} and $\upsilon^{1/2}$ is expected via Randles-Sevcik.[49,63] Mass-transfer independent redox reactions, like those observed in the rapid charge transfer limit, are expected to exhibit a linear relationship between current and υ.[63,64] Plots of both i_{pc} vs. $\upsilon^{1/2}$ (diffusion-limited) and i_{pc} vs. υ (mass-transfer independent) resulted in statistically linear relationships, R^2 = 0.99 and 0.97, respectively. However, there is a pronounced curvature visible in the i_{pc} vs. υ relation and, thus, the results are consistent with a diffusion-limited (k_{ct} < υ) redox reaction that occurs via redox hopping charge transport.

The first to propose a redox-hopping mechanism for charge transport were Kauffmann and Engler for polymers with incorporated redox-active pyrazoline units.[71-73] It has since been expanded to polymeric systems containing immobilized inorganic compounds (ferrocene and ruthenium trisbipyridine).[64,66-70,74] Qualitatively and quantitatively the results presented here agree with these prior investigations. More recently, Scholz predicted, through a theoretical treatment, that similar electrochemical responses would be observed for immobilized microcrystals, similar to MOFs.[22,75-77] Although Scholz's exact theoretical framework cannot be applied to the experimental data collected for CoPIZA/FTO due to the inhomogeneity of crystal packing, shape, and size, the results represent the first quantitative support for his model.

In CoPIZA/FTO there are two components that could be the source of the observed electrochemical response, CoTCPP and the trimeric cobalt clusters. Cyclic voltammetry only provides the potential required to transport electrons and does not identify the active species. Therefore, spectroelectrochemical measurements were utilized to determine the molecular origin of the observed electrochemical peaks. An electrochemical cell was constructed in a N_2-purged quartz cuvette and placed in a UV-vis spectrometer. The spectral changes were then monitored as a function of applied potential. At an applied potential of -1000 mV vs. ferrocyanide, there was an observed decrease in the Soret band of (Co^{III}TCPP)CoPIZA at 436 nm accompanied by an increase in the Soret band of (Co^{II}TCPP)CoPIZA at 419 nm with maintenance of isosbestic points at 430, 458 and 544 nm (Figure 2.7 top inset, red). Thus, the reduction peak observed at −1.04 V is due to ($Co^{III/II}$TCPP)CoPIZA reduction. With increasing negative potential, the Soret band of (Co^{II}TCPP)CoPIZA was found to decrease in intensity with the appearance of a split Soret (419 and 430 nm) and an increase in absorbance at 370 nm, attributed to

(Co^{I}TCPP)CoPIZA. The ($Co^{II/I}$TCPP)CoPIZA redox transition was also accompanied by isosbestic points at 390 and 449 nm.

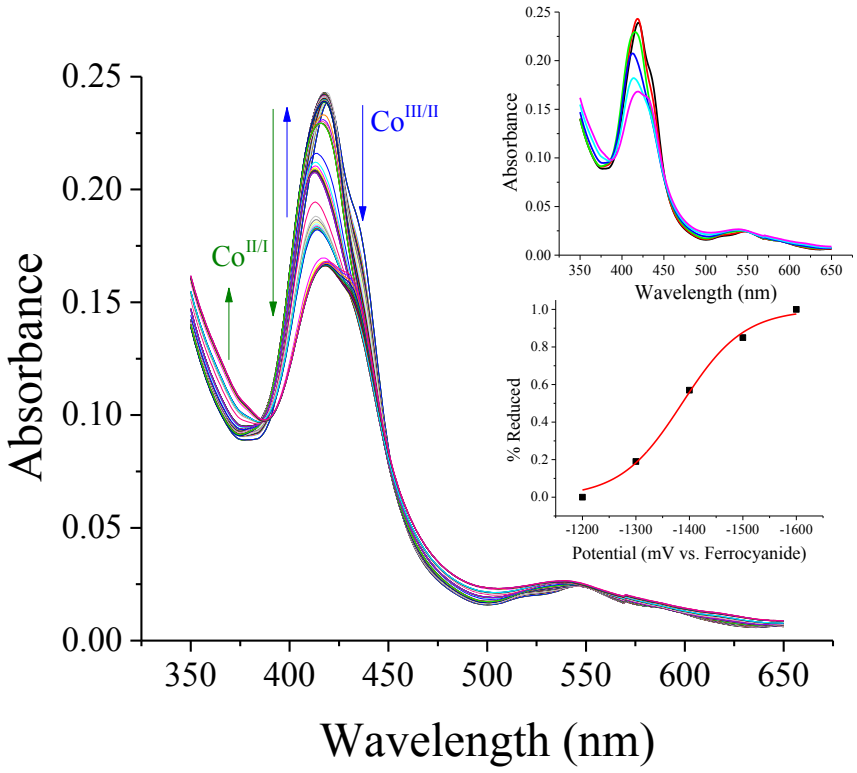

Figure 2.7. Absorption spectra recorded for CoPIZA/FTO as the applied potential was changed. Top inset shows the absorption spectra of CoPIZA/FTO (black) and with applied potentials (vs. ferrocyanide) of −1000 mV (red), −1300 mV (green), −1400 mV (blue), −1500 mV (cyan), and -1600 mV (magenta). Bottom inset displays the sigmoidal fit of the percent of reduced cobalt present at the applied potential (Equation 2.5).

The Nernst equation (Equation 2.2) states that when a redox couple is 50% reduced and 50% oxidized, the applied potential is equal to the $E_{1/2}$ (the standard reduction potential at non-unit molarity). Since the spectroelectrochemical data provides a direct measure of the ratio of reduced/oxidized species in the absence of other electrochemical events, a rearrangement of

the Nernst equation to solve for the percent reduced species (*x*) (Equation 2.3) allows for the determination of $E_{1/2}$ for the Co^{II}/Co^{I}TCPP redox couple. However, the spectral data could not be adequately fit to Eq. 2.3, suggesting the process deviates from Nernstian behavior.

$$E = E_{1/2} - \frac{59\,mV}{n}\log_{10}\left(\frac{[red]}{[ox]}\right) \tag{2.2}$$

$$\%\,reduced = x = \frac{1}{1+10^{(E_{app}-E_{1/2})/59}} \tag{2.3}$$

A modification of the Nernst equation with the inclusion of a non-ideality factor (*a*), a measure of deviation from Nernstian behavior, (Equation 2.4) and rearrangement to solve for *x* (Equation 2.5) allowed for an accurate fit of the spectral data. The non-ideality factor obtained was 2. Thus, for an order of magnitude change in [reduced CoPIZA]/[oxidized CoPIZA], 118 mV needs to be applied to the film.

$$E = E_{1/2} - \frac{59\,mV*a}{n}\log_{10}\left(\frac{[red]}{[ox]}\right) \tag{2.4}$$

$$\%\,reduced = x = \frac{1}{1+10^{(E_{app}-E_{1/2})/59a}} \tag{2.5}$$

Additionally, the $E_{1/2}$ for the ($Co^{II/I}$TCPP)CoPIZA transition was determined via Equation 2.5 to be −1386 ± 6 mV vs. ferrocyanide. This is consistent with the second redox feature in the CV. Hence, both peaks in the CV are attributed to CoTCPP reduction. The reduction potentials and assignments are summarized in Table 2.1.

Table 2.1. Reduction potentials (vs. ferrocyanide) for CoPIZA/FTO.

Reaction	$E_{1/2}$	E_p
$(Co^{III/II}TCPP)CoPIZA$	−1.04 V [a]	
$Co^{III/II}$cluster	~ −0.87 V [c]	
$(Co^{II/I}TCPP)CoPIZA$	−1.39 V [b]	−1.45 V [a]
$Co^{II/I}$cluster	~ −1.57 V [c]	

[a]From CV. [b]From spectroelectrochemistry. [c]From reference 78.

The question then becomes, at what potential are the trimeric cobalt clusters reduced? Unfortunately, spectral changes due to cluster reduction are not observed in the spectroelectrochemical experiments. This is not surprising due to the large discrepancy between the two molecular component's extinction coefficients.[27] However, the CV does have a large background current beginning at −900 mV that could be attributed to a molecular species. Similar molecular cobalt clusters have been investigated, and the Co^{III} clusters display a reduction potential of −0.87 V vs. ferrocyanide.[78] The $Co^{II/I}$ cluster reduction was found to occur at a potential of −1.57 V vs. ferrocyanide.[78] Therefore, it is likely that the observed background current is due in part to the reduction of the nodal cobalt clusters. More interestingly, the nodal clusters of the CoPIZA have very similar reduction potentials to the CoTCPP struts. Therefore, it is possible that the redox hopping chain may involve CoTCPP-cobalt cluster exchange interactions.

There are two components to efficiency that can be addressed by the data collected: rate and potential. For applications in electrocatalysis, both parameters are extremely important. If the rate of charge transfer through the film is slow, this can be the overall rate-determining step to reactivity. It is highly undesirable to have a process not directly involved with catalytic

transformation to be rate determining. Given that redox hopping is regarded as a diffusion process, the rate of charge transport is represented by the apparent diffusion coefficient (D_{app}) for charge transfer through the film. After a potential step experiment, the charge (Q) and time (t) relationship will proceed via the Anson equation (Equation 2.6), where S is the electrode surface area and C is the concentration of electroactive species.[49] The concentration of electroactive species within the film can be determined from the amount of charge required to reduce all of the redox centers in the film (Q_f) and the film thickness (d) (Equation 2.7), which can be substituted into Equation 2.6 to give Equation 2.8.[79] Since CoPIZA/FTO is active electrochemically and spectroscopically, the absorbance change is proportional to the amount of charge passed, and Equation 2.8 can be modified to Equation 2.9.[79,80] Therefore, the apparent diffusion coefficient was determined from a fitting of the time-dependent spectroelectrochemical data to Equation 2.9.

$$Q = \frac{2nFSC(D_{app})^{1/2}t^{1/2}}{\pi^{1/2}} \tag{2.6}$$

$$C = \frac{Q_f}{nFSd} \tag{2.7}$$

$$Q = \frac{2Q_f(D_{app})^{1/2}t^{1/2}}{d\pi^{1/2}} \tag{2.8}$$

$$\Delta A = \frac{2A_{max}{D_{app}}^{1/2}t^{1/2}}{d\pi^{1/2}} \tag{2.9}$$

The absorbance change at 419 nm was plotted as a function of $t^{1/2}$ following a potential step corresponding to the ($Co^{II/I}$TCPP)/CoPIZA redox couple (Figure 2.8). For CoPIZA/FTO, the D_{app} is 7.55 (±0.05) x 10^{-14} cm^2 s^{-1} (Figure 2.8). The D_{app} for charge transport between redox centers incorporated into polymer films range from 1 x 10^{-11} to 1 x 10^{-8} cm^2 s^{-1}.[65,66,78,79] However, these coefficients may contain a component due to redox center displacement, where charge is transferred through the physical displacement and diffusion of the molecular

components through the polymeric structure.[67,68,81,82] The theoretical analysis of diffusional transport in a single microcrystal performed by Scholz, et al. found diffusion coefficients on the order of 10^{-8} – 10^{-9} cm^2 s^{-1}.[75-77] Given that diffusion in the CoPIZA/FTO system occurs in the absence of redox center displacement and occurs across MOF grain boundaries, as well as within individual MOF particles, the observed D_{app} is reasonable for a redox hopping mechanism.

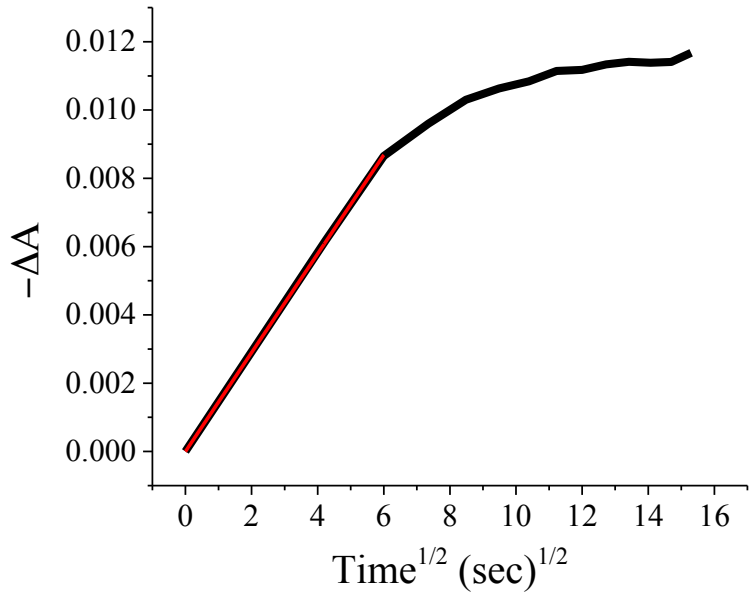

Figure 2.8. Absorption changes (ΔA) measured at 419 nm as a function of time$^{1/2}$ for CoPIZA/FTO at the ($Co^{II/I}$TCPP)/CoPIZA redox couple. The linear best fit of Equation 2.9 is shown on the data.

The diffusion of charge through CoPIZA/FTO is ambipolar in nature, with charge balancing anions/cations coupled to electron transport.[64,67,68,70,75] When CoPIZA is in the (Co^{III}TCPP)CoPIZA oxidation state, the film requires anions to balance the excess positive charge on the Co^{III}TCPP unit. Upon reduction to the neutral (Co^{II}TCPP)CoPIZA state, anion flow from the MOF is expected, Equation 2.10.

$$e^- + [(Co^{III}TCPP)CoPIZA] \cdot ClO_{4\ (s)} \rightarrow [(Co^{II}TCPP)CoPIZA]_{(s)} + ClO^-_{4\ (soln)} \quad (2.10)$$

Further reduction of (Co^{II}TCPP)CoPIZA to [(Co^{II}TCPP)CoPIZA]$^-$ results in an overall negatively charged MOF backbone, Equation 2.11. Therefore, cations are required to balance this excess charge.

$$Li^+_{(soln)} + [(Co^{II}TCPP)CoPIZA]_{(s)} + e^- \rightarrow [(Co^{I}TCPP)CoPIZA] \cdot Li_{(s)} \quad (2.11)$$

Electrochemical and spectroelectrochemical measurements do not allow for the individual components of the apparent diffusion coefficient, electron diffusion and cation/anion diffusion, to be distinguished; however, it is assumed that cation/anion diffusion is slower than electron diffusion and, therefore, rate determining.[65]

Potential efficiency, defined here as potential required for an order of magnitude change in the ratio of reduced to oxidized film species, determines a component of overpotential. Overpotential is the potential difference between the thermodynamic potential of a reaction and the actual potential required to overcome kinetic barriers and drive the electrochemical process. The most efficient catalytic processes are driven at the thermodynamic limit. The potential efficiency for CoPIZA/FTO reduction was quantified from the non-ideality factor in the Nernst equation fit to the spectroelectrochemical data (Figure 2.7, bottom inset). For accurate modeling, a non-ideality factor of 2 was included. This means an order of magnitude change in concentration from oxidized film to reduced film required twice the amount of applied potential in comparison to a perfectly Nernstian process (59 mV vs. 118 mV). Therefore, in the absence of overpotential for the catalysis itself, there is a built in overpotential of 59 mV from film reduction. Overall, this is relatively small and very few electrochemical couples behave Nernstianly.[83,84] We attribute this overpotential to the insulating nature of the carboxylate links,

which causes an ohmic drop over the thickness of the film. Hence, the molecular units far away from the CoPIZA/FTO interface "feel" a less negative potential than that applied to the FTO and, ultimately, require a more negative applied potential in order to reduce the metal centers.

For ultimate applications in electrocatalysis, efficiency is equally important as stability. The stability of metal organic frameworks to oxidation state change is quite contentious.[7] Upon oxidation and reduction of any inorganic complex, it is likely that bond lengths and angles will change. For the most extreme cases, complete changes in coordination environment can occur. The most well-known example of this is a Jahn-Teller distortion.[85] However, CoPIZA exhibited surprising stability over the time course of both cyclic voltammetric and spectroelectrochemical experiments. The films could be cycled multiple times (>25) without a loss in peak current. Also, the maintenance of sharp isosbestic points in the spectroelectrochemical experiments indicates that the film was stable to both degradation and desorption, both of which would cause the isosbestic points to drift to lower absorbance values as the concentration of bound CoTCPP changed.

To investigate long-term stability, controlled potential electrolysis was performed on CoPIZA/FTO. A potential of −1.04 V vs. ferrocyanide, corresponding to the ($Co^{III/II}$TCPP)CoPIZA reduction potential and beyond the expected $Co^{III/II}$cluster reduction potential, was applied to the CoPIZA/FTO for 24 h, after which time CoPIZA/FTO was characterized to determine whether structural degradation occurred. The SEM image showed no significant deterioration of the MOF film upon electrolysis (Figure 2.9A). Additionally, no absorption features due to CoTCPP in solution were observed post-electrolysis. This indicates that the CoPIZA/FTO is stable to both $Co^{III/II}$TCPP and, surprisingly, $Co^{III/II}$ cluster reduction.

The same was repeated for the potential corresponding to the ($Co^{II/I}$TCPP)CoPIZA reduction potential (−1.45 V vs. ferrocyanide), after which time the film appears to be pitted (Figure 2.9B) and absorption features due to dissolved CoTCPP were apparent in the spectrum of the solution post-electrolysis. While CoPIZA/FTO appears stable to ($Co^{II/I}$TCPP)CoPIZA reduction over the time course of the spectroelectrochemical measurements, upon prolonged electrolysis the film degrades. The applied potential is on the edge of the expected ($Co^{II/I}$cluster)CoPIZA reduction potential.[78] Therefore, reduction of the nodes would be inefficient and slow at this voltage. It follows that the observed CoPIZA/FTO degradation with prolonged electrolysis is most likely due to reduction of the framework nodes, breakdown of the cluster, and release of CoTCPP.

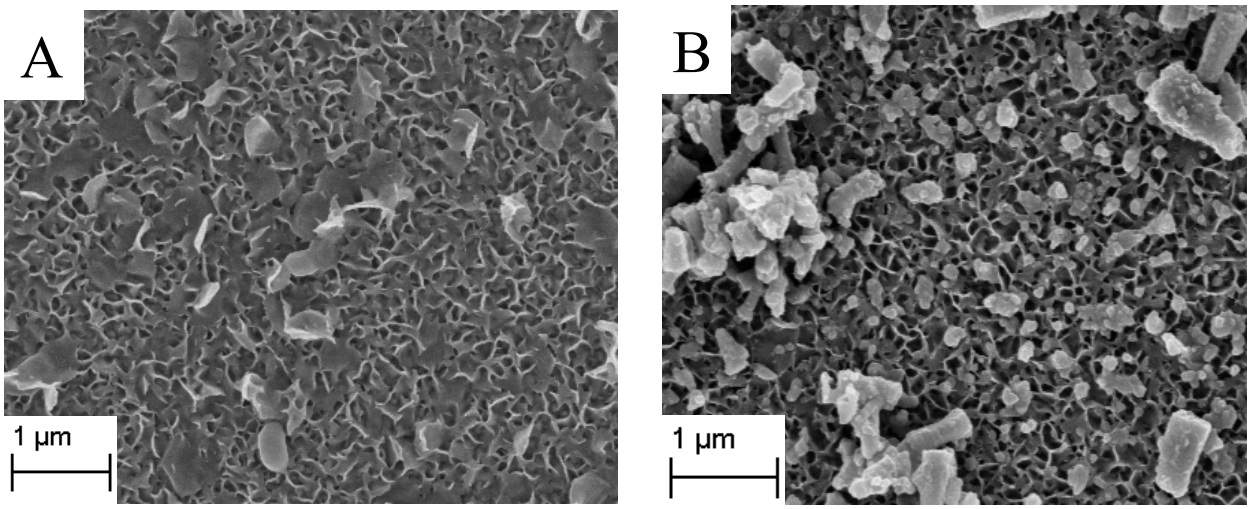

Figure 2.9. SEM image of (A) CoPIZA/FTO after controlled potential electrolysis at −1.04 V vs. ferrocyanide for 24 hours; and (B) CoPIZA/FTO after controlled potential electrolysis at −1.45 V vs. ferrocyanide for 24 hours.

In light of this instability, pophyrinic films provide the ideal scaffold for determination of active catalytic species. As demonstrated, spectroscopic measurements can be used to monitor oxidation state changes upon the reduction of a substrate. This is an advantage over previous electrocatalytic MOF studies, which were limited to conclusions drawn from voltammetric response alone. To investigate the catalytic ability of the MOF film, the reduction of carbon tetrachloride by (Co^{I}TCPP)CoPIZA was utilized. Metalloporphyrin organohalide reduction is well-known and used as a proof-of-concept example.[86,87] In the presence of carbon tetrachloride, an increase in current in the CV of CoPIZA/FTO at a potential commensurate with ($Co^{II/I}$TCPP)CoPIZA reduction was observed (Figure 2.10A). Such an increase in current is indicative of catalytic activity of (Co^{I}TCPP)CoPIZA toward CCl_4 reduction. To unequivocally assign the active catalytic state to (Co^{I}TCPP)CoPIZA, the spectral changes of the film were monitored during reactivity. After reduction to (Co^{I}TCPP)CoPIZA and injection of CCl_4, spectral features consistent with (Co^{II}TCPP)CoPIZA were recovered (Figure 2.10B). Therefore, the observed catalysis was indeed due to intact MOF and neither deposition of a metal or metal oxide at the electrode surface nor free linker in solution.

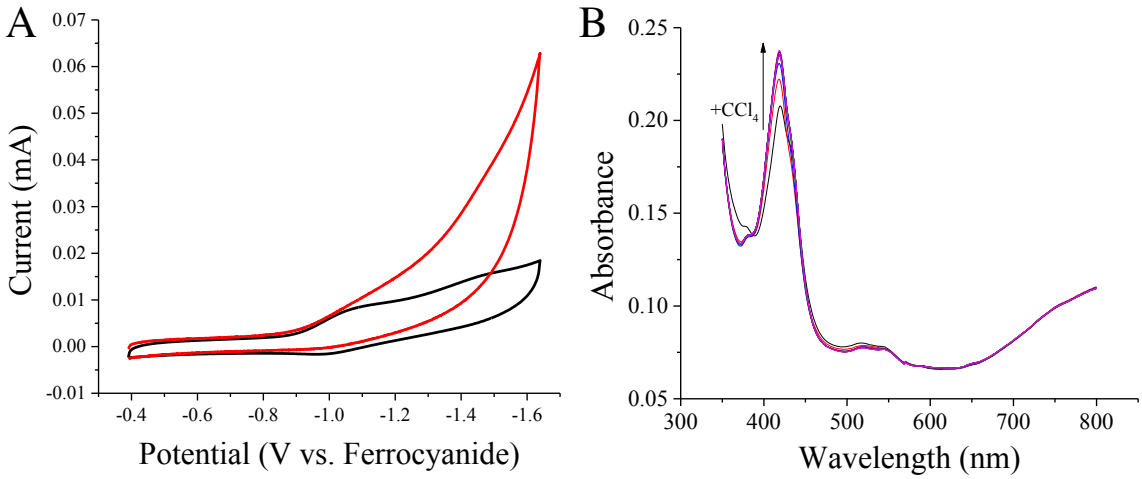

Figure 2.10. (A) Cyclic voltammetry of CoPIZA/FTO in 0.1 M $LiClO_4$/DMF (black) in the presence of CCl_4 (red) at 100 mV/s; (B) UV-vis spectra of the (Co^{I}TCPP)CoPIZA and its oxidation to (Co^{II}TCPP)CoPIZA with the addition of CCl_4.

2.5 Conclusions

In summary, a new metalloporphyrin MOF thin film, CoPIZA/FTO, was prepared solvothermally and the spectroscopic and electrochemical properties characterized. The open nature of the CoPIZA MOF network affords unrestricted access to the relatively large pores and unoccupied metal sites. Even with the moderate electrical conductivity exhibited by the CoPIZA/FTO, upon applied potential, the entire film could be reduced and remained stable for hours. The mechanism of charge transport was determined to be one of redox hopping, supported by both electrochemical and spectroelectrochemical analysis. The efficiency of reduction via redox hopping was found to be moderate with a rate consistent with a redox hopping mechanism and a slight overvoltage due to the potential drop across the film. The catalytic activity of

CoPIZA/FTO was successfully demonstrated via the electrocatalytic reduction of CCl_4. This work provides a vital framework for further development of MOF thin films and their applications as electrocatalysts for a variety of reactions.

2.6 Acknowledgements

The authors gratefully acknowledge Andrew Giordani for AFM analysis and the Nanoscale Characterization and Fabrication Laboratory (NCFL) at Virginia Tech, which is supported by the State of Virginia and the Commonwealth Research Initiative. We also thank Dr. Catherine Oertel and NSF grant DMR-0922588 for assistance with the thin film grazing angle PXRD and Dr. Robert Moore and Scott Forbey for assistance with impedance spectroscopy. This work was supported by Virginia Tech and a grant received from Virginia Tech's Institute for Critical Technology and Applied Science (ICTAS).

2.7 References

(1) Eddaoudi, M.; Kim, J.; Rosi, N.; Vodak, D.; Wachter, J.; O'Keeffe, M.; Yaghi, O. M. *Science* **2002**, *295*, 469.
(2) Rosi, N. L.; Eckert, J.; Eddaoudi, M.; Vodak, D. T.; Kim, J.; O'Keeffe, M.; Yaghi, O. M. *Science* **2003**, *300*, 1127.
(3) Caskey, S. R.; Wong-Foy, A. G.; Matzger, A. J. *J. Am. Chem. Soc.* **2008**, *130*, 10870.
(4) Sumida, K.; Rogow, D. L.; Mason, J. A.; McDonald, T. M.; Bloch, E. D.; Herm, Z. R.; Bae, T.-H.; Long, J. R. *Chem. Rev.* **2012**, *112*, 724.
(5) Ferey, G. *Chem. Soc. Rev.* **2008**, *37*, 191.
(6) Huxford, R. C.; Della, R. J.; Lin, W.-B. *Curr. Opin. Chem. Biol.* **2010**, *14*, 262.
(7) Lee, J. Y.; Farha, O. K.; Roberts, J.; Scheidt, K. A.; Nguyen, S. B. T.; Hupp, J. T. *Chem. Soc. Rev.* **2009**, *38*, 1450.
(8) Choi, J. H.; Choi, Y. J.; Lee, J. W.; Shin, W. H.; Kang, J. K. *Phys. Chem. Chem. Phys.* **2009**, *11*, 628.
(9) Ma, L.; Abney, C.; Lin, W. *Chemical Society Reviews* **2009**, *38*, 1248.
(10) Givaja, G.; Amo-Ochoa, P.; Gomez-Garcia, C. J.; Zamora, F. *Chem. Soc. Rev.* **2012**, *41*, 115.

(11) Khajavi, H.; Gascon, J.; Schins, J. M.; Siebbeles, L. D. A.; Kapteijn, F. *J. Phys. Chem. C* **2011**, *115*, 12487.
(12) Kuc, A.; Enyashin, A.; Seifert, G. *J. Phys. Chem. B* **2007**, *111*, 8179.
(13) Yang, L.-M.; Ravindran, P.; Vajeeston, P.; Tilset, M. *Phys. Chem. Chem. Phys.* **2012**, *14*, 4713.
(14) Pickup, P. G.; Murray, R. W. *J. Am. Chem. Soc.* **1983**, *105*, 4510.
(15) Wang, C.; Xie, Z.; de, K. K. E.; Lin, W. *J. Am. Chem. Soc.* **2011**, *133*, 13445.
(16) Narayan, T. C.; Miyakai, T.; Seki, S.; Dinca, M. *J. Am. Chem. Soc.* **2012**, *134*, 12932.
(17) Usov, P. M.; Fabian, C.; D'Alessandro, D. M. *Chem. Commun.* **2012**, *48*, 3945.
(18) Babu, K. F.; Kulandainathan, M. A.; Katsounaros, I.; Rassaei, L.; Burrows, A. D.; Raithby, P. R.; Marken, F. *Electrochem. Commun.* **2010**, *12*, 632.
(19) Hinogami, R.; Yotsuhashi, S.; Deguchi, M.; Zenitani, Y.; Hashiba, H.; Yamada, Y. *ECS Electrochem. Lett.* **2012**, *1*, H17.
(20) Senthil, K. R.; Senthil, K. S.; Anbu, K. M. *Electrochem. Commun.* **2012**, *25*, 70.
(21) Domenech, A.; Garcia, H.; Domenech-Carbo, M. T.; Llabres-i-Xamena, F. *Electrochem. Commun.* **2006**, *8*, 1830.
(22) Domenech, A.; Garcia, H.; Domenech-Carbo, M. T.; Llabres-i-Xamena, F. *J. Phys. Chem. C* **2007**, *111*, 13701.
(23) Lexa, D.; Saveant, J. M.; Soufflet, J. P. *J. Electroanal. Chem. Interfacial Electrochem.* **1979**, *100*, 159.
(24) Grinstaff, M. W.; Hill, M. G.; Labinger, J. A.; Gray, H. B. *Science* **1994**, *264*, 1311.
(25) Bhugun, I.; Lexa, D.; Saveant, J.-M. *J. Am. Chem. Soc.* **1996**, *118*, 1769.
(26) Chang, C. J.; Loh, Z.-H.; Shi, C.; Anson, F. C.; Nocera, D. G. *J. Am. Chem. Soc.* **2004**, *126*, 10013.
(27) Kadish, K., Guilard, R., Smith, K. *The Porphyrin Handbook*; Academic Press, 2003.
(28) Suslick, K. S.; Bhyrappa, P.; Chou, J. H.; Kosal, M. E.; Nakagaki, S.; Smithenry, D. W.; Wilson, S. R. *Acc. Chem. Res.* **2005**, *38*, 283.
(29) Farha, O. K.; Shultz, A. M.; Sarjeant, A. A.; Nguyen, S. T.; Hupp, J. T. *J. Am. Chem. Soc.* **2011**, *133*, 5652.
(30) Meng, L.; Cheng, Q.; Kim, C.; Gao, W.-Y.; Wojtas, L.; Chen, Y.-S.; Zaworotko, M. J.; Zhang, X. P.; Ma, S. *Angew. Chem. Int. Ed.* **2012**, *51*, 10082.
(31) Kosal, M. E.; Chou, J.-H.; Wilson, S. R.; Suslick, K. S. *Nat. Mater.* **2002**, *1*, 118.
(32) Kosal, M. E.; Suslick, K. S. *J. Solid State Chem.* **2000**, *152*, 87.
(33) Fateeva, A.; Chater, P. A.; Ireland, C. P.; Tahir, A. A.; Khimyak, Y. Z.; Wiper, P. V.; Darwent, J. R.; Rosseinsky, M. J. *Angew. Chem. Int. Ed.* **2012**, *51*, 7440.
(34) Chen, Y.; Hoang, T.; Ma, S. *Inorg. Chem.* **2012**, *51*, 12600.
(35) Burnett, B. J.; Barron, P. M.; Choe, W. *CrystEngComm* **2012**, *14*, 3839.
(36) Son, H.-J.; Jin, S.; Patwardhan, S.; Wezenberg, S. J.; Jeong, N. C.; So, M.; Wilmer, C. E.; Sarjeant, A. A.; Schatz, G. C.; Snurr, R. Q.; Farha, O. K.; Wiederrecht, G. P.; Hupp, J. T. *J. Am. Chem. Soc.* **2013**, *135*, 862.
(37) Betard, A.; Fischer, R. A. *Chem. Rev.* **2012**, *112*, 1055.
(38) Zacher, D.; Shekhah, O.; Woell, C.; Fischer, R. A. *Chem. Soc. Rev.* **2009**, *38*, 1418.
(39) Hermes, S.; Schroeder, F.; Chelmowski, R.; Woell, C.; Fischer, R. A. *J. Am. Chem. Soc.* **2005**, *127*, 13744.
(40) Shekhah, O.; Wang, H.; Kowarik, S.; Schreiber, F.; Paulus, M.; Tolan, M.; Sternemann, C.; Evers, F.; Zacher, D.; Fischer, R. A.; Woell, C. *J. Am. Chem. Soc.* **2007**, *129*, 15118.
(41) Shekhah, O.; Wang, H.; Strunskus, T.; Cyganik, P.; Zacher, D.; Fischer, R.; Woell, C. *Langmuir* **2007**, *23*, 7440.

(42) Li, W.-J.; Gao, S.-Y.; Liu, T.-F.; Han, L.-W.; Lin, Z.-J.; Cao, R. *Langmuir* **2013**, *29*, 8657.
(43) Stavila, V.; Volponi, J.; Katzenmeyer, A. M.; Dixon, M. C.; Allendorf, M. D. *Chem. Sci.* **2012**, *3*, 1531.
(44) So, M. C.; Jin, S.; Son, H.-J.; Wiederrecht, G. P.; Farha, O. K.; Hupp, J. T. *J. Am. Chem. Soc.* **2013**.
(45) Makiura, R.; Motoyama, S.; Umemura, Y.; Yamanaka, H.; Sakata, O.; Kitagawa, H. *Nat. Mater.* **2010**, *9*, 565.
(46) Xu, G.; Yamada, T.; Otsubo, K.; Sakaida, S.; Kitagawa, H. *J. Am. Chem. Soc.* **2012**, *134*, 16524.
(47) Motoyama, S.; Makiura, R.; Sakata, O.; Kitagawa, H. *J. Am. Chem. Soc.* **2011**, *133*, 5640.
(48) Moulder, J. F. S., W.F.; Sobol, P.E.; Bombem, K.D. *Handbook of X-ray Photoelectron Spectroscopy*; Physical Electronics, Inc., 1995.
(49) Bard, A. J. F., L.R. *Electrochemical Methods: Fundamentals and Applications, 2nd Edition.*; John Wiley & Sons, Inc.: New York, 2001.
(50) Burchill, P.; Welch, L. S. *Fuel* **1989**, *68*, 100.
(51) Glusker, J. P.; Trueblood, K. N. *Crystal Structura Analysis: A Primer, Third Edition*; Oxford University Press, Inc.: New York, 2010.
(52) Gouterman, M. *J. Mol. Spectrosc.* **1961**, *6*, 138.
(53) Balch, A. L.; Noll, B. C.; Olmstead, M. M.; Phillips, S. L. *Inorg. Chem.* **1996**, *35*, 6495.
(54) Silva, C. G.; Corma, A.; Garcia, H. *J. Mater. Chem.* **2010**, *20*, 3141.
(55) Alvaro, M.; Carbonell, E.; Ferrer, B.; Llabres, i. X. F. X.; Garcia, H. *Chem. - Eur. J.* **2007**, *13*, 5106.
(56) Fabregat-Santiago, F.; Garcia-Belmonte, G.; Bisquert, J.; Zaban, A.; Salvador, P. *J. Phys. Chem. B* **2002**, *106*, 334.
(57) Fikus, A.; Rammelt, U.; Plieth, W. *Electrochim. Acta* **1999**, *44*, 2025.
(58) Hotta, S.; Rughooputh, S. D. D. V.; Heeger, A. J.; Wudl, F. *Macromolecules* **1987**, *20*, 212.
(59) Xia, B. Y.; Wang, B.; Wu, H. B.; Liu, Z.; Wang, X.; Lou, X. W. *J. Mater. Chem.* **2012**, *22*, 16499.
(60) Wang, M.; Guo, D.-J.; Li, H.-L. *J. Solid State Chem.* **2005**, *178*, 1996.
(61) Li, L.; Duan, L.; Xu, Y.; Gorlov, M.; Hagfeldt, A.; Sun, L. *Chem. Commun.* **2010**, *46*, 7307.
(62) Huang, S.-Y.; Ganesan, P.; Popov, B. N. *Appl. Catal., B.* **2011**, *102*, 71.
(63) Bard, A. J. *Electroanalytical Chemistry Vol. 13*; Marcel Dekker, Inc.: New York, 1984.
(64) Daum, P.; Lenhard, J. R.; Rolison, D.; Murray, R. W. *J. Am. Chem. Soc.* **1980**, *102*, 4649.
(65) Rudge, A.; Raistrick, I.; Gottesfeld, S.; Ferraris, J. P. *Electrochim. Acta* **1994**, *39*, 273.
(66) Chidsey, C. E. D.; Bertozzi, C. R.; Putvinski, T. M.; Mujsce, A. M. *J. Am. Chem. Soc.* **1990**, *112*, 4301.
(67) Martin, C. R.; Rubinstein, I.; Bard, A. J. *J. Am. Chem. Soc.* **1982**, *104*, 4817.
(68) Buttry, D. A.; Anson, F. C. *J. Electroanal. Chem. Interfacial Electrochem.* **1981**, *130*, 333.
(69) Yagi, M.; Mitsumoto, T.; Kaneko, M. *J. Electroanal. Chem.* **1997**, *437*, 219.
(70) Daum, P.; Murray, R. W. *J. Electroanal. Chem. Interfacial Electrochem.* **1979**, *103*, 289.
(71) Kaufman, F. B.; Engler, E. M. *J. Am. Chem. Soc.* **1979**, *101*, 547.
(72) Kaufman, F. B.; Schroeder, A. H.; Engler, E. M.; Kramer, S. R.; Chambers, J. Q. *J. Am. Chem. Soc.* **1980**, *102*, 483.

(73) Schroeder, A. H.; Kaufman, F. B.; Patel, V.; Engler, E. M. *J. Electroanal. Chem. Interfacial Electrochem.* **1980**, *113*, 193.
(74) Yagi, M.; Sato, T. *J. Phys. Chem. B* **2003**, *107*, 4975.
(75) Lovric, M.; Scholz, F. *J. Solid State Electrochem.* **1997**, *1*, 108.
(76) Lovric, M.; Scholz, F. *J. Solid State Electrochem.* **1999**, *3*, 172.
(77) Schroder, U.; Oldham, K. B.; Myland, J. C.; Mahon, P. J.; Scholz, F. *J. Solid State Electrochem.* **2000**, *4*, 314.
(78) Beattie, J. K.; Beck, C. U.; Lay, P. A.; Masters, A. F. *Inorg. Chem.* **2003**, *42*, 8366.
(79) Bonhôte, P.; Gogniat, E.; Tingry, S.; Barbé, C.; Vlachopoulos, N.; Lenzmann, F.; Comte, P.; Grätzel, M. *J. Phys. Chem. B* **1998**, *102*, 1498.
(80) Trammell, S. A.; Meyer, T. J. *J. Phys. Chem. B* **1999**, *103*, 104.
(81) Yagi, M.; Sato, T. *J. Phys. Chem. B* **2003**, *107*, 4975.
(82) Yagi, M.; Mitsumoto, T.; Kaneko, M. *J. Electroanal. Chem.* **1997**, *437*, 219.
(83) Koval, C. A.; Anson, F. C. *Anal. Chem.* **1978**, *50*, 223.
(84) Kohl, P. A.; Bard, A. J. *J. Am. Chem. Soc.* **1977**, *99*, 7531.
(85) Longuet-Higgins, H. C.; Opik, U.; Pryce, M. L.; Sack, R. A. *Proc. R. Soc. London, Ser. A* **1958**, *244*, 1.
(86) Lexa, D.; Saveant, J. M.; Su, K. B.; Wang, D. L. *J. Am. Chem. Soc.* **1987**, *109*, 6464.
(87) Obare, S. O.; Ito, T.; Meyer, G. J. *Environ. Sci. Technol.* **2005**, *39*, 6266.

3. Thermodynamic study of CO_2 sorption by polymorphic microporous MOFs with open Zn(II) coordination sites

Reprinted with permission from S.R. Ahrenholtz, C. Landaverde-Alvarado, M. Whiting, S. Lin, C. Slebodnick, E. Marand, and A.J. Morris, *Inorg. Chem.*, **2015**, *54* (9), 4328–4336.

3.1 Motivation and Abstract

The combustion of carbon-based fossil fuels is responsible for the increasing atmospheric concentration of CO_2, and these elevated concentrations are having a detrimental effect on the global environment. As a result, there is considerable interest in the development of materials capable of selectively capturing CO_2 from the gaseous mixture that results from combustion processes to reduce its harmful effects. Metal-organic frameworks (MOFs) show promise for this application due to their porosity and tunability, which allows for the incorporation of desired functionalities to increase affinity for CO_2. In this study, two Zn-based MOFs have been prepared solvothermally, and their selectivity for CO_2 adsorption was investigated. In both frameworks, the inorganic structural building unit is composed of Zn(II) bridged by the 2-carboxylate or 5-carboxylate pendants of 2,5-pyridine dicarboxylate (pydc) to form a 1D zigzag chain. The zigzag chains are linked by the bridging 2,5-carboxylates across the Zn ions to form 3D networks with formulas of $Zn_4(pydc)_4(DMF)_2 \cdot 3DMF$ **(1)** and $Zn_2(pydc)_2(DEF)$ **(2)**. The framework **(1)** contains coordinated DMF as well as DMF solvates (DMF = *N*,*N*-dimethylformamide), while **(2)** contains coordinated DEF (DEF = *N*,*N*-diethylformamide). **(1)**

displays a reversible type-I sorption isotherm for CO_2 and N_2 with BET surface areas of 196 and 319 m^2/g, respectively. At low pressures, CO_2 and N_2 isotherms for **(2)** were not able to reach saturation, indicative of pore sizes too small for the gas molecules to penetrate. A solvent exchange to give **(2)-MeOH** allowed for increased CO_2 and N_2 adsorption onto the MOF surface with BET surface areas of 41 and 39 m^2/g, respectively. The binding of CO_2 into the framework of **(1)** was found to be exothermic with a zero coverage heat of adsorption, Q_{st}^0, of −27.7 kJ/mol. The Q_{st}^0 of **(2)** and **(2)-MeOH** were found to be −3 and −41 kJ/mol, respectively. The CO_2/N_2 selectivity for **(1)**, calculated from the estimated K_H at 296 K, was found to be 42. At pressures relevant to post-combustion capture, the selectivity was 14. The thermodynamic data are consistent with a mechanism of adsorption that involves CO_2 binding to the unsaturated Zn(II) metal centers present in the crystal structures.

3.2 Introduction

Metal-organic frameworks (MOFs) are synthetically tunable materials composed of metal or metal cluster nodes bound by multi-dentate organic linkers to form 3D crystalline structures with a network of interconnected pores.[1,2] The porous nature of MOFs allows for applications in areas such as gas storage and separation, heterogeneous catalysis, sensors, and drug delivery.[3-13] Specifically, porous materials show promise for applications in the separation of gas mixtures, such as O_2/N_2 for medical devices,[14] CO/H_2 for fuel cell applications,[15] N_2/H_2 for ammonia synthesis,[16] and CO_2/N_2 from combustion power plants.[7] An area of increased interest is the development of materials for CO_2 capture due to the rising levels of the greenhouse gas in the atmosphere. One of the main sources of increased atmospheric CO_2 is power plant emissions.[7,17]

CO_2 sequestration can be applied pre-combustion or post-combustion, and the material properties for each process are unique. Pre-combustion capture occurs under high-pressure conditions (up to 70 bar) with high concentrations of CO_2 (40%). Therefore, materials with moderate to high surface area are considered critical for these applications. Post-combustion capture, on the other hand, occurs near atmospheric pressure at low CO_2 concentration (15%) and, therefore, the interactions between the adsorbent and CO_2 play a crucial role.

There are two main mechanisms for gas separation: kinetic separation and thermodynamic separation. For kinetic separation, which is based on the diffusivities of the gases into the pores, design of the MOF pores with respect to the kinetic diameter for each component is crucial.[18] However, *a priori* design of 3D MOF structure is a difficult task despite recent advances with preformed secondary building units.[19] For thermodynamic separation, desired selectivity is the product of the affinity of the material toward each component.[18] With the composition of post-combustion flue gas being predominantly N_2 (~73-77%, kinetic diameter = 3.64 Å) followed by CO_2 (~15-16%, kinetic diameter = 3.30 Å), high selectivity of materials for CO_2 over N_2 is essential for post-combustion capture.[7,18,20] The small kinetic diameter of both N_2 and CO_2 requires the use of microporous materials to enable kinetic separation. However, it should be noted that the relatively similar kinetic diameters for N_2 and CO_2 preclude efficient separation from kinetic effects alone.

Many synthetic modifications to MOFs have been shown to increase the affinity of the material for CO_2 over N_2. These techniques often exploit the higher polarizability of CO_2 in comparison to the symmetric N_2 molecule. For example, the slight positive charge that rests on the carbon of the CO_2 is susceptible to attack by Lewis bases. This is well-known in the carbon

capture literature, as the formation of carbamates from the interaction between CO_2 and liquid amines is currently an industrial method for CO_2 sequestration.[21] The same functionality has been built into MOFs including Cu-BTTri-mmen,[22] CAU-1,[23] Bio-MOF-11,[24] and NH_2-Mil-53(Al)[25] resulting in impressive CO_2 storage capacities (15-24 wt% at 1 bar). Recently, a Zn-based MOF with multiple exposed Lewis basic sites on the linker displayed tremendous CO_2 sorption capacities. A high CO_2 uptake (36 wt% at 1 bar) was attributed to multipoint interactions between the CO_2 and the π-electrons and nitrogen atoms of the aromatic tetrazole ring as well as the alkane chains of the linker.[26] Another common approach is to include exposed cationic metal sites that can interact with the oxygen atoms of the CO_2. This is exemplified in the CPO-27-M (or M-MOF-74) series. Indeed, these materials exhibit extremely high CO_2 adsorption capacities of up to 27 wt% at 1 bar and 298 K.[27]

In this work, we report the solvothermal synthesis and characterization of two new microporous MOFs that have coordinatively unsaturated Zn(II) sites without the need for activation: $Zn_4(pydc)_4(DMF)_2 \cdot 3DMF$ **(1)** and $Zn_2(pydc)_2(DEF)$ **(2)**, where pydc is 2,5-pyridine dicarboxylate, DMF is dimethylformamide, and DEF is diethylformamide. The CO_2 and N_2 gas sorption properties of these two materials are presented and compared to known MOF-69C, $Zn_3(OH)_2(bdc)_2 \cdot 2DEF$,[28] where bdc is 1,4-benzene dicarboxylate. The thermodynamic parameters, Q_{st} and Q_{st}^0, for the structures were calculated. The selectivity of **(1)**, the most promising CO_2 adsorption material, was determined at pressures relevant to post-combustion CO_2 capture.

3.3 Experimental

3.3.1 Materials. The following reagents and solvents were purchased from the indicated commercial suppliers: zinc(II) nitrate hexahydrate (Sigma Aldrich, 98%); 2,5-pyridinedicarboxylic acid (Aldrich, 98%); 1,4-benzenedicarboxylic acid (Acros, 99%); *N,N*-dimethylformamide (DMF; Spectrum, spectrophotometric grade); *N,N*-diethylformamide (DEF; Acros, 99%); methanol (MeOH; Spectrum, HPLC grade); acetone (Spectrum, HPLC grade); chloroform (Spectrum, HPLC grade). Samples were submitted to Galbraith Laboratories, Inc. for elemental analysis.

3.3.2 Synthesis of $Zn_4(pydc)_4(DMF)_2 \cdot 3DMF$ (1). In a 20 mL vial, $Zn(NO_3)_2 \cdot 6H_2O$ (250 mg, 0.840 mmol) was dissolved in 10 mL DMF followed by the addition of 2,5-pyridinedicarboxylic acid (144 mg, 0.862 mmol). The vial was capped and sonicated until turbid and heated to 100 °C for 2 d. A vial containing colorless prisms was removed from the oven while hot and allowed to cool to RT. The crystals were collected via vacuum filtration and rinsed with DMF (257 mg, 95% yield based on $Zn(NO_3)_2 \cdot 6(H_2O)$). Anal Calcd for $C_{43}H_{47}N_9O_{21}Zn_4$ **(1)**: C, 40.12%; H, 3.68%, N, 9.79%; Zn, 20.31%. Found: C, 40.47%; H, 3.85%, N, 9.59%; Zn, 20.0%.

3.3.3 Synthesis of $Zn_2(pydc)_2(DEF)$ (2). In a 20 mL vial, $Zn(NO_3)_2 \cdot 6H_2O$ (177 mg, 0.596 mmol) was dissolved in DEF (4.883 mL). To the vial, 2,5-pyridinedicarboxylic acid (33 mg, 0.197 mmol) was added along with deionized water (0.177 mL). The vial was capped and sonicated until clear and heated to 75 °C for 3 d. A vial containing colorless parallelepipeds was removed from the oven while hot and allowed to cool to RT. The crystals were collected via vacuum filtration and rinsed with DEF (51.6 mg, 94% yield based on pydc). Anal Calcd for

$C_{19}H_{17}N_3O_9Zn_2$ **(2)**: C, 40.67%; H, 3.05%, N, 7.49%; Zn, 23.31%. Found: C, 39.93%; H, 3.12%, N, 7.48%; Zn, 22.2%.

3.3.4 Synthesis of MOF-69C: $Zn_3(OH)_2(bdc)_2 \cdot 2DEF$.[28] In a 20 mL vial, a solid mixture of $Zn(NO_3)_2 \cdot 6H_2O$ (177 mg, 0.596 mmol) and 1,4-benzenedicarboxylic acid (33 mg, 0.199 mmol) was dissolved in DEF (4.883 mL) by sonication. To the reaction solution, deionized water (0.177 mL) was added. The vial was capped and sonicated until clear and heated to 100 °C for 24 h. The vial containing round crystals was removed from the oven while hot and allowed to cool to RT. The crystals were collected via vacuum filtration and rinsed with DEF.

3.3.5 Single Crystal X-ray Diffraction. Datasets were collected on an Agilent Gemini E Ultra diffractometer operating with MoKα radiation. The data collection routine, unit cell refinement, and data processing were carried out with the program CrysAlisPro.[29] The structure was solved using SHELXS-97[30] and refined using SHELXL-97[30] via OLEX2.[31] Figures were generated with OLEX2[31] or Mercury.[32] Void spaces were calculated using OLEX2 v1.2.6 with resolution = 0.2/Å; distance = 0.0/Å, probe = 1.2/Å, and grid = 0.7/Å.[31]

3.3.5.1 Structure of (1): The Laue symmetry and systematic absences were consistent with the monoclinic space group $P2_1/n$. The structure is a 3D-framework with solvent channels containing 1.5 DMF/asymmetric unit. One DMF is located on a general position and modeled with 2-position disorder with relative occupancies that refined to 0.701(10) and 0.299(10). The minor conformation was modeled isotropically. The second DMF is disordered across an inversion center and constrained to ½-occupancy for each conformation. A PART -1 and FRAG/FEND commands were used to model the DMF, and an isotropic model was used. The final refinement model involved anisotropic displacement parameters for all non-hydrogen atoms

of the framework and the major conformation of the DMF. A riding model was used for all hydrogen atoms.

3.3.5.2 Structure of (2): The Laue symmetry and systematic absences were consistent with the orthorhombic space group *Pbca*. A 2-position disorder model was used for the DEF, with relative occupancies that refined to 0.889(10) and 0.111(10). The final refinement model involved anisotropic displacement parameters for non-hydrogen atoms and a riding model for all hydrogen atoms. A SIMU command was used to restrain the ADPs in the disordered region of the DEF.

3.3.6 Powder X-Ray Diffraction (PXRD). PXRD experiments were carried out on a Rigaku MiniFlex 600 with Cu(Kα)-radiation (Cu-Kα = 1.5418 Å). The PXRD measurements were carried out over a 2θ range of 3-60° in continuous scanning mode (1.0°/min) and a resolution of 0.1°. The powder patterns of the materials were simulated in Mercury[32] and compared to the experimental patterns for structural confirmation and sample purity. PXRD was also used to monitor the stability of the frameworks with temperature. Prepared samples of **(1)**, **(2)**, and MOF-69C were each held at the desired temperature under vacuum for 1 h, followed by the immediate collection of a room temperature PXRD pattern. The same samples were then heated to the next temperature and the same procedure followed.

3.3.7 Attenuated Total Reflectance Fourier-Transform Infrared Spectroscopy (ATR-FTIR). ATR-FTIR spectra were obtained on a Varian 670 FT-IR Spectrometer equipped with a diamond Specac Golden Gate attachment. All spectra are an average of 24 scans for powder samples and were recorded from 4000 to 400 cm^{-1} with 4 cm^{-1} resolution. A background spectrum collected

on air was subtracted from sample spectra. The spectra were not corrected for the depth of wavelength penetration.

3.3.8 Thermogravimetric Analysis (TGA). A Q-series TGA from TA instruments was used to analyze thermal stability. A ~10 mg sample was placed on an aluminum pan and heated at a rate of 10 °C/min under nitrogen over the temperature range of 25 °C to 600 °C.

3.3.9 Solvent Exchange. To allow for exchange with the solvents of crystallization within the MOFs, the as synthesized materials were immersed in a more volatile solvent (e.g. methanol, acetone, chloroform). The solvent was decanted and replaced with fresh solvent 3 times over the course of 48 h. The resulting exchanged MOF crystallites were collected via vacuum filtration and allowed to dry in air.

3.3.10 Gas Sorption Isotherms. The sorption isotherm measurements were collected on a Quantachrome Autosorb-1. The samples were synthesized according to the procedures above and placed in a 6 mm large bulb sample cell, which was degassed under vacuum for 24 h with a temperature of 90 °C for the first 5 h and no temperature for the remaining time. The surface areas of the materials were determined by fitting the adsorption data within the 0.05-0.3 P/P_0 pressure range to the BET[33] and Langmuir[34] equations[35] and the total pore volume was determined by a single point method taken at $P/P_0 = 0.99$. The pore size distribution was determined by applying the non-local density functional theory (NLDFT) method on a slit pore equilibrium model to the CO_2 isotherm data at 273 K using the Autosorb software.

3.4 Results and Discussion

3.4.1 Synthesis and Structure

3.4.1.1 Structure of $Zn_4(pydc)_4(DMF)_2 \cdot 3DMF$ (1). The asymmetric unit of **(1)** contains two unique Zn atoms, 2 pydc ligands, one metal-coordinated DMF, and 1.5 DMF solvates. The pydc plays two roles in the formation of the 3D MOF. First, pydc bridges the Zn atoms by a single carboxylate in a $\kappa O^5:O^{5'}$ fashion, a $\kappa N^1,O^2:O^2$, or a $\kappa O^2:O^{2'}$ fashion to form 1D chains of secondary building units. Second, pydc bridges Zn atoms across the aromatic ring via the 2- and 5-carboxylates. Overall, the two pydc ligands in the asymmetric unit are each tetradentate with coordination μ_4-($\kappa^5 N^1,O^2:O^2:O^5:O^{5'}$) and μ_4-($\kappa^5 N^1,O^2:O^{2'}:O^5:O^{5'}$).

The secondary building unit is comprised of Zn-dimers ($d_{Zn1—Zn2}$ = 3.464 Å) that are bridged by three different pydc ligands, one coordinated $\kappa N^1,O^2:O^2$ fashion and two coordinated $\kappa O^5:O^{5'}$ (Figure 3.1A). Zn1 has a distorted square pyramidal geometry, with three coordination sites filled by O atoms from the 3 bridging carboxylates, and the 4th and 5th coordination sites filled by a bidentate pydc ($\kappa N^1,O^2$). Zn2 has a distorted octahedral geometry, with four coordination-sites filled by a pyridyl nitrogen and 3 O atoms of the bridging pydc ligands, the 5th site is filled by a pydc O atom, and the 6th site filled by the O atom of the DMF. The dimers are linked along the *b*-axis by a pydc bridging in a $\kappa O^2:O^{2'}$ fashion to form 1D zig-zag chains (Figure 3.1B and C). The Zn—Zn distance between neighboring Zn-dimers is 5.356 Å. This unusual coordination has been reported previously.[36] In the earlier structure, however, the Zn-dimers bridge in the same $\kappa O^2:O^2$ fashion, but cyclize to form isolated Zn_4 clusters instead of zig-zag chains. The pydc organic linkers that connect the zig-zag chains run parallel to the crystallographic [101] and [10-1] direction to form the 3D framework.

In addition to the coordinated DMFs, there are 3 DMF solvates, giving a formula unit of $Zn_4(pydc)_4(DMF)_2 \cdot 3DMF$ (corresponds to 1.5 DMF solvates/asymmetric unit; 6 DMF solvates/unit cell). TGA and PXRD demonstrate that the crystals maintain their structural integrity upon removal of one DMF/formula unit (*vide infra*). Removal of a single DMF gives a void of 79.5 $Å^3$/formula unit (i.e. 2 symmetry equivalent voids totaling 159.1 $Å^3$/unit cell). If all 3 DMF solvates/formula unit are removed, the void volume is 317 $Å^3$ (634 $Å^3$/unit cell) and the void space is no longer an isolated cavity but instead channels through which solvent and gasses can permeate (Figure 3.1D). Although the crystal structure is not stable upon removal of all 3 DMF solvates/formula unit, PXRD does indicate the material is still crystalline, even if the structure has changed. In addition, it is conceivable that removal of a single DMF gives the remaining DMFs enough mobility for gas permeation. The structural purity of the as-synthesized MOF was confirmed by comparison of the experimental PXRD pattern with the pattern calculated from single crystal data (Figure 3.S1). The crystallographic information of **(1)** is summarized in Table 3.1 and Tables 3.S1-2.

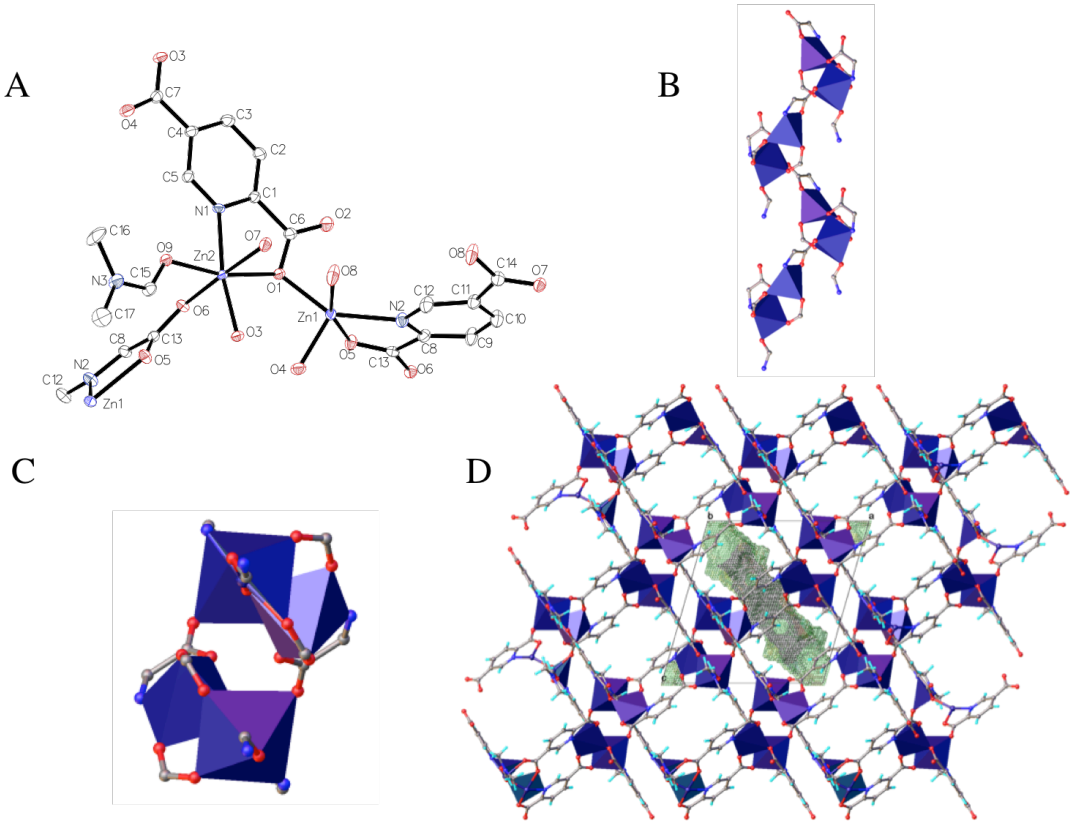

Figure 3.1. (A) Anisotropic ellipsoid drawing (50% probability) of **(1)** depicting the Zn-dimer. H-atoms and DMF solvate are omitted for clarity. (B) The 1D zig-zag chains as viewed down the *a*-axis. (C) The 1D zig-zag chains as viewed down the *b*-axis. (D) The packing diagram, as viewed down the *b*-axis, depicting the pydc linking of the 1D chains along the [101] and [10-1] crystallographic directions. The wireframe depicts the void space when all DMF solvate is removed.

3.4.1.2 Structure of $Zn_2(pydc)_2(DEF)$ (2). The asymmetric unit of **(2)** contains two unique Zn-atoms, 2 pydc ligands, one metal-coordinated DEF. The two unique Zn-atoms have the exact same connectivity as in **(1)** (Figure 3.2A) to generate the same 1D zig-zag chains (Figure 3.2B and C). The Zn—Zn distance in the dimer is 3.438 Å and the closest distance between dimers is 5.782 Å. The pydc organic linkers that connect the zig-zag chains run parallel

to the crystallographic *a*- and *b*-axes to form the 3D framework. Unlike **(1)**, structure **(2)** has no solvents of crystallization. The void volume/unit cell is 161.1 $Å^3$ and is comprised of 8 symmetrically equivalent voids of 20.1 $Å^3$ each. Comparison of the experimental PXRD pattern with the pattern calculated from the single crystal data confirmed sample homogeneity (Figure 3.S2). The crystallographic information of **(2)** is summarized in Table 3.1 and Tables 3.S3-4.

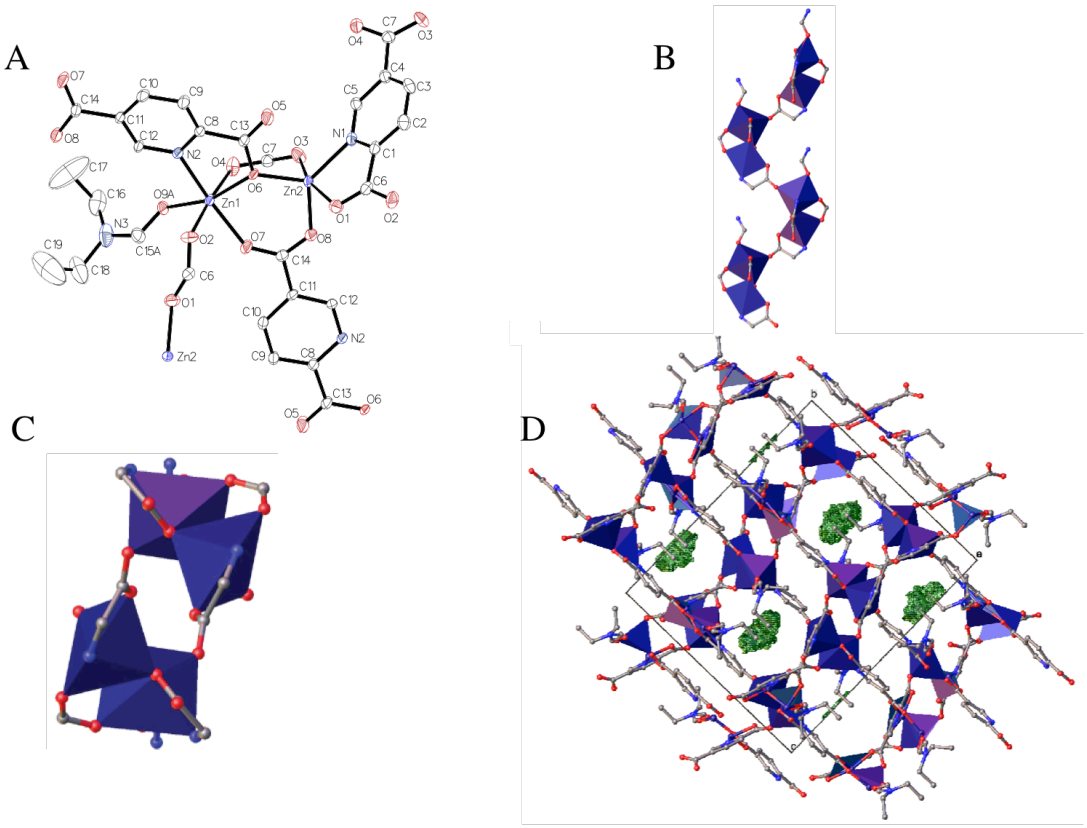

Figure 3.2. (A) Anisotropic ellipsoid drawing (50% probability) of **(2)** depicting the Zn-dimer. H-atoms and the minor conformation of the disordered DEF are omitted for clarity. (B) The 1D zig-zag chains as viewed down the *b*-axis. (C) The 1D zig-zag chains as viewed down the *a*-axis. (D) The packing diagram, as viewed down the *a*-axis, depicting the pydc linking of the 1D chains along the [010] and [001] crystallographic directions. The wireframe depicts the void spaces.

Table 3.1. Crystal data and structure refinement for MOFs **(1)** and **(2)**.

	(1)	**(2)**
Identification code	$Zn_4(pydc)_4(DMF)_2$•3DMF	$Zn_2(pydc)_2(DEF)$
Chemical Formula	$C_{43}H_{47}N_9O_{21}Zn_4$	$C_{19}H_{17}N_3O_9Zn_2$
Formula Mass	1287.38	561.09
Crystal System	Monoclinic	Orthorhombic
Space Group	$P2_1/n$ (No. 14)	*Pbca* (No. 61)
Wavelength/Å	0.71073	0.71073
a/Å	14.0003(3)	12.23325(19)
b/Å	12.1692(2)	17.4883(3)
c/Å	14.6711(3)	20.3322(5)
α/deg	90.00	90.00
β/deg	105.867(2)	90.00
γ/deg	90.00	90.00
Unit cell volume/$Å^3$	2404.33(8)	4349.85(14)
Z	2	8
μ/mm^{-1}	2.065	2.262
Density/g cm^{-3}	1.778	1.714
T/K	100	100
2θ range/degrees	3.46-32.33	3.53-30.52
Data measured	8062 [R(int) = 0.0607]	6633
Unique data	5913	5162
Goodness of Fit	1.040	1.110
R indices [I > 2σ(I)] [a,b]	R1 = 0.0468, wR2 = 0.1008	R1 = 0.0492, wR2 = 0.1036
R indices (all data)[a,b]	R1 = 0.0762, wR2 = 0.1150	R1 = 0.0677, wR2 = 0.1112

[a] $R1=\sum\left||F_o|-|F_c|\right| / \sum|F_o|$;

[b] $wR=\left(\sum \frac{\left[w(F_o^2-F_c^2)^2\right]}{\sum\left|w(F_o^2)^2\right|}\right)^{\frac{1}{2}}$, where $w = 1/[\sigma^2(F_o)^2 + (aP)^2 + bP]$, $P = [(F_o)^2 + 2(F_c)^2]/3$.

3.4.1.3 Structure of MOF-69C: $Zn_3(OH)_2(bdc)_2 \cdot 2DEF$. The structure of MOF-69C has been reported previously and consists of an extended 3D framework with infinite 1D chains of zinc oxyhydroxide bridged by the 1,4-benzenedicarboxylate ligand.[28,37] The structure of

MOF-69C contains octahedrally and tetrahedrally coordinated Zn(II) metal centers. To confirm the synthesis and determine phase purity, experimental PXRD patterns were compared to the calculated powder pattern from the literature reported single crystal data and TGA was performed (Figure 3.S3).

3.4.2 Characterization

Attenuated total reflectance Fourier-transform infrared spectroscopy (FTIR) was used to characterize the MOFs. The spectrum for the 2,5-pyridinedicarboxylic acid linker displays features corresponding to the C=O stretch of the carboxylic acids at 1720 cm^{-1} (Figure 3.3, red). The spectra of **(1)** and **(2)** demonstrate a shift in these peaks to lower wavenumbers (1608 and 1616 cm^{-1}, respectively) due to the chelation of the carboxylic oxygen atoms to the Zn metal in the MOF framework (Figure 3.3). Features due to the O-H stretch as well as the aromatic sp^2 C-H stretch (3093 cm^{-1} and 2844 cm^{-1}, respectively) are observed in the 2,5-pyridinedicarboxylic acid spectrum (Figure 3.3, red). The peaks present in all spectra between 700-800 cm^{-1} correspond to the aromatic sp^2 C-H bend of the 2,5-pyridinedicarboxylic acid linker molecule. The O-H stretch is not present in the spectra of **(1)** and **(2)** (Figure 3.3, black and blue), consistent with coordination of the oxygen to the metal atom of the MOF. The appearance of peaks at 1043 and 1039 cm^{-1} in the spectra for **(1)** and **(2)**, respectively, are also indicative of a M-N bond.[38] Additionally, the spectra of both **(1)** and **(2)** show peaks at 1040 cm^{-1} corresponding to the C-H bending modes of the methyl groups of DMF or DEF solvent, respectively, along with peaks at 1280 cm^{-1}, which correspond to the N-CH_3 asymmetric stretching mode of the solvents.[39]

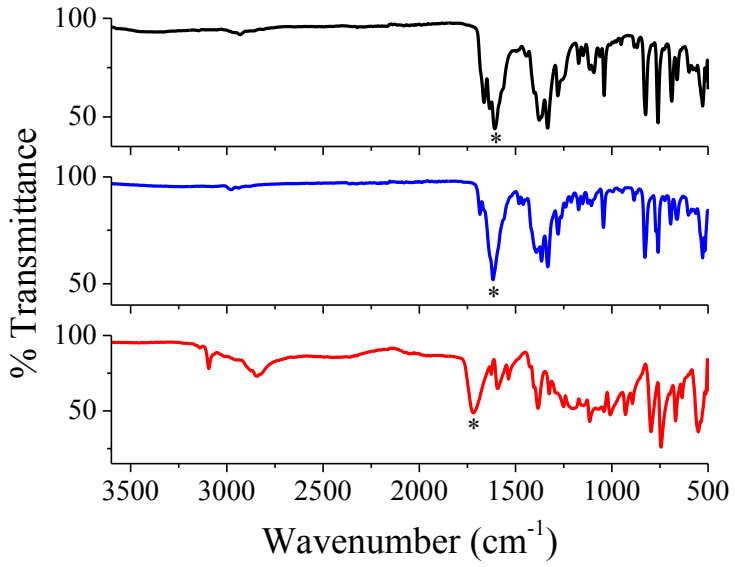

Figure 3.3. ATR-FTIR spectra with the designated (*) C=O stretches of the linker and the corresponding carboxylato stretches of the MOFs of **(1)** (black; 1608 cm^{-1}), **(2)** (blue; 1616 cm^{-1}), and 2,5-pyridine dicarboxylic acid (red; 1720 cm^{-1}). As the carboxylic oxygen becomes the carboxylato chelating functionality present in the MOF structures, there is a corresponding decrease in the frequency of this stretch.

The thermal stability and solvent loss of the MOFs was investigated using thermal gravimetric analysis (TGA). The TG curve of **(1)** reveals weight losses at 85 °C and 150 °C (obs: 6.38% and 10.5%, respectively; 16.88% total) consistent with the removal of 3 DMF solvates (calc: 17.04%). A third loss at 270 °C (obs: 6.4%) is consistent with desorption of Zn-coordinated DMF (calc: 5.68%). The removal of the second bound DMF occurs concomitantly with MOF degradation at ~350 °C (Figure 3.4A). The TG curve of **(2)**, with pore-contained solvate molecules, displays thermal stability up to 400 °C, where loss of bound DEF occurs concurrently with MOF degradation (Figure 3.4B). The TG curve of MOF-69C was consistent with previously reported results (Figure 3.S3).[37]

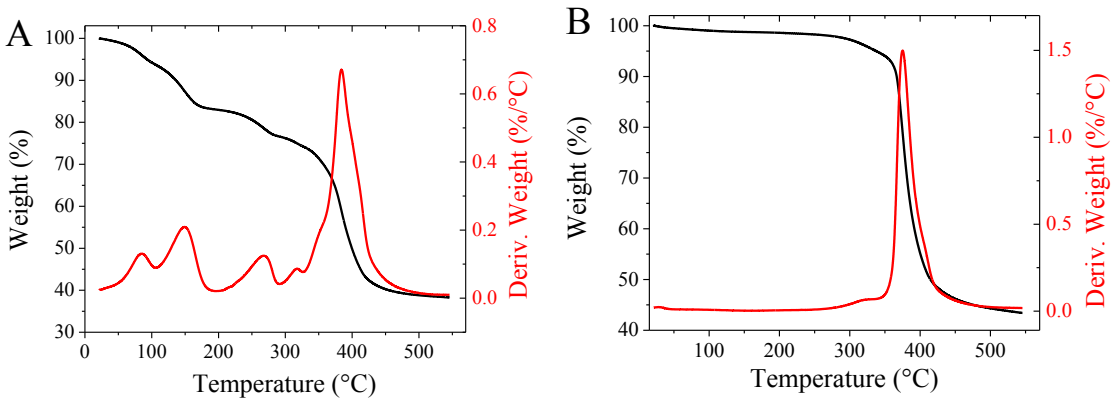

Figure 3.4. TG curves of (A) **(1)** and (B) **(2)**.

In addition to TGA, the effect of varied temperature on the structure was further investigated by PXRD after evacuation. Bulk crystalline samples were ground into powders and heated at the desired temperature under vacuum for 1 h followed by immediate PXRD analysis at room temperature (Figure 3.5). The crystalline structure of **(1)** is stable upon removal of one DMF solvate (loss at 85 °C) but undergoes a structural rearrangement upon removal of a 2nd DMF solvate (loss beginning at 150 °C) (Figure 3.5A). The crystal structure of **(2)** remains stable up to 260 °C, consistent with the TG curve (Figure 3.5B). MOF-69C undergoes a structural change between 130 °C and 196 °C, which is consistent with loss of a DEF solvate in the TG curve (Figure 3.5C). The removal of the second DEF molecule results in further change in the PXRD pattern at 230 °C. These results are consistent with the previously reported PXRD patterns for MOF-69C after removal of the DEF solvent at 200 °C.[40]

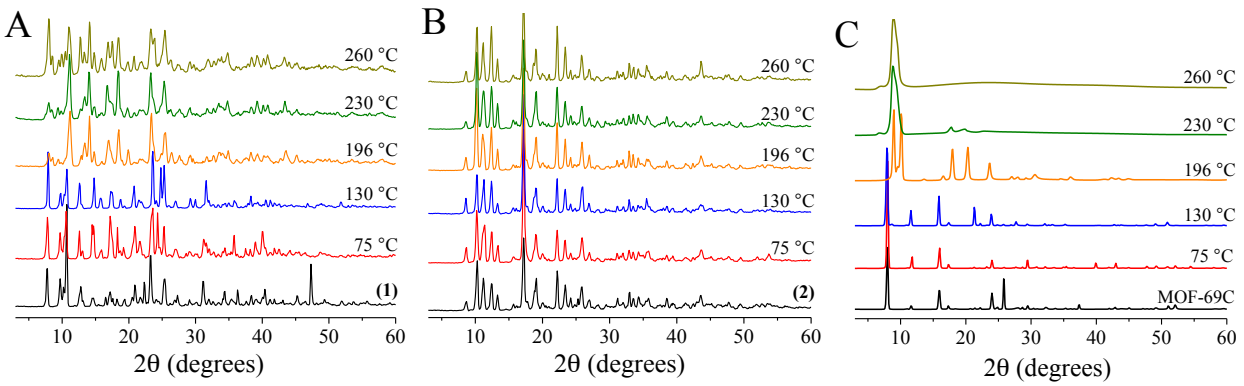

Figure 3.5. PXRD patterns after hourly evacuation at the designated temperature of (A) **(1)**; (B) **(2)**; (C) MOF-69C.

3.4.3 Gas Sorption Properties

Excess CO_2 gas sorption isotherms were measured for **(1)**, **(2)**, and MOF-69C at 273 K (Figure 3.6A and B, 3.S8, S9, and S10). **(1)** displays the greatest affinity for CO_2 (58.946 mL/g at ~1 atm) and exhibits a reversible type-I isotherm, consistent with a permanently microporous material.[35] The BET and Langmuir surface areas for **(1)** were calculated to be 196 and 390 m^2/g, respectively. The total pore volume was determined by the single point method to be 0.116 cm^3/g. Density Functional Theory (DFT) and Monte Carlo simulations determined a pore width of 7.17 Å, consistent with the crystal structure. The isotherms for **(2)** and MOF-69C display a lower affinity for CO_2 and did not reach a plateau within the pressure range observed, suggesting that the pore sizes of the frameworks are too small to reach equilibrium at the experimental pressure values (Figure 3.6, 3.S9, 3.S10).

In order to increase the adsorptive properties of the MOFs, exchange with methanol was performed on **(1)** and **(2)**. It can be observed that **(1)** undergoes a structural change after methanol is exchanged with DMF in the pores (Figures 3.S4). Even with exchange of DMF, the

resulting surface area of **(1)** did not increase (Figure 3.S5). Not surprisingly, the structure of **(2)**, which has no solvent of crystallization, was maintained after methanol exchange (Figure 3.S6A). The TG curve of the exchanged material, **(2)-MeOH**, shows that methanol is present (Figure 3.S6B). After evacuation of **(2)-MeOH** at 90 °C for 5 h, the TG curve recovers the as synthesized temperature dependent behavior (Figure 3.S6C). The sorption properties of **(2)-MeOH** were studied with CO_2 at 273 K and display a type-1 reversible isotherm with low CO_2 uptake of 12.7445 mL/g at ~1 atm (Figure 3.S7 and 3.S11) and surface areas of 41 and 74 m^2/g from BET and Langmuir analysis, respectively. The BET and Langmuir surface areas for all materials were calculated and are presented in Table 3.2.

The sorption properties of the MOFs were also investigated using N_2 at 77 K (Figure 3.S12). As was observed with CO_2, **(1)** exhibits a type-I isotherm and displays the greatest affinity for N_2. The BET and Langmuir surface areas for **(1)** were found to be 319 m^2/g and 464 m^2/g, respectively (Table 3.2). MOF-69C and **(2)** exhibited a lower affinity for N_2 as compared to **(1)**. The N_2 BET and Langmuir surface areas for **(2)** were found to be 5 and 59 m^2/g, respectively, and those for MOF-69C were found to be 8 m^2/g and 27 m^2/g, respectively. The N_2 BET and Langmuir surface areas of **(2)-MeOH** were 39 m^2/g and 59 m^2/g, respectively.

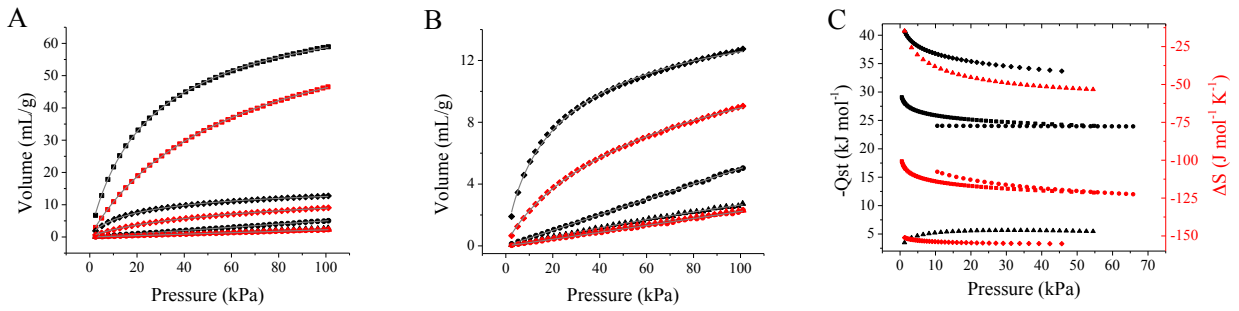

Figure 3.6. CO_2 isotherms at 273 K (black) and 296 K (red) with the Langmuir-Freundlich fit shown with solid line of **(1)** (squares), **(2)** (triangles), **(2)-MeOH** (diamonds), and MOF-69C (circles); (A) shows all MOFs; (B) shows zoom of lower adsorption; (C) Q_{st} (black) and ΔS (red) for **(1)** (squares), **(2)** (triangles), **(2)-MeOH** (diamonds), and MOF-69C (circles) as a function of pressure.

Table 3.2. Surface area and thermodynamic parameters for CO_2 and N_2 adsorption for **(1)**, **(2)**, **(2)-MeOH**, and MOF-69C.

	Determined from CO_2 sorption at 273 K					Determined from N_2 sorption at 77 K	
MOF	BET (m^2/g)	Langmuir (m^2/g)	Q_{st} [b] (kJ/mol)	Q_{st}^0 [c] (kJ/mol)	K_F (Pa)	BET (m^2/g)	Langmuir (m^2/g)
(1)	196	390	–29.1 ± 0.4	–27.7	45.9 ± 0.6	319	464
(2)	7	----[a]	–3 ± 1	–2.7	1.7 ± 0.2	5	59
(2)-MeOH	41	74	–41 ± 4	–33.4	72 ± 2	39	59
MOF-69C	11	114	–24.1 ± 0.3	–17.6	5.72 (±0.01) × 10^{-2}	8	27

[a] Value could not be determined.
[b] Determined from the Clausius-Clapeyron equation at the onset of adsorption
[c] Determined from the zero limit of the virial equation

The thermodynamic properties of CO_2 adsorption were investigated by collecting isotherm data at 296 K in addition to the reported data at 273 K (Figure 3.6A and B). The volume adsorbed decreases with temperature for all compounds, confirming an exothermic nature to the adsorption process. A fit to the Langmuir-Freundlich isothermal equation (Equation 3.1) was performed in order to determine the amount of gas adsorbed as a function of pressure,[41-43]

$$\frac{Q}{Q_m} = \frac{K_F P^{(1/t)}}{1+K_F P^{(1/t)}} \tag{3.1}$$

where Q is the moles of gas adsorbed, Q_m is the moles adsorbed at saturation, P is pressure, K_F is an affinity constant, and t is an index of heterogeneity ($0 < 1/t < 1$). Therefore, the Langmuir-Freundlich equation simplifies to the Langmuir equation when t=1. The values of t required for adequate fits to the experimental data were very close to 1 for the as synthesized MOFs, with a maximum deviation of 1.07 for **(1)**. In fact, for CO_2 sorption on both MOF-69C and **(2)** at 296 K and MOF-69C at 273 K, the fits indicate a homogenous binding environment with t equal to 1. However, **(2)-MeOH** gave a t value of 1.25 at 273 K, suggesting a heterogeneous binding environment,[42,43] which is consistent with CO_2 binding on the MOF/solvent surface rather than specifically within the pores of the MOF. Indeed, the lower value of Q_m for **(2)-MeOH** in comparison with **(1)** confirms that CO_2 does not penetrate the MOF pores. The sorption isotherms with the fits are shown in Figure 4.6 and the parameters are summarized in Table 3.2 and 3.S5.

Application of the Clausius-Clapeyron equation (Equation 3.2)[35] allows for the determination of the isosteric heats of adsorption, Q_{st},

$$ln(P_i) = \frac{Q_{st}}{RT_i} + \frac{\Delta S}{R} \tag{3.2}$$

where P_i is the pressure for isotherm i, T_i is the temperature for isotherm i, R is the universal gas constant, and ΔS is entropy. The Langmuir-Freundlich equation was rearranged to solve for pressure and substituted into the Clausius-Clapeyron equation, which was used to determine the Q_{st} and ΔS for the MOFs (Figure 3.6C). It was observed that the adsorption enthalpy for **(1)** slightly decreases as the CO_2 pressure increases, remaining at a constant high negative value throughout the adsorption due to the favorable interactions between CO_2 and **(1)**. The value of Q_{st} for **(1)** approaches −29.1 (±0.4) kJ/mol at low surface coverage. The adsorption enthalpy of **(2)** and MOF-69C at the onset of adsorption were found to be −3 (±1) kJ/mol and −24.1 (±0.3) kJ/mol, respectively, while the adsorption enthalpy for **(2)-MeOH** was −41 (±4) kJ/mol.

In order to further analyze the affinity of the framework for CO_2, the zero-coverage heat of adsorption (Q_{st}^0), which describes the strength of the binding sites within the material at the lowest pressures, can be determined by fitting the temperature dependent isothermal data to a virial-type equation (Equation 3.3),[7,44]

$$\ln P = \ln N + \frac{1}{T}\sum_{i=0}^{m} a_i N^i + \sum_{i=0}^{n} b_i N^i \tag{3.3}$$

where P is the pressure, N is the amount of CO_2 adsorbed, T is the temperature, m and n are the number of virial coefficients required for fitting, and a and b are virial coefficients. Contrary to the Langmuir equation, which goes to infinity at the zero pressure limit, the limit of the virial equation results in a numerical value used to estimate Q_{st}^0. In the equation, the parameters a_0 and b_0 are related to the Q_{st} and the Henry's Law constant (K_H), respectively. The enthalpies of adsorption can be estimated as a function of surface coverage (Equation 3.4),[44]

$$Q_{st} = -R\left(\frac{d\ln P}{d\left(\frac{1}{T}\right)}\right)_N = -R\sum_{i=0}^{m} a_i N^i \tag{3.4}$$

and the value of Q_{st}^0 determined by the limit of Equation 3.4, as follows, Equation 3.5:[7]

$$Q_{st}^0 = -R \lim_{N \to 0} \left(\sum_{i=0}^{m} a_i N^i \right) = -R a_0 \quad (3.5)$$

Values of b_0 are also related to the physically meaningful quantity K_0, which is related to the Henry's law adsorption constant, K_H, by Equations 3.6 and 3.7.[44]

$$K_H = K_0 exp\left(\frac{q_0}{Rt}\right) \quad (3.6)$$

$$K_0 = \exp(-b_0) \quad (3.7)$$

Values of Q_{st}^0 for CO_2 adsorption on **(1)**, **(2)**, **(2)-MeOH**, and MOF69-C are presented in Table 3.2 and the corresponding fits are provided in Figures 3.S13-S16.

The Q_{st}^0 values (from the onset of the Clausius-Clapeyron data and the virial equation) are consistent with a mechanism of CO_2 binding to **(1)** that involves the cationic Zn(II) metal sites present in the 3D structure. The calculated value of Q_{st}^0 (~ −28 kJ/mol) agrees well with that observed for CPO-27-Zn (MOF-74-Zn, −30.5 kJ/mol) in which adsorption to coordinatively unsaturated Zn(II) metal sites has been reported.[45] The larger Q_{st}^0 value for **(2)-MeOH** (~33 kJ/mol) combined with the low coverage of CO_2 at equilibrium (Q_m) suggests physical interaction between CO_2 and a limited number of binding sites on the solvent-modified MOF surface, resulting in a larger adsorption enthalpy per binding site. Structurally, there are two main binding sites for CO_2 sorption in the materials presented: the metal nodes and the aromatic linkers. A key component to sorption at the metal nodes is the degree to which the CO_2 can enter the coordination sphere of the metal. To achieve coordinatively unsaturated metal sites, CPO-27-M and other MOFs require activation, where a bound solvent molecule is removed through evacuation, solvent exchange followed by evacuation, or supercritical drying.[46]

In contrast, both **(1)** and **(2)** exhibit Zn(II) metal nodes with a distorted 5-coordinate square pyramidal geometry as synthesized (Figure 3.7). Relatively minor structural rearrangements are required, if at all, to incorporate CO_2 into a sixth coordination site (attack from bottom, Figure 3.7). MOF-69C has a tetrahedral Zn(II) center (preferred geometry) and the structural rearrangement required to incorporate an additional ligand is much greater in comparison to that of **(1)** and **(2)**. Therefore, it is likely that the mechanism of binding to MOF-69C is physisorption consistent with that of MOF-5 (IRMOF-1) and UMCM-1. This agrees well with the calculated Q_{st}^0 for MOF-69C of ~ −18 kJ/mol, whereas the measured Q_{st}^0 values for MOF-5 and UMCM-1 are −17 and −12 kJ/mol, respectively.[47,48] The sorption for **(2)** and **(2)-MeOH** is also likely a physisorption process on the surface of the MOF particles. While **(2)** exhibits binding sites that would be advantageous for CO_2 sorption, the void space is small (20.1 $Å^3$) and isolated, making gas permeation unfeasible. The DEF that is coordinated to the octahedral zinc would need to be removed to accommodate CO_2 and, therefore, the potential for binding is not realized.

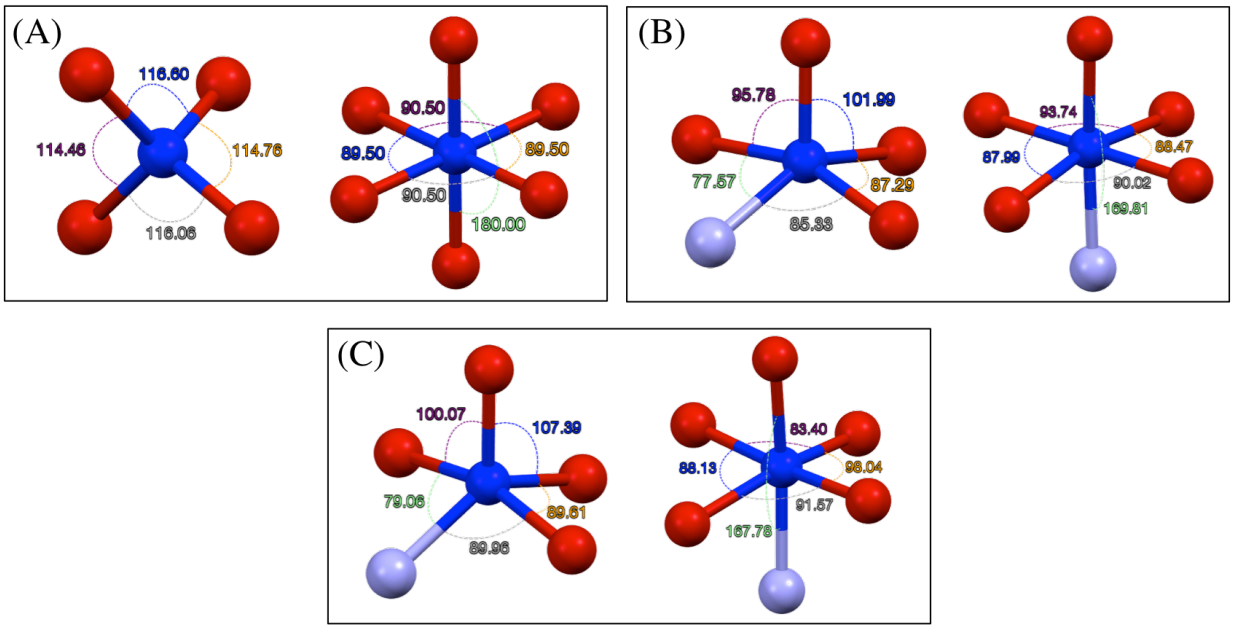

Figure 3.7. The metal coordination environments and selected bond angles for (A) MOF-69C (tetrahedral and octahedral); (B) **(1)** (distorted square pyramidal and octahedral); (C) **(2)** (distorted square pyramidal and octahedral). The red circles represent oxygen, the light blue circles represent nitrogen, and the blue circles represent zinc.

To quantify the selectivity of **(1)** for CO_2, isotherms for CO_2 and N_2 were recorded at the same temperature (296 K), allowing for a direct comparison of the amount of adsorbed gas. The selectivity of CO_2 over N_2 for **(1)** was calculated as the ratio of Henry's law constants obtained as the pressure of the system goes to zero, which was estimated from the ratio of the initial slopes of the gas uptake (Figure 3.S17).[24] **(1)** preferentially adsorbs CO_2 over N_2 with a selectivity of 42, consistent with the thermodynamic analysis. This can be attributed to the fact that CO_2 has a larger polarizability than N_2, allowing the Lewis acidic metal node to bind to an oxygen atom of CO_2.[7,18] Additionally, CO_2 has a smaller kinetic diameter (3.30 Å) compared to N_2 (3.64 Å), which allows for easier diffusion of CO_2 within the MOF pores.[7,18] The kinetic effects are expected to contribute to a lesser degree than thermodynamics in this case.

The selectivity factor (*S*), which relates the molar ratio of adsorbed gases at the partial pressures of the gases within a mixture, is given by Equation 3.8,[7]

$$S = \frac{q_1/q_2}{p_1/p_2} \tag{3.8}$$

where q_i is the mass of adsorbed gas i at the relevant partial pressure, and p_i is the partial pressure of component i. For post-combustion CO_2 capture processes, the partial pressures of CO_2 and N_2 are 0.15 and 0.75, respectively.[7] It should be noted that the amount of gas adsorbed is determined from the single component sorption isotherm and does not take the competition of the gas molecules for adsorption sites into consideration. Therefore, the selectivity is not an accurate measure of how the MOF would behave in an actual mixed gas setting. *S* for **(1)** was found to be 14.

3.5 Conclusions

The solvothermal synthesis of two previously unreported MOFs was performed and a thermodynamic study of their gas sorption properties conducted. The MOFs contain Zn(II) metal sites in a distorted square pyramidal molecular geometry without the need of activation. These coordinatively unsaturated metal nodes are ideal binding sites for the polarizable CO_2 molecule. The calculated isosteric heat of adsorption, Q_{st}, for **(1)** from both analysis by the Clausius-Clapeyron equation and the virial equation are consistent with this mechanism and other MOFs that exhibit Zn(II) metal binding sites (CPO-27-Zn). The microporous MOF, **(1),** displayed high selectivity for CO_2 over N_2 (42) as a result of both thermodynamic and, to a lesser extent, kinetic control.

3.6 Acknowledgements

The authors acknowledge the support of Virginia Tech's Institute for Critical Technologies and Applied Sciences for providing funding and the Sustainable Energy Lab for access to surface area and low-pressure characterization equipment.

3.7 Supplemental Information

3.7.1 Single crystal characterization of (1) and (2)

Table 3.S1. Crystal data and structure refinement for **(1)**.

Identification code	cs1905	
Empirical formula	$C_{43}H_{47}N_9O_{21}Zn_4$	
Formula weight	1287.38	
Temperature	100(1) K	
Wavelength	0.7107 Å	
Crystal system	monoclinic	
Space group	$P\ 1\ 2_1/n\ 1$	
Unit cell dimensions	a = 14.0003(3) Å	α = 90°.
	b = 12.1692(2) Å	β = 105.867(2)°.
	c = 14.6711(3) Å	γ = 90°.
Volume	2404.33(8) Å^3	
Z	2	
Density (calculated)	1.778 Mg/m^3	
Absorption coefficient	2.065 mm^{-1}	
F(000)	1312	
Crystal size	0.1806 x 0.116 x 0.0556 mm^3	
Theta range for data collection	3.46 to 32.33°.	
Index ranges	-20<=h<=20, -18<=k<=17, -21<=l<=21	
Reflections collected	30072	
Independent reflections	8062 [R(int) = 0.0607]	

Completeness to theta = 31.00°	99.5%
Absorption correction	Gaussian
Max. and min. transmission	0.898 and 0.720
Refinement method	Full-matrix least-squares on F^2
Data / restraints / parameters	8062 / 4 / 359
Goodness-of-fit on F^2	1.040
Final R indices [I>2sigma(I)]	R1 = 0.0468, wR2 = 0.1008
R indices (all data)	R1 = 0.0762, wR2 = 0.1150
Largest diff. peak and hole	1.696 and -1.057 e.$Å^{-3}$

Table 3.S2. Bond lengths [Å] and angles [°] for **(1)**.

Zn(1)-O(1)	2.008(2)	O(6)-C(13)	1.256(3)	C(8)-C(9)	1.385(4)
Zn(1)-O(4)#1	1.974(2)	O(7)-Zn(2)#2	2.180(2)	C(8)-C(13)	1.519(4)
Zn(1)-O(5)	2.073(2)	O(7)-C(14)	1.241(3)	C(9)-C(10)	1.401(4)
Zn(1)-O(8)#2	2.086(2)	O(8)-Zn(1)#2	2.086(2)	C(10)-C(11)	1.386(4)
Zn(1)-N(2)	2.105(2)	O(8)-C(14)	1.267(4)	C(11)-C(12)	1.392(4)
Zn(2)-O(1)	2.1523(19)	O(9)-C(15)	1.246(3)	C(11)-C(14)	1.519(4)
Zn(2)-O(3)#1	2.054(2)	N(1)-C(1)	1.345(3)	N(4)-C(18A)	1.341(9)
Zn(2)-O(6)#3	2.124(2)	N(1)-C(5)	1.333(3)	N(4)-C(19A)	1.376(7)
Zn(2)-O(7)#2	2.180(2)	N(2)-C(8)	1.346(4)	N(4)-C(20)	1.467(10)
Zn(2)-O(9)	2.0724(19)	N(2)-C(12)	1.338(4)	N(4)-C(18B)	1.12(3)
Zn(2)-N(1)	2.119(2)	N(3)-C(15)	1.318(4)	N(4)-C(19B)	1.57(2)
O(1)-C(6)	1.299(3)	N(3)-C(16)	1.458(4)	N(4)-C(20B)	1.62(3)
O(2)-C(6)	1.220(3)	N(3)-C(17)	1.458(4)	O(10A)-C(18A)	1.264(12)
O(3)-Zn(2)#4	2.054(2)	C(1)-C(2)	1.389(4)	O(10B)-C(18B)	1.59(3)
O(3)-C(7)	1.251(3)	C(1)-C(6)	1.514(4)	O(12)-C(21)	1.2167
O(4)-Zn(1)#4	1.974(2)	C(2)-C(3)	1.388(4)	N(6)-C(21)	1.2822
O(4)-C(7)	1.268(3)	C(3)-C(4)	1.385(4)	N(6)-C(22)	1.4112
O(5)-C(13)	1.260(3)	C(4)-C(5)	1.398(4)	N(6)-C(23)	1.5855
O(6)-Zn(2)#5	2.1243(19)	C(4)-C(7)	1.505(4)		

O(1)-Zn(1)-O(5)	100.96(8)	N(1)-C(1)-C(6)	116.1(2)
O(1)-Zn(1)-O(8)#2	87.29(9)	C(2)-C(1)-C(6)	121.5(2)
O(1)-Zn(1)-N(2)	146.09(9)	C(3)-C(2)-C(1)	118.5(3)
O(4)#1-Zn(1)-O(1)	101.99(9)	C(4)-C(3)-C(2)	119.4(3)
O(4)#1-Zn(1)-O(5)	95.77(9)	C(3)-C(4)-C(5)	118.3(3)
O(4)#1-Zn(1)-O(8)#2	100.48(10)	C(3)-C(4)-C(7)	122.2(3)
O(4)#1-Zn(1)-N(2)	111.88(10)	C(5)-C(4)-C(7)	119.5(3)
O(5)-Zn(1)-O(8)#2	159.85(9)	N(1)-C(5)-C(4)	122.6(3)
O(5)-Zn(1)-N(2)	77.56(9)	O(1)-C(6)-C(1)	115.0(2)
O(8)#2-Zn(1)-N(2)	85.33(9)	O(2)-C(6)-O(1)	125.0(3)
O(1)-Zn(2)-O(7)#2	90.01(8)	O(2)-C(6)-C(1)	120.0(3)
O(3)#1-Zn(2)-O(1)	96.89(8)	O(3)-C(7)-O(4)	127.1(3)
O(3)#1-Zn(2)-O(6)#3	93.46(8)	O(3)-C(7)-C(4)	117.2(2)
O(3)#1-Zn(2)-O(7)#2	85.62(8)	O(4)-C(7)-C(4)	115.7(2)
O(3)#1-Zn(2)-O(9)	96.20(8)	N(2)-C(8)-C(9)	121.8(3)
O(3)#1-Zn(2)-N(1)	169.82(9)	N(2)-C(8)-C(13)	113.9(2)
O(6)#3-Zn(2)-O(1)	87.99(7)	C(9)-C(8)-C(13)	124.3(3)
O(6)#3-Zn(2)-O(7)#2	177.68(8)	C(8)-C(9)-C(10)	119.1(3)
O(9)-Zn(2)-O(1)	166.67(8)	C(11)-C(10)-C(9)	119.1(3)
O(9)-Zn(2)-O(6)#3	93.74(8)	C(10)-C(11)-C(12)	117.8(3)
O(9)-Zn(2)-O(7)#2	88.47(8)	C(10)-C(11)-C(14)	123.6(3)
O(9)-Zn(2)-N(1)	89.63(8)	C(12)-C(11)-C(14)	118.6(3)
N(1)-Zn(2)-O(1)	77.05(8)	N(2)-C(12)-C(11)	123.3(3)
N(1)-Zn(2)-O(6)#3	94.49(8)	O(5)-C(13)-C(8)	115.6(2)
N(1)-Zn(2)-O(7)#2	86.20(8)	O(6)-C(13)-O(5)	126.9(3)
Zn(1)-O(1)-Zn(2)	112.69(9)	O(6)-C(13)-C(8)	117.5(2)
C(6)-O(1)-Zn(1)	116.20(18)	O(7)-C(14)-O(8)	127.6(3)
C(6)-O(1)-Zn(2)	115.10(17)	O(7)-C(14)-C(11)	118.5(3)
C(7)-O(3)-Zn(2)#4	135.61(19)	O(8)-C(14)-C(11)	113.9(3)
C(7)-O(4)-Zn(1)#4	126.22(19)	O(9)-C(15)-N(3)	125.1(3)
C(13)-O(5)-Zn(1)	117.97(18)	C(18A)-N(4)-C(19A)	126.0(7)

C(13)-O(6)-Zn(2)#5	124.34(18)	C(18A)-N(4)-C(20)	115.5(7)
C(14)-O(7)-Zn(2)#2	126.14(18)	C(19A)-N(4)-C(20)	118.6(7)
C(14)-O(8)-Zn(1)#2	139.5(2)	C(20)-N(4)-C(19B)	149.7(10)
C(15)-O(9)-Zn(2)	121.29(19)	C(20)-N(4)-C(20B)	47.0(10)
C(1)-N(1)-Zn(2)	114.62(18)	C(18B)-N(4)-C(20)	65.4(16)
C(5)-N(1)-Zn(2)	126.15(19)	C(18B)-N(4)-C(19B)	143.4(19)
C(5)-N(1)-C(1)	118.7(2)	C(18B)-N(4)-C(20B)	111.8(19)
C(8)-N(2)-Zn(1)	114.39(19)	C(19B)-N(4)-C(20B)	104.6(13)
C(12)-N(2)-Zn(1)	126.3(2)	O(10A)-C(18A)-N(4)	121.5(9)
C(12)-N(2)-C(8)	118.7(3)	N(4)-C(18B)-O(10B)	104(2)
C(15)-N(3)-C(16)	121.7(3)	C(21)-N(6)-C(22)	130.4
C(15)-N(3)-C(17)	120.4(3)	C(21)-N(6)-C(23)	117.6
C(17)-N(3)-C(16)	117.7(3)	C(22)-N(6)-C(23)	111.9
N(1)-C(1)-C(2)	122.4(3)	O(12)-C(21)-N(6)	121.2

Symmetry transformations used to generate equivalent atoms:

#1 ½+x, 1.5-y, ½+z #2 1-x ,1-y, 1-z

#4 - ½-x, 1.5-y, -½+z #5 ½-x, -½+y, 1.5-z

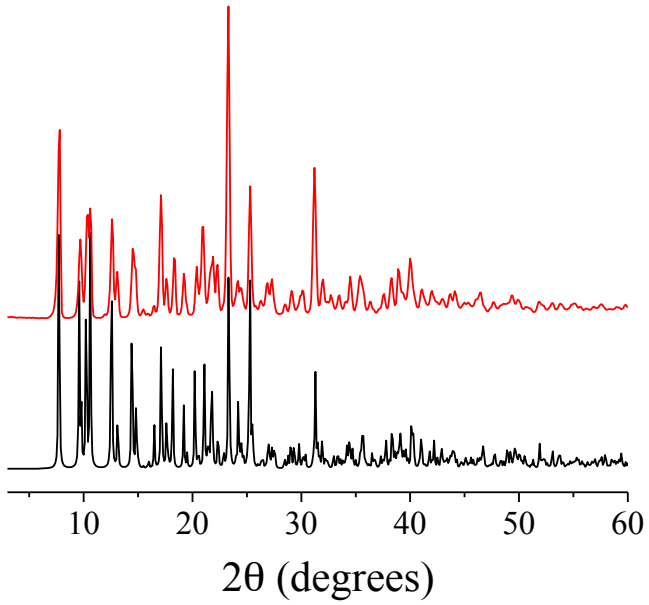

Figure 3.S1. Powder pattern of **(1)** simulated (black) and experimental (red).

Table 3.S3. Crystal data and structure refinement for **(2)**.

Identification code	cs1813	
Empirical formula	$C_{19}H_{16}N_3O_9Zn_2$	
Formula weight	561.09	
Temperature	100.0 K	
Wavelength	0.71073 Å	
Crystal system	orthorhombic	
Space group	*P b c a*	
Unit cell dimensions	a = 12.23325(19) Å	α = 90°.
	b = 17.4883(3) Å	β = 90°.
	c = 20.3322(5) Å	γ = 90°.
Volume	4349.85(14) $Å^3$	
Z	8	
Density (calculated)	1.714 Mg/m^3	
Absorption coefficient	2.262 mm^{-1}	
F(000)	2264	
Crystal size	0.2 x 0.13 x 0.07 mm^3	
Theta range for data collection	3.53 to 30.52°.	
Index ranges	-17<=h<=17, -24<=k<=24, -25<=l<=29	
Reflections collected	37739	
Independent reflections	6633 [R(int) = 0.0494]	
Completeness to theta = 30.00°	99.8%	
Absorption correction	Gaussian	
Max. and min. transmission	0.866 and 0.739	
Refinement method	Full-matrix least-squares on F^2	
Data / restraints / parameters	6633 / 24 / 319	
Goodness-of-fit on F^2	1.110	
Final R indices [I>2sigma(I)]	R1 = 0.0492, wR2 = 0.1036	
R indices (all data)	R1 = 0.0677, wR2 = 0.1112	
Largest diff. peak and hole	2.009 and -1.117 $e.Å^{-3}$	

Table 3.S4. Bond lengths [Å] and angles [°] for **(2)**.

Zn(1)-O(2)#1	2.046(3)	O(4)-C(7)	1.254(4)	C(1)-C(2)	1.387(5)
Zn(1)-O(4)#2	2.048(3)	O(5)-C(13)	1.214(4)	C(1)-C(6)	1.519(5)
Zn(1)-O(6)#3	2.164(2)	O(6)-C(13)	1.300(4)	C(2)-C(3)	1.398(5)
Zn(1)-O(7)	2.072(2)	O(7)-C(14)	1.246(4)	C(3)-C(4)	1.386(5)
Zn(1)-O(9A)	2.065(3)	O(8)-C(14)	1.258(4)	C(4)-C(5)	1.400(4)
Zn(1)-O(9B)	2.06(3)	O(9A)-C(15A)	1.243(6)	C(4)-C(7)	1.496(5)
Zn(1)-N(2)#3	2.150(2)	O(9B)-C(15B)	1.05(6)	C(8)-C(9)	1.389(4)
Zn(2)-O(1)	2.120(2)	N(1)-C(1)	1.348(4)	C(8)-C(13)	1.516(4)
Zn(2)-O(3)#2	2.102(2)	N(1)-C(5)	1.332(4)	C(9)-C(10)	1.386(5)
Zn(2)-O(6)#3	1.982(2)	N(2)-C(8)	1.338(4)	C(10)-C(11)	1.392(4)
Zn(2)-O(8)	1.983(2)	N(2)-C(12)	1.340(4)	C(11)-C(12)	1.393(4)
Zn(2)-N(1)	2.065(3)	N(3)-C(15A)	1.324(5)	C(11)-C(14)	1.506(4)
O(1)-C(6)	1.245(4)	N(3)-C(15B)	1.59(4)	C(16)-C(17)	1.487(7)
O(2)-C(6)	1.252(4)	N(3)-C(16)	1.461(6)	C(18)-C(19)	1.432(8)
O(3)-C(7)	1.256(4)	N(3)-C(18)	1.490(7)		

O(2)#1-Zn(1)-O(4)#2	175.23(10)	C(5)-N(1)-C(1)	118.7(3)
O(2)#1-Zn(1)-O(6)#3	91.56(9)	C(8)-N(2)-Zn(1)#6	114.99(19)
O(2)#1-Zn(1)-O(7)	86.55(11)	C(8)-N(2)-C(12)	118.4(3)
O(2)#1-Zn(1)-O(9A)	98.04(14)	C(12)-N(2)-Zn(1)#6	126.3(2)
O(2)#1-Zn(1)-O(9B)	80.9(10)	C(15A)-N(3)-C(16)	122.5(4)
O(2)#1-Zn(1)-N(2)#3	87.04(10)	C(15A)-N(3)-C(18)	117.9(5)
O(4)#2-Zn(1)-O(6)#3	88.12(9)	C(16)-N(3)-C(15B)	86.8(18)
O(4)#2-Zn(1)-O(7)	88.73(11)	C(16)-N(3)-C(18)	119.6(4)
O(4)#2-Zn(1)-O(9A)	83.41(13)	C(18)-N(3)-C(15B)	153.4(18)
O(4)#2-Zn(1)-O(9B)	99.7(9)	N(1)-C(1)-C(2)	122.8(3)
O(4)#2-Zn(1)-N(2)#3	97.49(10)	N(1)-C(1)-C(6)	114.9(3)
O(7)-Zn(1)-O(6)#3	93.80(9)	C(2)-C(1)-C(6)	122.3(3)
O(7)-Zn(1)-N(2)#3	167.80(11)	C(1)-C(2)-C(3)	118.2(3)
O(9A)-Zn(1)-O(6)#3	163.47(12)	C(4)-C(3)-C(2)	119.2(3)

O(9A)-Zn(1)-O(7)	100.15(12)	C(3)-C(4)-C(5)	118.6(3)
O(9A)-Zn(1)-N(2)#3	91.02(11)	C(3)-C(4)-C(7)	122.2(3)
O(9B)-Zn(1)-O(6)#3	171.6(8)	C(5)-C(4)-C(7)	119.2(3)
O(9B)-Zn(1)-O(7)	89.5(9)	N(1)-C(5)-C(4)	122.4(3)
O(9B)-Zn(1)-N(2)#3	99.7(9)	O(1)-C(6)-O(2)	128.0(3)
N(2)#3-Zn(1)-O(6)#3	76.01(8)	O(1)-C(6)-C(1)	117.1(3)
O(3)#2-Zn(2)-O(1)	162.86(10)	O(2)-C(6)-C(1)	114.9(3)
O(6)#3-Zn(2)-O(1)	100.07(9)	O(3)-C(7)-C(4)	118.7(3)
O(6)#3-Zn(2)-O(3)#2	96.84(10)	O(4)-C(7)-O(3)	127.0(3)
O(6)#3-Zn(2)-O(8)	107.39(9)	O(4)-C(7)-C(4)	114.3(3)
O(6)#3-Zn(2)-N(1)	120.56(9)	N(2)-C(8)-C(9)	123.0(3)
O(8)-Zn(2)-O(1)	88.00(10)	N(2)-C(8)-C(13)	116.1(3)
O(8)-Zn(2)-O(3)#2	89.62(10)	C(9)-C(8)-C(13)	120.9(3)
O(8)-Zn(2)-N(1)	131.72(10)	C(10)-C(9)-C(8)	118.5(3)
N(1)-Zn(2)-O(1)	79.06(10)	C(9)-C(10)-C(11)	119.1(3)
N(1)-Zn(2)-O(3)#2	89.97(10)	C(10)-C(11)-C(12)	118.5(3)
C(6)-O(1)-Zn(2)	114.3(2)	C(10)-C(11)-C(14)	120.9(3)
C(6)-O(2)-Zn(1)#4	137.4(2)	C(12)-C(11)-C(14)	120.6(3)
C(7)-O(3)-Zn(2)#5	124.1(2)	N(2)-C(12)-C(11)	122.5(3)
C(7)-O(4)-Zn(1)#5	134.1(2)	O(5)-C(13)-O(6)	125.3(3)
Zn(2)#6-O(6)-Zn(1)#6	111.98(10)	O(5)-C(13)-C(8)	120.5(3)
C(13)-O(6)-Zn(1)#6	116.22(18)	O(6)-C(13)-C(8)	114.1(3)
C(13)-O(6)-Zn(2)#6	118.56(19)	O(7)-C(14)-O(8)	127.1(3)
C(14)-O(7)-Zn(1)	140.0(2)	O(7)-C(14)-C(11)	116.3(3)
C(14)-O(8)-Zn(2)	127.1(2)	O(8)-C(14)-C(11)	116.5(3)
C(15A)-O(9A)-Zn(1)	126.8(3)	O(9A)-C(15A)-N(3)	122.7(5)
C(15B)-O(9B)-Zn(1)	123(4)	O(9B)-C(15B)-N(3)	112(4)
C(1)-N(1)-Zn(2)	113.7(2)	N(3)-C(16)-C(17)	114.2(4)
C(5)-N(1)-Zn(2)	127.3(2)	C(19)-C(18)-N(3)	115.4(5)

Symmetry transformations used to generate equivalent atoms:

#1	-0.5+x, 0.5-y, 1-z	#2	-0.5+x, +y, 1.5-z
#4	+x, +y, 1+z	#5	0.5+x, +y, 1.5-z

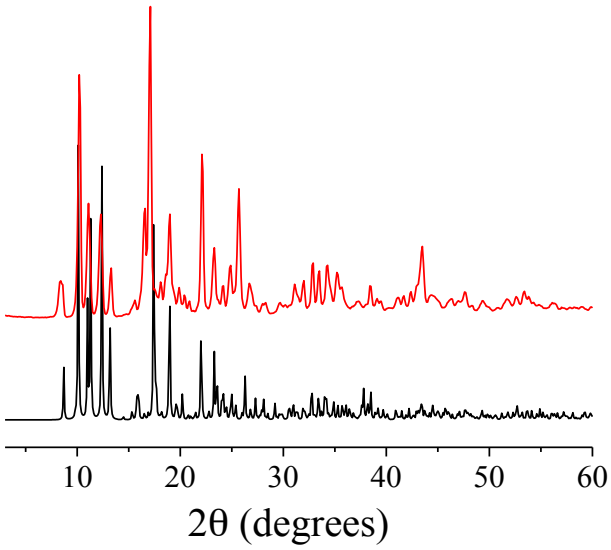

Figure 3.S2. Powder pattern of **(2)** simulated (black) and experimental (red).

3.7.2 MOF-69C characterization

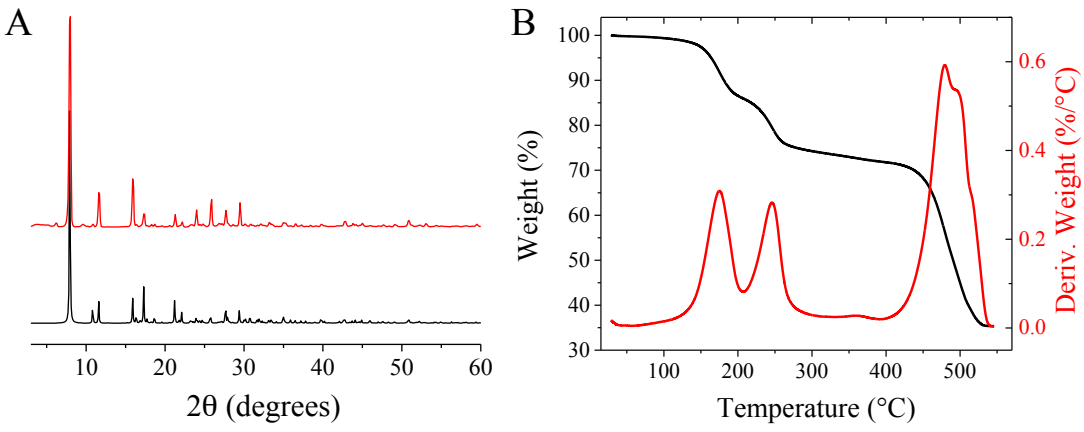

Figure 3.S3. (A) Powder pattern of MOF-69C simulated[28] (black) and experimental (red). (B) TG curve of MOF-69C. The weight losses observed are consistent with previously reported results.[37]

3.7.3 Solvent exchange characterization and gas sorption

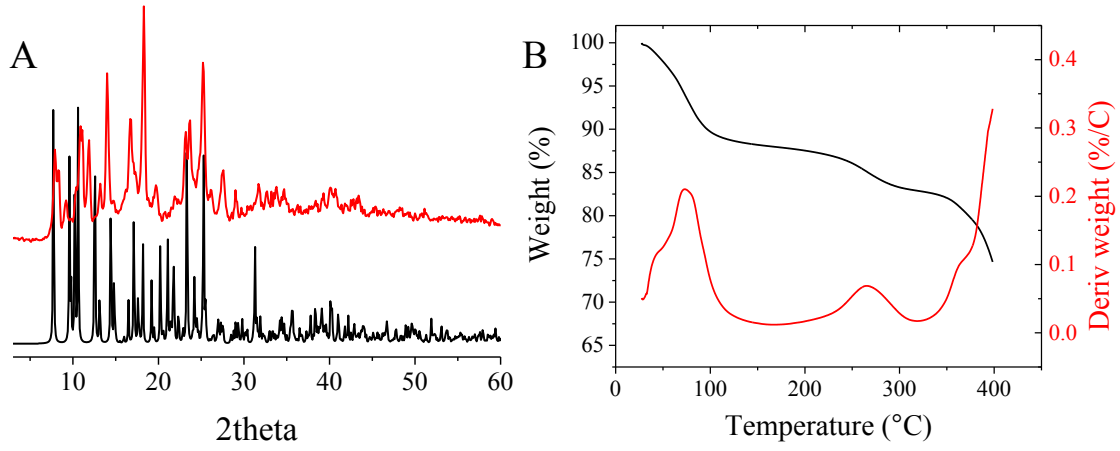

Figure 3.S4. (A) Powder pattern of **(1)** simulated (black) and after methanol exchange (red). (B) TG curve of **(1)-MeOH**.

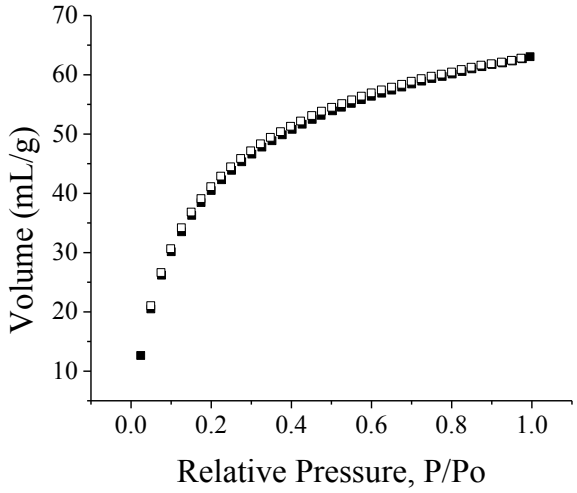

Figure 3.S5. CO_2 isotherm at 273 K of **(1)-MeOH**. Adsorption: closed symbols; desorption: open symbols. The BET and Langmuir surface areas were 206 and 353 m^2/g, respectively.

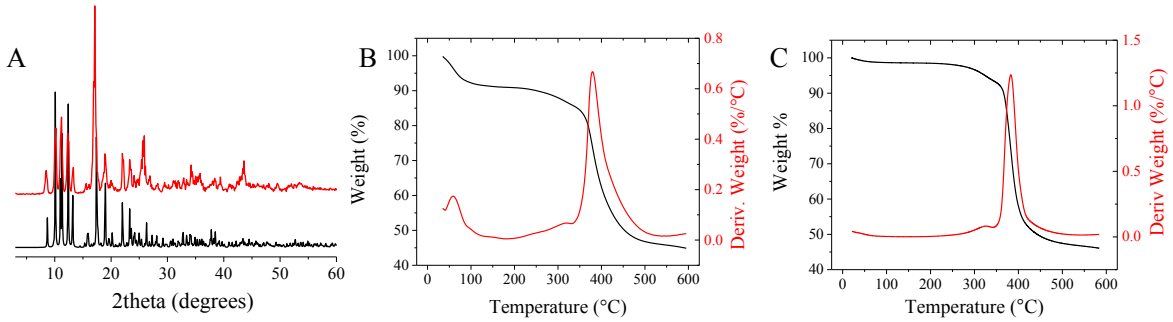

Figure 3.S6. (A) Powder pattern of **(2)** simulated (black) and after methanol exchange (red). (B) TG curve of **(2)-MeOH**. (C) TG curve of **(2)-MeOH** after evacuation at 90 °C for 5 h.

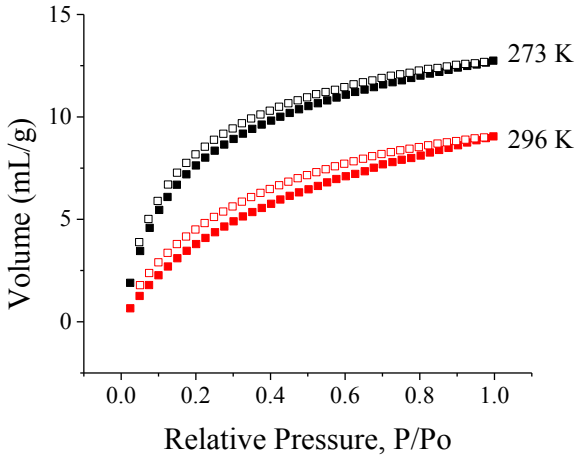

Figure 3.S7. CO_2 isotherms at 273 K (black) and 296 K (red) of **(2)-MeOH**. Adsorption: closed symbols; desorption: open symbols.

3.7.4 Experimental fits of isotherm data

3.7.4.1 Analysis of Gas sorption isotherms: Clausius-Clapeyron. The Clausius-Clapeyron equation[35] (3.S1) was applied via the following steps to determine the enthalpy of adsorption for CO_2, Q_{st}, as a function of quantity of gas adsorbed:

$$ln\left(\frac{P_1}{P_2}\right) = \frac{Q_{st}}{R} \times \left(\frac{T_2 - T_1}{T_1 T_2}\right) \quad (3.S1)$$

where P_i is the pressure for isotherm *i,* T_i is the temperature for isotherm *i*, and $R = 8.315\, J\, K^{-1} mol^{-1}$.

The isotherm data was fit to the Langmuir-Freundlich equation[41-43] (3.S2) in order to determine the pressure as a function of amount of gas adsorbed:

$$\frac{Q}{Q_m} = \frac{BP^{(1/t)}}{1 + BP^{(1/t)}} \quad (3.S2)$$

where Q is the moles gas adsorbed, Q_m is the moles adsorbed at saturation, P is pressure, B is an affinity constant, and t is an index of heterogeneity ((1/t)=1 for homogeneous material; 0 < (1/t) <1 for heterogeneous material).

With rearrangement to solve for pressure, Equation (3.S2) gives

$$P = \left(\frac{Q/Q_m}{B - B \times Q/Q_m}\right)^t \quad (3.S3)$$

which is substituted into (3.S1) to obtain:

$$Q_{st} = \frac{RT_1T_2}{T_2 - T_1} \times \ln \frac{\left(\frac{Q/Q_{m1}}{B_1 - B_1 \times Q/Q_{m1}}\right)^t}{\left(\frac{Q/Q_{m2}}{B_2 - B_2 \times Q/Q_{m2}}\right)^t} \quad (3.S4)$$

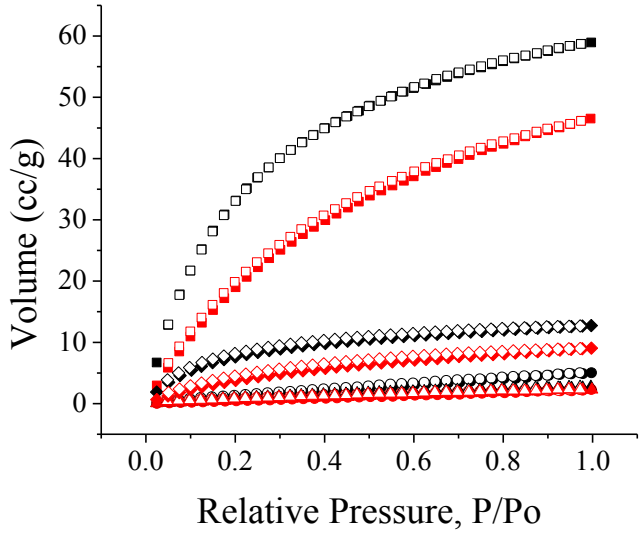

Figure 3.S8. CO_2 isotherms at 273 K (black) and 296 K (red) of **(1)** (squares), **(2)** (triangles), **(2)-MeOH** (diamonds) and MOF-69C (circles). Adsorption: closed symbols; desorption: open symbols.

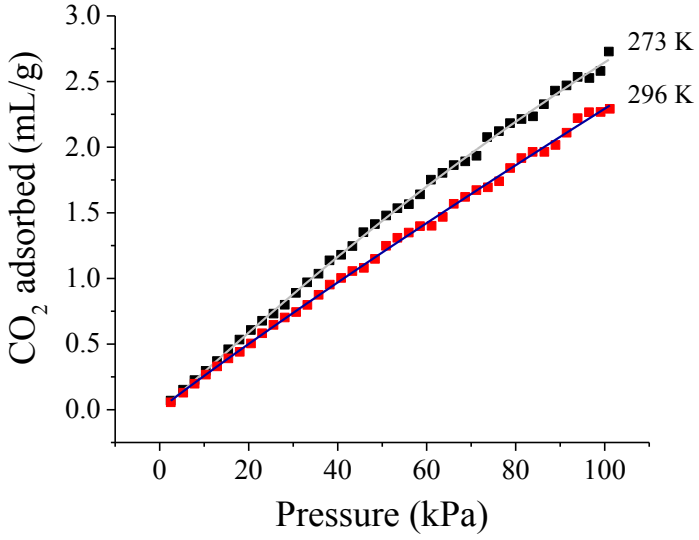

Figure 3.S9. Langmuir-Freundlich fits (solid lines) of the CO_2 isotherms for **(2)** at 273 K (black squares) and 296 K (red squares).

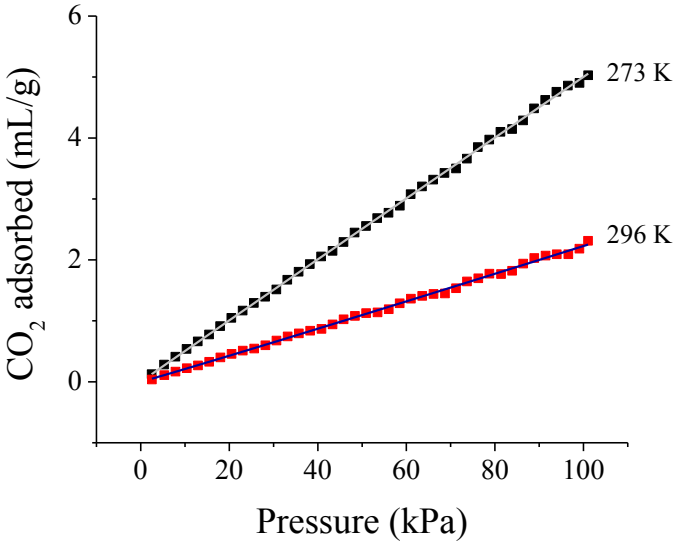

Figure 3.S10. Langmuir-Freundlich fits (solid lines) of the CO_2 isotherms for MOF-69C at 273 K (black squares) and 296 K (red squares).

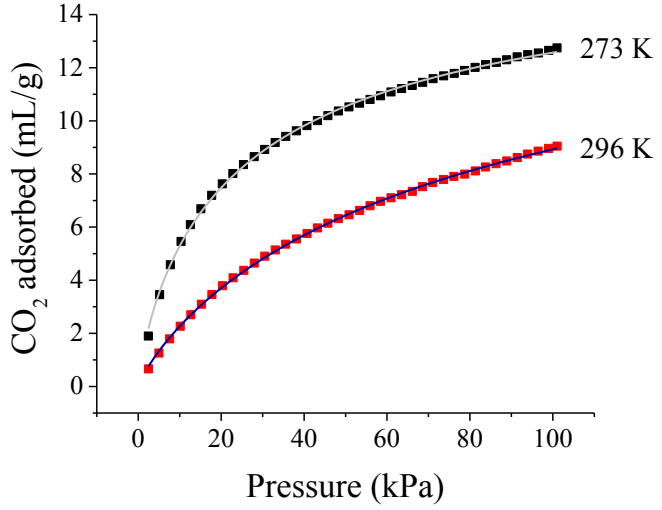

Figure 3.S11. Langmuir-Freundlich fits (solid lines) of the CO_2 isotherms for **(2)-MeOH** at 273 K (black squares) and 296 K (red squares).

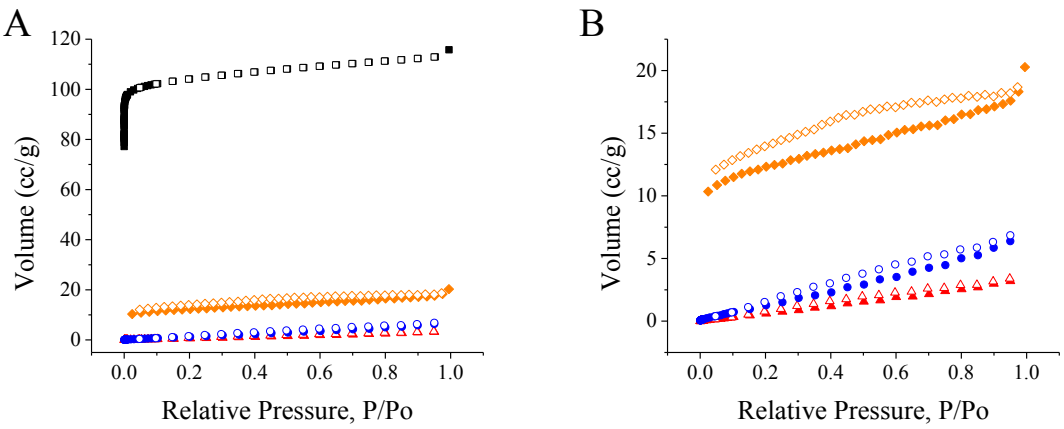

Figure 3.S12. N_2 sorption isotherms at 77 K for **(1)** (black squares), **(2)** (red triangles), **(2)-MeOH** (orange diamonds), and MOF-69C (blue circles); (A) shows all MOFs; (B) shows zoom of lower volume adsorption. Adsorption: closed symbols; desorption: open symbols.

Table 3.S5. Summary of the parameters from Langmuir-Freundlich fit of CO_2 isotherm data at the designated temperature.

273 K				
MOF	**K_F**	**t**	**Q_m**	**R^2**
(1)	0.0459	1.0713	75.9879	0.99984
(2)	0.00167	1	18.5648	0.99896
(2)-MeOH	0.0718	1.25046	16.97216	0.9989
MOF-69C	5.716×10^{-5}	1	880.3156	0.99957
296 K				
MOF	**K_F**	**t**	**Q_m**	**R^2**
(1)	0.0179	1.0325	76.0654	0.99996
(2)	0.000442	1.0383	63.8200	0.99868
(2)-MeOH	0.02136	1.16951	17.07221	0.99961
MOF-69C	1.018×10^{-7}	1	217106	0.99814

3.7.4.2 Analysis of Gas sorption isotherms: Virial Equation. In order to analyze the zero-coverage heat of adsorption (Q_{st}^0), the temperature dependent isothermal data was fit to a virial-type equation (Equation 3.S5),[7,44]

$$\ln P = \ln N + \frac{1}{T}\sum_{i=0}^{m} a_i N^i + \sum_{i=0}^{n} b_i N^i \quad (3.S5)$$

where P is the pressure, N is the amount of CO_2 adsorbed, T is the temperature, m and n are the number of virial coefficients required for fitting, and a and b are virial coefficients. Since this is an empirical model, the number of coefficients can be adjusted to best fit the data. However, the higher number of terms used will introduce an undesired curvature between data points and will produce physically meaningless coefficients. There is, therefore, a point after which adding more coefficients will not have any practical improvement in the description of the data and will hurt the validity of the data fit along with any parameters obtained from it. Adsorption data for **(1)**, **(2)**, **(2)-MeOH** and MOF69-C was fitted using 4, 3, 4, and 3 parameters, respectively. This increases accuracy of the physical meaning of the parameters obtained and it agrees with the good fit that can be obtained from the Langmuir equation, suggesting that there are no higher order interactions among molecules and between the molecules and the surface.

That said, the virial fits produced multiple local minima that result in a satisfactory fit to the experimental data. Therefore, the quantity obtained for Q_{st}^0 was dependent on the initial guess for the fitting parameters. The initial guesses entered for the virial fits were based on that calculated via analysis by the Clausius-Clapeyron equation for Q_{st} at the onset of adsorption and the initial slopes of the isothermal data for K_H (**e.g. Figure 3.S17**), which directly related to the virial parameter b_o via the following relations:

$$K_H = K_0 exp\left(\frac{q_0}{Rt}\right) \quad (3.S6)$$

$$K_0 = \exp(-b_0) \quad (3.S7)$$

The results of the fits are provided below (**Figure 3.S13-S16**).

3.7.4.2.1 Fitting Analysis for (1)

Virial Fit Equation:

$$lnP = lnv + \frac{1}{T}(a_o + a_1 v + a_2 v^2) + b_0 \quad (3.S8)$$

Parameters:

Parameters	Fit
a0	−3,325.1161
a1	0.8207
a2	0.1078
b0	11.1515

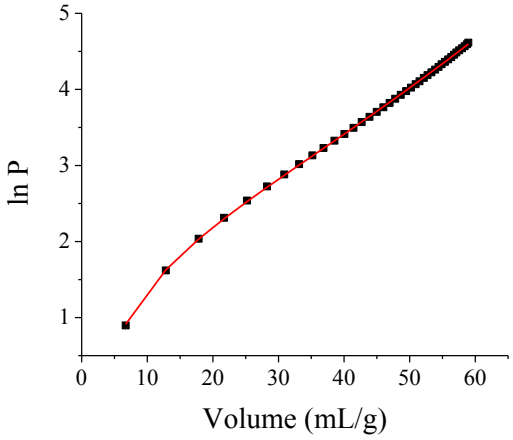

Figure 3.S13. Virial equation fit (solid red line) to the CO_2 isotherm for **(1)** at 273 K (black squares).

3.7.4.2.2 Fitting Analysis for (2)

Virial Fit Equation:

$$lnP = lnv + \frac{1}{T}(a_o + a_1 v) + b_0 \quad (3.S9)$$

Parameters:

Parameters	Fit
a0	−322.8803
a1	10.7022
b0	4.8667

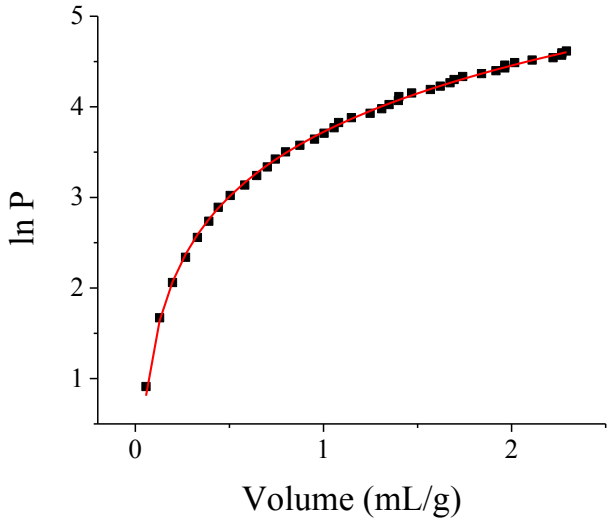

Figure 2.S14. Virial equation fit (solid red line) to the CO_2 isotherm for **(2)** at 273 K (black squares).

3.7.4.2.3 Fitting Analysis for (2)-MeOH

Virial Fit Equation:

$$lnP = lnv + \frac{1}{T}(a_o + a_1 v + a_2 v^2) + b_0 \quad (3.S10)$$

Parameters:

Parameters	Fit
a0	−4,016.852
a1	15.375
a2	2.143
b0	14.818

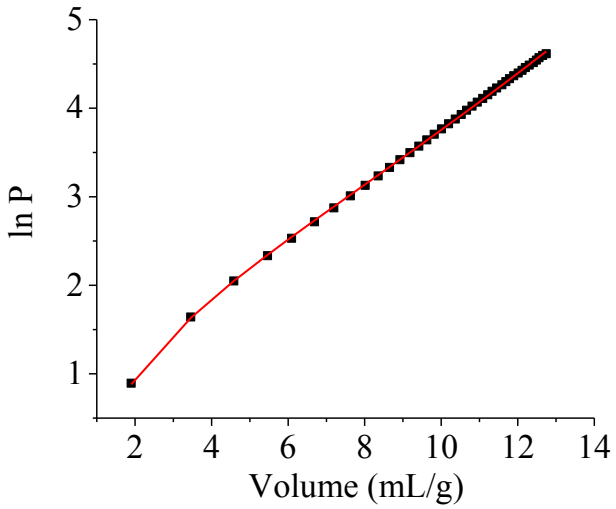

Figure 3.S15. Virial equation fit (solid red line) to the CO_2 isotherm for **(2)-MeOH** at 273 K (black squares).

3.7.4.2.4 Fitting Analysis for MOF-69C

Virial Fit Equation:

$$lnP = lnv + \frac{1}{T}(a_o + a_1 v) + b_0 \quad (3.S11)$$

Parameters:

Parameters	Fit
a0	−2,117.1260
a1	1.6729
b0	10.7266

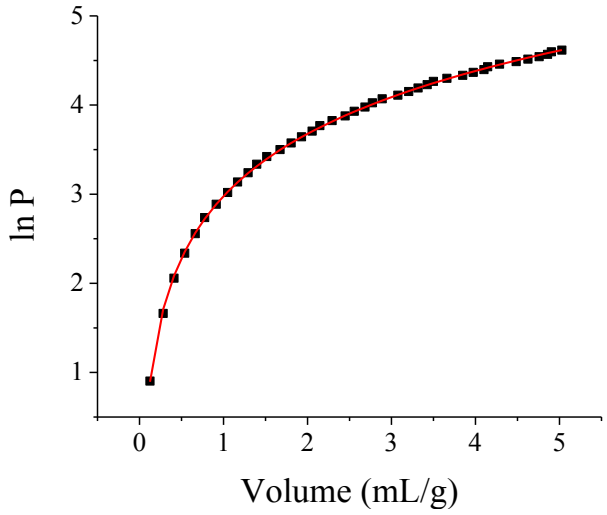

Figure 3.S16. Virial equation fit (solid red line) to the CO_2 isotherm for MOF-69C at 273 K (black squares).

3.7.5 Selectivity of (1)

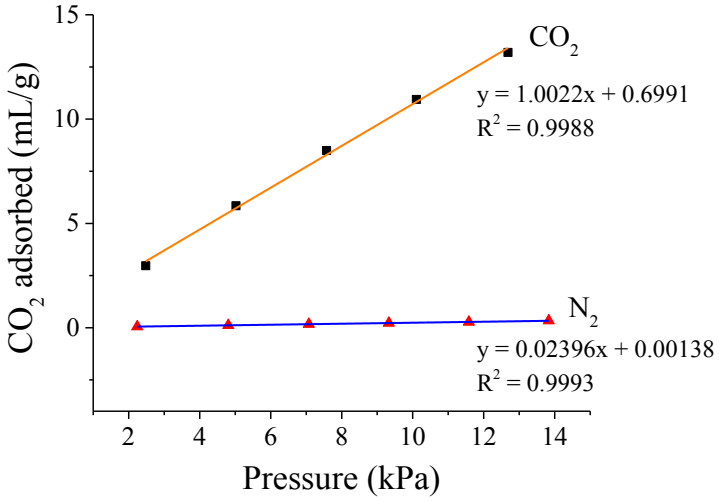

Figure 3.S17. The fitting of the initial slope of **(1)** adsorption isotherms at 296 K with CO_2 (black squares) and N_2 (red triangles).

3.8 References

(1) Rosi, N. L.; Eddaoudi, M.; Kim, J.; O'Keeffe, M.; Yaghi, O. M. *CrystEngComm* **2002**, *4*, 401.

(2) Rowsell, J. L. C.; Yaghi, O. M. *Microporous Mesoporous Mater.* **2004**, *73*, 3.

(3) Eddaoudi, M.; Jaheon, K.; Rosi, N.; Vodak, D.; Wachter, J.; O'Keeffe, M.; Yaghi, O. M. *Science* **2002**, *295*, 469.

(4) Rosi, N. L.; Eckert, J.; Eddaoudi, M.; Vodak, D. T.; Kim, J.; O'Keeffe, M.; Yaghi, O. M. *Science* **2003**, *300*, 1127.

(5) Collins, D. J.; Zhou, H.-C. *J. Mater. Chem.* **2007**, *17*, 3154.

(6) Suh, M. P.; Park, H. J.; Prasad, T. K.; Lim, D.-W. *Chem. Rev.* **2011**, *112*, 782.

(7) Sumida, K.; Rogow, D. L.; Mason, J. A.; McDonald, T. M.; Bloch, E. D.; Herm, Z. R.; Bae, T.-H.; Long, J. R. *Chem. Rev.* **2012**, *112*, 724.

(8) Kaye, S. S.; Long, J. R. *J. Am. Chem. Soc.* **2005**, *127*, 6506.

(9) Lee, J. Y.; Farha, O. K.; Roberts, J.; Scheidt, K. A.; Nguyen, S. B. T.; Hupp, J. T. *Chem. Soc. Rev.* **2009**, *38*, 1450.

(10) Valvekens, P.; Vermoortele, F.; De Vos, D. *Catal. Sci. Technol.* **2013**, *3*, 1435.

(11) Kreno, L. E.; Leong, K.; Farha, O. K.; Allendorf, M.; Van Duyne, R. P.; Hupp, J. T. *Chem. Rev.* **2012**, *112*, 1105.

(12) Huxford, R. C.; Della Rocca, J.; Lin, W.-B. *Curr. Opin. Chem. Biol.* **2010**, *14*, 262.

(13) Zhuang, J.; Kuo, C.-H.; Chou, L.-Y.; Liu, D.-Y.; Weerapana, E.; Tsung, C.-K. *ACS Nano* **2014**, *8*, 2812.
(14) Jeazet, H. B. T.; Staudt, C.; Janiak, C. *Chem. Commun.* **2012**, *48*, 2140.
(15) David, O. C.; Gorri, D.; Urtiaga, A.; Ortiz, I. *J. Membr. Sci.* **2011**, *378*, 359.
(16) Schrock, R. R. *Proc. Nat. Acad. Sci.* **2006**, *103*, 17087.
(17) Earth System Research Laboratory: http://www.esrl.noaa.gov/gmd/ccgg/trends/, 2014.
(18) Yang, R. T. *Adsorbents: Fundamentals and Applications*; John Wiley & Sons, Inc., 2003.
(19) Wang, K.; Feng, D.; Liu, T.-F.; Su, J.; Yuan, S.; Chen, Y.-P.; Bosch, M.; Zou, X.; Zhou, H.-C. *J. Am. Chem. Soc.* **2014**, *136*, 13983.
(20) Yang, S.; Sun, J.; Ramirez-Cuesta, A. J.; Callear, S. K.; DavidWilliam, I. F.; Anderson, D. P.; Newby, R.; Blake, A. J.; Parker, J. E.; Tang, C. C.; Schröder, M. *Nat Chem* **2012**, *4*, 887.
(21) D'Alessandro, D. M.; Smit, B.; Long, J. R. *Angew. Chem., Int. Ed.* **2010**, *49*, 6058.
(22) McDonald, T. M.; D'Alessandro, D. M.; Krishna, R.; Long, J. R. *Chem. Sci.* **2011**, *2*, 2022.
(23) Si, X.; Jiao, C.; Li, F.; Zhang, J.; Wang, S.; Liu, S.; Li, Z.; Sun, L.; Xu, F.; Gabelica, Z.; Schick, C. *Energy Environ. Sci.* **2011**, *4*, 4522.
(24) An, J.; Geib, S. J.; Rosi, N. L. *J. Am. Chem. Soc.* **2010**, *132*, 38.
(25) Arstad, B.; Fjellvaag, H.; Kongshaug, K. O.; Swang, O.; Blom, R. *Adsorption* **2008**, *14*, 755.
(26) Cui, P.; Ma, Y.-G.; Li, H.-H.; Zhao, B.; Li, J.-R.; Cheng, P.; Balbuena, P. B.; Zhou, H.-C. *J. Am. Chem. Soc.* **2012**, *134*, 18892.
(27) Yazaydin, A. O.; Snurr, R. Q.; Park, T.-H.; Koh, K.; Liu, J.; LeVan, M. D.; Benin, A. I.; Jakubczak, P.; Lanuza, M.; Galloway, D. B.; Low, J. J.; Willis, R. R. *J. Am. Chem. Soc.* **2009**, *131*, 18198.
(28) Rosi, N. L.; Kim, J.; Eddaoudi, M.; Chen, B.; O'Keeffe, M.; Yaghi, O. M. *J. Am. Chem. Soc.* **2005**, *127*, 1504.
(29) CrysAlisPro Software system, v., Agilent Technologies, 2011, Agilent Technologies UK Ltd. Oxford, UK.
(30) Sheldrick, G. M. *Acta. Cryst.* **2008**, *A64*, 112.
(31) Dolomanov, O. V.; Bourhis, L. J.; Gildea, R. J.; Howard, J. A. K.; Puschmann, H. *J. Appl. Crystallogr.* **2009**, *42*, 339.
(32) Macrae, C. F. E., P. R.; McCabe, P.; Pidcock, E.; Shields, G. P.; Taylor, R.; Towler, M.; van de Streek, J. *J. Appl. Cryst.* **2006**, *39*, 453.
(33) Brunauer, S.; Emmett, P. H.; Teller, E. *J. Am. Chem. Soc.* **1938**, *60*, 309.
(34) Langmuir, I. *J. Am. Chem. Soc.* **1932**, *54*, 2798.
(35) Lowell, S., Shields, J.E., Thomas, M.A., Thommes, M. *Characterization of Porous Solids and Powders: Surface Area, Pore Size and Density*; Kluwer Academic, 2004.
(36) Li, Z.-G.; Wang, G.-H.; Jia, H.-Q.; Hu, N.-H.; Xu, J.-W.; Batten, S. R. *CrystEngComm* **2008**, *10*, 983.
(37) Loiseau, T.; Muguerra, H.; Ferey, G.; Haouas, M.; Taulelle, F. *J. Solid State Chem.* **2005**, *178*, 621.
(38) Nugent, W. A.; Haymore, B. L. *Coord. Chem. Rev.* **1980**, *31*, 123.
(39) Sharma, A.; Kaur, S.; Mahajan, C. G.; Tripathi, S. K.; Saini, G. S. S. *Mol. Phys.* **2007**, *105*, 117.
(40) Hausdorf, S.; Wagler, J.; Mossig, R.; Mertens, F. O. R. L. *J. Phys. Chem. A* **2008**, *112*, 7567.
(41) Yang, R. T. *Gas Separation By Adsorption Processes*; Buttersworth: Boston, 1987.
(42) Jeppu, G. P.; Clement, T. P. *J. Contam. Hydrol.* **2012**, *129-130*, 46.

(43) Turiel, E.; Perez-Conde, C.; Martin-Esteban, A. *Analyst* **2003**, *128*, 137.
(44) Czepirski, L.; Jagiello, J. *Chem. Eng. Sci.* **1989**, *44*, 797.
(45) Valenzano, L.; Civalleri, B.; Sillar, K.; Sauer, J. *J. Phys. Chem. C* **2011**, *115*, 21777.
(46) Mondloch, J. E.; Karagiaridi, O.; Farha, O. K.; Hupp, J. T. *CrystEngComm* **2013**, *15*, 9258.
(47) Choi, J.-S.; Son, W.-J.; Kim, J.; Ahn, W.-S. *Microporous Mesoporous Mater.* **2008**, *116*, 727.
(48) Mu, B.; Schoenecker, P. M.; Walton, K. S. *J. Phys. Chem. C* **2010**, *114*, 6464.

4. Structure dependent conductivity investigations using electrochemical impedance spectroscopy with Zn-based MOFs

S.R. Ahrenholtz, B.E. Kidd, L.A. Madsen, and A.J. Morris

4.1 Motivation and Abstract

Charge transport through a metalloporphyrin-based framework has been previously investigated (Chapter 2) and attributed to a redox hopping mechanism, where electrons hop between adjacent redox centers (Co metal nodes) of the metal-organic framework (MOF). A requirement of this mechanism of transport is the proximity of these redox centers to each other, as well as their ability to undergo redox transitions. Therefore, changing the properties of the MOF components will affect the mechanism of charge transport throughout the framework. Because of these interesting results, we wanted to investigate the conduction mechanism in frameworks containing redox inactive metal centers, which would eliminate a possible mechanism involving the metal. A series of structurally similar Zn^{II}-based MOFs have been prepared and investigated for their conductive properties to determine the relationship between framework structure and connectivity to charge transport. Specifically, two MOFs containing 5- and 6-coordinate Zn(II) metal centers by 2,5-pyridinedicarboxylic acid (pydc) linker molecules with molecular formulas of $Zn_4(pydc)_4(DMF)_2 \cdot 3DMF$ **(1)** and $Zn_2(pydc)_2(DEF)$ **(2)** were prepared and compared with previously reported MOF-69C, $Zn_3(OH)_2(bdc)_2 \cdot 2DEF$ (bdc = 1,4-benzenedicarboxylic acid), to understand the dependence of conductivity on the framework structure. Electrochemical impedance spectroscopy was employed to study the conductivity of

the Zn-based MOFs. The room temperature conductivity values for MOFs **(1)**, **(2)**, and MOF-69C were found to be $3.6 \pm 0.3 \times 10^{-6}$ S cm^{-1}, $1.35 \pm 0.03 \times 10^{-6}$ S cm^{-1}, and $1.8 \pm 0.2 \times 10^{-6}$ S cm^{-1}, respectively. The presence of free solvent molecules within the internal void space as well as bound to the metal centers provided an extended network for charge transport and facilitated increased conductivity. Temperature dependent conductivity and differential scanning calorimetry studies revealed that MOF-69C undergoes a solid-solid phase transition at ~46 °C. These results were correlated with variable temperature solid-state NMR to reveal that the DEF solvate molecules play an active role in the mechanism of conduction.

4.2 Introduction

Metal-organic frameworks (MOFs) are porous, crystalline materials comprising multi-dentate linker molecules coordinated to metal nodes forming extended multidimensional networks.[1,2] These materials possess a wide range of chemical and structural properties as well as high degree of synthetic tunability, which can be used to obtain frameworks with specific properties and functionalities. Because of their large accessible internal surface area, MOFs have been explored for applications in gas sorption,[3-6] drug delivery,[7-9] and catalysis.[10,11]

More recently, MOFs have been designed to facilitate charge transport and mobility throughout their structure.[12,13] Incorporation of charge transport ability into tailorable, porous frameworks can lead to novel materials with potential applications in areas such as batteries, electronics, and sensors.[14-16] However, due to their inherent design and original intended applications in gas storage, MOFs traditionally have insignificant overlap between the linker π orbitals and the metal d orbitals. As a result, electron transport is facilitated through a redox

hopping mechanism,[12,17] linker-mediated transport,[18] or guest interactions within the MOF pores[19,20] rather than a delocalized conduction band. The reports of electronically conductive MOFs in the literature have been sporadic until the last few years. One such report presents a series of porous metal-triazolate frameworks ($M(C_2N_3H_2)_2$, where M=Mg, Mn, Fe, Co, Cu, or Zn), where only the Fe(II) analog displayed electronic conductivity on the order of 10^{-5} S cm^{-1}.[21] In this framework, conduction likely occurs via hopping between low-spin Fe^{II} centers in close proximity.[21,22] Doping the framework with I_2 resulted in the oxidation of the Fe^{II} centers to Fe^{III}, which increased conductivity by two orders of magnitude and confirmed the activity of the metal center on charge conduction. Another example is based on a microporous Cu(II) framework comprised of Ni(II)pyrazine-dithiolate ($Ni(pdt)_2$) linker molecules, $Cu[Ni(pdt)_2]$, where the framework itself displayed poor conductivity (1×10^{-8} S cm^{-1}).[23] Again, with doping of I_2, the MOF demonstrated a marked increase in conductivity (10^{-4} S cm^{-1}) due to partial oxidation of the ($Ni(pdt)_2$) to generate unpaired electrons as mobile charge carriers.[23]

These results demonstrate that the nature of the metal centers, linkers, dopants, and internal pore space can directly affect conductivity, which provides the basis for the rational design of MOFs with increased conductivity.[20,21,23-27] However, the effect of the framework structure on the electronic and ionic conductivity has received limited attention. Herein, the investigation of structure-dependent conductivity is realized with a series of three Zn-based MOFs containing different metal-ligand connectivity and 3D orientation. Two of the frameworks consist of 2,5-pyridinedicarboxylate (pydc) linker molecules connected to Zn(II) metal centers in a 1D chain, $Zn_4(pydc)_4(DMF)_2 \cdot 3DMF$ **(1)** and $Zn_2(pydc)_2(DEF)$ **(2)** with bound DMF or DEF solvent molecules, respectively.[6] These MOFs were compared to the known MOF-69C, whose

framework consists of 1,4-benzenedicarboxylate (bdc) linker molecules, which contains DEF solvate molecules inside the pores.[28] Frameworks **(1)** and **(2)** contain an additional linker-metal coordination mode via the pyridine nitrogen atom, which is absent in MOF-69C and whose coordination sites are occupied solely by carboxylate groups. In addition, MOF-69C was found to undergo a solid-to-solid phase transition at ~46 °C, which was attributed to rotation of the carbonyl carbon of the formamide group of DEF solvate. The temperature of this transition correlates with increase in conductivity of the framework, which suggests that solvent molecules are involved in the conduction mechanism.

4.3 Experimental

4.3.1 Materials. The following reagents and solvents were purchased from the indicated commercial suppliers and used without further purification unless otherwise specified: zinc(II) nitrate hexahydrate ($Zn(NO_3)_2 \cdot 6H_2O$, Sigma-Aldrich, 98%); 2,5-pyridinedicarboxylic acid (pydc; Aldrich, 98%); 1,4-benzenedicarboxylic acid (bdc; Acros, 99%); *N,N*-dimethylformamide (DMF; Spectrum, spectrophotometric grade); *N,N*-diethylformamide (DEF; Acros, 99%).

4.3.2 Synthesis of $Zn_4(pydc)_4(DMF)_2 \cdot 3DMF$ (1).[6] In a 20 mL vial, $Zn(NO_3)_2 \cdot 6H_2O$ (250 mg, 0.840 mmol) was dissolved in DMF (10 mL). Solid 2,5-pyridinedicarboxylic acid (144 mg, 0.862 mmol) was added to the vial and sonicated until turbid. The reaction mixture was heated at 100 °C in an oven for 2 d. A vial containing colorless prisms was removed from the oven while hot and allowed to cool to RT. The crystals were collected via vacuum filtration and rinsed with DMF.

4.3.3 Synthesis of $Zn_2(pydc)_2(DEF)$ (2).[6] In a 20 mL vial, $Zn(NO_3)_2 \cdot 6H_2O$ (177 mg, 0.596 mmol) was dissolved in DEF (4.883 mL) followed by the addition of 2,5-pyridinedicarboxylic acid (33 mg, 0.197 mmol) and deionized water (0.177 mL). The vial was capped and sonicated until all the starting material was dissolved and heated at 75 °C in an oven for 3 d. A vial containing colorless parallelepipeds was removed from the oven while hot and allowed to cool to RT. The crystals were collected via vacuum filtration and rinsed with DEF.

4.3.4 Synthesis of MOF-69C: $Zn_3(OH)_2(bdc)_2 \cdot 2DEF$.[28] In a 20 mL vial, $Zn(NO_3)_2 \cdot 6H_2O$ (177 mg, 0.596 mmol) and 1,4-benzenedicarboxylic acid (33 mg, 0.199 mmol) were dissolved in DEF (4.883 mL) by sonication. Deionized water (0.177 mL) was added to the reaction solution. The vial was capped, sonicated briefly, and heated at 100 °C in an oven for 24 h. The vial containing cubic crystals was removed from the oven while hot and allowed to cool to RT. The crystals were collected via vacuum filtration and rinsed with DEF.

4.3.5 Powder X-Ray diffraction (PXRD). PXRD experiments were performed on a Rigaku MiniFlex 600 with Cu(Kα)- radiation (Cu-Kα = 1.5418 Å). The PXRD measurements were carried out over a 2θ range of 3-60° in continuous scanning mode (1°/min) with 0.1° resolution.

4.3.6 Differential Scanning Calorimetry (DSC). DSC was performed on the as-synthesized MOF powders using a TA Instruments Q2000. A heat/cool/heat procedure was applied to the sample with a temperature range of 0 to 100 °C at a rate of ± 10 °C/minute.

4.3.7 Electrochemical Impedance Spectroscopy (EIS). EIS was performed with a Solartron SI 1260 Impedance analyzer controlled with a PC interface and Zplot 2.9 software. The powdered sample was positioned between two brass electrodes to measure through-plane

conductivity using a Solartron 12960 sample holder with a built-in micrometer and a frequency range of 3.2 MHz to 100 Hz. The AC amplitude of 10 mV was applied with a frequency range of 1.6×10^7 – 0.01 Hz. The MOF conductivity was obtained using the high frequency intercept in the obtained Nyquist plot.

4.3.7.1 Bulk conductivity. For bulk conductivity measurements, the MOFs were synthesized as described above and dried under vacuum. The powders were pressed between the electrodes of the Solartron sample holder and the through plane conductivity was measured.

4.3.7.2 Temperature dependent conductivity. The MOFs were synthesized as described above and pressed into a pellet 13 mm in diameter. The pellet was painted on both sides with silver paint and annealed in a 40 °C oven for 5-10 minutes. The Ag-coated pellet was placed in a tube furnace with electrical connection and temperature was ramped from 22-80 °C at 2 °C/minute.

4.3.8 Variable Temperature ^{13}C Solid-State NMR (VT-SSNMR). All variable temperature (30 – 60 °C) solid-state NMR experiments were performed on a Bruker Avance III 300 MHz spectrometer using a 3.2 mm HXY probe. MOF-69C was packed into a 3.2 mm magic angle spinning (MAS) zirconia rotor and capped. Experiments were performed at 15 kHz spinning speeds at the magic angle (54.7°) so that no spinning side bands were observed. A short $\pi/2$ pulse of 1 μs was used in order to achieve uniform excitation and spectra were collected with 1024 scans with a relaxation delay of 3 s. Each temperature was allowed to equilibrate for 30 min prior to acquisition.

4.4 Results and Discussion

4.4.1 Synthesis and Structural Characterization

The frameworks **(1)** and **(2)** have been prepared and characterized previously.[6] They are composed of 5- and 6-coordinate Zn(II) metal centers bridged by a carboxylate oxygen atom of the pydc linker to form Zn-dimers (Figure 4.1A and B).[6] These dimers are connected via the 2- and 5-carboxylate oxygen atoms of two pydc ligand molecules. In addition, the sixth coordination site in one of the Zn metal centers for **(1)** and **(2)** is occupied by the oxygen atom of a DMF or DEF solvent molecule, respectively. The pores of **(1)** contain 3 DMF solvate molecules, whereas **(2)** has no solvents of crystallization.[6] MOF-69C has also been characterized previously and is composed of 1D chains of Zn-oxyhydroxide that are bridged by the 1,4-benzenedicarboxylate linker molecules (Figure 4.1C).[28] The pores of MOF-69C contain DEF solvate molecules that hydrogen bond via the oxygen atom to the μ_3-hydroxy of the Zn-oxyhydroxide chain.[29] The structural purity of the MOFs was determined by comparing the powder X-ray diffraction (PXRD) of the bulk sample with the simulated pattern from single crystal data (Figures 4.S1-3).

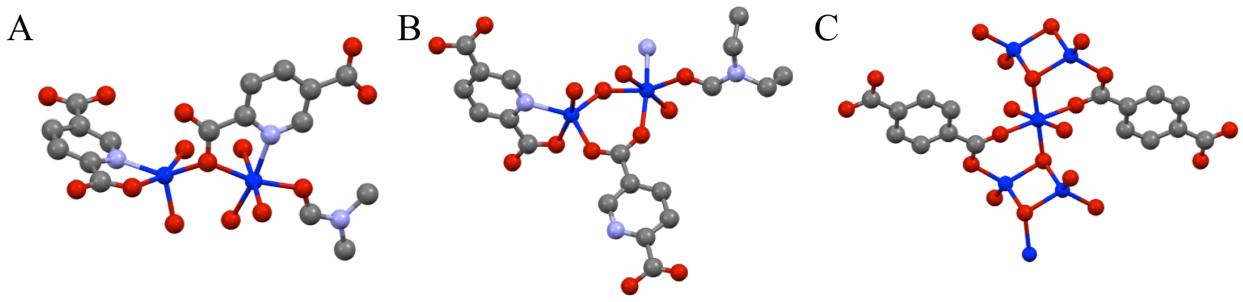

Figure 4.1. Zn-dimers of (A) **(1)** and (B) **(2)** displaying the 5- and 6-coordinate Zn metal centers with bound DMF and DEF, respectively;[6] (C) Zn-oxyhydroxy chains present in MOF-69C structure and the connectivity to the bdc linkers.[28] Hydrogen atoms have been omitted for clarity. Gray: C; Red: O; Light blue/gray: N; Blue: Zn.

4.4.2 Conductivity Investigations

Electrochemical impedance spectroscopy (EIS) is a common technique used to probe the electrical response of materials. In through-plane impedance measurements, the material is placed between two electrodes and an AC potential of fixed amplitude is applied with varying frequency.[30,31] The current output is measured and represented by a Nyquist plot, which displays the relationship between the real (Z') and imaginary (Z'') impedance components. The conductivity (σ) can be calculated via Equation 4.1,[30]

$$\sigma = \frac{d}{RS} \tag{4.1}$$

where d is sample thickness (cm), R is the resistance determined from the real component of impedance (Ω), and S is the surface area of the sample (cm^2). The Nyquist plots obtained for the MOFs are shown in Figure 4.2 and the conductivity values summarized in Table 4.1.

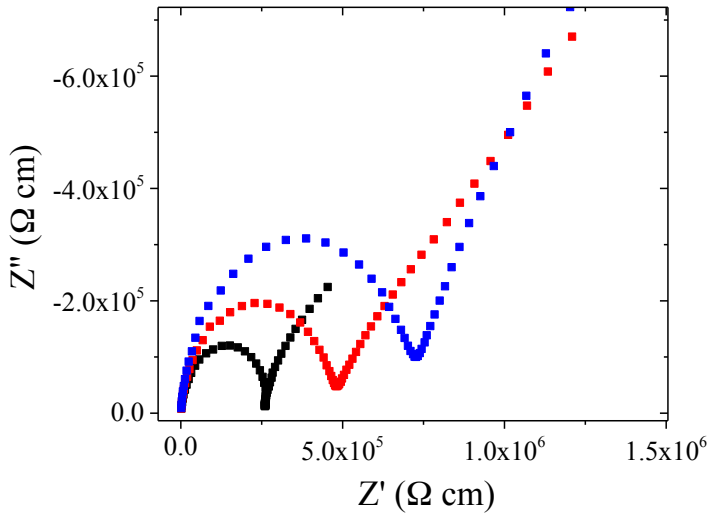

Figure 4.2. Nyquist plots of **(1)** (black), MOF-69C (red), and **(2)** (blue).

Table 4.1. Conductivity values for the MOF powders.

MOF	Conductivity ($\mu S\ cm^{-1}$)
(1)	3.6 ± 0.3
MOF-69C	1.8 ± 0.2
(2)	1.35 ± 0.03

An equivalent circuit can be developed and fit to the experimental data to compare the electrical response of the material to appropriate circuit components. For example, the impedance of polycrystalline materials can be described by an equivalent circuit consisting of two parallel resistor-capacitor series (circuit 1, Figure 4.3A inset), which gives a Nyquist plot with two semicircular arcs with their centers on the x-axis (Figure 4.3A). The microstructure of polycrystalline materials represents a heterogeneous system containing components with differing conducting properties. The two processes responsible for this impedance signature are grain and grain boundary resistances, represented by the x-intercept at high and low frequencies (ω), respectively.[31-35]

However, at lower frequencies, polycrystalline materials have been shown to deviate from the purely capacitive behavior, resulting in a broadening of the second arc of the Nyquist plot (Figure 4.3B).[36-39] The deformation of this arc can be represented by the substitution of the second capacitor in the equivalent circuit model with a constant phase element (CPE) (circuit 2, Figure 4.3B, inset).[36-39] This observed behavior, characterized by the CPE, has been attributed to surface disorder or inhomogeneity, specifically with porosity and the distribution of orientations characteristic of crystalline materials.[39-41]

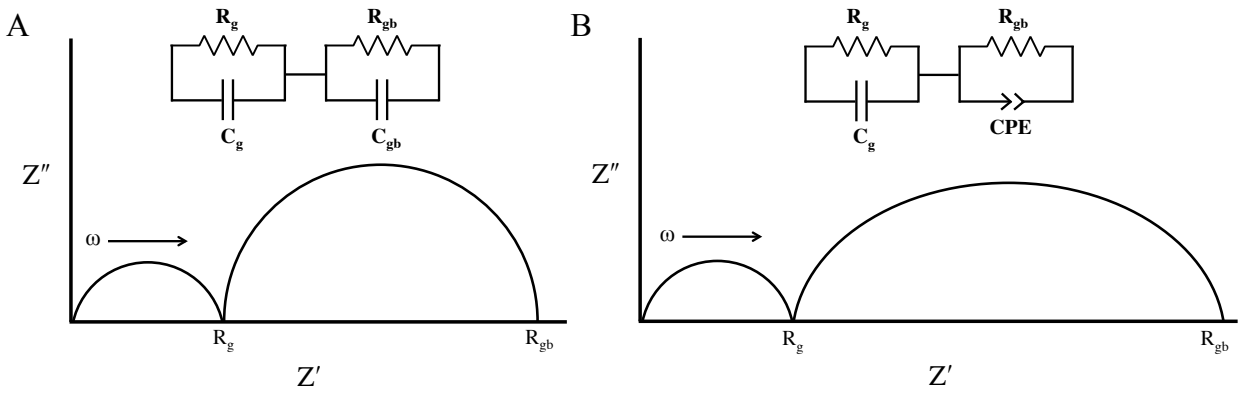

Figure 4.3. Nyquist plots of the impedance response for polycrystalline materials for (A) ideal capacitive behavior with the inset of the equivalent circuit 1; (B) deviations from ideal capacitive behavior with the inset of equivalent circuit 2. The high frequency intercept represents the grain resistance (R_g) while the low frequency intercept represents grain boundary resistance (R_{gb}).

The Nyquist plots of the frameworks were fit to each circuit (insets, Figure 4.3) and are shown in Figure 4.4. The fit of circuit 1, consisting of two parallel resistor-capacitor series (Figure 4.4, red lines), generates the two semicircular arcs as discussed above. This trend, however, does not accurately represent the data. Instead, the fitting of circuit 2, with substitution of the CPE for the second capacitor, results in an improved fit to the experimental data (Figure 4.4, blue lines). Both circuit models fit the first arc very well, suggesting that the first resistor-capacitor representing grain conductivity is accurate. However, the substitution of the CPE for the second capacitor results in a much better simulated fit to the experimental second arc, confirming deviations from the a true capacitor. Therefore, the microstructure of the frameworks indeed contains regions of with differing conduction properties, which are affected by surface inhomogeneities represented by the CPE.

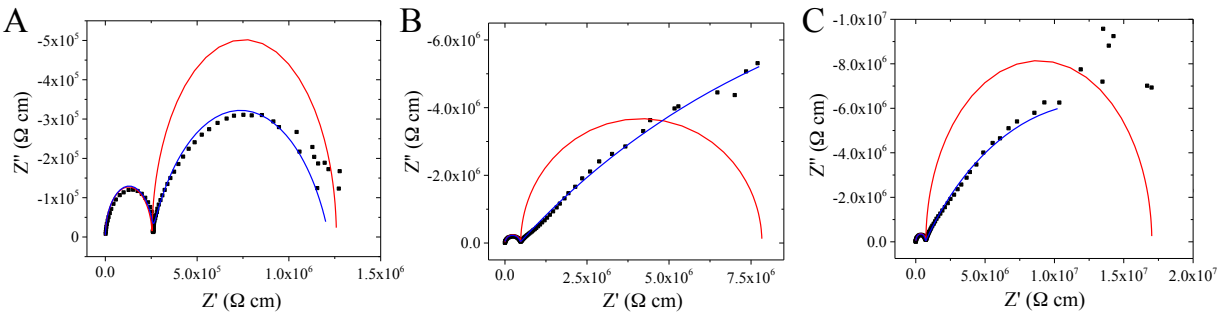

Figure 4.4. Nyquist plots of (A) **(1)**, (B) MOF-69C, and (C) **(2)** with fittings of equivalent circuit 1 (red) and circuit 2 (blue).

4.4.3. Mechanism of Conduction

There are several mechanisms which explain charge conduction within frameworks: (1) delocalized valence and conduction bands, which mediate migration of electrons and holes throughout crystalline materials;[42] (2) a redox hopping mechanism, where charge propagation can be facilitated through discrete electron donor/acceptor sites within materials containing redox available states;[12,17,18,42] (3) a through-bond approach where continuous binding networks between SBUs, either through M-linker bonds (i.e. M-N or S)[13,43] or via guest molecules,[19] facilitate a pathway for charge mobility throughout the framework; (4) conduction via through-space interactions, which utilizes π-π stacking of aromatic organic linker molecules.[44,45]

As the coordination in the MOFs investigated here is a carboxylate-metal bond, there is insufficient overlap between the π orbitals of the linker with the d metal orbitals to justify a band delocalization mechanism of conduction.[46] In addition, the redox hopping and linker-mediated mechanisms are not feasible for MOFs comprised of closed shell metals, such as Zn^{2+} and Zr^{4+}, as there are no available redox states and conduction through these nodes is precluded.

Therefore, the conduction observed in the Zn-based frameworks **(1)**, **(2)**, and MOF-69C is proposed to be a linker-to-linker mechanism facilitated by guest solvent molecules.

Framework **(1)**, which contains an extended network of DMF solvate molecules within the pores (Figure 4.5A, green) in addition to DMF bound to the Zn^{2+} metal center (Figure 4.5A, pink), displayed the greatest conductivity (3.6 ± 0.3 μS cm^{-1}).[6] Similarly, MOF-69C contains DEF solvate molecules in the pores (Figure 4.5B, green), which contribute to the mechanism of conduction (*vide infra*). Framework **(2)** has no solvents of crystallization and only contains DEF bound to the Zn^{2+} center (Figure 4.5C, pink). Therefore, **(2)** was found to be the least conductive of the frameworks investigated.

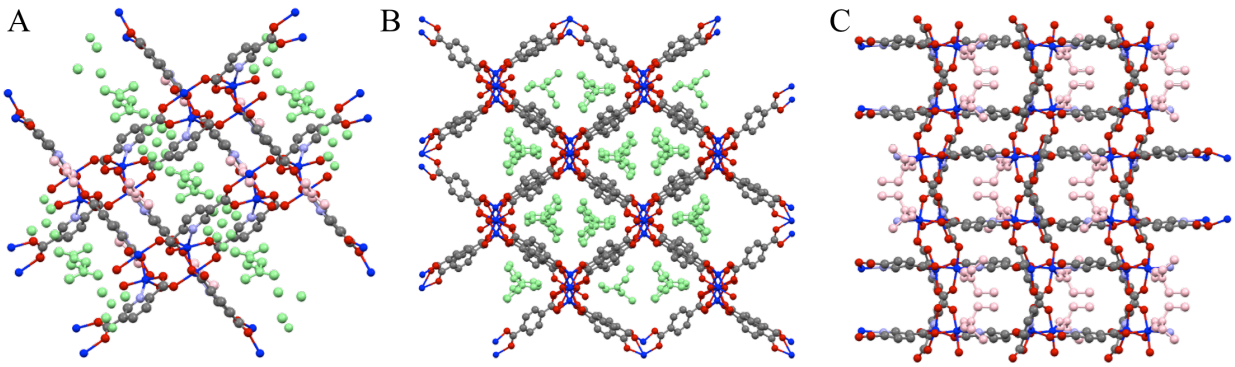

Figure 4.5. (A) View along the [010] axis of **(1)** displaying the DMF solvate molecules in green and bound DMF in pink;[6] (B) View along the [001] axis of MOF-69C displaying the DEF solvate molecules in green;[28] (C) View along the [100] axis of **(2)** displaying the bound DEF in pink.[6] Gray: C; Red: O; Light blue/gray: N; Blue: Zn. Hydrogen atoms have been omitted for clarity.

The conductivity of MOF-69C was investigated as a function of temperature (Figure 4.6, top). Upon heating, the conductivity was found to increase until ~45 °C followed by an abrupt decrease in conductivity at temperatures greater than 45 °C, suggesting a structural

transformation of the framework. Differential scanning calorimetry (DSC) was employed to probe possible causation of the observed temperature dependent conduction mechanism. Interestingly, MOF-69C was found to undergo a reversible first-order solid-to-solid phase transition with a peak centered at ~46 °C and an enthalpy change of 8.2 J g^{-1} (Figure 4.6, bottom).

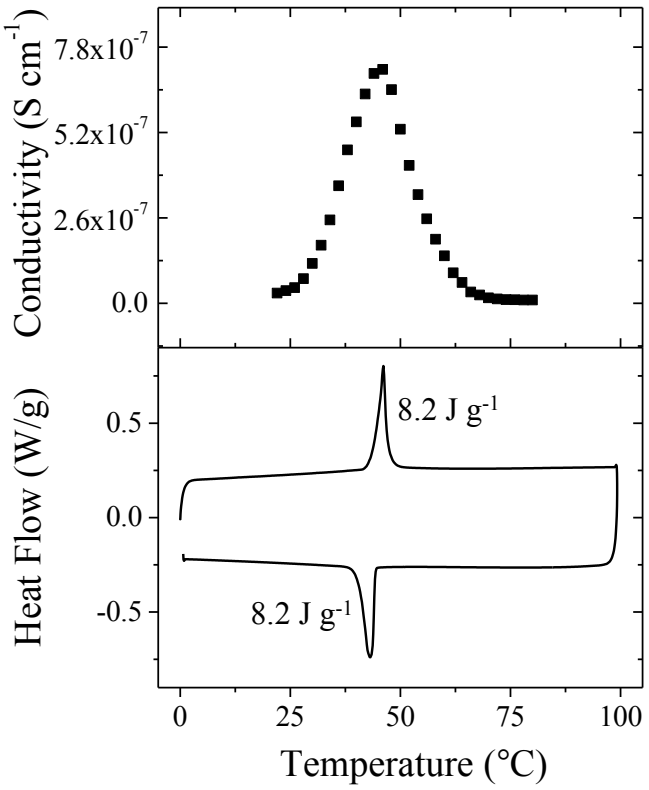

Figure 4.6. Top: Temperature dependent conductivity of MOF-69C; Bottom: DSC trace of MOF-69C.

To better understand how the solid-solid phase transition and conductivity measurement are correlated, variable temperature ^{13}C solid-state NMR (VT-SSNMR) was employed. ^{13}C

allows for onset of bond-specific rotations that may occur at the phase transition to be investigated (Figure 4.7).

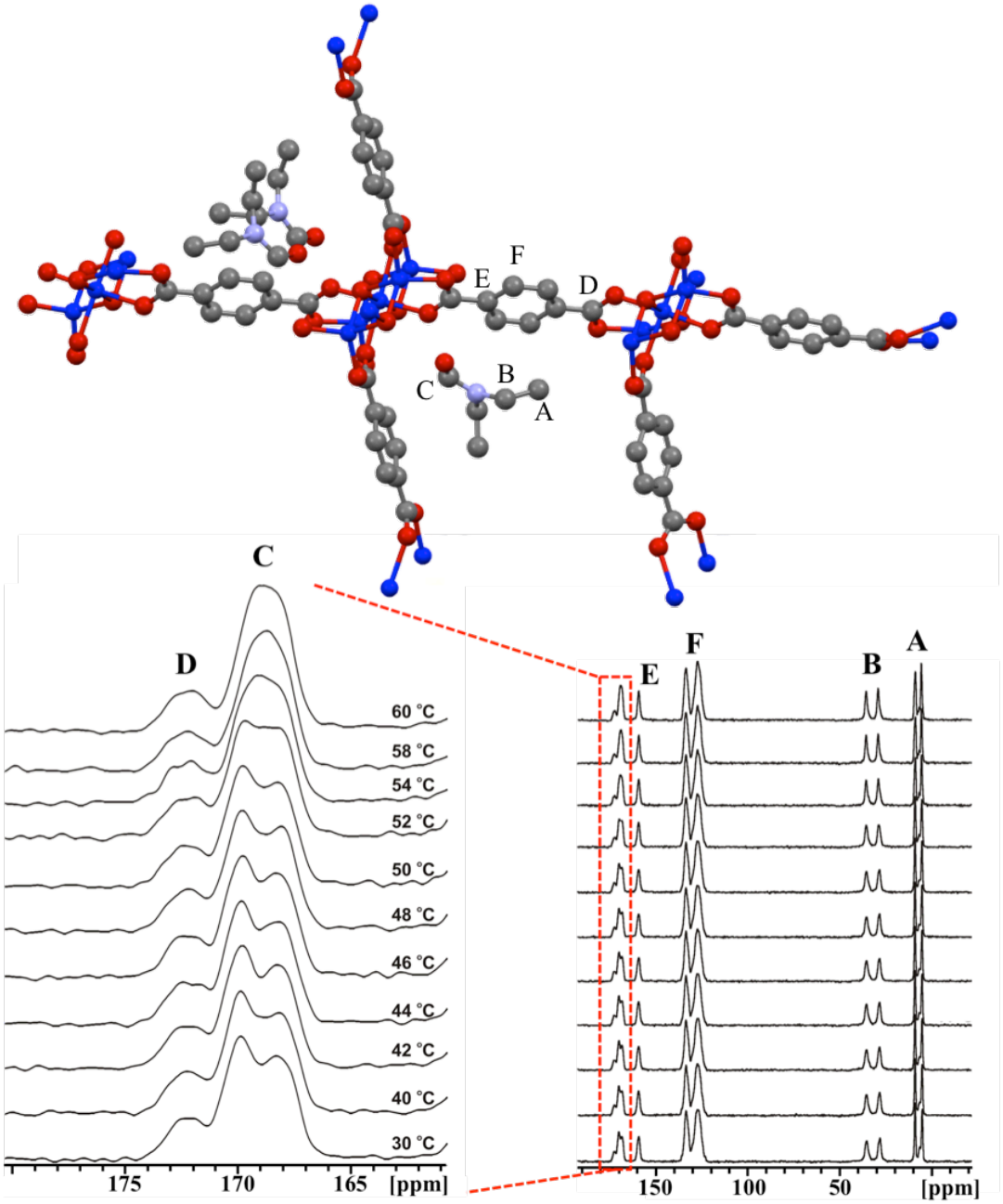

Figure 4.7. Variable temperature ^{13}C SSNMR of MOF-69C. The onset of rotational dynamics of the ^{13}C-H formamide group of DEF (signal C) is seen at ~54 °C, suggestive of an assisted conduction mechanism throughout the framework.

Figure 4.7 shows two resonances for signals A, B, C, D, and F, indicative of two unique environments within the MOF-69C crystal structure. Interestingly, signal C (^{13}C-H formamide functional group) reveals a gradual decrease in separation of the two resonances from 30 – 52 °C until ~54 °C, where a more abrupt change to a broad singlet is observed. These results suggest an onset of rotational dynamics about the formamide group of DEF that is faster than the MAS rotor spinning frequency (15 kHz) due to the crystalline lattice volume expansion at slightly elevated temperatures. This correlates well with the observed solid-solid phase transition. Since no other resonance demonstrates such dependence, the rapid increase in conductivity observed at the solid-solid phase transition is due to the onset of rotational dynamics of the formamide ^{13}C-H of DEF. Therefore, conduction throughout the framework can proceed via the network of adjacent DEF solvent molecules lining the pores, which are hydrogen bonded through the oxygen of the formamide function to the μ_3-OH of the Zn-node (Figure 4.8).

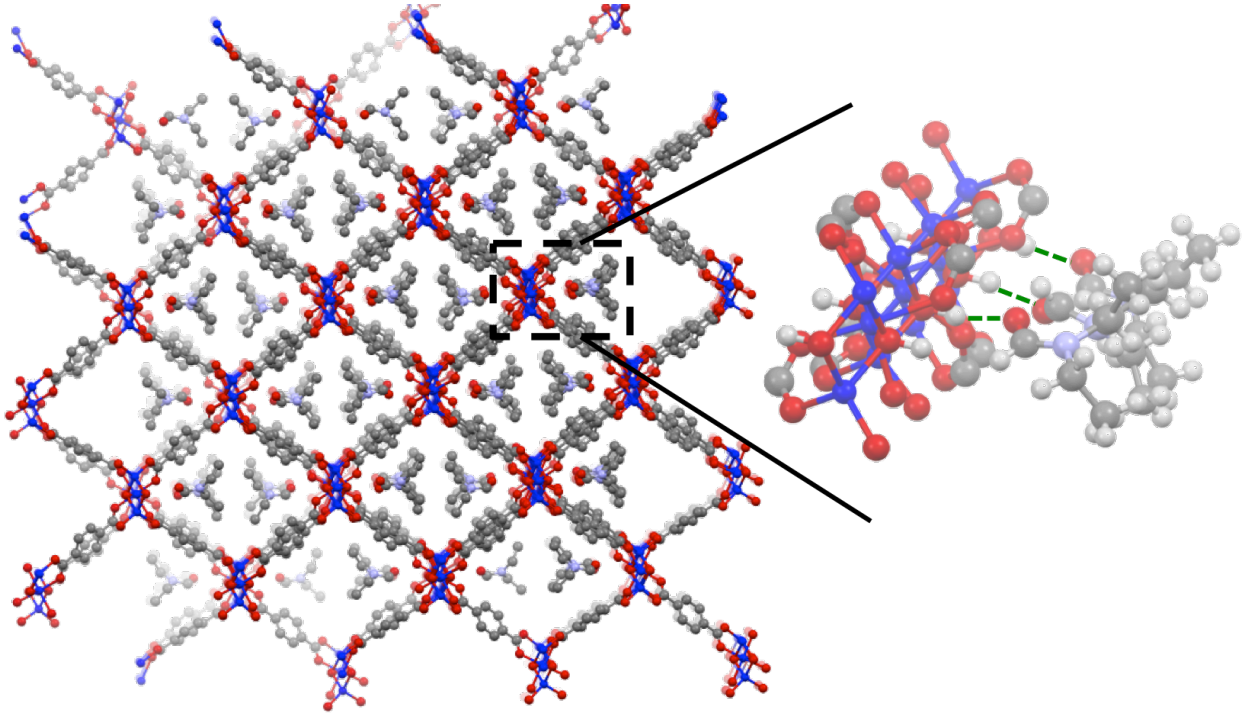

Figure 4.8. MOF-69C crystal structure[28] (with hydrogen atoms omitted) highlighting the DEF in the pores (right, zoom in), where the formamide O of DEF is H-bonded (green dash line) to the μ_3-OH of the Zn chains. Gray: C; Red: O; Light blue/gray: N; White: H; Blue: Zn.

MOFs have been shown to undergo phase transitions as a function of temperature or with the removal or adsorption of guest molecules.[47,48] These transitions consist of a reversible "breathing" or a change in the pore shape and size, resulting in a change in the lattice parameters, with temperature.[47,49] Similarly, some frameworks have exhibited a response to adsorption/desorption of gas molecules, resulting in guest-induced breathing.[50-53] In large part, however, investigations into the nature of these temperature-induced transitions have been predominantly done using Raman and IR spectroscopy, which found an ordering and H-bonding of solvent molecules to the framework,[54] variable temperature diffraction to determine changes

in atom positions and lattice parameters as well as guest molecule orientations,[51,55-57] and computational studies to justify interactions between the framework and hydroxide bridging ligands.[58] Variable temperature NMR measurements can also be a useful tool to investigate these dynamic properties of MOFs and in fact have been used to study guest mobility in frameworks.[59,60] The VT-SSNMR results attribute the thermal transition observed in the MOF-69C DSC to the rotation of the formamide group of DEF solvate molecules within the pores of the framework.

4.5 Conclusions

In summary, a series Zn-based MOFs were prepared and their conductivity investigated using electrochemical impedance spectroscopy. Framework **(1)** ($Zn_4(pydc)_4(DMF)_2 \cdot 3DMF$) was found to be the most conductive, followed by MOF-69C ($Zn_3(OH)_2(bdc)_2 \cdot 2DEF$) and framework **(2)** ($Zn_2(pydc)_2(DEF)$). The mechanism of conduction was found to be dependent on the presence of solvent in the MOF pores as well as bound solvent, as observed in the structure of **(1)**. The extended solvent network provided a pathway for charge transport throughout the framework and resulted in increased conductivity. This was further evidenced by temperature dependent conductivity coupled with DSC and VT-SSNMR, which demonstrated that MOF-69C undergoes a reversible solid-solid phase transition as a result of rotation of the carbonyl carbon atom of DEF solvate molecules. This suggests that solvent is involved in the mechanism of conduction of charge throughout the framework and that MOFs display conduction properties facilitated by guest molecules in the frameworks. These results have demonstrated that there are several approaches that can be taken to realize charge transport in MOFs: (1) through a redox

hopping mechanism in frameworks comprised of redox active nodes and linker molecules; and (2) through the incorporation of solvent or guest molecules, which form an extended network capable of mediating charge transport throughout the framework. The structural and mechanistic insights gained from these investigations show promise for the smart design of MOFs with possible applications in electronic devices.

4.6 Acknowledgements

The authors gratefully acknowledge Dr. Robert Moore for access to electrochemical impedance spectroscopy instrumentation.

4.7 Supplemental Information

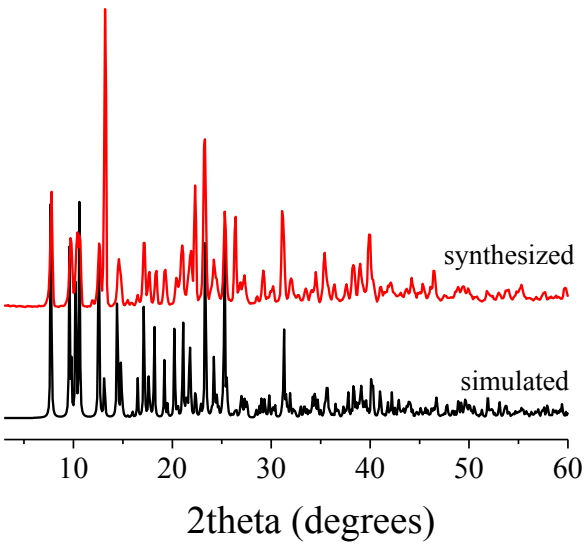

Figure 4.S1. Powder X-ray diffraction pattern of **(1)** simulated[6] (black) and synthesized (red).

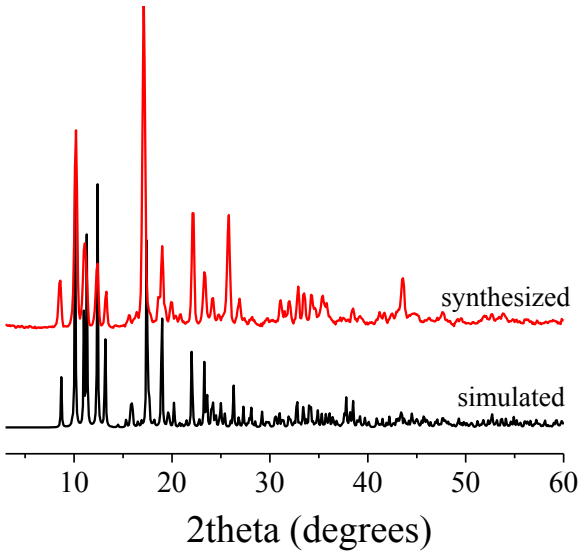

Figure 4.S2. Powder X-ray diffraction pattern of **(2)** simulated[6] (black) and synthesized (red).

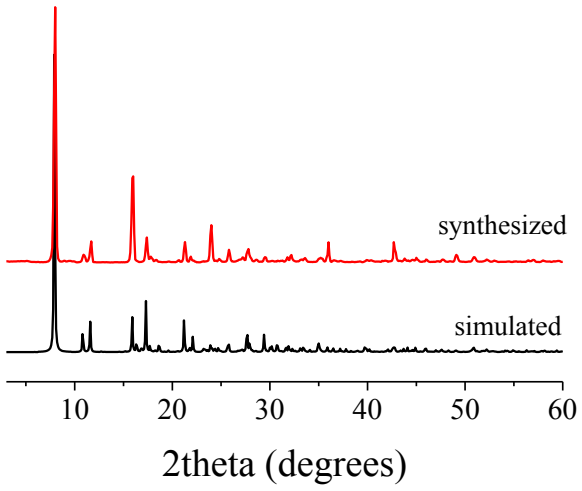

Figure 4.S3. Powder X-ray diffraction pattern of MOF-69C simulated[28] (black) and synthesized (red).

4.8 References

(1) Eddaoudi, M.; Kim, J.; Rosi, N.; Vodak, D.; Wachter, J.; O'Keeffe, M.; Yaghi, O. M. *Science* **2002**, *295*, 469.

(2) Ferey, G. *Chem. Soc. Rev.* **2008**, *37*, 191.

(3) Rosi, N. L.; Eckert, J.; Eddaoudi, M.; Vodak, D. T.; Kim, J.; O'Keeffe, M.; Yaghi, O. M. *Science* **2003**, *300*, 1127.

(4) Suh, M. P.; Park, H. J.; Prasad, T. K.; Lim, D.-W. *Chem. Rev.* **2011**, *112*, 782.

(5) Sumida, K.; Rogow, D. L.; Mason, J. A.; McDonald, T. M.; Bloch, E. D.; Herm, Z. R.; Bae, T.-H.; Long, J. R. *Chem. Rev.* **2012**, *112*, 724.

(6) Ahrenholtz, S. R.; Landaverde-Alvarado, C.; Whiting, M.; Lin, S.; Slebodnick, C.; Marand, E.; Morris, A. J. *Inorg. Chem.* **2015**, *54*, 4328.

(7) Horcajada, P.; Serre, C.; Vallet-Regi, M.; Sebban, M.; Taulelle, F.; Ferey, G. *Angew. Chem., Int. Ed.* **2006**, *45*, 5974.

(8) An, J.; Geib, S. J.; Rosi, N. L. *J. Am. Chem. Soc.* **2009**, *131*, 8376.

(9) Huxford, R. C.; Della Rocca, J.; Lin, W.-B. *Curr. Opin. Chem. Biol.* **2010**, *14*, 262.

(10) Lee, J. Y.; Farha, O. K.; Roberts, J.; Scheidt, K. A.; Nguyen, S. B. T.; Hupp, J. T. *Chem. Soc. Rev.* **2009**, *38*, 1450.

(11) Wee, L. H.; Alaerts, L.; Martens, J. A.; De Vos, D.; Wiley-VCH Verlag GmbH & Co. KGaA: 2011, p 191.

(12) Ahrenholtz, S. R.; Epley, C. C.; Morris, A. J. *J. Am. Chem. Soc.* **2014**, *136*, 2464.

(13) Sun, L.; Miyakai, T.; Seki, S.; Dincă, M. *J. Am. Chem. Soc.* **2013**, *135*, 8185.

(14) Allendorf, M. D.; Schwartzberg, A.; Stavila, V.; Talin, A. A. *Chem. - Eur. J.* **2011**, *17*, 11372.

(15) Patwardhan, S.; Schatz, G. C. *J. Phys. Chem. C* **2015**, *119*, 24238.

(16) Morozan, A.; Jaouen, F. *Energy Environ. Sci.* **2012**, *5*, 9269.

(17) Pickup, P. G.; Murray, R. W. *J. Am. Chem. Soc.* **1983**, *105*, 4510.

(18) Cameron, C. G.; Pittman, T. J.; Pickup, P. G. *J. Phys. Chem. B.* **2001**, *105*, 8838.

(19) Talin, A. A.; Centrone, A.; Ford, A. C.; Foster, M. E.; Stavila, V.; Haney, P.; Kinney, R. A.; Szalai, V.; El Gabaly, F.; Yoon, H. P.; Léonard, F.; Allendorf, M. D. *Science* **2014**, *343*, 66.

(20) Allendorf, M. D.; Foster, M. E.; Léonard, F.; Stavila, V.; Feng, P. L.; Doty, F. P.; Leong, K.; Ma, E. Y.; Johnston, S. R.; Talin, A. A. *J. Phys. Chem. Lett.* **2015**, *6*, 1182.

(21) Gándara, F.; Uribe-Romo, F. J.; Britt, D. K.; Furukawa, H.; Lei, L.; Cheng, R.; Duan, X.; O'Keeffe, M.; Yaghi, O. M. *Chem. Eur. J.* **2012**, *18*, 10595.

(22) Sun, L.; Campbell, M. G.; Dincă, M. *Angew. Chem., Int. Ed.* **2016**, *55*, 3566.

(23) Kobayashi, Y.; Jacobs, B.; Allendorf, M. D.; Long, J. R. *Chem. Mater.* **2010**, *22*, 4120.

(24) Ameloot, R.; Aubrey, M.; Wiers, B. M.; Gomora-Figueroa, A. P.; Patel, S. N.; Balsara, N. P.; Long, J. R. *Chem. Eur. J.* **2013**, *19*, 5533.

(25) Kim, S.; Dawson, K. W.; Gelfand, B. S.; Taylor, J. M.; Shimizu, G. K. H. *J. Am. Chem. Soc.* **2013**, *135*, 963.

(26) Takaishi, S.; Hosoda, M.; Kajiwara, T.; Miyasaka, H.; Yamashita, M.; Nakanishi, Y.; Kitagawa, Y.; Yamaguchi, K.; Kobayashi, A.; Kitagawa, H. *Inorg. Chem.* **2008**, *48*, 9048.

(27) Sadakiyo, M.; Kasai, H.; Kato, K.; Takata, M.; Yamauchi, M. *J. Am. Chem. Soc.* **2014**.

(28) Rosi, N. L.; Kim, J.; Eddaoudi, M.; Chen, B.; O'Keeffe, M.; Yaghi, O. M. *J. Am. Chem. Soc.* **2005**, *127*, 1504.

(29) Loiseau, T.; Muguerra, H.; Ferey, G.; Haouas, M.; Taulelle, F. *J. Solid State Chem.* **2005**, *178*, 621.

(30) Lvovich, V. F. *Impedance spectroscopy: applications to electrochemical and dielectric phenomena*; Wiley: Hoboken, N.J, 2012; Vol. 1.
(31) Barsoukov, E.; Macdonald, J. R. *Impedance spectroscopy: theory, experiment, and applications*; 2nd ed. ed.; Wiley-Interscience: Hoboken, N.J, 2005; Vol. 2nd;2;.
(32) Sinclair, D. C.; West, A. R. *J. Appl. Phys.* **1989**, *66*, 3850.
(33) Mahato, D. K.; Dutta, A.; Sinha, T. P. *J. Mater. Sci.* **2010**, *45*, 6757.
(34) Hashim, M.; Alimuddin; Kumar, S.; Koo, B. H.; Shirsath, S. E.; Mohammed, E. M.; Shah, J.; Kotnala, R. K.; Choi, H. K.; Chung, H.; Kumar, R. *J. Alloys Compd.* **2012**, *518*, 11.
(35) Abdullah Dar, M.; Majid, K.; Batoo, K. M.; Kotnala, R. K. *J. Alloys Compd.* **2015**, *632*, 307.
(36) Brug, G. J.; Van den Eeden, A. L. G.; Sluyters-Rehbach, M.; Sluyters, J. H. *J. Electroanal. Chem. Interfacial Electrochem.* **1984**, *176*, 275.
(37) Kerner, Z.; Pajkossy, T. *J. Electroanal. Chem.* **1998**, *448*, 139.
(38) Kerner, Z.; Pajkossy, T. *Electrochim. Acta* **2000**, *46*, 207.
(39) Shoar Abouzari, M. R.; Berkemeier, F.; Schmitz, G.; Wilmer, D. *Solid State Ionics* **2009**, *180*, 922.
(40) De Levie, R. *Electrochim. Acta* **1965**, *10*, 113.
(41) Córdoba-Torres, P.; Mesquita, T. J.; Nogueira, R. P. *J. Phys. Chem. C* **2015**, *119*, 4136.
(42) Hendon, C. H.; Tiana, D.; Walsh, A. *Phys. Chem. Chem. Phys.* **2012**, *14*, 13120.
(43) Sun, L.; Hendon, C. H.; Minier, M. A.; Walsh, A.; Dincă, M. *J. Am. Chem. Soc.* **2015**, *137*, 6164.
(44) Narayan, T. C.; Miyakai, T.; Seki, S.; Dincă, M. *J. Am. Chem. Soc.* **2012**, *134*, 12932.
(45) Park, S. S.; Hontz, E. R.; Sun, L.; Hendon, C. H.; Walsh, A.; Van Voorhis, T.; Dincă, M. *J. Am. Chem. Soc.* **2015**, *137*, 1774.
(46) Allendorf, M. D.; Schwartzberg, A.; Stavila, V.; Talin, A. A. *Chem. Eur. J.* **2011**, *17*, 11372.
(47) Schneemann, A.; Bon, V.; Schwedler, I.; Senkovska, I.; Kaskel, S.; Fischer, R. A. *Chem. Soc. Rev.* **2014**, *43*, 6062.
(48) Chang, Z.; Yang, D.-H.; Xu, J.; Hu, T.-L.; Bu, X.-H. *Adv. Mater.* **2015**, *27*, 5432.
(49) Henke, S.; Schneemann, A.; Fischer, R. A. *Adv. Funct. Mater.* **2013**, *23*, 5990.
(50) Bourrelly, S.; Llewellyn, P. L.; Serre, C.; Millange, F.; Loiseau, T.; Ferey, G. *J. Am. Chem. Soc.* **2005**, *127*, 13519.
(51) Henke, S.; Wieland, D. C. F.; Meilikhov, M.; Paulus, M.; Sternemann, C.; Yusenko, K.; Fischer, R. A. *CrystEngComm* **2011**, *13*, 6399.
(52) Loiseau, T.; Serre, C.; Huguenard, C.; Fink, G.; Taulelle, F.; Henry, M.; Bataille, T.; Ferey, G. *Chem. - Eur. J.* **2004**, *10*, 1373.
(53) Henke, S.; Schneemann, A.; Wuetscher, A.; Fischer, R. A. *J. Am. Chem. Soc.* **2012**, *134*, 9464.
(54) Maczka, M.; Ptak, M.; Macalik, L. *Vib. Spectrosc.* **2014**, *71*, 98.
(55) Liu, Y.; Her, J.-H.; Dailly, A.; Ramirez-Cuesta, A. J.; Neumann, D. A.; Brown, C. M. *J. Am. Chem. Soc.* **2008**, *130*, 11813.
(56) Lama, P.; Das, R. K.; Smith, V. J.; Barbour, L. J. *Chem. Comm.* **2014**, *50*, 6464.
(57) Sahoo, S. C.; Kundu, T.; Banerjee, R. *J. Am. Chem. Soc.* **2011**, *133*, 17950.
(58) Nanthamathee, C.; Ling, S.; Slater, B.; Attfield, M. P. *Chem. Mater.* **2015**, *27*, 85.
(59) Gonzalez, J.; Nandini Devi, R.; Tunstall, D. P.; Cox, P. A.; Wright, P. A. *Microporous Mesoporous Mater.* **2005**, *84*, 97.
(60) Lucier, B. E. G.; Chan, H.; Zhang, Y.; Huang, Y. *Eur. J. Inorg. Chem.* **2016**, *2016*, 2017.

5. Metal-organic framework electrochemically derived cobalt oxides for water oxidation at neutral pH

S.R. Ahrenholtz, B.Q. Kolb, C.C. Epley, and A.J. Morris

5.1 Motivation and Abstract

For ultimate applications in water oxidation electrocatalysis, metal-organic frameworks (MOFs) must possess the ability to efficiently transport charge from the catalytic site to the electrode surface. With our previous studies confirming the redox hopping charge transport ability with a Co-based framework (Chapter 2), we began investigations into electrocatalytic water oxidation with a MOF film. Specifically, a cobalt-based MOF containing 2-pyrimidinolate (pymo) linkers, designated as $Co(pymo)_2$, has been prepared solvothermally and deposited on conductive glass in order to investigate its electrocatalytic activity toward water oxidation. During the course of electrochemical measurements, the Co^{II} metal centers of the $Co(pymo)_2$ framework became oxidized to form Co-oxide species on the electrode surface, which were responsible for the observed catalytic water oxidation. In pH 6.8 electrolyte solution, a large catalytic wave is observed following the oxidation of the Co^{II} centers to Co^{III} to facilitate catalytic water oxidation at low overpotential (~200 mV). From electrochemical measurements, the oxidation of water was found to be first order with respect to $[H_2O]$ and proceeds via binding of water to the Co^{II} center followed by subsequent oxidations and intramolecular proton-coupled electron transfer (PCET) to generate Co^{III}-OH. The Tafel slope was found to be 230 (± 30) mV/decade with an exchange current density of $5 \pm 3 \times 10^{-6}$ A cm^{-2}, suggesting a rate-

determining electrochemical step followed by a chemical reaction. Assuming every Co center of the catalyst is active, oxygen was generated with a turnover number (TON) of 3.1 (± 0.9) over 40 min and corresponding turnover frequency (TOF) of 1.4 (± 0.6) × 10^{-3} s^{-1}.

5.2 Introduction

With worldwide energy consumption persistently increasing, the implementation of a carbon neutral, renewable fuel source is necessary to shift global reliance from fossil fuels.[1] Enough solar energy reaches the surface of the earth in 1.5 hours to satisfy the world's energy demands for an entire year.[2] However, in order to utilize the sun as a sustainable energy source, an efficient means of capturing the energy when it is available and storing it until needed must be developed.[3] Nature has elegantly accomplished this feat in the form of photosynthesis, where solar energy is captured at light harvesting centers and channeled to a Mn-based catalytic center, where 2 H_2O molecules are oxidized to produce 1 O_2 molecule, 4 protons, and 4 electrons.[4] This bond-breaking event releases electrons necessary for the plant to produce energy and fuel its lifecycle. The natural system available in plants provides an excellent example for the essential properties required to generate a catalyst capable of utilizing solar energy to produce fuel.[5] Therefore, the development of robust water oxidation catalysts composed of earth abundant materials will be advantageous in order to meet the world's energy demands in a cost-effective manner.[6] The challenge of mimicking the photosynthetic blueprint and developing a water oxidation catalyst driven by solar energy is complicated by coupling absorption of 4 photons and the 4 electron transfer to produce 1 molecule of O_2.[1] Also, in order to maximize the efficiency of the catalyst, water oxidation must occur near the thermodynamic limit of water oxidation (1.23 V

vs. NHE at pH = 0 and 25 °C), which will minimize the required energy input.[7,8] In addition, the kinetic limit for H_2O oxidation must approach the solar photon flux (1000 W m^{-2}).[9]

Metal oxides have been extensively investigated for their ability to catalyze water oxidation due to their innate stability, multiple oxidation states available, and open coordination sites for substrate binding.[10,11] Specifically, oxides of Ru and Ir have demonstrated some of the highest efficiencies for water oxidation.[12-15] Unfortunately, the scarcity of these elements makes the use of these catalysts prohibitively expensive on a large-scale basis. For this reason, earth-abundant metals, such as Co and Mn, are being investigated for their ability to catalyze water oxidation.[11,16,17] These metal oxide materials are typically deposited onto a suitable substrate using an electrochemical or thermal treatment of a metal salt in order to electrochemically or photoelectrochemically generate O_2 in the presence of a sacrificial oxidant.[11,18,19] For example, Frei et al. have prepared nanostructured Co_3O_4 clusters on a mesoporous silica support via a wet impregnation method using a cobalt nitrate precursor to generate spherical rods of approximately 70 nm in length.[18] These clusters were shown to oxidize water under mildly acidic conditions in the presence of a $[Ru^{II}(bpy)_3]$/persulfate (where bpy = 2,2′-bipyridine) visible light sensitizer system. However, a lower than expected efficiency was observed and is attributed to the restricted access of water molecules and sensitizers to the clusters within the support matrix.[10,18] Similarly, Nocera et al. have investigated a cobalt oxide based water oxidation catalyst prepared via electrochemical deposition from cobalt(II) buffered solutions, Co-Pi.[20,21] While the catalyst operated at near 100% Faradaic efficiency, the films suffered from reductive dissolution and fell apart in the absence of an applied potential.[11,16]

Herein, we report the investigations of a cobalt-based water oxidation catalyst generated from a metal-organic framework (MOF) precursor. The framework contains cobalt(II) metal centers bound by pyrimidinolate (pymo) linkers to form an extended 3D framework, designated as $Co(pymo)_2$.[22] $Co(pymo)_2$ was prepared as a film on fluorine doped tin oxide (FTO) and investigated for its electrocatalytic water oxidation ability. As a result of an applied potential, $Co(pymo)_2$ underwent a redox-induced structural transformation to form cobalt oxide species on the surface of FTO, which was characterized using energy-dispersive X-ray analysis (EDX) and X-ray photoelectron spectroscopy (XPS). Electrochemical investigations presented here demonstrate that the MOF-based cobalt oxide catalyst is active toward water oxidation and operates with low overpotential at a neutral pH and reasonable TOF. Analysis of the current-voltage behavior of the catalyst allowed for a proposed mechanism of catalysis occurring via oxidation of the Co^{II} metal centers to the catalytically active Co^{III} species commensurate with the binding of hydroxide. These results demonstrate catalytic water oxidation by the MOF-derived metal oxide species prepared from earth abundant materials.

5.3 Experimental

5.3.1 Materials. The following reagents and solvents were purchased from the indicated commercial suppliers and used without further purification unless otherwise specified: cobalt(II) chloride hexahydrate ($CoCl_2 \cdot 6H_2O$, Fluka Analytical, ≥98.0%); 2-hydroxypyrimidine hydrochloride (2-Hpymo, Acros Organics, 98%); ammonium hydroxide (Fisher Scientific, certified A.C.S. Plus); sodium chloride (NaCl; Fisher Scientific, certified A.C.S.); lithium perchlorate ($LiClO_4$; Acros Organics, 99+%); acetonitrile (Spectrum, HPLC grade; distilled

before use); fluorine doped tin oxide (FTO; Hartford Glass); Alconox®; isopropyl alcohol (Spectrum, HPLC grade); acetone (Spectrum, HPLC grade); *N,N*-dimethylformamide (DMF; Spectrum, spectrophotometric grade); hydrochloric acid (Spectrum, reagent A.C.S., 37%).

5.3.2 Synthesis of $Co(pymo)_2$. $Co(pymo)_2$ was prepared according to a previously published procedure.[22] An aqueous solution of $CoCl_2 \cdot 6H_2O$ (2.38 g, 1 mmol in 30 mL) was prepared and 2-Hpymo (3.31 g, 2.5 mmol) was added with stirring. The clear pink solution was stirred at room temperature for 20 min, and the temperature was increased to 90 °C. Aqueous ammonium hydroxide (30%) was added until an approximate pH of 10 was reached. The solution was stirred at 90 °C for 1.5-2 h. A bright pink solid was filtered from the solution and washed with ~100 mL hot water.

5.3.3 Characterization.

5.3.3.1 Powder X-Ray diffraction (PXRD). PXRD experiments were performed on a Rigaku MiniFlex 600 with Cu(Kα)- radiation (Cu-Kα = 1.5418 Å). The PXRD measurements were carried out over a 2θ range of 3-60° in continuous scanning mode (1°/min) with 0.1° resolution.

5.3.3.2 Scanning electron microscopy imaging (SEM) and energy-dispersive X-ray analysis (EDX). A LEO (Zeiss) 1550 field-emission scanning electron microscope, equipped with an in-lens detector, operating at 5.0 kV was used for high-resolution images of the thin films. EDX was collected using a built in Oxford INCA Energy E2H X-ray Energy Dispersive Spectrometer (EDS) system with a Silicon Drifted detector.

5.3.3.3 X-Ray photoelectron spectroscopy (XPS). XPS was conducted using a PHI 5300 spectrometer with a Perkin-Elmer Dual Anode X-Ray source operating with

monochromatic Mg Kα radiation (1253.6 eV) at 13 kV and 250 W and a pass energy of 17.9 eV. A step size of 0.025 eV was used and 600 sweeps were averaged for the Co 2p analysis while a step size of 0.05 eV. The photoelectrons emitted were detected by a hemispherical analyzer. Operating pressure in the sampling chamber was below 1×10^{-7} Torr. The spectral scanning range for cobalt 2p was 765-815 eV and 410-390 eV for nitrogen 1s. The spectra were calibrated according to the C 1s peak, which is known to occur at 284.6 eV.[23] Curve-fitting of the core-level XPS lines was carried out by AugerScan software with an integrated background subtraction.

5.3.4 Thin film preparation. $Co(pymo)_2$ thin films were prepared by drop-casting a pre-formed MOF suspension onto FTO. To prepare the suspension, 25 mg of MOF powder was sonicated in 3 mL of DMF for 5 min until uniformly dispersed. Prior to deposition, the FTO was sonicated for 10 min in separate solutions of aqueous Alconox®, isopropanol, acetone, and H_2O followed by rinsing with H_2O and drying. Subsequently, 200 μL of MOF/DMF suspension was pipetted onto a 1 cm^2 area of the conductive FTO side and the solvent allowed to evaporate.

5.3.5 Electrochemical measurements.

5.3.5.1 Cyclic Voltammetry (CV). CV was performed using a BASi Epslion potentiostat in a three-electrode arrangement with a MOF-modified thin film working electrode, aqueous Ag/AgCl (saturated KCl) reference electrode, and a platinum mesh counter electrode. The scan rate was varied over the range 10 – 1000 mV/sec. The Ag/AgCl was calibrated against $Fe(CN)_6^{3-}/Fe(CN)_6^{4-}$, where the expected $E_{1/2}$ is +560 mV vs. NHE.[24] Distilled acetonitrile with 0.1 M $LiClO_4$ and aqueous 0.5 M NaCl were used as electrolyte solutions. All potentials reported are versus the normal hydrogen electrode (NHE) unless otherwise noted.

5.3.5.2 Tafel Analysis. A potential jump experiment was set up using aqueous 0.5 M NaCl electrolyte in the standard three-electrode arrangement described above. Overpotentials ($\eta = V - E^o$) ranging from η = 0 to 700 mV were applied with 25 mV steps. The solution resistance (iR) was taken into consideration when calculating overpotentials, such that $V = V_{appl} - iR$.

5.3.5.3 pH Dependence. A Mettler-Toledo SevenMulti pH meter was used to measure pH of aqueous solutions. Hydrochloric acid or ammonium hydroxide solutions were added to aqueous 0.5 M NaCl to obtain the desired pH. A three-electrode electrochemical arrangement was set up, and the potential applied was held constant for 5 min to ensure that the steady state current had been reached. The potential applied corresponded to an overpotential of 300 mV and was corrected for solution resistance ($V_{appl} = E^o + \eta + iR$). The potential ($V$) was held for ~1 min until a steady state current was reached.

5.3.5.4 Controlled Potential Electrolysis. Controlled potential electrolysis experiments were conducted on a BASi Epsilon potentiostat in a two-compartment electrochemical cell. The compartments were separated by a fine spun-glass frit to allow for ion exchange. The supporting electrolyte in both compartments was 0.5 M NaCl purged with Ar. In one compartment, a MOF-modified thin film working electrode and aqueous Ag/AgCl (saturated KCl) reference electrode were immersed. The second compartment contained a platinum mesh counter electrode. For *in situ* oxygen detection, an Oakton Acorn Series DO6 electrochemical dissolved O_2 meter was immersed in the working electrode compartment. The O_2 meter readout was recorded every 5 sec for the first 9 min and every 30 sec for the remainder of the experiment.

5.4 Results and Discussion

5.4.1 Synthesis and Structural Characterization.

$Co(pymo)_2$ was synthesized by a solvothermal reaction of $CoCl_2$ with 2-hydroxypyrimidine hydrochloride in basic aqueous conditions to yield a deep pink powder.[22] $Co(pymo)_2$ crystallizes in a tetragonal crystal system with Co^{II} ions bound to four nitrogen atoms of different linker molecules in exobidentate μ_2-η^1-η^1 coordination. This gives a tetrahedral geometry about the metal centers with Co-N distances of 2.032 Å and Co-Co bridging distances of 5.655 Å (Figure 5.1A).[22] To confirm the structure and purity of synthesized $Co(pymo)_2$ sample, the experimental powder pattern measured with PXRD was compared to the simulated powder pattern from the literature reported structure (Figure 5.1B).[22] A thin film of $Co(pymo)_2$ was prepared by immobilizing pre-formed crystallites on a clean fluorine-doped tin oxide (FTO) substrate to form a weakly-bound MOF-FTO working electrode, $Co(pymo)_2$/FTO (Figure 5.1C).

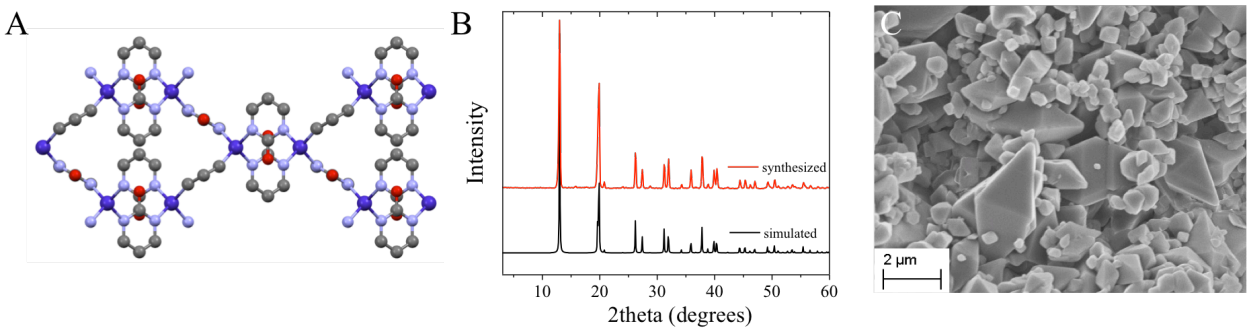

Figure 5.1. (A) Unit cell of $Co(pymo)_2$ viewed down the (010) axis.[22] Gray: C; Red: O; Light blue/gray: N; Blue: Co. Hydrogen atoms have been omitted for clarity; (B) Powder pattern of $Co(pymo)_2$ as synthesized (red) and simulated[22] (black); (C) SEM image of $Co(pymo)_2$/FTO film.

5.4.2 Electrochemical Water Oxidation.

The electrochemical behavior of $Co(pymo)_2$ was investigated by cyclic voltammetry (CV) in both non-aqueous and aqueous environments (Figure 5.2). In a non-aqueous electrolyte (0.1 M $LiClO_4$/distilled CH_3CN), an irreversible oxidation wave was observed over the scan rates employed for $Co(pymo)_2$ with an anodic peak current at ~1.5 V vs. NHE (Figure 5.2A, red). This electrochemical signature was attributed to the $Co^{II/III}$ oxidation of the metal centers within the framework, an essential step for water oxidation activity and which has been previously demonstrated in cobalt-based water oxidation catalysts.[19,25-27] Additionally, the lack of a return wave in the reverse scan corresponding to this oxidation suggests that the framework of $Co(pymo)_2$ undergoes a chemical transformation (*vide infra*).[26] The inset in Figure 5.2A displays the relationship between the anodic peak current (i_{pa}) as a function of scan rate (υ) in a 2.5% H_2O/CH_3CN electrolyte. The correlation coefficients for a linear fit of i_{pa} as a function of υ (red) and $\upsilon^{1/2}$ (black) were found to be 0.89 and 0.99, respectively, where a linear relationship between current and $\upsilon^{1/2}$ suggests a diffusion limited process, which has been reported previously with a MOF thin film.[24,28] In aqueous electrolyte (0.5 M NaCl, pH = 6.8), the CV displayed a sharp rise in current at the potentials observed for the $Co^{II/III}$ oxidation, indicative of electrocatalytic water oxidation (Figure 5.2A, blue). The application of the Nicholson and Shain diagnostic technique, where current function ($i_p/\upsilon^{1/2}$) is plotted as a function of the scan rate (υ) on a log scale, is suggestive of an electrochemical step followed by a catalytic reaction (Figure 5.2B).[29]

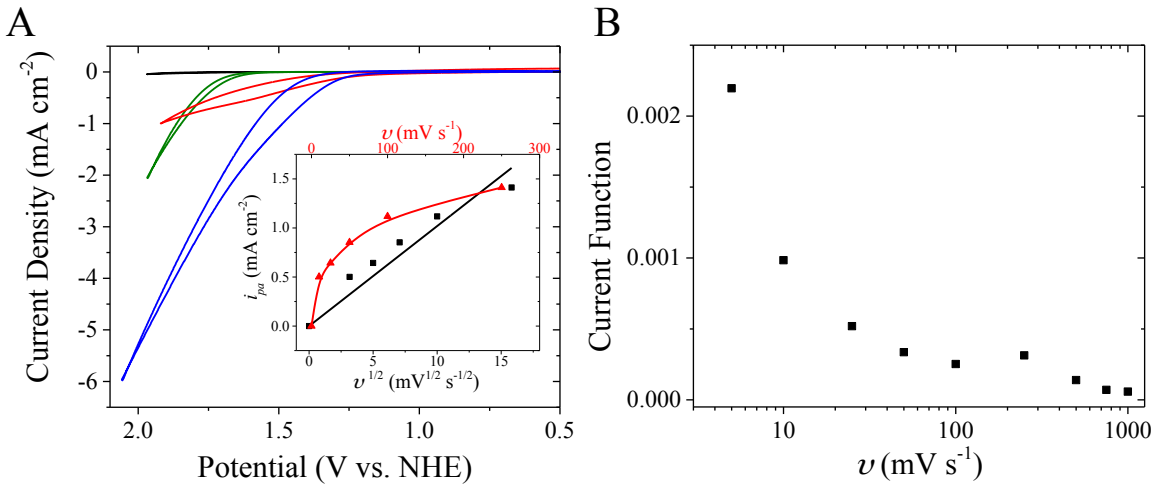

Figure 5.2. (A) Cyclic voltammograms (CV) in 0.1 M $LiClO_4$/distilled CH_3CN of FTO (black) and $Co(pymo)_2$/FTO (red); and FTO (green) and $Co(pymo)_2$/FTO (blue) in aqueous 0.5 M NaCl. Inset shows i_{pa} as a function of υ (red) and $\upsilon^{1/2}$ (black) in 2.5% H_2O/CH_3CN. (B) Nicholson and Shain diagnostic plot displaying behavior corresponding to an electrochemical process followed by a catalytic reaction.[29]

To investigate the dependence of reactivity on the presence of H_2O, CVs were taken in a 0.1 M $LiClO_4$/distilled CH_3CN electrolyte with incremental water additions ranging from 2.5% to 30% (Figure 5.3A). For $Co(pymo)_2$, a plot of the current at 1.5 V (vs. NHE) versus $[H_2O]^{1/2}$ concentration results in a linear dependence, indicating that the catalytic reaction is first order with respect to H_2O (Figure 5.3A, inset).[30]

A pH dependent study was performed on $Co(pymo)_2$/FTO to investigate the reaction order in H^+ activity. The potential applied was corrected for solution resistance and held constant at η = 300 mV for 5 min until the steady state current was attained in solutions of pH ranging from 6-9.5. This pH range was investigated because at more acidic pH values, protonation of the pyrimidinolate linker becomes possible, which would result in degradation of the framework. Whereas at more basic conditions, hydroxide can competitively bind with the metal centers to

form cobalt hydroxide species in solution. The current density of $Co(pymo)_2$ displayed no dependence on $[H^+]$ over the range investigated (Figure 5.3B).

The current-voltage (Tafel) behavior of $Co(pymo)_2$/FTO was measured in the potential range where water oxidation was observed. Various potential step experiments were conducted over a ~700 mV range in 25 mV steps. The current density (i) reported for each potential is the steady state value reached at ~1 min after application of the potential. The potentials were then converted to overpotential values (η) by subtraction of the thermodynamic potential for water oxidation under the experimental conditions (at pH 6.8, E^o = 0.828 V vs. NHE) and corrected for the solution resistance and ohmic potential losses. From the onset of catalytic current based on the linearity in the Tafel slope, the overpotential for water oxidation catalysis was determined to be 200 mV for $Co(pymo)_2$ (Figure 5.3C). The Tafel slope of the linear portion of the plot, which was maintained over at least 2 orders of magnitude, was found to be 230 (± 30) mV/dec. This Tafel slope is comparable to the ZIF-9 ($[Co(bim)_2]$, where bim = benzimidazolate) water oxidation electrocatalyst, whose Tafel slope was found to be ~193 mV/dec.[25] Additionally, a Co-based naphthalene MOF was employed as a precursor to obtain Co_3O_4C nanoarrays, which were investigated for catalytic water oxidation. This MOF displayed a Tafel slope of 142 mV/dec, while the Co_3O_4C nanoarrays displayed a much lower Tafel slope of 70 mV/dec.[31] In general, the Tafel slopes for framework electrocatalysts are much greater than those reported for heterogeneous Co-phosphonate and Co-oxide materials (with values ranging from ~ 60-80 mV/dec).[31-34] The exchange current density (i_o) represents the rate at which the electrochemical reaction occurs at equilibrium with zero overpotential and provides a measure of catalytic efficiency.[35] The value of i_o obtained from the Tafel plot of $Co(pymo)_2$/FTO was

$5 \pm 3 \times 10^{-6}$ A cm^{-2}. This value is several orders of magnitude larger than recently reported Co-based heterogeneous water oxidation films on FTO (with i_o values ranging from 10^{-7} A cm^{-2} to 10^{-2} A cm^{-2})[36-38] as well as mixed metal oxide thin films composed of varying amounts of Co, Ni, and Fe metals (values ranging from 10^{-7} to 10^{-8} A cm^{-2}).[39]

Over the course of the electrochemical experiments, $Co(pymo)_2$ breaks down to deposit oxide species on the surface of FTO. However, it is apparent that both species are active for water oxidation and the decomposition of the framework is the result of the $Co^{II/III}$ oxidation and concomitant loss of linker to form oxides (*vide infra*). Therefore, the difference in observed Tafel slopes can be attributed to the different mechanism of the water oxidation reaction, specifically, the rate-determining step.

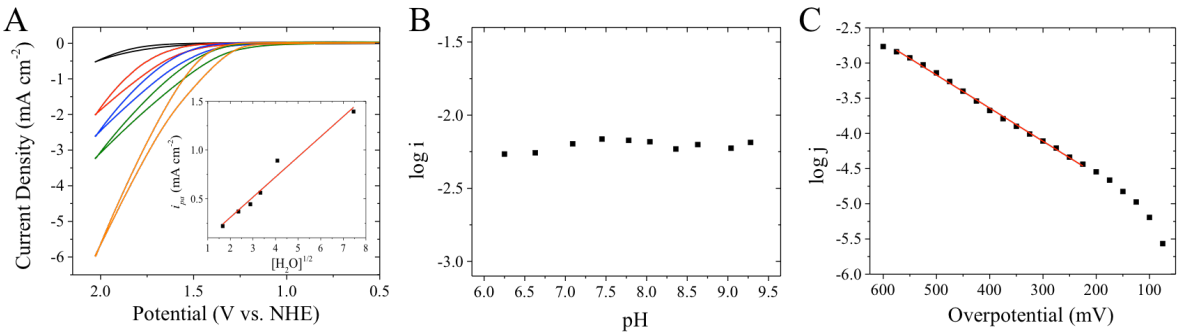

Figure 5.3. (A) Cyclic voltammograms of $Co(pymo)_2$/FTO in 0.1 M $LiClO_4$/distilled CH_3CN (black) with additions of 5% (red), 15% (blue), 30% (green) H_2O and in 0.5 M NaCl/H_2O (orange). Inset shows the current magnitude at 1.5 V vs. NHE to be linear with $[H_2O]^{1/2}$; (B) pH dependence of steady-state catalytic current density at constant potential (η = 300 mV) for $Co(pymo)_2$/FTO in aqueous 0.5 M NaCl.; (C) Tafel plot ($\eta = V_{appl} - E^o - iR$) of $Co(pymo)_2$/FTO in aqueous 0.5 M NaCl. Due to variations in the films (e.g., amount of MOF on surface and Co centers, electrical contact, etc.), the error in the current densities is ±10%.

Electrocatalytic water oxidation was further investigated via controlled potential electrolysis (CPE) in a two-compartment cell with Ar-purged 0.5 M NaCl. The amount of evolved oxygen was quantified using a Clark-type electrode immersed in solution. The amount of oxygen produced by $Co(pymo)_2$ at an applied potential of 1.5 V vs. NHE is shown in Figure 5.4 and Figure 5.S1. Based on the amount of MOF attached onto FTO (~1-2 mg), the TON (mol O_2 produced per mol of Co centers) and TOF (TON per second) at η = ~ 670 mV were determined to be 3.1 (± 0.9) and 1.4 (± 0.6) × 10^{-3} s^{-1}, respectively. The TOF calculation assumed that all Co centers in the film are catalytically active, which is an overestimation, and therefore, represents a lower bound, such that the actual TOF is expected to be much larger. That said, this lower limit for the TOF is comparable to several recently reported Co-based thin film water oxidation catalysts (~1-2 × 10^{-3} s^{-1}).[25,37,40] The Faradaic efficiency taken after 25 min of electrolysis was found to be 8.8% and indicates that the electrons are being generated in another oxidative process in addition to water oxidation. Since these electrochemical investigations were performed in NaCl electrolyte, the competitive oxidation of Cl^- to Cl_2 can occur at similar potentials. Initial investigations in other electrolytes have indicated that some current have originated from oxidation of Cl^- when NaCl is used as electrolyte (Figure 5.S2).

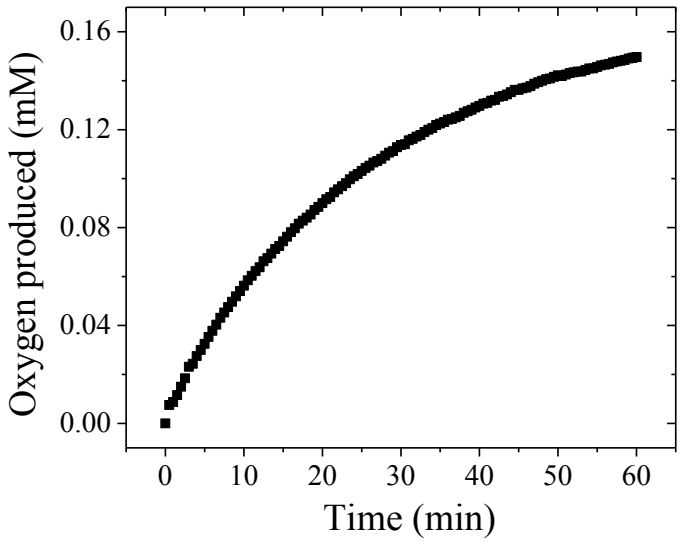

Figure 5.4. The oxygen produced as measured with a Clark electrode during electrolysis of $Co(pymo)_2$/FTO at 1.5 V vs. NHE in 0.5 M NaCl (η = ~ 670 mV).

During the course of the CPE experiment, a darkening of the MOF film on FTO was observed, where the color changed from bright pink to a dark green/brown. The films pre- and post-electrolysis were analyzed using SEM, energy-dispersive X-ray analysis (EDX), and XPS (Figure 5.5 and Table 5.1). As a result of applied potential, the MOF has lost its crystallinity, resulting in a dark film deposited on the FTO (Figure 5.5, middle). EDX was used to determine the weight % of elements, with the results in Table 5.1. In the pre-electrolysis film, the elemental percentages are approximately equal to those expected from the molecular formula of $Co(pymo)_2$ ($CoC_8H_6N_4O_2$).[22] However, the percentages in the post-electrolysis film decreased by more than half for C and N while a 3-fold increase in the amount of O was observed. This result, combined with the SEM images, suggests that cobalt oxide species have been formed as a result of extended application of oxidative potential in aqueous electrolyte.

In order to investigate the oxidation state of the Co species within the films, XPS analysis was performed and the Co 2p region of the spectra were each fit with 4 Gaussian curves (Figure 5.5, right). A similar analysis has been reported previously, from which it was determined that the Co $2p_{3/2}$ peak for Co^{II} and Co^{III} species should be centered at ~780 eV and ~779 eV, respectively, while the $2p_{1/2}$ peak for Co^{II} and Co^{III} species should be located at 796 eV and 794 eV, respectively.[41,42] No significant change in the $2p_{3/2}$ and $2p_{1/2}$ binding energies was observed between the films pre- and post-electrolysis (Figure 5.5, magenta and green curves, respectively). Therefore, the binding energies of both the $2p_{3/2}$ (~780 eV) and $2p_{1/2}$ (~796 eV) peaks of the films pre- and post-electrolysis are consistent with the expected peaks for Co^{II} species.[23,41,42] The presence of the satellite peak (centered at ~785.5 eV; blue curve) appearing at ~5 eV higher binding energy than the $2p_{3/2}$ peaks is characteristic of a Co^{II} species and is consistent between the two spectra.[26,42] These results suggest that the post-electrolysis film contains predominantly Co^{II} metal centers. Further structural characterization of the material post-electrolysis proved difficult due to the loss of crystallinity; however, it likely consists of cobalt(II) oxide species. The formation of cobalt-oxide materials from cobalt-based MOFs has been previously demonstrated, as these frameworks readily degrade under oxidizing conditions.[26,43] From the XPS and EDX results, it is clear that cobalt oxides are formed with some of the original framework still present, which makes it difficult to dissociate the two catalysts.

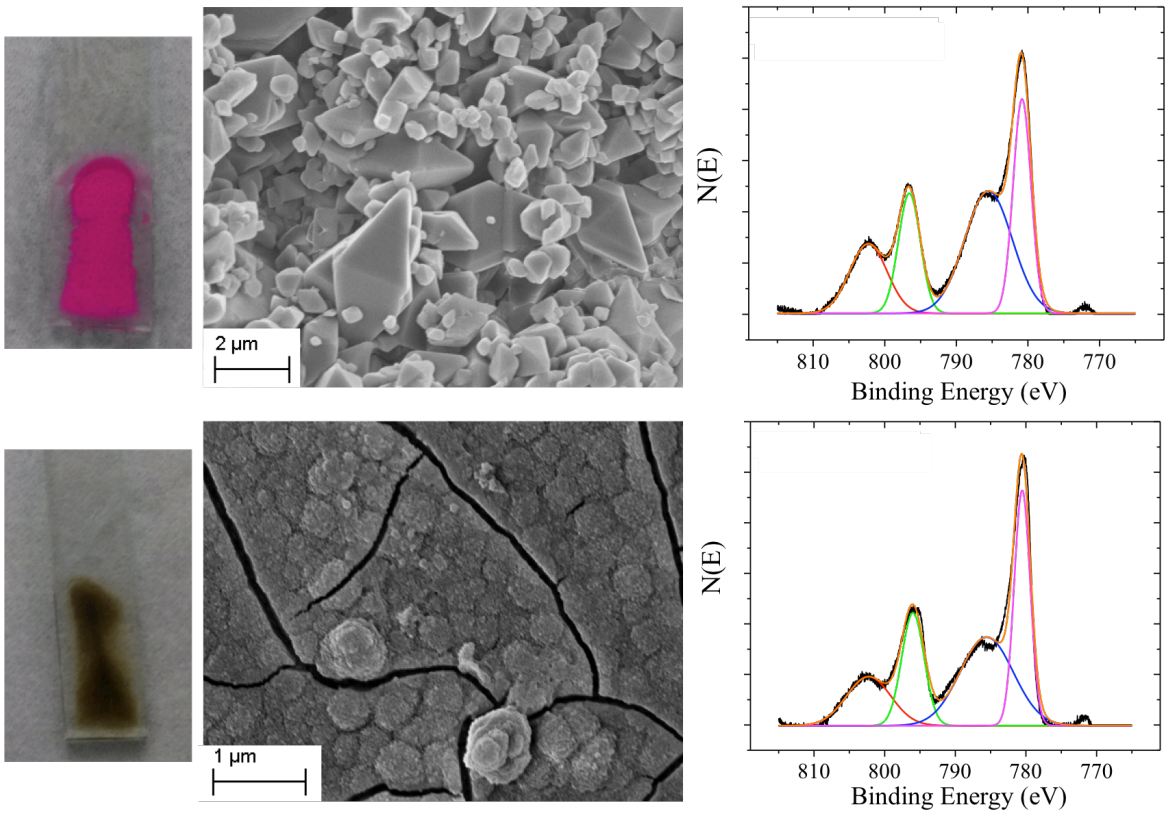

Figure 5.5. Pictures of the films pre- (top left) and post-electrolysis (bottom left) display the color change as a result of the applied potential. Middle: SEM image of the film pre- (top) and post-electrolysis (bottom). Right: XPS analysis of the film pre- (top) and post-electrolysis (bottom) in black solid line with curve fitting displayed in colored lines.

Table 5.1. Summary of atomic weight % determined by EDX analysis of the film pre- and post-electrolysis.

Film	%C	%N	%O	%Co
Pre-electrolysis	37 ± 2	26 ± 5	17 ± 4	20 ± 7
Post-electrolysis	15 ± 4	11 ± 5	49 ± 6	25 ± 7

5.4.3. Mechanism of Water Oxidation.

The reported electrochemical measurements can be used to gain insight into the reaction mechanism of water oxidation. In particular, four pieces of supporting evidence have led to the proposed mechanism: (1) Nicholson and Shain diagnostics indicate a catalytic process with an electrochemical charge transfer step (E) followed by a chemical reaction (C); (2) Tafel analysis suggests EC mechanism; (3) the pH independent nature of the reaction; and (4) first order with respect to H_2O.

The first step in the proposed mechanism of water oxidation is an electron transfer process as the Co^{II} metal centers are oxidized to Co^{III} to generate the active catalytic sites. Coordination of water molecules to these electrogenerated centers facilitates the electron transfer.[19] The Tafel slope of > 120 mV/decade also supports this catalytic mechanism.[35,44,45] While it has been established that a Tafel slope of ∞ (>> 120 mV/decade) indicates a rate-determining chemical reaction (C) followed by an electrochemical step (E),[45] we believe a CE mechanism for H_2O oxidation is not likely in this case due to the required oxidation of metal centers.[19]

Numerous reaction intermediates to water oxidation with various reaction pathways have been identified, making the absolute elucidation of the mechanism difficult.[44] The lack of dependence on $[H^+]$ suggests that proton transfer is not rate limiting and may occur intramolecularly via the pyrimidinolate linker rather than through solvent. This, in addition to the first order dependence on $[H_2O]$, allows for a plausible catalytic mechanism involving a surface bound hydroxide.[30,44] The binding of hydroxide to the Co metal center has been shown to be thermodynamically favorable in a related framework, ZIF-9, where the imidazolate linker is thought to accept the abstracted proton.[25] A similar mechanism is likely with the $Co(pymo)_2$

framework, where the hydroxide binds to the Co^{III} metal center and the pyrimidinolate linker acts as the proton acceptor. The structural changes associated with these processes results in degradation of the MOF and deposition of the cobalt oxide material. The rest of the mechanism could proceed via several different pathways to ultimately yield one O_2 molecule from 2 H_2O molecules.[44]

5.5 Conclusions

A cobalt-based MOF was investigated as an electrocatalyst for the water oxidation reaction. Electrochemical studies show that the oxidation of Co^{II} to Co^{III} generates the active catalytic state and allows for catalytic water oxidation to proceed at low overpotentials (η = 200 mV) and via a first order reaction in terms of [H_2O]. The TOF of $Co(pymo)_2$ was determined to be greater than 1.4 (± 0.6) × 10^{-3} s^{-1}, which is comparable to other thin film catalysts. As a result of electrolysis, $Co(pymo)_2$ underwent a chemical transformation to a cobalt-oxide material, which was deposited onto the electrode surface and characterized using SEM, EDX, and XPS. The proposed reaction pathway involves the binding of water to Co^{III} metal centers followed by proton abstraction through the pyrimidinolate linker as the MOF decomposes to deposit cobalt-oxide on the electrode surface. This work demonstrates a feasible route to obtaining an earth abundant, first row transition metal based catalyst from a MOF precursor for efficient and economical H_2O oxidation.

5.6 Acknowledgements

This material is based upon work supported by U.S. Department of Energy, Office of Basic Energy Sciences under Award Number DE-SC0012446.

5.7 Supplemental Information

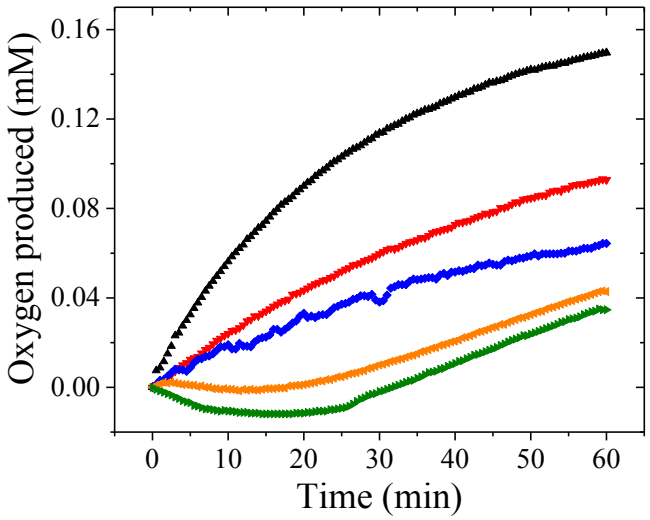

Figure 5.S1. Oxygen produced with an applied potential of 1.5 V vs. NHE with cobalt-based catalyst/FTO (black), 2-hydroxypyrimidinolate linker (red), $CoCl_2$ (blue), FTO (orange), and stirring solution (green) in aqueous 0.5 M NaCl.

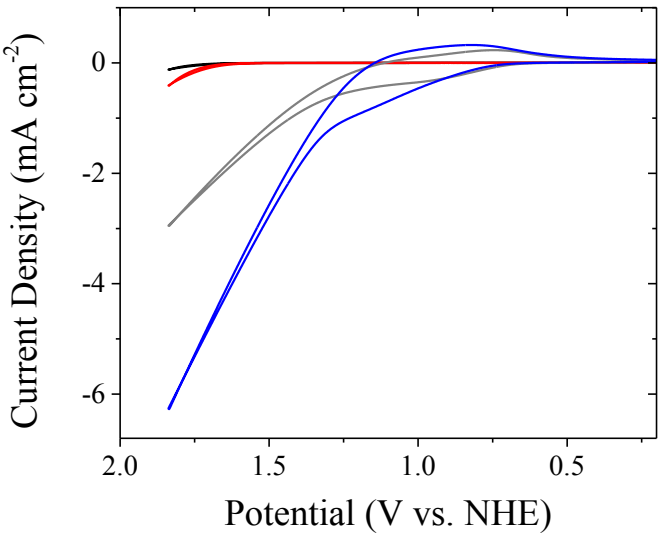

Figure 5.S2. Cyclic voltammograms of FTO (black) and $Co(pymo)_2$/FTO (gray) in aqueous 0.1 M $LiClO_4$ and FTO (red) and $Co(pymo)_2$/FTO (blue) in aqueous 0.5 M NaCl.

5.8 References

(1) Lewis, N. S.; Nocera, D. G. *Proc. Natl. Acad. Sci. U. S. A.* **2006**, *103*, 15729.

(2) Lewis, N. S. *Science* **2007**, *315*, 798.

(3) Walter, M. G.; Warren, E. L.; McKone, J. R.; Boettcher, S. W.; Mi, Q.; Santori, E. A.; Lewis, N. S. *Chem. Rev.* **2010**, *110*, 6446.

(4) Barber, J. *Philos. Trans. R. Soc., A* **2007**, *365*, 1007.

(5) Kärkäs, M. D.; Verho, O.; Johnston, E. V.; Åkermark, B. *Chem. Rev.* **2014**, *114*, 11863.

(6) Gray, H. B. *Nat. Chem.* **2009**, *1*, 7.

(7) Bard, A. J.; Fox, M. A. *Acc. Chem. Res.* **1995**, *28*, 141.

(8) Dau, H.; Limberg, C.; Reier, T.; Risch, M.; Roggan, S.; Strasser, P. *ChemCatChem* **2010**, *2*, 724.

(9) http://rredc.nrel.gov/solar/spectra/am1.5/.

(10) Jiao, F.; Frei, H. *Energy Environ. Sci.* **2010**, *3*, 1018.

(11) Singh, A.; Spiccia, L. *Coord. Chem. Rev.* **2013**, *257*, 2607.

(12) Kiwi, J.; Graetzel, M. *Angew. Chem., Int. Ed.* **1979**, *18*, 624.

(13) Beni, G.; Schiavone, L. M.; Shay, J. L.; Dautremont-Smith, W. C.; Schneider, B. S. *Nature* **1979**, *282*, 281.

(14) Toma, F. M.; Sartorel, A.; Iurlo, M.; Carraro, M.; Parisse, P.; Maccato, C.; Rapino, S.; Gonzalez, B. R.; Amenitsch, H.; Da Ros, T.; Casalis, L.; Goldoni, A.; Marcaccio, M.; Scorrano, G.; Scoles, G.; Paolucci, F.; Prato, M.; Bonchio, M. *Nat. Chem.* **2010**, *2*, 826.

(15) Hintermair, U.; Hashmi, S. M.; Elimelech, M.; Crabtree, R. H. *J. Am. Chem. Soc.* **2012**, *134*, 9785.
(16) McAlpin, J. G.; Stich, T. A.; Casey, W. H.; Britt, R. D. *Coord. Chem. Rev.* **2012**, *256*, 2445.
(17) Deng, X.; Tüysüz, H. *ACS Catalysis* **2014**, *4*, 3701.
(18) Jiao, F.; Frei, H. *Angew. Chem.* **2009**, *121*, 1873.
(19) Kanan, M. W.; Surendranath, Y.; Nocera, D. G. *Chem. Soc. Rev.* **2009**, *38*, 109.
(20) Kanan, M. W.; Nocera, D. G. *Science* **2008**, *321*, 1072.
(21) Kanan, M. W.; Yano, J.; Surendranath, Y.; Dincă, M.; Yachandra, V. K.; Nocera, D. G. *J. Am. Chem. Soc.* **2010**, *132*, 13692.
(22) Masciocchi, N.; Ardizzoia, G. A.; LaMonica, G.; Maspero, A.; Sironi, A. *Eur. J. Inorg. Chem.* **2000**, 2507.
(23) Moulder, J. F.; Stickle, W. F.; Sobol, P. E.; Bombem, K. D. *Handbook of X-ray Photoelectron Spectroscopy*; Physical Electronics, Inc., 1995.
(24) Bard, A. J.; Faulkner, L. R. *Electrochemical Methods*; 2nd ed.; John Wiley & Sons, Inc.: New York, 2001.
(25) Wang, S.; Hou, Y.; Lin, S.; Wang, X. *Nanoscale* **2014**, *6*, 9930.
(26) Usov, P. M.; McDonnell-Worth, C.; Zhou, F.; MacFarlane, D. R.; D'Alessandro, D. M. *Electrochim. Acta* **2015**, *153*, 433.
(27) Wasylenko, D. J.; Ganesamoorthy, C.; Borau-Garcia, J.; Berlinguette, C. P. *Chem. Commun.* **2011**, *47*, 4249.
(28) Ahrenholtz, S. R.; Epley, C. C.; Morris, A. J. *J. Am. Chem. Soc.* **2014**, *136*, 2464.
(29) Nicholson, R. S.; Shain, I. *Anal. Chem.* **1964**, *36*, 706.
(30) DuBois, D. L.; Miedaner, A.; Haltiwanger, R. C. *J. Am. Chem. Soc.* **1991**, *113*, 8753.
(31) Ma, T. Y.; Dai, S.; Jaroniec, M.; Qiao, S. Z. *J. Am. Chem. Soc.* **2014**, *136*, 13925.
(32) Zhou, T.; Wang, D.; Chun-Kiat Goh, S.; Hong, J.; Han, J.; Mao, J.; Xu, R. *Energy Environ. Sci.* **2015**, *8*, 526.
(33) Liu, X.; Chang, Z.; Luo, L.; Xu, T.; Lei, X.; Liu, J.; Sun, X. *Chemistry of Materials* **2014**, *26*, 1889.
(34) Xiao, Q.; Zhang, Y.; Guo, X.; Jing, L.; Yang, Z.; Xue, Y.; Yan, Y.-M.; Sun, K. *Chem. Commun.* **2014**, *50*, 13019.
(35) Gileadi, E. *Electrode Kinetics for Chemists, Engineers, and Materials Scientists*; VCH Publishers, Inc.: New York, 1993.
(36) Dey, S.; Mondal, B.; Dey, A. *Phys. Chem. Chem. Phys.* **2014**, *16*, 12221.
(37) Surendranath, Y.; Kanan, M. W.; Nocera, D. G. *J. Am. Chem. Soc.* **2010**, *132*, 16501.
(38) Surendranath, Y.; Bediako, D. K.; Nocera, D. G. *Proc. Nat. Acad. Sci.* **2012**, *109*, 15617.
(39) Smith, R. D. L.; Prévot, M. S.; Fagan, R. D.; Trudel, S.; Berlinguette, C. P. *J. Am. Chem. Soc.* **2013**, *135*, 11580.
(40) Esswein, A. J.; Surendranath, Y.; Reece, S. Y.; Nocera, D. G. *Energy Environ. Sci.* **2011**, *4*, 499.
(41) Chuang, T. J.; Brundle, C. R.; Rice, D. W. *Surface Science* **1976**, *59*, 413.
(42) Gautier, J. L.; Rios, E.; Gracia, M.; Marco, J. F.; Gancedo, J. R. *Thin Solid Films* **1997**, *311*, 51.
(43) Miles, D. O.; Jiang, D.; Burrows, A. D.; Halls, J. E.; Marken, F. *Electrochem. Commun.* **2013**, *27*, 9.
(44) Fang, Y.-H.; Liu, Z.-P. *ACS Catalysis* **2014**, *4*, 4364.
(45) Fletcher, S. *J. Solid State Electrochem.* **2009**, *13*, 537.

6. Cooperative electrochemical water oxidation by Zr nodes and Ni-porphyrin linkers of a PCN-224-Ni MOF thin film

S.R. Ahrenholtz, P.M. Usov, W.A. Maza, B. Stratakes, C.C. Epley, M.C. Kessinger, J. Zhu, and A.J. Morris.

6.1 Motivation and Abstract

To facilitate the efficient transformation sunlight into chemical fuels via artificial photosynthesis, complex assemblies capable of combined light harvesting, charge separation, proton management, and catalysis must be developed. An additional crucial requirement of these systems is their ability to remain structurally stable as a result of the catalytic reaction. It has previously been demonstrated that metal-organic framework (MOF) materials are capable of transporting charge and, as a result, facilitating catalytic reactions (Chapters 2 and 4). However, frameworks constructed of redox active metal centers, such as Co, are often not stable upon applied potentials due to conformational changes about the metal center associated with the redox reactions (Chapter 5). As a result, the catalytic mechanism degrades the framework, and metal-oxides, rather than the MOF, are responsible for the catalytic activity. Therefore, more stable frameworks prepared from structurally complex, redox inactive metal nodes, such as Zr, need to be explored for catalytic applications. Additionally, the incorporation of a homogeneous molecular catalyst into the framework backbone can be beneficial for several reasons: (1) it allows for better control over the active site surroundings; (2) possible degradation pathways associated with the homogeneous catalytic mechanism are removed due to the separation of molecules and rigidity of the framework; (3) a higher concentration of accessible active sites is

available on the electrode surface; (4) the reaction is not limited by the diffusion of catalyst to the electrode surface. With these ideas in mind, a framework can be designed that is capable of facilitating the desired catalytic reaction.

In this work, we demonstrate a new strategy for cooperative catalysis and proton abstraction via the incorporation of independent species competent in the desired reactivity into a MOF thin film. The MOF, designated as PCN-224-Ni, is constructed by Zr-oxo nodes and nickel(II) meso-tetrakis(4-carboxyphenyl)porphyrin (Ni(II)TCPP) linkers. Films of PCN-224-Ni were grown *in situ* on FTO and were found to electrochemically facilitate the water oxidation reaction at near neutral pH. The mechanism of water oxidation at PCN-224-Ni proceeds via initial oxidation of the porphyrin linker followed by binding of water to the Ni(II) of Ni(II)TCPP. Subsequent proton transfer to the Zr nodes enables the eventual release of O_2. Extensive characterization of films post-electrolysis revealed that the MOF is stable and retains its structure over the course of electrocatalysis.

6.2 Introduction

Increasing energy demands and steadily accumulating levels of detrimental greenhouse gases necessitates the continued search for alternative, renewable energy sources.[1] Solar energy has the capacity to power all of human civilization and therefore, has emerged as a leading carbon-neutral energy alternative.[2] However, two challenges remain in the harnessing of solar energy: (1) the intermittent nature of the sun necessitates energy storage technology, and (2) the cost of efficient solar cell installations provides a barrier to widespread adoption. Artificial photosynthesis – the direct conversion of sunlight into a stored fuel – is one possible method by which to overcome the first barrier. At the simplest level, an artificial photosynthetic system

must (1) absorb light, generating an excited state; (2) separate charge, resulting in long-lived redox equivalents, and (3) catalyze desired reactivity. The reactivity catalyzed is the oxidation of water and the reduction of either CO_2 or protons to yield a combustible fuel, Equations (6.1-6.4).

$$2H_2O \rightleftharpoons O_2 + 4H^+ + 4e^- \quad (6.1)$$

$$CO_2 + 6H^+ + 6e^- \rightleftharpoons CH_3OH + H_2O \quad (6.2)$$

$$CO_2 + 8H^+ + 8e^- \rightleftharpoons CH_4 + H_2O \quad (6.3)$$

$$2H^+ + 2e^- \rightleftharpoons H_2 \quad (6.4)$$

Akin to natural photosynthesis, a current thrust in catalyst development is to build proton management capabilities about the periphery of the catalytically active site. Indeed, proton management has been used to produce impressive enhancements in catalytic activity across all aspects of artificial photosynthesis – proton reduction,[3] CO_2 reduction,[4-6] and water oxidation.[7] The aforementioned reactions are proton-coupled electron transfer processes (PCET) with three possible reaction pathways to traverse: (1) proton transfer followed by electron transfer (PTET), (2) electron transfer followed by proton transfer (ETPT), or concerted PCET. Manipulation of the proton transfer pathway via the secondary coordination sphere directly affects kinetic and thermodynamic barriers. Therefore, at the simplest level reaction rates can increase, if proton-transfer is rate limiting. Alternatively, the balance between the barriers of PTET, ETPT, and PCET could shift such that the overall reaction mechanism is altered. Herein, we report an alternative to traditional catalyst approaches, metal-organic frameworks (MOFs), which provide a new paradigm for how to manipulate proton management and catalytic activity in heterogeneous electrocatalysis.

The properties and ease of design offered by MOFs presents a unique alternative to common water oxidation catalysts. MOFs are porous, 3D coordination polymers commonly

comprised of metal-oxo clusters bridged by organic linker molecules.[8] In this regard, MOFs bridge the gap between molecular and material based approaches to water oxidation. The pore size and environment, surface area, and morphology of MOFs can be synthetically tuned to generate ideal properties for a variety of applications. The porosity imparted by the size and geometry of the linkers, as well as the coordination sphere around the metal clusters affords MOFs an increased surface area and a higher density of accessible catalytic sites as compared to traditional catalysts.[9,10]

In particular, MOFs containing porphyrinic macrocycles as linkers are attractive due to the reactive nature of these molecules.[11-14] Porphyrin-based moieties are ubiquitous in nature, capable of catalyzing a wide range of reactions.[15-18] However, MOFs incorporating free-base and metallo-porphyrins are often limited by their structural stability in polar solvents, particularly water. Recently, this limitation has been addressed by the development of porphyrinic MOFs comprised of highly oxophilic metal ions, such as Zr^{4+} and Al^{3+} (e.g. PCN-222, 223, 224, 225, MOF-525, 545 and Al-PMOF), which provide considerable improvement in structural and chemical stabilities of the resulting frameworks.[19-26] Several of these porphyrinic MOFs have shown promise as electrocatalytic agents facilitating the reduction of CO_2.[18,27]

The chemical properties of metal clusters that comprise MOF structures also contribute to the overall framework reactivity. A high diversity of available metal ions and their synthetic tunability makes them attractive candidates as catalytic sites. In particular, Brønsted and Lewis acid/base properties of nodes, as well as coordinated guest molecules, such as water, have been previously utilized for the catalysis of a number of organic transformations.[28] Furthermore, additional reactive sites can be generated within the framework by doping with different metal ions[29] or through introduction of missing linker defects at the metal node.[30] Overall, there is a

considerable potential for engineering framework nodes and combining their properties with the organic linkers in order to achieve novel cooperative behavior.

In this report a porphyrin-containing MOF, PCN-224-M (PCN = porous coordination network, M = Ni^{2+}) constructed with nickel(II) meso-tetrakis(4-carbxyphenyl) porphyrin, Ni(II)TCPP, linkers is presented as an active water oxidation promoter. PCN-224-Ni is a Zr(IV)-based MOF in which the octahedral $Zr_6(\mu_3\text{-}O)_4(\mu_3\text{-}OH)_4(OH)_6(OH_2)_6(COO^-)_6$ secondary building units (SBUs) are connected by six Ni(II)TCPP ligands, forming two open channels with node-to-node diameters of 23.7 and 15.1 Å, respectively, and a pore diameter of ~19 Å (Figure 6.1 and 6.S1).[20] The open structure and large pores afford PCN-224-Ni a BET surface area of 2600 $m^2\,g^{-1}$, one of the largest amongst porphyrinic MOFs, and a total pore volume of 1.59 $cm^3\,g^{-1}$ as calculated from N_2 adsorption isotherms.[20] Due to the large surface area and pore volume of PCN-224-Ni, the high density of catalytic sites per area could be easily accessible by water molecules, which would result in considerably improved catalytic efficiency compared to non-porous heterogeneous catalysts. For example, in a film one unit cell thick, PCN-224-Ni has a density of *ca.* 8×10^{13} catalytic sites cm^{-2}, approximately 3 times greater than a monolayer of Ni(II)TCPP.

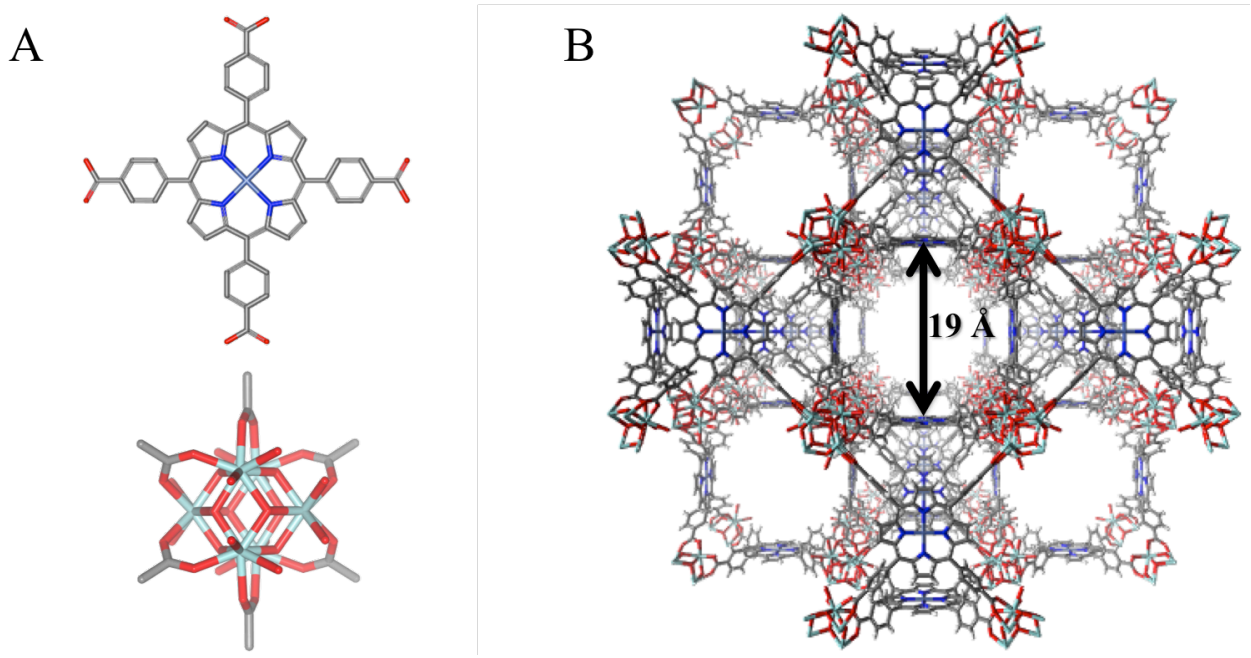

Figure 6.1. (A) Ni(II)TCPP linker (top) and the $Zr_6(\mu_3\text{-}O)_4(\mu_3\text{-}OH)_4(OH)_6(OH_2)_6(COO^-)_6$ secondary building unit of PCN-224-Ni (bottom); (B) PCN-224 structure with the Ni(II)-to-Ni(II) distance illustrated.[20] Hydrogen atoms have been omitted for clarity. Gray: C; Red: O; Blue: N; Green: Ni; Light Blue: Zr.

6.3 Experimental

6.3.1 Materials. The following reagents and solvents were purchased from the indicated commercial suppliers: propionic acid (99% Acros); pyrrole (Aldrich); methyl 4-formylbenzoate (Aldrich); zirconium chloride ($ZrCl_4$, ≥99.5%, Sigma Aldrich); meso-Tetra(4-carboxyphenyl)porphine (TCPP, Frontier Scientific); *N,N*-dimethylformamide (DMF; spectrophotometric grade, Spectrum); formic acid (reagent grade, ≥99.5%, Sigma Aldrich); nickel(II) chloride hexahydrate ($NiCl_2{\cdot}6H_2O$, 99.3% Alfa Aesar); fluorine-doped tin oxide (FTO, cleaned via sonication in Alconox/H_2O, isopropanol, acetone, then H_2O with rinsing with H_2O and drying in between, Hartford Glass); acetonitrile (distilled before use, HPLC grade, Spectrum); sodium perchlorate ($NaClO_4$; 99+%, Aldrich); tetrabutylammonium

hexafluorophosphate ($TBAPF_6$; recrystallized × 4 from ethanol, electrochemical grade, Fluka Analytical).

6.3.2 Synthesis of Ni(II)TCPP. Free-base 5,10,15,20-(4-carboxymethoxyphenyl)-porphyrin, H_2TMeCPP, was synthesized by the Adler method.[31] Briefly, a 1 L round bottom flask was charged with 500 mL of propionic acid, 9.3 mL pyrrole, and 21.8 g methyl 4-formylbenzoate, and the mixture refluxed for 12 h under N_2. After cooling to room temperature, the product was filtered and washed with acetone. Saponification of H_2TMeCPP to yield free-base 5,10,15,20-(4-carboxyphenyl)-porphyrin, H_2TCPP, was done by stirring 1.0 g H_2TMeCPP in THF (25 mL) and MeOH (25 mL) followed by the addition of aqueous KOH (2.63 g in 25 mL H_2O). The reaction mixture was refluxed for 16 h. After cooling to room temperature, the solvent was reduced under vacuum followed by the addition of 50 mL H_2O. This solution was acidified with 1 M HCl until no further precipitate was formed. The H_2TCPP solid was filtered and washed with H_2O. The metalloporphyrin, Ni(II)TCPP, was prepared by refluxing H_2TCPP (0.8 g) in 100 mL DMF with excess $NiCl_2 \cdot 6H_2O$ (2.5 g) for 6 h.[20,32] The crimson product was precipitated out by addition of water then filtered, washed with water, and allowed to dry: ^{1}H NMR (400 MHz, d_6-DMSO) δ – 8.11 (d, 8H), 8.29 (d, 8H), 8.73 ppm (s, 8H).

6.3.3 Synthesis of potassium salt of Ni(II)TCPP. 5,10,15,20-(4-carboxymethoxyphenyl)-porphyrin (H_2TMeCPP) (0.83 g, 0.918 mmol) was dissolved and THF (25 mL) and MeOH (25 mL) followed by the addition of aqueous KOH (2.63 g in 25 mL H_2O) The reaction mixture was refluxed for 16 h. After cooling to room temperature, the solvent was removed under vacuum resulting in a dark brown residue, which was suspended in EtOH (100 mL). The precipitate was isolated by vacuum filtration, washed with copious amounts of EtOH and THF and dried under vacuum giving a bright red solid: ^{1}H NMR (400 MHz, D_2O) δ – 7.33 (s, 8H), 7.93 (s, 8H),

8.06 ppm (s, 8H).

6.3.4 Synthesis of PCN-224 thin films. Films of the PCN-224 MOF[20] were prepared solvothermally. In a 6 dram glass vial, 30 mg $ZrCl_4$ and 10 mg Ni(II)TCPP (for PCN-224-Ni) or H_2TCPP (for PCN-224-fb) were dissolved in 10 mL DMF followed by the addition of 2 mL formic acid. A clean FTO slide was placed in the vial and heated to 120 °C for 16-18 h, after which time the vials were removed from the oven and allowed to cool to room temperature. The films were rinsed with fresh DMF and acetone and allowed to dry.

6.3.5 Characterization.

6.3.5.1 Powder X-ray diffraction (PXRD). PXRD measurements were performed on powder samples using a Rigaku MiniFlex 600 with Cu(Kα) radiation (Cu−Kα = 1.5418 Å). The PXRD experiments were carried out over a 2θ range of 3−60° in continuous scanning mode (10.0°/min) and a resolution of 0.1°.

6.3.5.2 Scanning electron microscopy imaging (SEM) and energy-dispersive X-ray analysis (EDX). A LEO (Zeiss) 1550 field-emission scanning electron microscope, equipped with an in-lens detector, operating at 5.0 kV was used for high-resolution images of the thin films. EDX was collected using a built in Oxford INCA E2H X-ray Energy Dispersive Spectrometer (EDS) system with a Silicon Drifted detector.

6.3.5.3 X-ray photoelectron spectroscopy (XPS). XPS measurements were collected using a PHI 5000 Versa Probe III spectrometer with an aluminum anode X-ray source and photon energy of 1486.6 eV. Survey spectra were collected using a 200 μm beam size at 50 W and 15 kV, scanning a range from 1100 eV to 0 eV at a pass energy of 224.0 eV and a step size of 0.8 eV/step. Elemental peak data were collected using a 100 μm beam size at 25 W and 15 kV with a pass energy of 69.0 eV and a step size of 0.1250 eV/step. The emitted photoelectrons were

detected by a 32-channel hemispherical analyzer, and the operating pressure of the main chamber was below 10^{-7} Pa during the time of measurement.

6.3.5.4 Inductively Coupled Plasma−Mass Spectrometry (ICP-MS). The PCN-224-Ni thin films were digested in 70% nitric acid and heated to 90 °C for 1 h. After filtration through a syringe filter (<0.2 μM), the solution was diluted with water so that the final concentration of nitric acid was 7% by volume. All samples were analyzed for nickel and zirconium content using a Thermo Electron X-Series inductively coupled plasma mass spectrometer (ICP-MS) in accordance with Standard Method 3125-B.

6.3.6 Electrochemistry. Electrochemical experiments were performed on a Basi EC epsilon potentiostat using a Ag/AgCl (aqueous saturated KCl) reference electrode. The Ag/AgCl electrode was calibrated against $Fe(CN)_6^{3-}/Fe(CN)_6^{4-}$, where the expected $E_{1/2}$ is +560 mV vs. NHE.[33] For all aqueous electrochemical experiments, 18.3 mΩ–cm ultrapure water was obtained using a Barnstead EASYpure UV system.

6.3.6.1 Cyclic Voltammetry (CV). CV measurements were collected in a three-electrode arrangement using Pt mesh as a counter electrode, Ag/AgCl reference electrode, and PCN-224-Ni/FTO as working electrode. The scan rate was varied over the range of 25-800 mV/s.

6.3.6.2 Square-Wave Voltammetry (SWV). SWV measurements were collected in the electrochemical cell described above with a 1 mV step size, 100 mV amplitude, and 3 Hz frequency.

6.3.6.3 pH Dependence. The pH dependence of PCN-224-Ni current density of was performed in the electrochemical cell described above in aqueous 0.1 M $NaClO_4$ electrolyte. Electrodes were immersed in the solution and a potential of 1500 mV vs. NHE was applied. The

current density was taken after steady-state current was reached after 5 minutes.

6.3.6.4 Tafel Analysis. A potential jump experiment was set up using aqueous 0.1 M $NaClO_4$ electrolyte in the standard three-electrode arrangement described above. Overpotentials ($\eta = V - E^o$) ranging from η = 400 to 800 mV were applied with 50 mV steps. The current was allowed to equilibrate for 5 min.

6.3.6.5 Oxygen Evolution. Controlled potential electrolysis (CPE) experiments were performed in a homemade two-compartment bulk electrolysis glass cell. One compartment housed the PCN-224-Ni/FTO working electrode, Ag/AgCl reference electrode, and dissolved oxygen probe, whereas the counter electrode was housed in the secondary compartment separated by a finely porous glass frit. The cell was purged with Argon and sealed prior to experiments. The evolution of oxygen was monitored in solution using a Unisense OXY-Meter.

6.3.7 Hydrogen peroxide test. WaterWorks Peroxide Check H_2O_2 indicator strips were used and immersed into the electrolyte solution after the CPE experiment. The color code was used to estimate the H_2O_2 concentration.

6.4 Results and Discussion

6.4.1 Synthesis and Structural Characterization

While there have been three reports of MOFs as water oxidation catalysts, the work reported herein demonstrates the first example of cooperative chemistry driven by the combination of an active, catalytic linker and proton-accepting node in a MOF thin film formed *in situ*.[34-36] The PCN-224-Ni thin films have been prepared by a solvothermal reaction on fluorine-doped tin oxide (FTO) conductive substrates. The heterogeneous MOF catalyst is active towards the oxidation of water at near neutral pH with Faradaic efficiencies consistent with that

of the Ni(II)TCPP in solution. PCN-224-Ni films produced significantly more oxygen compared to films prepared with the non-metallated (or free-base) H_2TCPP ligand, designated as PCN-224-fb. Films were prepared via incubation of a FTO substrate in a solvothermal reaction containing $ZrCl_4$ and Ni(II)TCPP (for PCN-224-Ni) or H_2TCPP (for PCN-224-fb) in the presence of formic acid as a modulator. Powder X-ray diffraction (PXRD) was used to confirm the structure of the MOF powder, which was consistent with the PCN-224 topology (Figure 6.2A).[20] SEM imaging of the films shows crystallite features consistent with the cubic PCN-224 unit cell with a film thickness of *ca.* 30 µm (Figure 6.2B-D).

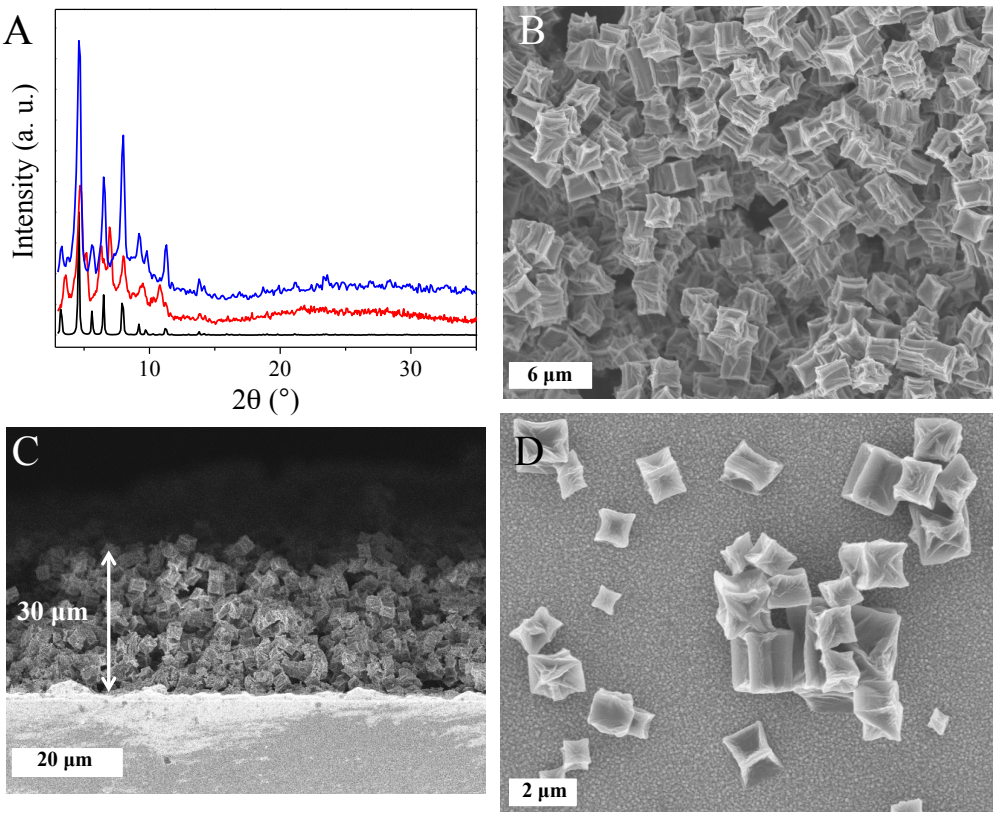

Figure 6.2. (A) PXRD pattern of simulated PCN-224-Ni from single crystal data[20] (black), synthesized PCN-224-fb (red), and PCN-224-Ni (blue) powders; (B) SEM of PCN-224-Ni film; (C) SEM image of solvothermally prepared PCN-224-Ni on FTO showing a film thickness of *ca.* 30 µm; (D) SEM of PCN-224-fb film.

6.4.2 Electrochemical Characterization

The catalytic activity of PCN-224-Ni for water oxidation was investigated using electrochemical techniques. Cyclic voltammetric analysis of PCN-224-Ni under aqueous conditions revealed a rapid increase in current at 1.0 V vs. NHE (Figure 6.3A, blue). The PCN-224-Ni current was significantly larger in magnitude compared to FTO (Figure 6.3A, black) and the non-metallated PCN-224-fb film (Figure 6.3A, red) and consistent with catalytic behavior. Square-wave voltammetry (SWV) of the films (Figure 6.3B, blue and S2) reveals an underlying broad electrochemical signature at 1.05 V vs. NHE attributed to the formation of a porphyrin cation radical species $[Ni^{II}TCPP]^{+\bullet}$, which is in thermal equilibrium with $[Ni^{III}TCPP]^{+}$. This process is overlapped with a second electrochemical event attributed to formation of the dication radical $[Ni^{III}TCPP]^{2+\bullet}$.[37,38] The oxidation of the porphyrin macrocycle to generate the initial radical species was also observed with PCN-224-fb films (Figure 6.3B, red).[39,40]

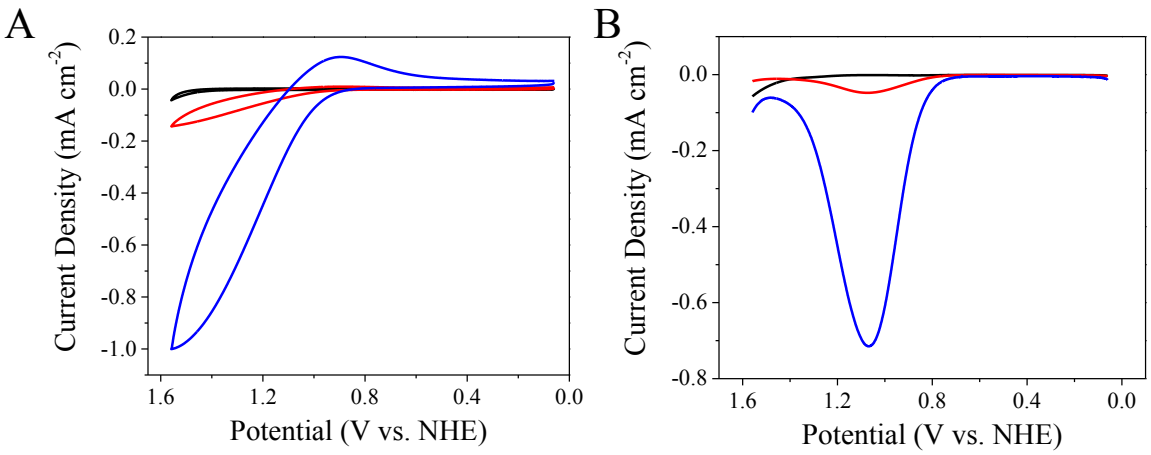

Figure 6.3. (A) Cyclic voltammetry at 100 mV/s and (B) Square wave voltammetry of FTO (black), PCN-224-fb (red), and PCN-224-Ni (blue) in aqueous 0.1 M $NaClO_4$.

The dependence of pH on the PCN-224-Ni water oxidation mechanism was determined by taking steady-state current measurements at constant potential in aqueous electrolyte (0.1 M $NaClO_4$). The pH of the solution was adjusted using 0.1 M $HClO_4$ and 0.1 M NaOH. PCN-224-Ni was found to demonstrate no dependence on proton concentration (Figure 6.4A). This behavior is attributed to the fact that the redox-activity of the metalloligand is dominated by the $[Ni^{II}TCPP]^{0/+\bullet}$ process, which was reported to be pH independent for an analogous compound in solution.[38] The current-voltage (Tafel) behavior of PCN-224-Ni was investigated over a 200 mV overpotential range in 50 mV increments (Figure 6.4B). From the onset of linearity in the Tafel plot, the overpotential for the water oxidation reaction was determined to be 450 mV. The Tafel slope obtained from the linear portion was 150 mV $decade^{-1}$ with a corresponding exchange current density (j_o) of 7.7×10^{-10} A cm^{-2}, which are similar to other heterogeneous water oxidation catalysts.[41-45] The Tafel slope is indicative of an EC catalytic mechanism, consistent with electrochemical oxidation of the porphyrin macrocycle and Ni(II) metal centers followed by a chemical step.[46,47]

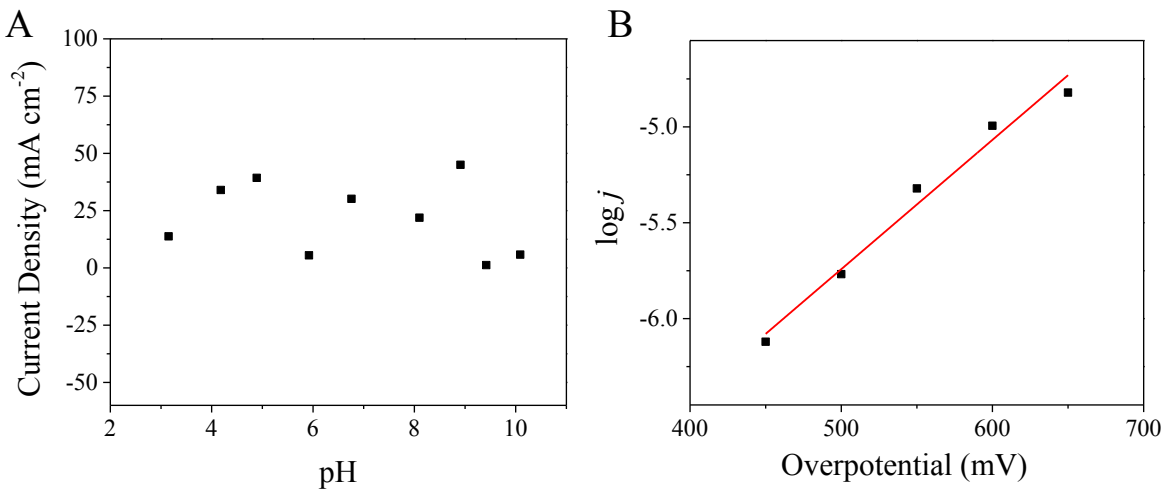

Figure 6.4. (A) pH dependence of steady-state catalytic current density at constant potential (E_{appl} = 1500 mV vs. NHE) for PCN-224-Ni in aqueous 0.1 M $NaClO_4$; (B) Tafel plot of PCN-224-Ni in aqueous 0.1 M $NaClO_4$. Due to film variations (e.g., amount of MOF on the surface and available Ni centers, electrical contact, etc.), the error associated with the current densities is ±10%.

Under non-aqueous conditions ($TBAPF_6/CH_3CN$), the CVs of PCN-224-Ni exhibit a weak oxidation wave at 1.75 V vs. NHE, which appears as a shoulder on the backgrounds current (Figure 6.5A) assigned to the $[Ni^{II}TCPP]^{0/+\bullet}$ process. The plot of log(j) vs. log(ν) (where j = current density and ν = scan rate) showed a linear trend with the slope of 0.6 (Figure 6.5B). This relationship suggests diffusion limited electron transport through the film, which likely occurs by a charge hopping mechanism between the porphyrin moieties. A similar behavior has been observed previously for porphyrin-based MOF electrodes.[18,27,48] The water oxidation activity of PCN-224-Ni was supported by the increase in catalytic current with increasing water additions (Figure 6.5C). The catalytic current density was found to increase linearly with $[H_2O]^{1/2}$, suggesting a first order reaction with respect to water (Figure 6.5D and S3).[49]

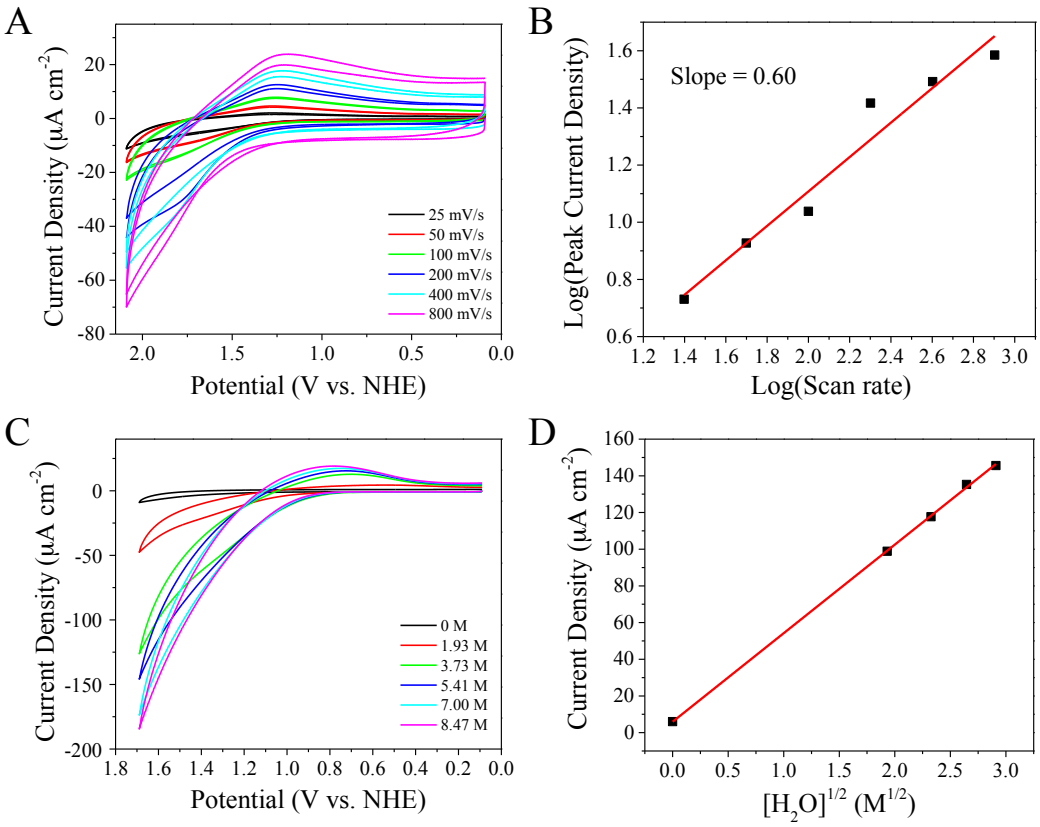

Figure 6.5. (A) CV of PCN-224-Ni in 0.1 M $TBAPF_6/CH_3CN$ as a function of scan rate; (B) A plot of the log (Peak Current Density) vs. log (Scan Rate) gives a slope of 0.6, suggesting diffusion limiting electrochemical behavior; (C) CV of PCN-224-Ni in 0.1 M $TBAPF_6/CH_3CN$ (black) with increasing H_2O concentrations; (D) Plot of Current Density at 1.6 V (vs. NHE) vs. $[H_2O]^{1/2}$ demonstrates a linear relationship. Due to film variations (e.g., amount of MOF on the surface and available Ni centers, electrical contact, etc.), the error associated with the current densities is ±10%.

Controlled potential electrolysis (CPE) was performed on PCN-224-Ni in aqueous 0.1 M $NaClO_4$ at an applied potential of 1500 mV vs. NHE for 60 min. PCN-224-Ni maintained a higher current compared to bare FTO and PCN-224-fb films (Figure 6.6A), as well as increased oxygen production (Figure 6.6B). The fact that the Ni analogue generated significantly higher current than the free base MOF indicates that the Ni(II) center is critical to the observed electrocatalytic activity. Interestingly, the deposition of the free base PCN-224 on FTO resulted

in lower current compared to the unmodified FTO electrode, which suggests that PCN-224-fb forms an insulating layer and inhibits the activity of FTO. From this behavior it can also be concluded that the other components of the PCN-224 framework, such as Zr-oxo nodes, are inactive in the redox processes.

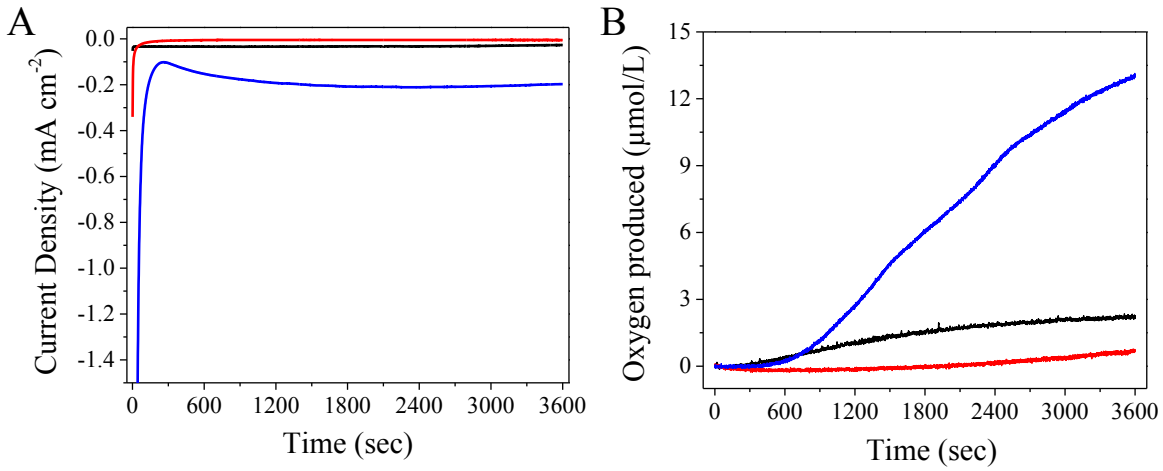

Figure 6.6. (A) Controlled potential electrolysis (CPE) at 1500 mV vs. NHE in aqueous 0.1 M $NaClO_4$ and (B) Oxygen evolved during CPE experiment of FTO (black), PCN-224-fb (red), and PCN-224-Ni (blue).

The Faradaic efficiency of PCN-224-Ni was conserved with that of the Ni(II)TCPP ligand in solution under the same conditions (Figure 6.7). However, the efficiency was less than that of the similar water-soluble catalyst due to the mechanistic importance of phosphate buffer used in their study (*vide infra*).[38]

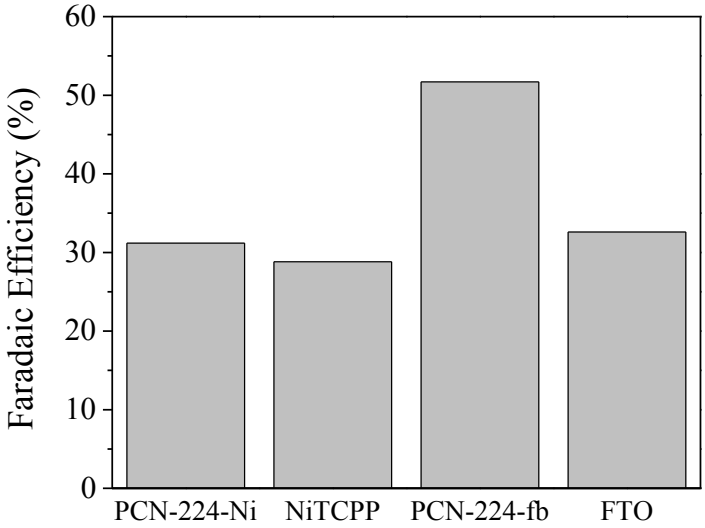

Figure 6.7. Faradaic efficiencies after electrolysis at 1500 mV vs. NHE in aqueous 0.1 M $NaClO_4$.

The turnover frequency (TOF) of PCN-224-Ni was determined by digesting the MOF films in concentrated HNO_3 followed by ICP analysis for nickel content (Table 6.1). The TOF was calculated under the assumption that all Ni centers of the film are catalytically active, which is an overestimation, and therefore, representative of the lower limit of TOF (Equation (6.5)). That said, the TOF for PCN-224-Ni was found to be 2 (±1) × 10^{-4} s^{-1}.

$$TOF = \frac{mol\ O_2}{(mol\ Ni(II)TCPP)\times(electrolysis\ duration)} \tag{6.5}$$

Given Faradaic efficiencies < 100% for O_2 production by PCN-224-Ni films, the alternative 2 electron reaction pathway resulting in H_2O_2 was considered. The immersion of indicator strips into the electrolyte at the end of electrolysis experiment did not detect any noticeable amount of H_2O_2, which means that its concentration in solution is below 0.5 mg L^{-1}. A similar lack of peroxide formation was reported by Han et al. for a water-soluble Ni(II)

porphyrin electrocatalyst, suggesting that O_2 is the primary product of water oxidation in this case.[38]

Table 6.1. Summary of ICP-MS data for digested PCN-224-Ni films and solutions.

Sample	Ni (mol)	Zr (mol)	Zr:Ni
PCN-224-Ni as synthesized	4.63×10^{-7}	2.38×10^{-6}	5.15:1
PCN-224-Ni post-electrolysis	$3.05 (\pm 1.22) \times 10^{-7}$	$1.44 (\pm 0.59) \times 10^{-6}$	4.71:1
Solution post-electrolysis	$2.37 (\pm 1.16) \times 10^{-8}$	$2.62 (\pm 0.74) \times 10^{-8}$	1.23:1

Since the nickel center of the Ni(II)TCPP linkers serves as the active catalytic site within the MOF, the mechanism for water oxidation by PCN-224-Ni is expected to proceed via similar reaction steps to that of a homogeneous Ni(II) porphyrin in solution. Due to the rigid nature of the PCN-224-Ni MOF and the fact that the distances between Ni(II)-centers within the framework are ~19 Å between co-facial porphyrins lining the same channel and ~14 Å between orthogonal porphyrins of the same channel (Figure 6.S1), it is unlikely that the catalytic mechanism involves interactions between neighboring Ni(II) porphyrins. It has been proposed previously by Han *et al*. for a cationic, water soluble Ni(II) tetrakis(4-*N*-methylpyridil)porphyrin molecular catalyst that the first step of the catalytic cycle is the oxidation of the porphyrin to generate the radical cation species, $Por^{\bullet+}$-Ni(II).[38] This mechanistic step is supported by the Tafel analysis, which suggests that an electrochemical reaction occurs as the necessary first step. The porphyrin oxidation is followed by binding of a water molecule to the Ni(II) metal center

(Scheme 6.1) to generate $Por^{\bullet+}$-Ni(II)-OH_2. Sequential proton and electron transfer reactions result in the deprotonation of the coordinated water molecule with concomitant oxidation of the Ni(II) center to give the hydroxide bound species, $Por^{\bullet+}$-Ni(III)-OH. The intramolecular electron transfer from the hydroxide to the porphyrin ring coupled with the abstraction of a proton gives rise to Por-Ni(III)-$O^{\bullet}$. Following the O–O bond formation step, the peroxide bound species, Por-Ni(II)-OOH, is generated, which undergoes another proton-coupled electron transfer reaction to give Por-Ni(II)-$OO^{\bullet}$. The final oxidation process results in the release of O_2 and the regeneration of the starting Por-Ni(II) complex.[38]

Proton management is required for catalysts to operate at neutral pH.[50] At pH 7, water is a very weak base and present at too low of a concentration (1×10^{-7} M) to effectively fill the role of proton acceptor. In this sense, the mechanism of PCN-224-Ni and the homogeneous catalyst differ dramatically. Computational modeling of the homogeneous catalyst performed by Han *et al*. indicated that the O–O bond formation and subsequent deprotonation proceeds via a low energy route when mediated by an added molecular base, such as phosphate or acetate. Both of these weak bases are incompatible with the PCN-224-Ni framework. However, with the Ni(II) porphyrin situated inside the framework another possibility presents itself. It was recently reported by Hupp *et al.* that Zr-oxo nodes in related PCN and UiO MOFs could act as proton acceptors, particularly coordinated water ($Zr–OH_2$) and hydroxyl (Zr–OH) species for which pK_a values were measured in 5.71-6.80 and 8.11-8.32 ranges, respectively.[51] Therefore, we propose that the Zr-oxo nodes serve as the proton acceptors in a cooperative fashion with the linker catalyst, providing a new class of secondary proton management possibilities. To our knowledge, this is the first example of cooperative linker-node interactions that promote chemistry not possible under different constructs.

The coordinated water ($Zr–OH_2$) and hydroxyl (Zr–OH) groups typically originate at missing-linker defect sites, however, Zr-oxo clusters inside PCN-224-Ni already contain 6 terminal oxygen atoms, each of which could potentially accept protons from the water oxidation reaction. The number of available Zr-oxo nodes present in the framework is limited (node:linker ratio is 2:3) and is only sufficient to complete one electrochemical cycle, assuming that each node can accept 6 protons and each linker generates 4 protons per cycle. This limitation would account for the low TON observed (0.72) during the electrolysis experiment. It is also possible that Zr-oxo clusters merely serve as conduits and the proton is transferred to the bulk water. The exact role of the nodes in the electrochemical oxidation of water by Ni(II)TCPP remains elusive and studies are underway to gain deeper insights into the nature of proton transfer in this MOF. That said, the prospect of cooperative behavior between redox-active linkers and Brønsted basic SBUs could lead to the development of novel MOF-based electrocatalysts.

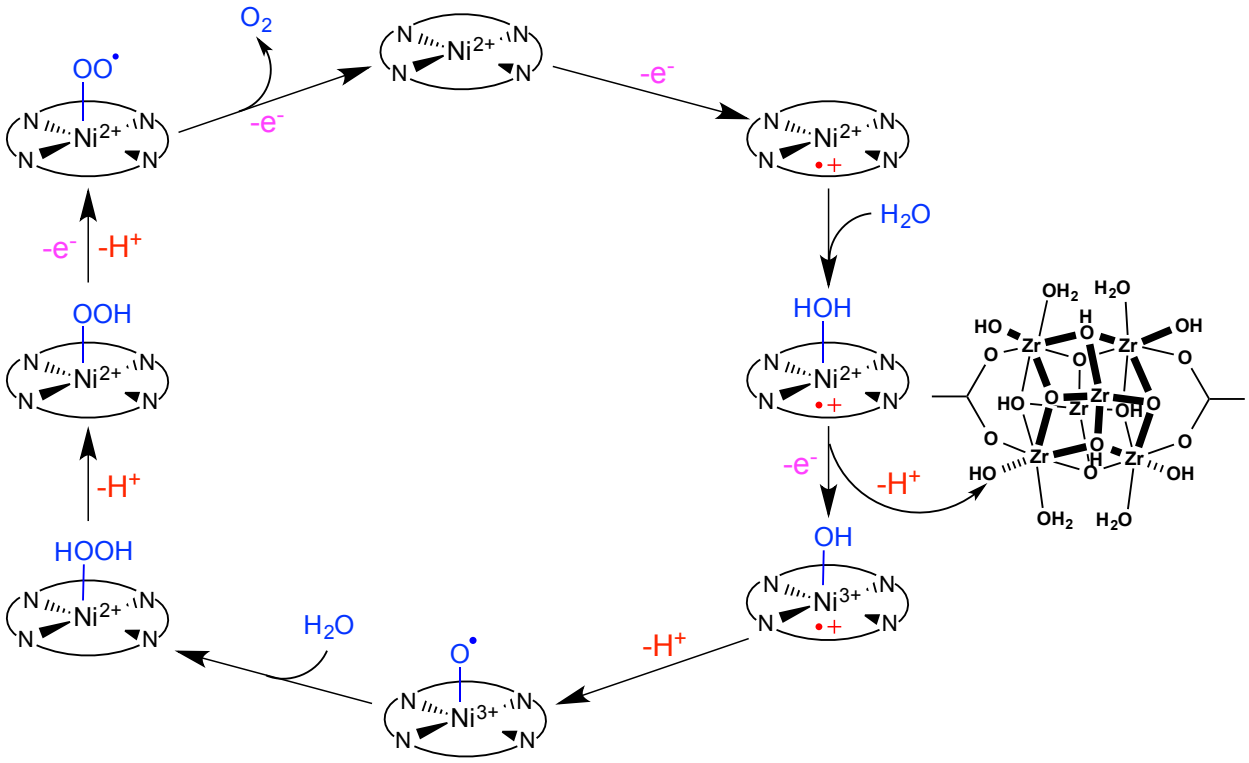

Scheme 6.1. Proposed mechanism for the electrochemical water oxidation reaction catalyzed by PCN-224-Ni.[38] Some carboxylate groups have been omitted from the Zr node for clarity.

Thorough stability investigations are crucial in establishing that the MOF is indeed an active electrocatalytic species and not merely acting as a precursor for its formation, as metal ions often undergo considerable rearrangements of their coordination spheres during the redox cycling. This has been demonstrated in the Co-based ZIF-67, which is comprised of redox-active metal nodes that underwent irreversible decomposition upon anodic potentials.[52] Therefore, certain porphyrin-containing frameworks, such as $[Pb_2(H_2TCPP)]\cdot 4DMF\cdot H_2O$, despite showing electrocatalytic activity towards water oxidation, are less likely to retain their structure during the electrolysis.[34] To the best of our knowledge, only 3 examples of intrinsic MOF water oxidation electrocatalysts were reported in the literature to date.[34-36] Within these reports, however, extensive characterization of the framework pre- and post-electrolysis is lacking. In the case of

nickel-based systems, electrocatalytically-active oxide and hydroxide films have been formed from soluble nickel complexes at the oxidative potentials used for water oxidation experiments.[53,54] As a result, the present work provides a detailed characterization of the MOF and demonstrates the stability of the PCN-224-Ni films towards electrolysis conditions using several characterization techniques.

X-ray photoelectron spectroscopy (XPS) was applied to identify the binding environments of Ni and N within the frameworks pre- and post-electrolysis (Figure 6.8A-B). The position of the Ni2p peak is expected to change with different oxidation state or binding environment, which could be attributed to degradation of the MOF and formation of nickel oxides or nickel hydroxides on the surface.[55,56] The signals obtained for the PCN-224-Ni films are of low intensity due to the low concentrations of both Ni and N within the MOF and the area being analyzed. Despite this limitation, it appears that the position of the Ni2p peak remained largely unchanged before and after electrolysis (Figure 6.8A). Furthermore, the appearance of the N1s peak in the post-electrolysis film confirms the presence of porphyrin linker molecule (Figure 6.8B). In addition, SEM images (Figure 6.8C-D) showed that MOF particles retained their size and morphology, while the formation of metal-oxide particles as a result of electrolysis would be apparent in conformational changes of the crystallites.[54] Thus, the MOF particles did not undergo any solid-solid transformations or dissolution. These results suggest that the Ni(II)TCPP core did not experience any significant coordination geometry rearrangements or degradation to form oxides as a result of electrolysis.

Further analysis on digested PCN-224-Ni films after electrolysis via ICP found the Zr:Ni ratio to be 4.71:1, which is comparable to the ratio found in the as-synthesized framework (the theoretical Zr:Ni ratio should be 4:1 in based on the molecular formula of PCN-224-Ni,

$C_{144}H_{72}N_{12}O_{64}Ni_3Zr_{12}$).[20] These results suggest that the MOF remaining on FTO after electrolysis is indeed PCN-224-Ni. Additionally, the amounts of Ni and Zr detected in solution post-electrolysis represent 7.2% and 1.8% of the total contents of the MOF films, respectively (Table 6.1). This result could be attributed to the detachment of mechanically-bound MOF particles from FTO substrate into solution.

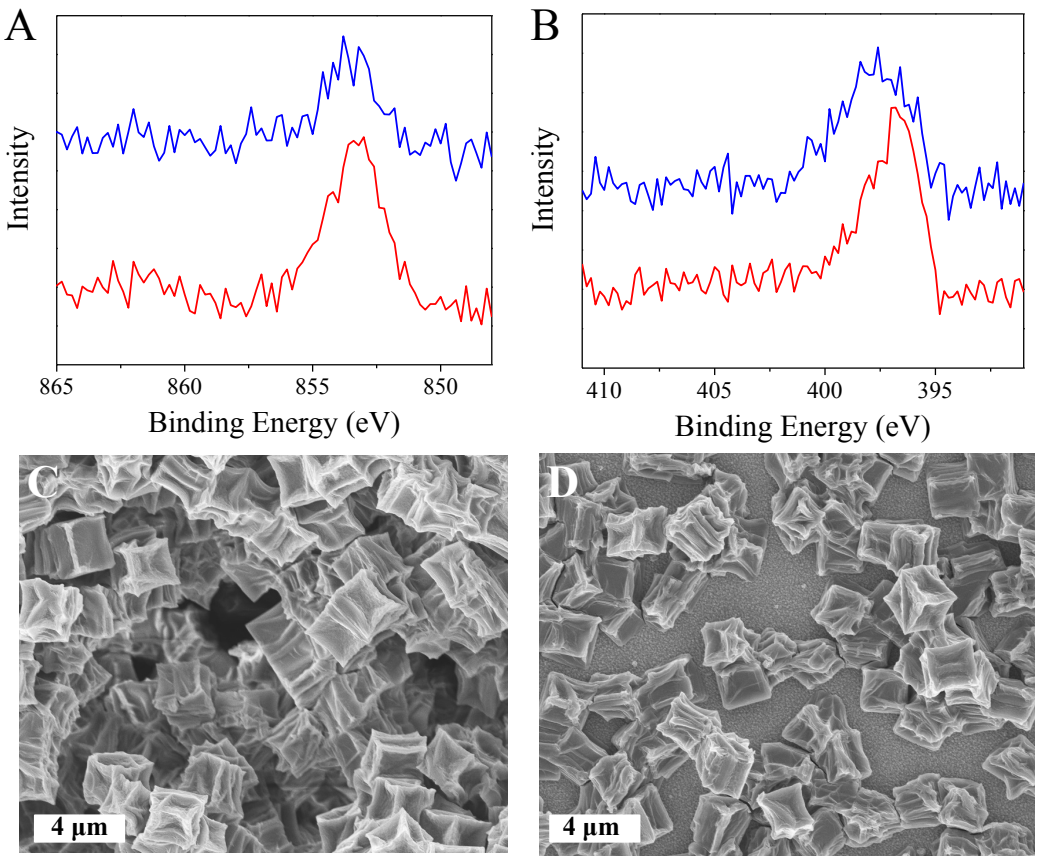

Figure 6.8. XPS of PCN-224-Ni films pre- (red) and post- (blue) electrolysis experiments displaying (A) Ni2p3 and (B) N1s binding energy; SEM images of PCN-224-Ni films pre- (C) and post- (D) electrolysis.

6.5 Conclusions

To summarize, the Zr(IV)-based MOF with Ni(II)TCPP linkers, PCN-224-Ni, was grown solvothermally onto conductive FTO substrates and shown to be capable of electrochemically oxidizing water. The mechanism of water oxidation was found to be best described by a rate-determining electrochemical step followed by a chemical reaction with Ni(II)TCPP playing the role of the active catalytic sites and Zr nodes acting as proton abstractors. The work demonstrates the ability to promote unique reactivity within MOFs through the dual design of both the linker and node. The structure of the PCN-224-Ni was found to remain intact during the electrochemical reaction. As such, incorporation of active molecular catalysts into highly robust Zr-based scaffolds can be used as a viable strategy for the design of electrocatalytic frameworks. These results have allowed for a deeper understanding of desirable properties and mechanistic insight for the future design of stable catalysts for the water oxidation reaction.

6.6 Acknowledgements

This material is based upon work supported by U.S. Department of Energy, Office of Basic Energy Sciences under Award Number DE-SC0012446.

6.7 Supplemental Information

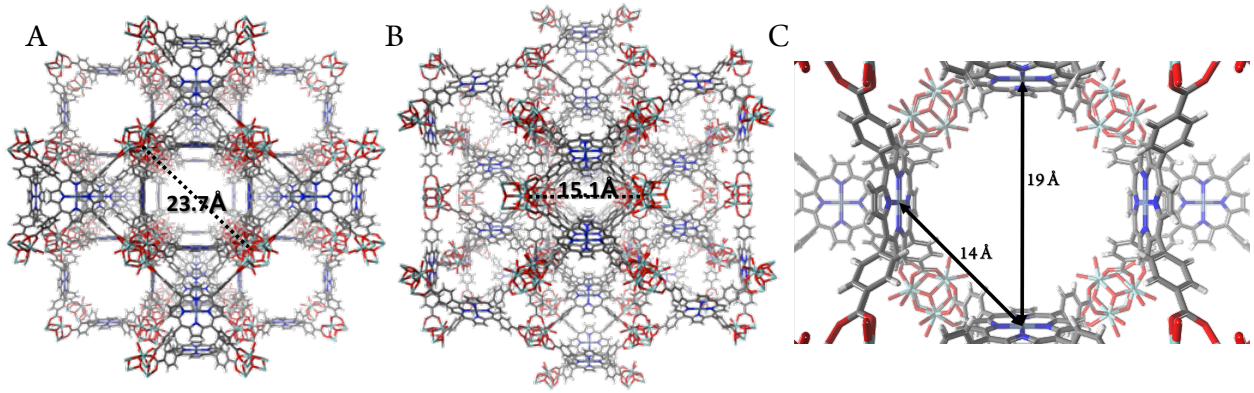

Figure 6.S1. The distances between Zr nodes of PCN-224-Ni shown in (A) and (B). (C) The distances between Ni(II)-to-Ni(II) metal centers of co-facial and orthogonal porphyrins within the same channel.[20]

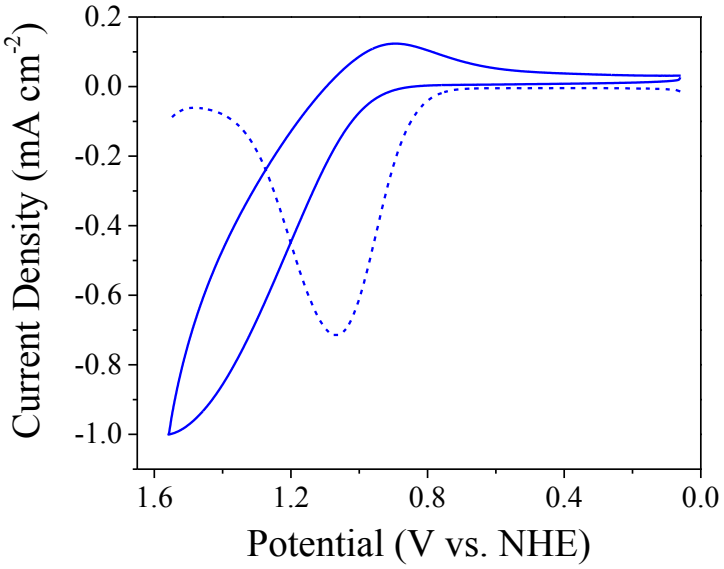

Figure 6.S2. CV (solid blue) and SWV (dash blue) of PCN-224-Ni in aqueous 0.1 M $NaClO_4$.

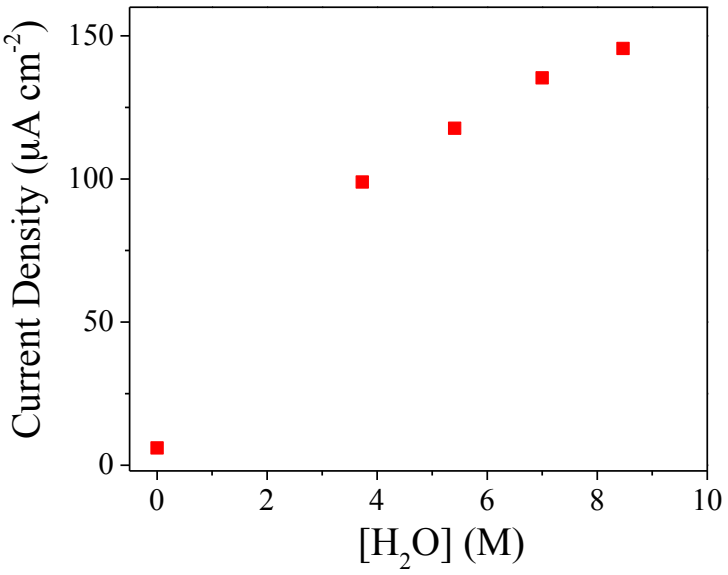

Figure 6.S3. Plot of Current density vs. [H_2O] generated from CVs of PCN-224-Ni in 0.1 M $TBAPF_6/CH_3CN$ with increasing H_2O concentrations.

6.8 References

(1) Lewis, N. S. *Chem. Rev.* **2015**, *115*, 12631.
(2) Lewis, N. S.; Nocera, D. G. *Proc. Natl. Acad. Sci. U. S. A.* **2006**, *103*, 15729.
(3) Lee, C. H.; Dogutan, D. K.; Nocera, D. G. *J. Am. Chem. Soc.* **2011**, *133*, 8775.
(4) Costentin, C.; Drouet, S.; Robert, M.; Savéant, J.-M. *Science* **2012**, *338*, 90.
(5) DuBois, D. L. *Inorg. Chem.* **2014**, *53*, 3935.
(6) Raebiger, J. W.; Turner, J. W.; Noll, B. C.; Curtis, C. J.; Miedaner, A.; Cox, B.; DuBois, D. L. *Organometallics* **2006**, *25*, 3345.
(7) Zhao, Y.; Swierk, J. R.; Megiatto, J. D., Jr.; Sherman, B.; Youngblood, W. J.; Qin, D.; Lentz, D. M.; Moore, A. L.; Moore, T. A.; Gust, D.; Mallouk, T. E. *Proc. Natl. Acad. Sci. U. S. A.* **2012**, *109*, 15612.
(8) Eddaoudi, M.; Kim, J.; Rosi, N.; Vodak, D.; Wachter, J.; O'Keeffe, M.; Yaghi, O. M. *Science* **2002**, *295*, 469.
(9) Farrusseng, D.; Aguado, S.; Pinel, C. *Angew. Chem. Int. Ed.* **2009**, *48*, 7502.
(10) Lee, J. Y.; Farha, O. K.; Roberts, J.; Scheidt, K. A.; Nguyen, S. B. T.; Hupp, J. T. *Chem. Soc. Rev.* **2009**, *38*, 1450.
(11) Zha, Q. Z.; Rui, X.; Wei, T. T.; Xie, Y. S. *CrystEngComm* **2014**, *16*, 7371.
(12) Gao, W. Y.; Chrzanowski, M.; Ma, S. Q. *Chem. Soc. Rev.* **2014**, *43*, 5841.
(13) Zha, Q.; Rui, X.; Wei, T.; Xie, Y. *CrystEngComm* **2014**, *16*, 7371.
(14) Guo, Z.; Chen, B. *Dalton Trans.* **2015**, *44*, 14574.

(15) Bhugun, I.; Lexa, D.; Saveant, J.-M. *J. Am. Chem. Soc.* **1996**, *118*, 1769.
(16) Grinstaff, M. W.; Hill, M. G.; Labinger, J. A.; Gray, H. B. *Science* **1994**, *264*, 1311.
(17) Kadish, K., Guilard, R., Smith, K. *The Porphyrin Handbook*; Academic Press, 2003.
(18) Hod, I.; Sampson, M. D.; Deria, P.; Kubiak, C. P.; Farha, O. K.; Hupp, J. T. *ACS Catal.* **2015**, *5*, 6302.
(19) Feng, D.; Gu, Z. Y.; Li, J. R.; Jiang, H. L.; Wei, Z.; Zhou, H. C. *Angew. Chem.* **2012**, *124*, 10453.
(20) Feng, D.; Chung, W.-C.; Wei, Z.; Gu, Z.-Y.; Jiang, H.-L.; Chen, Y.-P.; Darensbourg, D. J.; Zhou, H.-C. *J. Am. Chem. Soc.* **2013**, *135*, 17105.
(21) Deibert, B. J.; Li, J. *Chem. Commun.* **2014**, *50*, 9636.
(22) Zheng, J.; Wu, M.; Jiang, F.; Su, W.; Hong, M. *Chem. Sci.* **2015**, *6*, 3466.
(23) Fateeva, A.; Chater, P. A.; Ireland, C. P.; Tahir, A. A.; Khimyak, Y. Z.; Wiper, P. V.; Darwent, J. R.; Rosseinsky, M. J. *Angew. Chem.* **2012**, *124*, 7558.
(24) Feng, D.; Gu, Z.-Y.; Chen, Y.-P.; Park, J.; Wei, Z.; Sun, Y.; Bosch, M.; Yuan, S.; Zhou, H.-C. *J. Am. Chem. Soc.* **2014**, *136*, 17714.
(25) Morris, W.; Volosskiy, B.; Demir, S.; Gándara, F.; McGrier, P. L.; Furukawa, H.; Cascio, D.; Stoddart, J. F.; Yaghi, O. M. *Inorg. Chem.* **2012**, *51*, 6443.
(26) Yuan, S.; Liu, T.-F.; Feng, D.; Tian, J.; Wang, K.; Qin, J.; Zhang, Q.; Chen, Y.-P.; Bosch, M.; Zou, L.; Teat, S. J.; Dalgarno, S. J.; Zhou, H.-C. *Chem. Sci.* **2015**, *6*, 3926.
(27) Kornienko, N.; Zhao, Y.; Kley, C. S.; Zhu, C.; Kim, D.; Lin, S.; Chang, C. J.; Yaghi, O. M.; Yang, P. *J. Am. Chem. Soc.* **2015**, *137*, 14129.
(28) Herbst, A.; Khutia, A.; Janiak, C. *Inorg. Chem.* **2014**, *53*, 7319.
(29) Lammert, M.; Wharmby, M. T.; Smolders, S.; Bueken, B.; Lieb, A.; Lomachenko, K. A.; Vos, D. D.; Stock, N. *Chem. Commun.* **2015**, *51*, 12578.
(30) Vermoortele, F.; Bueken, B.; Le Bars, G.; Van de Voorde, B.; Vandichel, M.; Houthoofd, K.; Vimont, A.; Daturi, M.; Waroquier, M.; Van Speybroeck, V.; Kirschhock, C.; De Vos, D. E. *J. Am. Chem. Soc.* **2013**, *135*, 11465.
(31) Adler, A. D.; Longo, F. R.; Finarelli, J. D.; Goldmacher, J.; Assour, J.; Korsakoff, L. *J. Org. Chem.* **1967**, *32*, 476.
(32) Adler, A. D.; Longo, F. R.; Kampas, F.; Kim, J. *J. Inorg. Nucl. Chem.* **1970**, *32*, 2443.
(33) Bard, A. J.; Faulkner, L. R. *Electrochemical Methods*; 2nd ed.; John Wiley & Sons, Inc.: New York, 2001.
(34) Dai, F.; Fan, W.; Bi, J.; Jiang, P.; Liu, D.; Zhang, X.; Lin, H.; Gong, C.; Wang, R.; Zhang, L.; Sun, D. *Dalton Trans.* **2016**, *45*, 61.
(35) Wang, S.; Hou, Y.; Lin, S.; Wang, X. *Nanoscale* **2014**, *6*, 9930.
(36) Flügel, E. A.; Lau, V. W. h.; Schlomberg, H.; Glaum, R.; Lotsch, B. V. *Chem. Eur. J.* **2016**, *22*, 3676.
(37) Chang, D.; Malinski, T.; Ulman, A.; Kadish, K. M. *Inorg. Chem.* **1984**, *23*, 817.
(38) Han, Y. Z.; Wu, Y. Z.; Lai, W. Z.; Cao, R. *Inorg. Chem.* **2015**, *54*, 5604.
(39) Kalyanasundaram, K.; Neumannspallart, M. *J. Phys. Chem.* **1982**, *86*, 5163.
(40) Renner, M. W.; Fajer, J. *J. Biol. Inorg. Chem.* **2001**, *6*, 823.
(41) Dey, S.; Mondal, B.; Dey, A. *Phys. Chem. Chem. Phys.* **2014**, *16*, 12221.
(42) Esswein, A. J.; Surendranath, Y.; Reece, S. Y.; Nocera, D. G. *Energy Environ.*

Sci. **2011**, *4*, 499.
(43) Smith, R. D. L.; Prévot, M. S.; Fagan, R. D.; Trudel, S.; Berlinguette, C. P. *J. Am. Chem. Soc.* **2013**, *135*, 11580.
(44) Surendranath, Y.; Bediako, D. K.; Nocera, D. G. *Proc. Natl. Acad. Sci.* **2012**, *109*, 15617.
(45) Surendranath, Y.; Kanan, M. W.; Nocera, D. G. *J. Am. Chem. Soc.* **2010**, *132*, 16501.
(46) Fletcher, S. *J. Solid State Electrochem.* **2009**, *13*, 537.
(47) Gileadi, E. *Electrode Kinetics for Chemists, Engineers, and Materials Scientists*; VCH Publishers, Inc.: New York, 1993.
(48) Ahrenholtz, S. R.; Epley, C. C.; Morris, A. J. *J. Am. Chem. Soc.* **2014**, *136*, 2464.
(49) DuBois, D. L.; Miedaner, A.; Haltiwanger, R. C. *J. Am. Chem. Soc.* **1991**, *113*, 8753.
(50) Kanan, M. W.; Nocera, D. G. *Science* **2008**, *321*, 1072.
(51) Klet, R. C.; Liu, Y.; Wang, T. C.; Hupp, J. T.; Farha, O. K. *J. Mater. Chem. A* **2016**, *4*, 1479.
(52) Usov, P. M.; McDonnell-Worth, C.; Zhou, F.; MacFarlane, D. R.; D'Alessandro, D. M. *Electrochim. Acta* **2015**, *153*, 433.
(53) Singh, A.; Chang, S. L.; Hocking, R. K.; Bach, U.; Spiccia, L. *Catal. Sci. Technol.* **2013**, *3*, 1725.
(54) Singh, A.; Chang, S. L. Y.; Hocking, R. K.; Bach, U.; Spiccia, L. *Energ. Environ. Sci.* **2013**, *6*, 579.
(55) Qin, M.; Maza, W. A.; Stratakes, B. M.; Ahrenholtz, S. R.; Morris, A. J.; He, Z. *Journal of The Electrochemical Society* **2016**, *163*, F437.
(56) Moulder, J. F.; Stickle, W. F.; Sobol, P. E.; Bombem, K. D. *Handbook of X-ray Photoelectron Spectroscopy*; Physical Electronics, Inc., 1995.

7. Conclusions and Future Work

The ability of a material to transport charge is a critical requirement in order for ultimate applications in catalysis. In this work, metal-organic framework (MOF) materials have been investigated for their charge transport properties to be utilized for catalytic processes for alternative energy generation. There are several mechanisms which can explain charge conduction within frameworks depending on the properties of the MOF: (1) delocalized valence and conduction bands, which mediate migration of electrons and holes throughout crystalline materials; (2) a redox hopping mechanism, where charge propagation can be facilitated through discrete electron donor/acceptor sites within materials containing redox available states; (3) a through-bond approach where continuous binding networks between framework components, either through M-linker bonds (i.e. M-N or S) or via guest molecules, facilitate a pathway for charge mobility throughout the framework; (4) conduction via through-space interactions, which utilizes π-π stacking of aromatic organic linker molecules.

In order to gain a deeper understanding of charge transport properties in MOFs and what structural features facilitate conduction, we began our investigations by selecting a MOF comprised of components capable of undergoing redox reactions and studying its ability to transport charge throughout the framework using electrochemical techniques. Specifically, a thin film of a metalloporphyrin MOF (CoPIZA) consisting of [5,10,15,20-(4-carboxyphenyl)porphyrin]Co(III) (CoTCPP) struts bound by linear trinuclear Co^{II}-carboxylate clusters has been prepared solvothermally on conductive fluorine doped tin oxide (FTO) substrates. The MOF film, designated as CoPIZA/FTO, contains large cavities with unrestricted access to the metal centers throughout the framework. The conductivity of the film was

determined using electrochemical impedance spectroscopy and found to be on the order of 10^{-8} S cm^{-1}. Even with this moderate electrical conductivity exhibited by CoPIZA/FTO, upon applied potential, the entire film could be reduced and remained stable over the time frame of several hours. As a result, the mechanism of charge transport was determined to be one of redox hopping, supported by both electrochemical and spectroelectrochemical analysis. The efficiency of reduction via redox hopping was found to be moderate with a rate consistent with a redox hopping mechanism. Future work with this project involves replacing the Co-clusters of the framework with insulating nodes, such as Zn or Zr metal centers, to confirm the role of the clusters in electron transport. If the nodes are indeed active in the conduction mechanism, it would be expected that changing the redox active nodes to inactive metals would decrease the rate of electron transfer throughout the framework. Also, changing the metal centers of the metalloporphyrin strut (i.e., Ni^{II}, Fe^{III}, Zn^{II}, etc.) and studying the electron transport properties would allow for structural insight into properties required for efficient conduction. Additionally, since metalloporphyrin molecules have demonstrated catalytic activity for the reduction of organohalide substrates, the catalytic activity of CoPIZA/FTO was successfully demonstrated via the electrocatalytic reduction of CCl_4. This work has provided a vital scaffold for further development of MOF thin films and their applications as electrocatalysts. In fact, these groundbreaking results have sparked research interest for the use of metalloporphyrin MOF thin films for CO_2 reduction and H_2O oxidation.

Additionally, due to their porosity, high surface areas, and tunability, MOFs have shown promise for applications in gas separation and storage. For catalytic applications (e.g., CO_2 reduction or H_2O oxidation), it is advantageous if the material demonstrates an innate affinity for the substrate, which can be investigated using gas sorption isotherm measurements. As a result,

there is considerable interest in the development of MOFs capable of selectively capturing CO_2 from the gaseous mixture that results from combustion of carbon-based fossil fuels, which could be followed by catalytic reduction of CO_2, in order to reduce the harmful effects the greenhouse gas is having on the global environment. There are several functionalities that can be incorporated into MOFs in order to demonstrate greater adsorptive properties and selectivity for CO_2. MOFs whose pores are functionalized with nitrogen-containing organic linkers have shown enhanced CO_2 adsorption due to increased interactions with the gas molecule. Another approach involves the generation of unsaturated metal centers within the framework, which are typically obtained following an activation or desolvation procedure to remove bound solvent molecules.

We have developed two MOFs containing unsaturated Zn metal centers without the need for an activation procedure and investigated their gas sorption properties and selectivity for CO_2. The inorganic structural building unit of the frameworks is comprised of Zn(II) bridged by the 2-carboxylate or 5-carboxylate pendants of 2,5-pyridine dicarboxylate (pydc) to form a 1D zigzag chain. The zigzag chains are linked by the bridging 2,5-carboxylates across the Zn ions to form 3D networks with formulas of $Zn_4(pydc)_4(DMF)_2 \cdot 3DMF$ **(1)** and $Zn_2(pydc)_2(DEF)$ **(2)**. The framework **(1)** contains coordinated DMF as well as DMF solvates molecules in the framework pores (DMF = *N*,*N*-dimethylformamide), while **(2)** contains coordinated DEF (DEF = *N*,*N*-diethylformamide). **(1)** displayed a reversible type-I sorption isotherm for CO_2 and N_2 gases, while isotherms of **(2)** were not able to reach saturation, indicative of pore sizes too small for the gas molecules to penetrate. The binding of CO_2 into the framework of **(1)** was found to be exothermic with a zero coverage heat of adsorption of −27.7 kJ/mol, which is consistent with a mechanism of adsorption that involving CO_2 binding to the unsaturated Zn(II) metal centers present in the crystal structure. Additionally, **(1)** demonstrated selectivity for CO_2 over N_2 at 296

K due to increased affinity of the Lewis acidic metal centers toward CO_2. The incorporation of unsaturated metal centers in the frameworks resulted in increased CO_2 sorption capability and selectivity and has allowed for a deeper understanding of desirable properties for the design of MOFs for CO_2 capture applications.

With these Zn-based frameworks comprising different structural units than the previously investigated metalloporphyrin-based MOF, the mechanism of charge transport throughout the MOF powders was investigated to gain insight into the structure-function relationship of conduction. The previously discussed redox hopping electron transport mechanism throughout the CoPIZA framework requires close proximity of the redox centers (linkers and metal nodes of the framework), as well as their ability to undergo redox transactions at similar potentials. With the incorporation of redox inactive Zn metal centers, a conduction pathway involving the metal would not be viable. Electrochemical impedance spectroscopy was used to determine the conductivity of frameworks **(1)**, **(2)**, and MOF-69C ($Zn_3(OH)_2(bdc)_2$·2DEF, where bdc = 1,4-benzenedicarboxylic acid), which were $3.6 \pm 0.3 \times 10^{-6}$ S cm^{-1}, $1.35 \pm 0.03 \times 10^{-6}$ S cm^{-1}, and $1.8 \pm 0.2 \times 10^{-6}$ S cm^{-1}, respectively. The mechanism of conduction was found to be dependent on the presence of solvent in the MOF pores as well as bound solvent, as observed in the structure of **(1)**. The extended solvent network provided a pathway for charge transport throughout the framework and resulted in increased conductivity. This was further evidenced by temperature dependent conductivity coupled with differential scanning calorimetry (DSC) and variable temperature solid-state nuclear magnetic resonance experiments (VT-SSNMR), which demonstrated that MOF-69C undergoes a reversible solid-solid phase transition as a result of rotation of the carbonyl carbon atom of DEF solvate molecules. This suggests that solvent is involved in the mechanism of conduction of charge throughout the framework and that MOFs

display conduction properties facilitated by guest molecules in the frameworks.

These results have demonstrated that there are several approaches that can be taken to realize charge transport in MOFs: (1) through a redox hopping mechanism in frameworks comprised of redox active nodes and linker molecules; and (2) through the incorporation of solvent or guest molecules, which form an extended network capable of mediating charge transport throughout the framework. The structural and mechanistic insights gained from these investigations show promise for the smart design of MOFs with possible applications in electronic devices. An area of further study with this project would be to investigate the conduction in the presence of different solvents (i.e. after solvent exchange with methanol, acetone, ethanol, etc.) or following an activation procedure to remove solvent molecules from the pores. As the solvent molecules have proven crucial to the overall conduction mechanism, changing the properties of the solvent or removing it entirely would be expected to alter the charge transport throughout the frameworks.

For ultimate applications in the catalytic processes for renewable energy generation, specifically water oxidation, complex assemblies capable of efficiently separating charge and managing proton and electron transfer processes must be developed. With our previous studies confirming the redox hopping charge transport ability with a Co-based MOF, we began investigations into electrocatalytic water oxidation with a MOF film. Specifically, a cobalt-based MOF containing 2-pyrimidinolate (pymo) linkers, designated as $Co(pymo)_2$, was chosen to investigate its electrocatalytic activity toward water oxidation. However, during the course of electrochemical measurements, the Co metal centers of the $Co(pymo)_2$ framework became oxidized to form Co-oxides on the electrode surface, which were ultimately the species responsible for the observed catalytic water oxidation. The proposed reaction pathway involves

the binding of water to Co^{III} metal centers followed by proton abstraction through the pyrimidinolate linker, which occurs concurrently with MOF decomposition to deposit cobalt-oxides on the electrode surface. While we were able to demonstrate electrochemical water oxidation catalysis, the observed catalysis is due to cobalt-oxides, as the framework is unstable due to conformational changes about the metal center associated with the redox reactions.

Therefore, in addition to the requirements mentioned above for the development of catalytic species, these systems must also remain structurally stable as a result of the applied potentials and consequent catalytic reactions. Frameworks prepared from higher valency, redox inactive metal nodes, such as Zr, have recently gained attention in the literature for their stability in a variety of chemical environments. While these frameworks demonstrate increased stability, the Zr-nodes are not active for catalytic applications. Therefore, the incorporation of a homogeneous molecular catalyst into the framework backbone can be beneficial for several reasons: (1) it allows for better control over the active site surroundings; (2) possible degradation pathways associated with the homogeneous catalytic mechanism are removed due to the separation of molecules and the rigidity of the framework; (3) a higher concentration of accessible active sites is available on the electrode surface; (4) the reaction is not limited by the diffusion of catalyst to the electrode surface.

Considering these design features, we have demonstrated a new strategy for cooperative catalysis and proton abstraction in a Zr-based MOF. A metalloporphyrin linker (nickel(II) meso-tetrakis(4-carboxyphenyl)porphyrin (Ni(II)TCPP)) inspired by a known water oxidation catalyst, operating in the presence of phosphate buffer, was incorporated into the framework of a PCN-224-Ni MOF thin film. Films of PCN-224-Ni were found to electrochemically facilitate the water oxidation reaction at near neutral pH. The mechanism of water oxidation proceeded via

initial oxidation of the porphyrin linker followed by binding of water to the Ni(II) centers with subsequent proton transfer to the Zr nodes. However, over the course of 60 min of applied potential, PCN-224-Ni failed to complete one catalytic cycle, which is attributed to the limited availability of proton-abstraction sites on the Zr-oxo nodes of the framework.

The presence of a base (phosphate was used for the homogeneous catalyst) in solution could serve as the proton abstractor and circumvent the restricted binding sites available on the Zr clusters. However, electrochemical measurements cannot be conducted in phosphate buffer solutions because Zr-based frameworks are unstable in the presence of phosphates due to the competitive binding with the carboxylate functionalities that bind Zr-clusters and linker molecules. As a result of this limitation, future work in this project would involve the development of Zr frameworks comprised of metal-phosphonate linkages rather than metal-carboxylate bonds. Electrochemical measurements on these new frameworks could then be conducted in phosphate buffer, which would serve as the proton abstractor species in the catalytic mechanism, and potentially result in greater efficiencies.

We have established frameworks capable of facilitating electron transport through redox active components, as well as through extended networks of solvent molecules in the pores. The studies of electron transport mechanisms throughout these materials have resulted in the design a MOF that is capable of facilitating the electrocatalytic water oxidation reaction. These results have allowed us to gain a deeper understanding of desirable properties of MOFs for charge transport and catalytic applications, and therefore, will serve as the foundation for the future design and development of MOFs for alternative energy catalysis.